Supersonic Close-coupled Atomization: Experimental Insights

Vom Fachbereich Maschinenbau
der Technischen Universität Darmstadt
zur
Erlangung des Grades eines Doktor-Ingenieurs (Dr.-Ing.)
genehmigte

Dissertation

vorgelegt von

Niklas Apell, M.Sc.

aus Kassel

Berichterstatter:	Prof. Dr.-Ing. habil. Cameron Tropea
1. Mitberichterstatter:	Prof. Dr. rer. nat. habil. Andreas Dreizler
2. Mitberichterstatter:	Apl. Prof. Dr. Sc. Ilia V. Roisman
Tag der Einreichung:	31.05.2023
Tag der mündlichen Prüfung:	03.08.2023

Darmstadt 2023

D 17

Apell, Niklas:
Supersonic Close-coupled Atomization: Experimental Insights

Darmstadt, Technische Universität Darmstadt
Jahr der Veröffentlichung der Dissertation auf TUprints: 2023
Tag der mündlichen Prüfung: 03.08.2023

Bitte zitieren Sie dieses Dokument als:
URN: urn:nbn:de:tuda-tuprints-244739
URI: https://tuprints.ulb.tu-darmstadt.de/id/eprint/24473

Erklärung

Hiermit erkläre ich, dass ich die vorliegende Arbeit, abgesehen von den in ihr ausdrücklich genannten Hilfen, selbständig verfasst habe.

Darmstadt, den 31.05.2023

N. Apell

Dedicated to my brother Jan

Abstract

Along with the growing economic importance of metal additive manufacturing by processes such as laser-based powder bed fusion, the demand for high-quality metal powders as the corresponding raw material is also increasing. These powders must have a variety of specific properties and be characterized, among other things, by a well-defined particle size distribution. They are primarily produced by the expensive supersonic close-coupled atomization of molten metals, which often results in a significant proportion of powder that is not suitable for additive manufacturing. In order to nevertheless meet the increasing demand and to increase the economic efficiency of the process, it is necessary to develop predictive modeling capabilities, which allow the process parameters to be specifically adjusted to a desired powder quality.

In this thesis, the atomization of liquids by means of a generic supersonic close-coupled atomizer is investigated experimentally. The design of the atomizer is based on a real powder production plant. However, instead of molten metal, various substitute liquids are atomized to improve the accessibility for a variety of measurement techniques. In order to investigate the influence of the operational parameters on the atomization result, measurements are carried out using the phase Doppler measurement technique. This allows for determining the local particle size and velocity as well as their distributions. Insights into the atomization mechanisms are gained by different imaging techniques.

The results of this thesis contribute to an improved understanding of the supersonic close-coupled atomization process. They show how the interaction between the gas flow and the liquid flow leads to the formation of the spray. Furthermore, they illustrate how the particle size distribution is influenced by the operational parameters and the physical properties of the liquid. They also provide insights into the mechanisms responsible for primary and secondary atomization. Consequently, this thesis provides a foundation for formulating novel models describing the supersonic close-coupled atomization process.

Kurzfassung

Einhergehend mit der wachsenden wirtschaftlichen Bedeutung der additiven Fertigung von metallischen Bauteilen durch Prozesse wie etwa das selektive Laserschmelzen steigt auch die Nachfrage nach qualitativ hochwertigen Metallpulvern als dem entsprechenden Rohmaterial. Diese Pulver müssen eine Vielzahl von spezifischen Eigenschaften aufweisen und sich unter anderem durch eine wohldefinierte Partikelgrößenverteilung auszeichnen. Hergestellt werden sie vornehmlich durch die aufwändige Überschall-Gaszerstäubung von Metallschmelzen, bei der häufig ein nicht unerheblicher Anteil von Pulver anfällt, der ungeeignet für die additive Fertigung ist. Um dennoch der steigenden Nachfrage gerecht zu werden und die Wirtschaftlichkeit des Verfahrens zu erhöhen, ist es notwendig, Zerstäubungsmodelle zu entwickeln, welche ein gezieltes Abstimmen der Prozessparameter auf eine gewünschte Pulverqualität ermöglichen.

Im Rahmen der vorliegenden Arbeit wird die Zerstäubung von Flüssigkeiten mittels eines generischen Überschall-Gaszerstäubers experimentell untersucht. Die Konstruktion des Zerstäubers orientiert sich an einer realen Pulverproduktionsanlage. Anstelle von Metallschmelzen werden jedoch verschiedene Ersatzflüssigkeiten zerstäubt, um die Zugänglichkeit für eine Vielzahl von Messtechniken zu verbessern. Zur Untersuchung des Einflusses von Betriebsparametern auf das Zerstäubungsergebnis werden Messungen mittels Phasen-Doppler-Messtechnik durchgeführt. Diese erlaubt das ortsaufgelöste Vermessen von Tropfengrößen und -geschwindigkeiten sowie deren Verteilungen. Einblicke in die Zerstäubungsmechanismen werden durch bildgebende Verfahren ermöglicht.

Die Ergebnisse dieser Arbeit tragen zu einem verbesserten Verständnis von der Überschall-Gaszerstäubung bei. Sie zeigen, wie die Interaktion zwischen Gas- und Flüssigkeitsströmung zur Ausbildung des Sprühkegels führt. Weiterhin verdeutlichen sie, wie die Partikelgrößenverteilung von den Betriebsparametern und den physikalischen Eigenschaften der Flüssigkeit beeinflusst

wird. Außerdem liefern sie einen Einblick in die Mechanismen, die für die Primärzerstäubung sowie die Sekundärzerstäubung verantwortlich sind. Somit stellt diese Thesis eine Grundlage dar, um neuartige Modelle zur Beschreibung der Überschall-Gaszerstäubung zu formulieren.

Acknowledgments

First and foremost, I would like to express my sincere gratitude to Prof. Dr.-Ing. habil. Cameron Tropea for providing me with the opportunity to conduct my research at the Institute for Fluid Mechanics and Aerodynamics (SLA) and for supervising me over the past three years. I am very grateful for his trust in me and the many lessons I have learned during this time. Furthermore, I would like to thank Prof. Dr. rer. nat. habil. Andreas Dreizler for refereeing this thesis. I am very thankful to apl. Prof. Dr. Sc. Ilia V. Roisman for the many discussions we have had, which have often challenged and broadened my views. Prof. Dr.-Ing. Jeanette Hussong's support during my time at the Institute for Fluid Mechanics and Aerodynamics is greatly appreciated.

The financial support from the Indo German Science & Technology Centre (IGSTC) as part of the 2+2 project *Metal Powder Production for Additive Manufacturing* (PPAM) is gratefully acknowledged. Along with the Technical University of Darmstadt (TUDa), three other institutions have contributed to this project. I would like to thank Prof. Dr. Suman Chakraborty and his group at the Indian Institute of Technology Kharagpur (IIT) as well as Prof. Dr. Saptarshi Basu, Prof. Dr. Aloke Kumar and their students at the Indian Institute of Science Bengaluru (IISc) for their valuable contributions to this collaborative project. Without a doubt, I have fond memories of my short but joyful stay in Bangalore. I am very grateful for the many discussions I have had with apl. Prof. Dr.-Ing. Hans-Jürgen Odenthal and Dr.-Ing Norbert Vogl from the SMS group GmbH (SMS). Their continued interest in my work has greatly improved this thesis.

It has been a very rewarding experience for me to work with my students Tobias Schrimpl, Santhoshkumar Piskala Dilipkumar and Daniel Mirschinka. Their commitment and contributions have certainly enhanced the outcome of this thesis.

I am very thankful to Ilona Kaufhold and her team in the mechanical workshop as well as Martin Weiss in the electrical workshop for their help in bringing my ideas to life. Furthermore, I very much appreciate Alexander Beck's constant efforts to ensure that I was quite literally always *under pressure.*

Many wonderful colleagues have made the past three years a memorable time of my life. It has been an absolute pleasure to share this journey from start to finish with Louis Reitter, Bastian Stumpf and Kilian Köbschall. I am very grateful to Max Luh, Andreas Bauer and Lingxi Li for welcoming me with open arms in Griesheim. Needless to say, I cherish the memories of the time I have spent with Ivan Joksimovic exploring beautiful Lisbon. I really appreciate Benedikt Schmidt for always being helpful and Johannes Kissing for encouraging me when I needed him to. I have enjoyed many short walks and long discussions with Max Lausch and have found a like-minded person in Philipp Brockmann, who has followed me down many rabbit holes without hesitation. Finally, I am very grateful for the chaos that has been brought into my daily work-life by my *lab buddy* Marija Gajevic Joksimovic.

Many thanks to Max Lausch and Philipp Brockmann for proofreading parts of this thesis.

Last but certainly not least, I would like to wholeheartedly thank my family for their unconditional support. Lothar, Petra and Jan, words cannot describe how grateful I am for having you by my side.

Thank you.

Niklas

Contents

Part I

Preface

1 Introduction

1.1 Motivation

In recent years, additive manufacturing (AM) has evolved from rapid prototyping as a means for fabricating part representations (i.e., visualization models) to a manufacturing technology employed across a wide range of industries not only for prototyping, but also for tooling, final part production and education (Milewski, 2017; Gibson et al., 2021; Wohlers et al., 2022). This development has led to a strong growth in the economic importance of the additive manufacturing industry, as can be seen in Fig. 1.1, which shows the evolution of the estimated global annual revenue from related products and services over a period of 13 years. In fact, the global revenue of the additive manufacturing industry has been estimated at \$15.2 billion in 2021, representing a growth of 19.5 % compared to 2020, and is expected to reach \$44.5 billion by 2026 (Wohlers et al., 2022; Simon & Gurley, 2022).

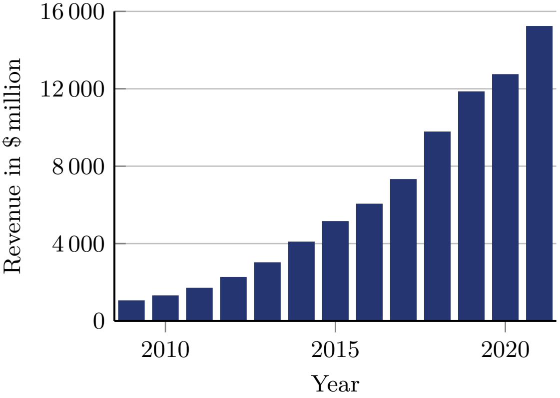

Figure 1.1: Evolution of the estimated global annual revenue from additive manufacturing products and services according to Wohlers et al. (2022).

According to the German Institute for Standardization (2022), additive manufacturing is defined as the "process of joining materials to make parts from 3D model data, usually layer upon layer, as opposed to subtraction manufacturing and formative manufacturing methodologies". Hence, the main distinction between additive manufacturing and conventional manufacturing techniques is that in the former material is added together in order to create a part which is larger than the material itself (Gibson et al., 2021). In general, the industrial application of additive manufacturing is primarily driven by enhancing part performance and reducing costs (Wohlers et al., 2022). Indeed, for the final part production, the benefits of additive manufacturing include a faster and simpler product development process due to a reduction in steps and resources, the possibility of on-demand manufacturing with reduced lead times and a reduction in tooling and waste (Yang et al., 2017; Gibson et al., 2021; Wohlers et al., 2022). Furthermore, it allows for designing lightweight parts with optimized topology, which adds value beyond what is possible employing conventional manufacturing techniques, providing an additional competitive advantage (Milewski, 2017; Moreau, 2018; Wohlers et al., 2022).

Metal additive manufacturing by means of laser-based powder bed fusion (PBF-L), in particular, has become a major driver in the adoption of additive manufacturing (Moreau, 2018; Gibson et al., 2021). This is due to the fact that it is well suited for final manufacturing applications, allowing for high part quality and desirable mechanical properties (Wohlers et al., 2022). Indeed, an estimated 2379 metal additive manufacturing machines have been sold in 2021, an increase of 10.7 % compared to 2020 (Wohlers et al., 2022).

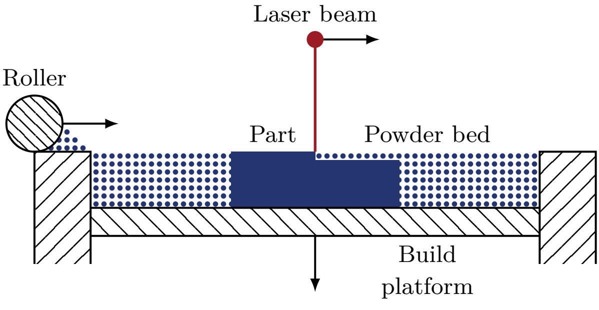

Figure 1.2: Schematic illustration of the laser-based powder bed fusion process.

A schematic illustration of the basic laser-based powder bed fusion process, which is based on the work of Carter Jr. and Jones (1993), is shown in Fig. 1.2. Here, powder is spread on a build platform, forming a continuous powder bed. A focused laser beam scans the powder bed, selectively fusing regions of its surface due to the local input of thermal energy. After the scanning is completed, the build platform is lowered slightly and a new thin layer of powder is applied and smoothed with a roller. These steps are repeated in an iterative process until the part is completed (Milewski, 2017; Yang et al., 2017). In this way, the part is built layer-by-layer, with each layer representing a thin slice of the final geometry (Gibson et al., 2021).

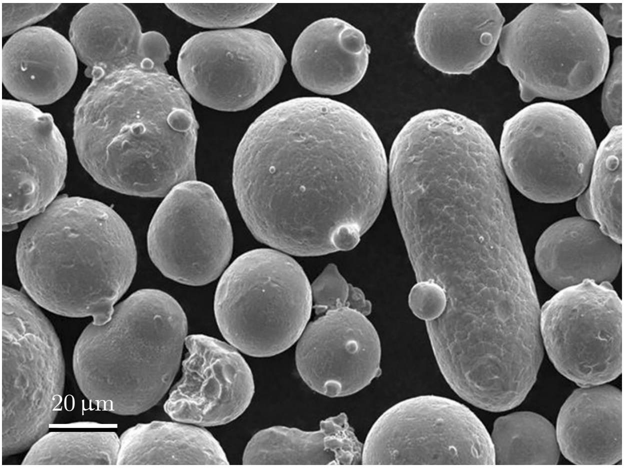

Figure 1.3: Scanning electron microscopy image of stainless steel powder particles showing a variety of different morphologies. (Reprinted from Slotwinski & Garboczi, 2015, with permission from Springer Nature. © 2015 Springer Nature.)

The quality and consistency of parts manufactured additively depends, among other things, on the properties of the employed feedstock material (Dawes et al., 2015). For example, the mechanical properties of a metal part are strongly influenced by its microstructure, that is, a finer microstructure results in a higher tensile strength but also in a lower ductility (Gibson et al., 2021). Considering the production of metal parts by means of the laser-based powder bed fusion process, the respective feedstock material is metal powders, the majority of which are various types of steel and alloys based on titanium, nickel, copper or aluminum (Gibson et al., 2021; Wohlers et al., 2022). These powders are mainly characterized by the size distribution and the morphology of the corresponding particles. An exemplary scanning electron microscopy (SEM) image of stainless steel powder particles is shown in Fig. 1.3. Here, the individual particles exhibit a variety of different morphologies, including non-sphericity and surface defects. However, the laser-based powder bed fusion process, in particular, requires a small layer thickness, a high packing density and a good powder flowability in order to allow for a high part quality (Gibson et al., 2021; Wohlers et al., 2022). This results in the following requirements for the particles of suitable metal powders (Dawes et al., 2015; Milewski, 2017; Yang et al., 2017; Neikov et al., 2019; Brennen, 2022):

- Size in the range from 15 µm to 45 µm
- High degree of sphericity
- Low number of surface defects
- Low porosity
- Low number of satellite particles
- High chemical purity

While, in general, there are a number of processes available for the production of metal powders, including chemical, physical and mechanical methods (Upadhyaya, 2002; Neikov et al., 2019), meeting these demanding requirements poses a challenge, especially in large-scale production. Typically, the powders used in metal additive manufacturing are produced by means of gas atomization (Brennen, 2022). Here, the kinetic energy provided by a high-pressure flow of inert gas is employed for breaking up a stream of molten metal into fine droplets (Gibson et al., 2021). This approach has the advantage of producing fine spherical powder particles of high chemical purity (Milewski, 2017). Supersonic close-coupled atomization (CCA), in particular, has been found to be well suited for producing particularly fine powders (Espina & Piomelli, 1998; Heck et al., 2000). However, like other powder production methods, this process results in a particle size distribution of finite width, with only a fraction of the particles in the size range needed for the laser-based powder bed fusion process (Dawes et al., 2015; Li et al., 2019). As a result, expensive post-treatment in the form of sieving is often required in order to achieve the optimal particle size range and to remove any irregularly shaped particles (Milewski, 2017). This is certainly a major contributor to the cost of these metal powders (Wohlers et al., 2022), which is crucial, as they are the largest ongoing expense throughout the lifecycle of an additive manufacturing machine (Dawes et al., 2015). Consequently, the high cost of metal powders remains a limiting factor in the widespread adoption of metal additive manufacturing (Milewski, 2017).

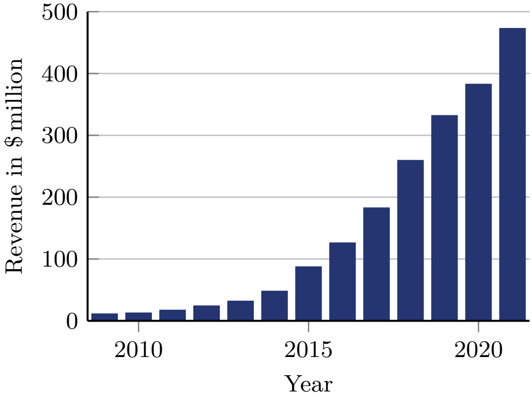

Figure 1.4: Evolution of the estimated global annual revenue from metals for additive manufacturing according to Wohlers et al. (2022).

Still, the demand for high-quality metal powders suitable for additive manufacturing is increasing, as can be seen in Fig. 1.4, which shows the evolution of the estimated global annual revenue from metals for additive manufacturing over a period of 13 years. In fact, the global revenue has been estimated at $473.6 million in 2021, representing a growth of 23.5 % compared to 2020 (Wohlers et al., 2022).

It is evident that improvements in the supersonic close-coupled atomization process are needed not only to meet the increasing demand for high-quality metal powders, but also to reduce the associated production costs, making it more economically viable. This requires a better understanding of the physics involved in the process and, ultimately, predictive modeling capabilities, which allow the process parameters to be tailored to the desired powder quality.

1.2 Outline

This thesis is dedicated to providing experimental insights into the supersonic close-coupled atomization process, which contribute to improving the understanding of the process and provide a foundation for the future development of novel physics-based predictive modeling capabilities. Its contents are structured as follows:

An introduction to the application of the supersonic close-coupled atomization process for the production of metal powders is given in **Chapter 2**. Furthermore, a brief overview of existing approaches to modeling the atomization process as well as the resulting particle size is provided. This serves the purpose of identifying open research questions.

In **Chapter 3**, the experimental methods employed for studying the supersonic close-coupled atomization process are described. This includes a detailed description of the atomizer research facility. In addition, the applied measurement techniques and the methods used for the data evaluation are presented. These include the phase Doppler measurement technique as well as two different imaging techniques.

A first understanding of the characteristics of the supersonic close-coupled atomization process is developed in **Chapter 4**. This is done by separately studying the gas-only flow and the liquid-only flow. Furthermore, the multiphase flow is considered, which provides insight into the coupling between the gas flow and the liquid flow.

The resulting spray is investigated in **Chapter 5** by means of the phase Doppler measurement technique. The focus is on analyzing the influence of the operational parameters, the geometric design of the atomizer unit and the physical liquid properties on the atomization result.

In **Chapter 6**, the actual atomization process is studied in more detail. A distinction is made between the primary atomization and the secondary atomization. Different imaging techniques are employed for identifying and describing relevant breakup mechanisms. Furthermore, means for influencing theses mechanisms are investigated.

Chapter 7 completes this thesis by providing a summary of the most important conclusions as well as recommendations for possible future investigations.

Part II

Background

2 Modeling of Supersonic Close-coupled Atomization

In order to establish a general understanding of the basic principle of the supersonic close-coupled atomization process, this chapter provides an introduction to its fundamentals. In Section 2.1, the application of the process to the production of metal powders is briefly described. This includes an outline of the basic process and the components involved, with a focus on the unique characteristics of this particular atomization process. Furthermore, a concise overview of the existing approaches to modeling the supersonic close-coupled atomization process is given in Section 2.2. This serves the purpose of highlighting relevant challenges and of identifying open research questions. Finally, in Section 2.3, the objectives of this thesis are formulated based on the identified open research questions.

2.1 Supersonic Close-coupled Atomization

Supersonic close-coupled atomization is a two-fluid atomization process. This means that the working fluid is atomized with the aid of an additional fluid, in this case due to the interaction with a supersonic gas flow (Henein et al., 2017). Here, the term *close-coupled* refers to the geometrically close coupling of the two fluid flows downstream of the respective nozzles, that is, the liquid interacts with the gas flow immediately upon exiting the liquid nozzle (Anderson & Terpstra, 2002). Both of these characteristics of the supersonic close-coupled atomization process (i.e., supersonic gas flow and close coupling) are crucial for the application to the production of metal powders. However, before discussing the reasons for this in more detail, it is necessary to understand the basic process employed for the production of metal powders.

In Fig. 2.1, a schematic illustration of a plant used for the production

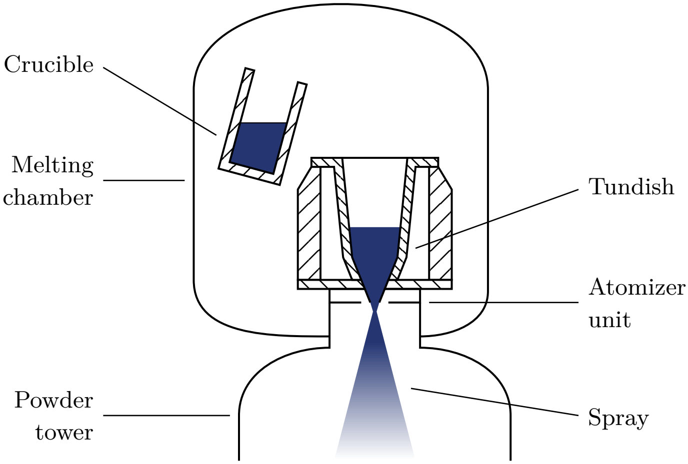

Figure 2.1: Schematic illustration of a plant used for the production of metal powder by means of the supersonic close-coupled atomization of molten metal.

of metal powders by means of the supersonic close-coupled atomization of molten metal is shown. As can be seen, the production plant is divided into a melting chamber and a powder tower (Bauckhage, 1992). The former allows the metal to be melted in an inert atmosphere in a pivoted crucible, which provides means for pouring the molten metal into a tundish. The outlet at the bottom of the tundish is connected to the atomizer unit and feeds the molten metal into the liquid nozzle (Bauckhage, 1992). However, there are variations of this configuration where the crucible is positioned directly above the atomizer unit (Allimant et al., 2009). This eliminates the need for tilting the crucible. The melting chamber and the powder tower are connected by the atomizer unit, which comprises the liquid nozzle and the gas nozzle and is responsible for the actual atomization. Depending on the design of the production plant, the flow of the molten metal through the liquid nozzle, which is characterized by the liquid mass flow rate $\dot{m}_\mathrm{l}$, is either driven by gravity alone or augmented by an additional pressure difference between the melting chamber and the powder tower (Li et al., 2019). Often, a stopper rod is employed for starting and stopping the outflow of the molten metal (Wolf & Bergmann, 2002). The spray forms downstream of the atomizer unit in an inert atmosphere in the powder tower, which is tall enough to allow the individual particles to cool down and solidify in-flight before reaching the bottom (Bergmann et al., 2000). This is possible due to the particularly high cooling rates of more than $10^4\,\mathrm{K\,s^{-1}}$ caused by the strong difference in the temperature ΔT between the molten metal and the gas (Pérez-de León et al., 2016; Si et al., 2017). The use of inert gases such as argon, nitrogen and helium for the atomization allows for the production of chemically pure powders (Bauckhage, 1992). Since neither the powder collection at the bottom of the powder tower nor any of the subsequent process steps are relevant to the actual atomization, they are neither shown in Fig. 2.1 nor discussed here.

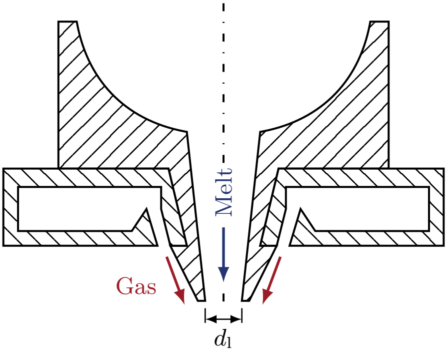

Figure 2.2: Schematic illustration of the atomizer unit of a typical supersonic close-coupled atomizer. The two fluid flows through the respective nozzles are indicated. (Adapted from Apell et al., 2021.)

The most important component of the powder production plant is the atomizer unit, since it comprises the liquid nozzle as well as the gas nozzle. A schematic illustration of the atomizer unit of a typical supersonic close-coupled atomizer is shown in Fig. 2.2. The circular liquid nozzle is located right at the center of the atomizer unit and protrudes slightly from the surrounding coaxial gas nozzle, which is aimed at a point slightly downstream of the liquid nozzle (Aksoy & Ünal, 2006). The diameter of the liquid nozzle d_l (see Fig. 2.2) is typically in the order of 1 mm (Baram et al., 1988). Responsible for the actual atomization and, therefore, for the formation of the spray is the interaction between the gas flow and the liquid flow downstream of the liquid nozzle. The geometric design of the atomizer unit, that is, the shape and the dimensions of the liquid nozzle tip and the configuration of the gas nozzle, has a strong influence on the atomization, as it determines the coupling of the gas flow and the liquid flow and, therefore, the flow field downstream of the atomizer unit (Anderson & Figliola, 1988; Anderson & Terpstra, 2002). However, a common feature of all geometric designs of close-coupled atomizers is the close coupling of the two fluid nozzles, which results in the liquid interacting with the gas flow immediately upon exiting the liquid nozzle. This has the advantage of reducing the distance the gas has to travel before impacting on the liquid, which reduces losses and allows for a more efficient transfer of kinetic energy during the interaction between the gas and the liquid (Anderson & Terpstra, 2002; Ting et al., 2002). Indeed, this is an important aspect of the application of the supersonic close-coupled atomization to the production of metal powders. Considering that molten metal is generally characterized by particularly high values of the liquid dynamic viscosity μ_l and the surface tension σ (Bauckhage, 1992), high-velocity gas flows are required in order to effectively break up the stream of molten metal and to produce particularly fine particles (Mates & Settles, 1996).

Table 2.1: Physical properties of liquid stainless steel 316L at a liquid temperature T_l of 1700 °C according to Odenthal et al., 2021.

Property	Value
Density	$6879\,\mathrm{kg\,m^{-3}}$
Dynamic viscosity	$6.4\,\mathrm{mPa\,s}$
Surface tension	$1570\,\mathrm{mN\,m^{-1}}$

As an example, the physical properties of liquid stainless steel 316L at a liquid temperature T_l of 1700 °C according to Odenthal et al. (2021) are given in Table 2.1. This includes the liquid density ρ_l, the liquid dynamic viscosity μ_l and the surface tension σ. As can be seen, all three properties exhibit particularly high values. For instance, the surface tension σ is two orders of magnitude higher than for water at a liquid temperature T_l of 20 °C (i.e., $\sigma \approx 73\,\mathrm{mN\,m^{-1}}$). While this makes the atomization of the molten metal more difficult, the high surface tension σ has the advantage of facilitating the formation of spherical particles during the solidification (Schwenck et al., 2017).

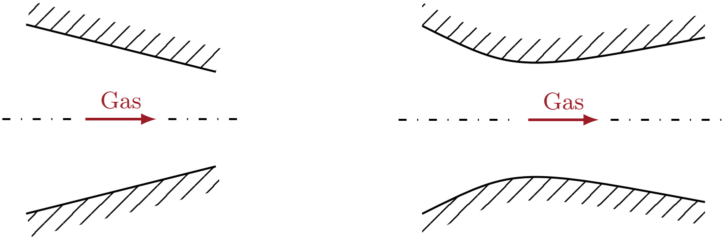

(a) Convergent **(b)** Convergent-divergent

Figure 2.3: Schematic illustration of gas nozzle designs employed in supersonic close-coupled atomization. The flow direction of the gas is indicated. (Adapted from Apell, 2019.)

Another characteristic of the industrial application of the supersonic close-coupled atomization is that the gas nozzle is typically operated at particularly high gas stagnation pressures[1] $p_{\mathrm{t,g}}$ (Anderson & Figliola, 1988). This serves the purpose of achieving particularly high local absolute gas velocities u_{g} by employing gas nozzle designs which allow for producing locally supersonic gas flows. This condition is expressed in terms of the Mach number Ma, which is defined as (Anderson, 1990):

$$Ma = \frac{u_{\mathrm{g}}}{a_{\mathrm{g}}}. \tag{2.1}$$

Here, a_{g} is the local speed of sound in the gas flow field. Consequently, the Mach number Ma is also a local quantity. For supersonic conditions, the local absolute gas velocity u_{g} is higher than the local speed of sound a_{g}, that is, the Mach number Ma is higher than unity. Typically, two different gas nozzle designs are employed for the production of metal powders, which are shown schematically in Fig. 2.3 (Motaman et al., 2013). While both designs allow for achieving locally supersonic conditions in the gas flow field, there are distinct differences between them. For instance, the purely convergent design shown in Fig. 2.3a does not provide means for internally accelerating the gas flow beyond the speed of sound a_{g} (Anderson, 1990). In fact, in *choked* condition, that is, when the gas stagnation pressure $p_{\mathrm{t,g}}$ is at least equal to the critical pressure $p_{\mathrm{t,g,crit}}$, a Mach number Ma of unity is reached at the exit of the gas

---

[1] Hence, it is also referred to as *high-pressure gas atomization*.

nozzle (i.e., in the smallest cross-sectional area $A_{\mathrm{g,e}}$) (Anderson, 1990). In contrast, the convergent-divergent design shown in Fig. 2.3b allows the gas flow to be further accelerated in the divergent part of the gas nozzle. In this way, a supersonic gas flow is achieved, where the Mach number at the exit of the gas nozzle Ma_{e} depends on the geometric design of the gas nozzle as well as on the physical properties of the gas (e.g., the heat capacity ratio κ) (Anderson, 1990).

The reason that the purely convergent design still results in locally supersonic conditions in the flow field downstream of the gas nozzle is that, independent of the gas nozzle design, the close-coupled atomizers employed for the production of metal powder are typically operated at gas stagnation pressures $p_{\mathrm{t,g}}$ much higher than the critical pressure $p_{\mathrm{t,g,crit}}$ (Mi et al., 1996). In other words, the gas nozzle is operated in highly underexpanded condition, which is characterized by the pressure at the exit of the gas nozzle $p_{\mathrm{g,e}}$ being higher than the back pressure $p_{\mathrm{g,back}}$ (Franquet et al., 2015). In a powder production plant, the latter is equal to the pressure in the powder tower (see Fig. 2.1). The operational condition of a gas nozzle is usually expressed in terms of the pressure ratio[2] PR, which is defined as (Franquet et al., 2015):

$$PR = \frac{p_{\mathrm{g,e}}}{p_{\mathrm{g,back}}} \begin{cases} < 1 & \text{Overexpanded} \\ = 1 & \text{Fully expanded} \\ > 1 & \text{Underexpanded} \end{cases} \tag{2.2}$$

In highly underexpanded condition (i.e., for $PR \gg 1$), the gas flow expands strongly upon exiting the gas nozzle in order to match the back pressure $p_{\mathrm{g,back}}$. This leads to a rapid acceleration of the gas flow as well as complex patterns of expansion and compression waves downstream of the gas nozzle (Crist et al., 1966; Franquet et al., 2015). The latter are another characteristic of the supersonic close-coupled atomization of molten metal.

For the gas nozzle, two different configurations are typically used for the production of metal powders, both of which are shown schematically in Fig. 2.4. The first configuration actually comprises several discrete circular gas nozzles, which are arranged in a circumferential array around the central liquid nozzle (see Fig. 2.4a). The second configuration, on the other hand,

---

[2] Note that a gas nozzle featuring a purely convergent design cannot be operated in overexpanded condition.

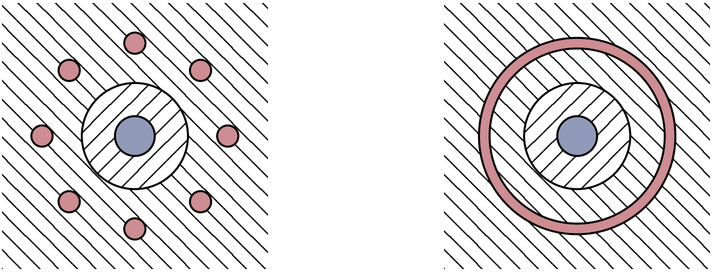

(a) Circumferential array **(b)** Annular slit

Figure 2.4: Schematic illustration of the bottom view of the atomizer unit showing the gas nozzle configuration. The exit of the liquid nozzle and of the gas nozzle are indicated in blue and red, respectively.

consists of a single annular slit gas nozzle surrounding the central gas nozzle (see Fig. 2.4b). However, it is important to note that both configurations can feature either a convergent or a convergent-divergent design (Motaman et al., 2013). Thus, both configurations are capable of producing locally supersonic gas flows. Still, which configuration is more suitable for the production of fine metal powders remains the subject of further investigations. In fact, while Zeoli and Gu (2008b), Zeoli et al. (2011) and Urionabarrenetxea et al. (2022) have emphasized the widespread adoption of the annular slit configuration in the industry and its superior performance, Anderson et al. (2005), Mullis et al. (2011, 2012) and Motaman et al. (2013) have argued that discrete gas nozzles provide means for an improved process control, since the reduced cross-sectional area at the nozzle exit $A_{\mathrm{g,e}}$ allows for higher gas stagnation pressures $p_{\mathrm{t,g}}$ at the same gas consumption.

In summary, supersonic close-coupled atomization allows for producing fine, spherical and chemically pure metal powders. Furthermore, the process exhibits the following important characteristics. First, as a two-fluid atomization process, the actual atomization is determined by the interaction between the gas and the liquid (i.e., by the multiphase flow). Second, molten metal as the working liquid is characterized by particularly high values of the liquid density ρ_{l}, the liquid dynamic viscosity μ_{l} and the surface tension σ, which makes high absolute gas velocities u_{g} necessary for the atomization. Third, the gas flow is characterized by locally supersonic conditions and compressibility effects. Fourth, the atomization result (i.e., the particle size distribution) depends on the operational parameters (e.g., the liquid mass flow rate $\dot{m}_\mathrm{l}$ and the gas stagnation pressure $p_\mathrm{t,g}$), the geometric design of the atomizer unit and the physical properties of the fluids involved. As a result, the supersonic close-coupled atomization of molten metal is considered to be a complex problem. In fact, Ting and Anderson (2004) have come to the following conclusion:

> “[...] close-coupled atomization can be difficult to practice and it is considered by many to be more an art than a science.”

This not only highlights the challenges in applying the supersonic close-coupled atomization process to the production of metal powders, but it also motivates the need for an improved understanding of the physics involved in the process and, ultimately, the development of reliable predictive modeling capabilities.

2.2 Modeling Approaches

The purpose of modeling supersonic close-coupled atomization as a process for the production of metal powders is twofold. First, models provide guidelines for the design of new powder production plants tailored to specific applications. Second, models allow precise adjustments to be made to the operational parameters in order to achieve a specific powder quality. Both applications have in common that they require reliable predictive capabilities. That is, models are required to accurately predict the atomization result in terms of the particle size distribution.

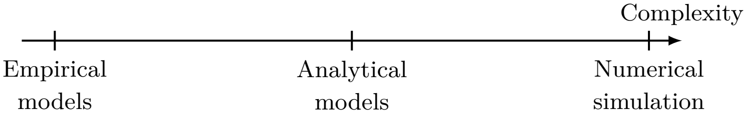

Figure 2.5: Qualitative classification of modeling approaches of the supersonic close-coupled atomization according to their complexity.

Historically, the various approaches to modeling the supersonic close-coupled atomization of molten metal can be divided into the following three categories: empirical models, analytical models and numerical simulations. These categories also roughly correlate with the complexity of the corresponding models (see Fig. 2.5). It is important to note, however, that while, for a given application, a higher level of complexity does not necessarily translate into more accurate results, it does usually provide more flexibility in terms of, for instance, parameter variations.

2.2.1 Dimensionless Numbers

Before discussing the three categories of approaches to modeling the atomization introduced in Section 2.2 as well as the corresponding models, it is necessary to establish quantities defining the conditions under which atomization takes place. This serves the purpose of ensuring comparability. The atomization of liquids is usually discussed in terms of the forces acting on the liquid. Considering two-fluid atomization processes such as the supersonic close-coupled atomization of molten metal, that is, the atomization of a liquid jet by means of an additional gas flow, these forces mainly include viscous forces, surface tension forces and inertia forces, the latter of which include the disrupting force imposed by the gas flow (Lefebvre & McDonell, 2017). These forces are used to define dimensionless numbers characteristic of the atomization, which are based on the characteristic length scale l (Henein et al., 2017).

As the first dimensionless number, the liquid Reynolds number Re_l is introduced. It is defined as (Ashgriz, 2011):

$$Re_\mathrm{l} = \frac{\rho_\mathrm{l} u_\mathrm{l} l}{\mu_\mathrm{l}}, \tag{2.3}$$

where u_l is the absolute liquid velocity. The liquid Reynolds number Re_l can be understood as the ratio of the inertia forces of the liquid to the internal viscous forces (Lasheras et al., 1998; Lasheras & Hopfinger, 2000).

The second dimensionless number considered is the gas Weber number[3] We_g, which is defined as (Ashgriz, 2011):

$$We_\mathrm{g} = \frac{\rho_\mathrm{g} \left(u_\mathrm{g} - u_\mathrm{l}\right)^2 l}{\sigma}. \tag{2.4}$$

---

[3] Often also referred to as *aerodynamic* Weber number.

Here, ρ_g is the gas density. The gas Weber number We_g represents the ratio of the inertia forces due to the difference in the absolute velocity $\Delta u = u_\mathrm{g} - u_\mathrm{l}$ to the surface tension forces.

The Ohnesorge number Oh is the third dimensionless number considered. Its definition is a follows (Ashgriz, 2011):

$$Oh = \frac{\mu_\mathrm{l}}{\sqrt{\rho_\mathrm{l}\sigma l}}. \tag{2.5}$$

Notably, the Ohnesorge number is only a function of the physical liquid properties and the characteristic length scale l (Ashgriz, 2011). It relates the internal viscous forces to the inertia forces of the liquid and the surface tension forces.

All of the dimensionless numbers introduced so far can be taken as both local quantities and global quantities. The former are based on local flow properties and physical fluid properties and are characteristic of the local liquid breakup. Consequently, the characteristic length scale l has to be chosen accordingly, for instance in the case of the breakup of a droplet as its diameter d. In contrast, global dimensionless numbers are assumed to be characteristic of the entire atomization process. Therefore, they are based on representative flow properties and physical fluid properties and on a length scale l characteristic of the entire flow field.

Finally, in the context of the supersonic close-coupled atomization of molten metal, the gas-to-liquid ratio GLR is often introduced as a purely global quantity (Henein et al., 2017). It is defined as the ratio of the two fluid mass flow rates:

$$GLR = \frac{\dot{m}_\mathrm{g}}{\dot{m}_\mathrm{l}}. \tag{2.6}$$

Here, $\dot{m}_\mathrm{g}$ is the gas mass flow rate. According to Miller et al. (1996), the gas-to-liquid ratio GLR can be understood as a measure of the efficiency of the atomization process. That is, for a constant powder quality, a decreased gas-to-liquid ratio GLR corresponds to a reduced gas consumption and, therefore, to an increased efficiency. Furthermore, the gas-to-liquid ratio GLR is often employed as a single quantity for characterizing the set point of operation of the close-coupled atomizer, which is useful for modeling the atomization process (Kamenov et al., 2021). For this purpose, the gas mass flow rate $\dot{m}_\mathrm{g}$

is assumed to be characteristic of the gas flow, instead of the gas stagnation pressure $p_{\mathrm{t,g}}$.

2.2.2 Empirical Models

Empirical models are defined as models based on empirical observations, that is, on experimental data. They are obtained by correlating the quantity of interest, for instance the resulting particle size, to a number of input quantities characteristic of the set point of operation, the physical fluid properties and the geometric dimensions of the atomizer. In other words, the correlations are obtained by performing a fit, often employing global dimensionless numbers similar to those introduced in Section 2.2.1. While this has the advantage of resulting in an easy to use tool for predicting the particle size, which is especially important in industrial applications, the accuracy of the models depends on the input data and the number of fitting parameters. In particular, estimates outside of the range of the input parameters are often not accurate. Furthermore, empirical models are usually limited to the geometric design of the atomizer used for obtaining the correlation. Consequently, since empirical models rely on input data, they do not allow for predicting results during the early development of an atomizer for a specific application.

A comprehensive review of empirical models suitable for the application to the supersonic close-coupled atomization of molten metal has been given by Mehrotra (1981a, 1981b). However, only a few of these models have been adopted. This is due to the fact that most of the models included in this review are based on the atomization of liquids with physical properties close to those of water. Considering the large difference to the physical properties of molten metal, as shown in Table 2.1 and discussed in Section 2.1, and the limitations of empirical models described above, this is reasonable.

Probably the most well-known empirical model is the correlation proposed by Lubanska (1970), which is based on experimental data for the atomization of liquid metal using a spray ring atomizer. Notably, this atomizer design is different from the typical close-coupled atomizers described in Section 2.1. In fact, it is more reminiscent of a free-fall atomizer and does not feature the geometrically close coupling of the two fluid flows involved. The correlation relates the resulting mass median diameter $d_{0.5,m}$, which is non-dimensionalized using the liquid nozzle diameter d_l, to a number of input parameters:

$$\frac{d_{0.5,m}}{d_\mathrm{l}} = C \left[\frac{\mu_\mathrm{l}}{\mu_\mathrm{g}} \frac{\rho_\mathrm{g}}{\rho_\mathrm{l}} \frac{\sigma}{\rho_\mathrm{l} u_\mathrm{g}^2 d_\mathrm{l}} \left(1 + \frac{\dot{m}_\mathrm{l}}{\dot{m}_\mathrm{g}} \right) \right]^{\frac{1}{2}} . \tag{2.7}$$

Here, μ_g is the gas dynamic viscosity. As can be seen, the model is based on the ratio of the fluid dynamic viscosities, the ratio of the fluid densities, a quantity similar to the gas Weber number[4] We_g and the gas-to-liquid ratio GLR. The fitting parameter C included in Eq. (2.7) has been found to be in the range from 40 to 50, depending on the particular atomization process (Lubanska, 1970).

An extension of the correlation given in Eq. (2.7) has been proposed by Rao and Mehrotra (1981) in order to better account for differences in the particular geometric design of the atomizer:

$$\frac{d_{0.5,m}}{d_\mathrm{l}} = C_1 \left[\frac{\mu_\mathrm{l}}{\mu_\mathrm{g}} \frac{\rho_\mathrm{g}}{\rho_\mathrm{l}} \frac{\sigma}{\rho_\mathrm{l} u_\mathrm{g}^2 d_\mathrm{l}} \left(1 + \frac{\dot{m}_\mathrm{l}}{\dot{m}_\mathrm{g}} \right) \right]^{C_2} . \tag{2.8}$$

As can be seen, Eq. (2.8) includes as second fitting parameter C_2, which replaces the exponent of 0.5 in Eq. (2.7) and allows for an improved fit to experimental data.

As part of their experimental study of the supersonic close-coupeld atomization of molten metal, Urionabarrenetxea et al. (2021) have adapted an empirical model proposed by Kishidaka (1972) for water atomization for the application to the supersonic close-coupled atomization of molten metal. Similar to the model proposed by Lubanska (1970), this model also predicts the mass median diameter $d_{0.5,m}$, non-dimensionalized using the liquid nozzle diameter d_l:

$$\frac{d_{0.5,m}}{d_\mathrm{l}} = C_1 \left(\frac{\rho_\mathrm{l} u_\mathrm{g} d_\mathrm{l}}{\mu_\mathrm{l}} \right)^{C_2} \left(\frac{\rho_\mathrm{l} u_\mathrm{g}^2 d_\mathrm{l}}{\sigma} \right)^{C_3} \left(\frac{\dot{m}_\mathrm{g}}{\dot{m}_\mathrm{l}} \right)^{C_4} . \tag{2.9}$$

The three dimensionless numbers considered in Eq. (2.9) are variations of the liquid Reynolds number Re_l and the gas Weber number We_g as well as the gas-to-liquid ratio GLR. Furthermore, four fitting parameters C_1 to C_4 have been introduced.

---

[4] Note the use of the liquid density ρ_l instead of the gas density ρ_g and the neglect of the absolute liquid velocity u_l.

Another approach has been proposed by Anderson and Achelis (2017), who have adapted the *acceleration wave model*, which is based on the analytical treatment of the size of particles resulting from the atomization of a liquid jet due to the formation of surface instabilities caused by a cross-flowing gas by Adelberg (1968). These considerations have subsequently been taken up by Ingebo (1981) and compared to experimental data for water, resulting in the following empirical correlation for the arithmetic mean diameter $\bar{d}$, also non-dimensionalized using the liquid nozzle diameter d_l:

$$\frac{\bar{d}}{d_\mathrm{l}} = \frac{1}{C_1} \left(\frac{\rho_\mathrm{g} \left(u_\mathrm{g} - u_\mathrm{l} \right)^2 d_\mathrm{l}}{\sigma} \frac{\rho_\mathrm{l} \left(u_\mathrm{g} - u_\mathrm{l} \right) d_\mathrm{l}}{\mu_\mathrm{l}} \right)^{-C_2} \tag{2.10}$$

As can be seen, the model reduces the problem of the atomization to the gas Weber number We_g and a variation of the liquid Reynolds number Re_l. Furthermore, the fitting constants C_1 and C_2 have been determined to equal 0.027 and 0.4, respectively.

Finally, Kamenov et al. (2021) have proposed a simple empirical model relating the Sauter mean diameter d_{32} to the gas-to-liquid ratio GLR:

$$d_{32} = C_1 \left(\frac{\dot{m}_\mathrm{g}}{\dot{m}_\mathrm{l}} \right)^{C_2} . \tag{2.11}$$

Here, C_1 and C_2 are fitting parameters depending on the particular atomization process.

2.2.3 Analytical Models

In contrast to the empirical models discussed in Section 2.2.2, analytical models are based on an analytical description of the atomization process, which aims at not having to rely on experimental data and at providing more flexibility in terms of the range of the input quantities. However, due to the high level of complexity inherent to most atomization processes, analytical models require strong assumptions in order to simplify the description of the process. This is particularly relevant in the case of the supersonic close-coupled atomization of molten metal, which exhibits many challenging characteristics, as has been discussed in Section 2.1. Consequently, the number of available analytical models is limited.

Bradley (1973a) has mathematically modeled the close-coupled atomization of molten metal by treating it as the uniform inviscid flow of a compressible gas over a liquid in a two-dimensional domain, causing disturbances on the liquid surface. Notably, here only the subsonic case has been considered (i.e., $Ma < 1$). Employing a linearization of the corresponding equations of motion, this has led to a dispersion relation, predicting the growth rate of the individual disturbances in dependence of their wavelength λ_{dist}. Assuming that the wavelength corresponding to the maximum growth rate $\lambda_{\mathrm{dist,max}}$ determines the most probable resulting particle size, the following relationship for the particle diameter d_{p} has been obtained:

$$d_{\mathrm{p}} = \frac{1}{4} \lambda_{\mathrm{dist,max}}. \tag{2.12}$$

Here, the wavelength corresponding to the maximum growth rate $\lambda_{\mathrm{dist,max}}$ is a function of the flow parameters as well as of the physical properties of the fluids involved. Good agreement has been found with data obtained for the atomization of water. Later, Bradley (1973b) has relaxed some of the assumptions made in (Bradley, 1973a). While this has made the dispersion relation more complicated, it has allowed for extending the model to the case of supersonic gas flows (i.e., to $Ma > 1$).

Interestingly, the models proposed by Bradley (1973a, 1973b) haven been adapted by Antipas (2006, 2009) for the use in spatially resolved numerical simulations, an approach termed as the *surface wave formation model*. Notably, the model has been used for the primary atomization and for the subsequent secondary atomization. In general, the model has been found to agree reasonably well with experimental data obtained for the atomization of molten metal.

Finally, a second analytical model has been proposed by Bürger et al. (1989, 1992), which is based on an approach similar to that used by Bradley (1973a, 1973b). However, as a distinct difference, the gas flow has not been demanded to be inviscid. Consequently, the formation of a non-uniform velocity profile in the gas flow featuring a boundary layer over the liquid surface has been considered.

2.2.4 Numerical Simulation

The increasing availability of tools suitable for the numerical simulation of multiphase flows and atomization processes has resulted in important advances in modeling the supersonic close-coupled atomization process. A comprehensive review of the methods typically used has recently been given by Mandal et al. (2022). Furthermore, an extensive overview can be found in (Sarkar et al., 2016).

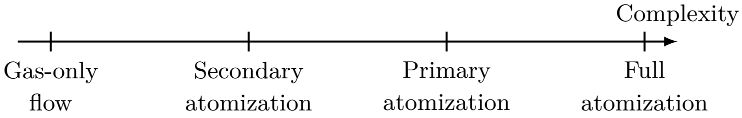

Figure 2.6: Qualitative classification of modeling approaches of the supersonic close-coupled atomization based on numerical simulations according to their complexity.

In general, according to Amatriain et al. (2022), the various approaches to numerically simulating the supersonic close-coupled atomization of molten metal can be divided into the following four categories: gas-only flow, secondary atomization, primary atomization and full atomization. These categories also roughly correlate with the complexity of the corresponding approaches (see Fig. 2.6). This is an important aspect of the modeling by means of numerical simulations, since the computational cost often determines the suitability of a particular model for the application to the supersonic close-coupled atomization of molten metal, especially in an industrial context. This is due to the fact that the characteristics of the process discussed in Section 2.1 result in particularly short time scales and small length scales, requiring a high temporal and spatial resolution. Consequently, computational cost is a limiting factor.

Gas-only flow

Numerically simulating the gas-only flow does not allow for actually predicting the atomization result, that is, the particle size distribution. However, historically, it has been used to characterize the gas-only flow field downstream of the liquid nozzle as well as for improving the understanding of the significance of compressibility effects. Consequently, this approach is mentioned here for the sake of completeness. The results obtained form the simulations have usually been used to infer in a purely qualitative manner how changes to the gas stagnation pressure $p_{\mathrm{t,g}}$ and the geometric design of the atomizer unit influence the atomization result. An example for this approach are the studies performed by Mi et al. (1996, 1997).

Secondary Atomization

As a further development, the secondary atomization has been investigated by means of numerical simulations. Here, the main idea is to locally introduce spherical droplets in the gas flow field downstream of the liquid nozzle and to follow their trajectories. This allows for calculating the local forces acting on the droplets, providing means for modeling their breakup. Furthermore, this approach allows for modeling the solidification of the droplets by considering heat transfer in the temperature field downstream of the atomizer.

Important examples for the application of this approach of modeling the atomization result to the supersonic close-coupled atomization of molten metal are the studies reported by Zeoli and Gu (2006, 2008a), Sarkar et al. (2011), Firmansyah et al. (2014) and Kaiser et al. (2018). The main differences between these studies include the treatment of the solidification of the droplets as well as the coupling between the gas flow and the droplets taken into account. The former is important, because a premature solidification terminates the secondary atomization process. Similarly, the latter is crucial for achieving an accurate result. This is due to the fact that the introduction of liquid into the fully developed gas flow field has been found to significantly alter the gas flow field[5] (Amatriain et al., 2022). Consequently, a simple one-way coupling neglecting the influence of the liquid on the gas flow results in inaccuracies, making the implementation of a suitable two-way coupling necessary.

Another important difference is the choice of the breakup model used for describing the secondary atomization. Typically, the breakup model is chosen depending on the local gas Weber number We_{g} defined in Eq. (2.4), which determines the breakup mechanism and allows to differ between bag breakup (i.e., for $We_{\mathrm{g}} < 80$) and stripping breakup (i.e., for $We_{\mathrm{g}} > 80$) (Hsiang &

---

[5] This is also referred to as *mass loading effects*.

Faeth, 1992, 1995). The former has been found to be well described using the *Taylor Analogy Breakup* (TAB) model while the latter has been found to be governed by the *Kelvin-Helmholtz Instability* model (Zeoli & Gu, 2006).

Finally, it is interesting to note that the initial droplet size distribution employed in the mentioned studies is often based on the experimental result reported by Markus et al. (2002). These indicate that the droplets resulting from the primary atomization and undergoing secondary atomization are characterized by an initial size in the range of 10 % to 100 % of the liquid nozzle diameter d_l. However, these results have been discussed in the context of a free-fall atomizer, which features a geometric design which is distinctly different from those of typical close-coupled atomizers described in Section 2.1. In particular, free-fall atomizers do not feature a geometrically close-coupling of the two fluid flows involved.

Primary Atomization

Considering that the numerically simulations modeling the secondary atomization described above rely on realistic particle size distributions resulting from the primary atomization as input parameters, modeling the primary atomization by means of numerical simulations has been the focus of further developments. Here, the difficulty lies in reducing the computational cost while still resolving the mechanisms involved in the primary atomization. This is especially important due to the fact that the gas flow during the supersonic close-coupled atomization is highly turbulent, which requires special attention during the modeling.

Initial attempts at numerically simulating the primary atomization have been based on combining the Reynolds-averaged Navier–Stokes (RANS) equations for modeling the time-averaged turbulent motion of the fluid and a suitable method for tracking the gas-liquid interface, for instance the Eulerian-Eulerian Volume-of-Fluid (VoF) method. Examples for this are the investigations reported by Zhao et al. (2012) and Wei et al. (2020), which have allowed for studying the distribution of molten metal in close proximity to the liquid nozzle during the primary atomization of the supersonic close-coupled atomization process.

Further work has focused on improving the modeling of the turbulent motion by relying on the Large Eddy Simulation (LES) approach, which allows for resolving large turbulent structures at an increased computational cost. In fact, Zeoli et al. (2012) and Arachchilage et al. (2019) have obtained time-resolved results for the primary atomization of molten metal, showing the evolution of the gas-liquid interface.

Finally, attempts have been made to employ Direct Numerical Simulation (DNS) for gaining further insights into the primary atomization in the supersonic close-coupled atomization of molten metal. However, due to particularly high computational cost involved with this approach, these attempts have required strong assumptions to be made in order to simplify the calculations. For instance, Tong and Browne (2007, 2008) have resorted to a two-dimensional domain neglecting the compressibility of the gas flow. While this is a major restriction considering the characteristics of the supersonic close-coupled atomization of molten metal described in Section 2.1, the results still have captured the evolution of the topology of the melt stream and confirmed the significance of the liquid mass loading effects for the gas flow field.

Full Atomization

The ultimate goal of developing tools based on numerical simulations is to allow for modeling the entire atomization process, including the primary atomization, the secondary atomization and the solidification of the resulting droplets. This is expected to provide improved predictive capabilities for the supersonic close-coupled atomization of molten metal, which are required in order to increase the process control as well as the efficiency during the production of high-quality metal powders. However, the development of these tools is challenging due to the complex phenomena involved in the atomization process (see Section 2.1) and the limitations imposed by the high computational costs. As a result, numerical simulations governing the full atomization remain scarce.

Examples of investigations involving numerical simulations of the full atomization include the work of Luo et al. (2021), Wang et al. (2021), Zhang et al. (2021) and Shi et al. (2022), who have employed various combinations of the approaches to numerically simulating the primary atomization and the secondary atomization discussed above. This has successfully been used to study, for instance, the spray formation and the mechanisms responsible for particle defects. However, the high computational costs involved remain a limitation (Zhang et al., 2021). For this reason, recently, the focus has been placed on the application of the Eulerian-Lagrangian Spray Atomization (ELSA) model to the numerical simulation of the supersonic close-coupled atomization of molten metal (Amatriain et al., 2022). This model allows for dividing the spray into the following three regions, based on the local liquid volume fraction: Eulerian mixture zone, transition zone, Lagrangian zone. In other words, the model treats the primary atomization in an Eulerian way, but automatically resorts to Lagrangian tracking of the droplets for the secondary atomization, which results in an increased efficiency (Hoyas et al., 2013). Furthermore, this approach can be coupled with arbitrary turbulence models, providing additional flexibility (Amatriain et al., 2022). Indeed, the successful application to the supersonic close-coupled atomization has been shown by Amatriain et al. (2022).

2.3 Objectives

Based on the description of the supersonic close-coupled atomization of molten metal for the production of metal powders in Section 2.1 and the existing approaches to modeling the process presented in Section 2.2, the following objectives are defined for this thesis.

The experimental investigation of the supersonic close-coupled atomization poses a challenge for a number of reasons. For instance, the handling of molten metal in a laboratory environment is dangerous and inconvenient. It is therefore desirable to employ substitute liquids instead of molten metal, which are not only easier to handle but, additional, have the advantage of improving the accessibility for various measurement techniques. The objective of this thesis is to set up a research facility suitable for this task and to provide insight into whether the use of substitute liquids is a valid means for investigating the atomization of molten metal.

One reason why the development of predictive modeling capabilities remains challenging in the context of the supersonic close-coupled atomization is the lack of comprehensive experimental data on the atomization result, that is, the local particle size distribution, which is required for the development and validation of atomization models. As a result, another objective of this thesis is to provide data suitable for this task and to identify how the operational parameters and the physical properties of the liquid affect the atomization result.

Many of the existing modeling approaches suitable for the industrial application either do not take into account the primary atomization or use models which are not based on the characteristics of the supersonic close-coupled atomization process. Whether and how the primary atomization affects the atomization result, that is, the particle size distribution, remains an open research question. Similarly, the parameters influencing the primary atomization have not been identified. Therefore, another objective of this thesis is to provide insight into the mechanisms involved in the primary atomization.

Finally, for the secondary atomization, many of the existing modeling approaches rely on conventional breakup models, which do not explicitly take into account the physics involved in the supersonic close-coupled atomization process. This is due to the lack of experimental insight into the atomization process. In order to overcome this shortcoming, another objective of this thesis is the identification of the mechanisms responsible for the secondary atomization.

Consequently, this thesis serves the purpose of providing a foundation for the future development of novel physics-based predictive modeling capabilities for the supersonic close-coupled atomization of molten metal.

Part III

Methods

3 Experimental Methods

In this chapter, an overview of the experimental research facility as well as the measurement techniques and the data evaluation methods utilized to gain insight into the atomization process is given. The supersonic close-coupled atomizer research facility which has been employed to carry out the experimental investigations is described in Section 3.1, along with a summary of the operational parameter range and a quantitative comparison with a typical industrial powder production plant. In Section 3.2, the focus is on the phase Doppler measurement technique used for the characterization of the atomization result. Besides the optical configuration, this includes considerations for the treatment and the evaluation of raw data and the estimation of measurement uncertainties. Finally, in Section 3.3, the imaging techniques employed for visualizing the atomization process are presented and methods for the quantitative image evaluation are introduced.

Parts of this chapter have already been covered in the theses of Apell (2019), Schrimpl (2021) and Mirschinka (2022), presented in Odenthal et al. (2021) and Apell et al. (2021, 2022b) and published in Apell et al. (2023).

3.1 Supersonic Close-coupled Atomizer

The experimental investigations have been carried out at the supersonic close-coupled atomizer research facility at the Institute for Fluid Mechanics and Aerodynamics.

3.1.1 Dimensional Analysis

Experimental investigations of supersonic close-coupled atomization in the context of the metal powder production present several challenges, as they are complex, expensive and pose a potential safety risk. This is mostly due to the challenging handling of molten metal at high liquid temperatures

T_l. Consequently, it is desirable to use instead a substitute liquid, such as water. This has the additional benefit of making the atomization process more accessible to a number of measurement techniques. Employing a substitute liquid is possible by applying the concept of similitude, which states that a reliable transfer of information is ensured if identical or at least adequately identical boundary conditions are met. In detail, three similarity laws have to be observed. First, geometric similarity demands that all dimensions in all directions are scaled similarly. Second, kinematic similarity is given, when, in addition, all time scales are scaled similarly. This results in the ratios of all velocity scales being preserved. Third, dynamic similarity demands kinematic similarity as well as all force ratios to be maintained (Longo, 2021).

For this experimental investigation, a supersonic close-coupled atomizer research facility has been set up, which follows the concept of similitude. It is based on the powder production plant described by Odenthal et al. (2021), but employs substitute liquids and air for the atomization instead of molten metal and argon gas. The facility observes the law of geometric similarity by being designed as a one-to-one replica of the powder production plant. In order to also observe the laws of kinematic and dynamic similarity, a dimensional analysis has been performed employing the set point of operation of the powder production plant detailed in (Odenthal et al., 2021) as a reference. For this purpose, selected dimensionless numbers characteristic of the supersonic close-coupled atomization process have been considered (Henein et al., 2017). These include the Mach number Ma defined in Eq. (2.1) and the pressure ratio PR defined in Eq. (2.2), which determine the gas flow, as well as the gas Weber number We_g defined in Eq. (2.4), the liquid Reynolds number Re_l defined in Eq. (2.3) and the Ohnesorge number Oh defined in Eq. (2.5), which govern the two-fluid atomization of a liquid jet (see Section 2.2.1). Furthermore, the gas-to-liquid ratio GLR defined in Eq. (2.6) has been taken into account.

In detail, the dimensionless numbers have been evaluated as global quantities (see Section 2.2.1), using the liquid nozzle diameter d_l as the characteristic length scale l (Mates & Settles, 2005b). Furthermore, the flow properties and the physical fluid properties of the gas and the liquid have been evaluated at the exits of the respective nozzles. In particular, the absolute liquid velocity at the liquid nozzle exit $u_\mathrm{l,e}$ has been defined as the following area-weighted average:

$$u_{\mathrm{l,e}} = \frac{4\dot{m}_{\mathrm{l}}}{\rho_{\mathrm{l,e}}\pi d_{\mathrm{l}}^2} \tag{3.1}$$

In terms of the gas properties at the gas nozzle exit, the flow through the nozzle has been assumed to be steady, quasi-one-dimensional and isentropic and the gas to be calorically perfect. This allows for relating the gas properties at the gas nozzle exit to the gas stagnation properties in a reservoir upstream of the gas nozzle (Anderson et al., 1991) and, ultimately, for an evaluation of all the required properties at the gas nozzle exit, including the flow properties and the physical gas properties.

The main finding of the dimensional analysis, the details of which can be found in (Odenthal et al., 2021), is that the use of water as a substitute for molten metal results in most of the dimensionless numbers considered to be either perfectly matched or to be of the same order of magnitude. The only exception to this is the gas Weber number We_{g} due to the large difference in the surface tension σ between water and molten metal (see Table 2.1 and Section 2.1). In fact, the gas Weber number We_{g} is one order of magnitude higher for water than for molten metal. This is consistent with the results obtained by Heck et al. (2000) for a free-fall atomizer. However, as Heck et al. (2000) have noted, due to the particularly high absolute gas velocity u_{g} characteristic of the supersonic close-coupled atomization process, both the atomization of water and the atomization of molten metal exhibit gas Weber numbers We_{g} in the same atomization regime defined for the two-fluid atomization of a liquid jet (Lasheras & Hopfinger, 2000). This suggests that both cases are governed by the same mechanisms.

In conclusion, the dimensional analysis suggests that water can be employed as a substitute for molten metal during the supersonic close-coupled atomization in order to investigate the atomization process. That is, the same mechanisms governing the atomization of molten metal are expected to be observed during the atomization of water. Still, it is important to note that the above considerations are based on the main assumptions that the following phenomena are of no consequence to the atomization process: coalescence, evaporation, solidification and heat transfer. However, the objective of this experimental investigation is not to provide quantitatively comparable results, but, instead, to identify the mechanisms responsible for the atomization as well as the qualitative dependency of the atomization result on the operational parameters and the physical liquid properties (see Section 2.3). In this context, the above assumptions are deemed to be reasonable.

3.1.2 Atomizer Unit

The main component of the research facility is the atomizer unit comprising the central liquid nozzle and the surrounding gas nozzle. Its geometric design determines not only the gas flow field, but also the interaction between the liquid and the gas flow (see Section 2.1). Consequently, the design of the atomizer unit is critical to the atomizer performance and has to be well-defined. In order to meet the requirement of geometric similarity when applying the concept of similitude, the atomizer unit of the research facility is a one-to-one replica of an atomizer unit designed for the metal powder production plant that has been used as a reference for the dimensional analysis in Section 3.1.1.

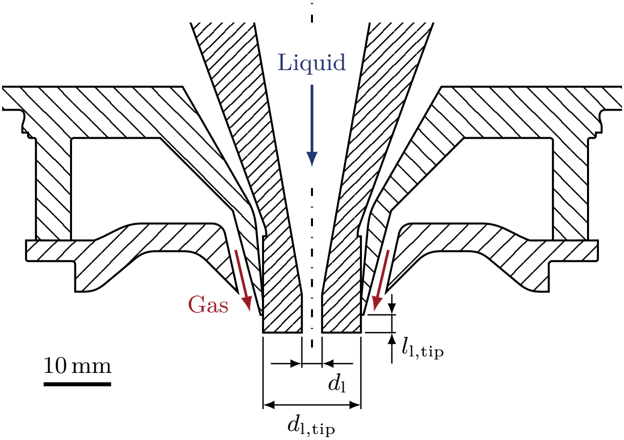

Figure 3.1: Cross-sectional view of the atomizer unit. The two fluid flows through the respective nozzles as well as characteristic geometric dimensions of the liquid nozzle are indicated. (Adapted from Apell et al., 2023, with permission from Elsevier Ltd. © 2023 Elsevier Ltd.)

In Fig. 3.1, a cross-sectional view of the atomizer unit of the research facility is shown. The gas nozzle is designed as a single annular slit nozzle with an apex angle of about 28°. It is manufactured from stainless steel and features a convergent-divergent design. For air (heat capacity ratio $\kappa = 1.4$), the nozzle results in an exit Mach number Ma_e of about 1.2, assuming the steady, quasi-one-dimensional, isentropic flow of a calorically perfect gas (Anderson, 1990). The back pressure $p_\mathrm{g,back}$ of the nozzle is equal to the ambient air pressure p_a. Consequently, using the same assumptions for the gas flow, the nozzle can be estimated to operate in perfectly expanded conditions for a gas stagnation pressure $p_\mathrm{t,g}$ of 0.24 MPa (Anderson, 1990). For higher gas stagnation pressures $p_\mathrm{t,g}$, which are commonly used in supersonic close-coupled atomization (Mandal et al., 2022), the gas nozzle is operated in an underexpanded condition (i.e., at $PR > 1$, see Section 2.1). As a consequence, the flow field downstream of the atomizer is characterized by complex patterns of compression and expansion waves.

By design, the liquid nozzle of a close-coupled atomizer is in close proximity to the gas nozzle, often with its tip protruding into the gas flow. Consequently, the design of the liquid nozzle tip directly influences the gas flow field as well as the interaction between the gas and the liquid flow. For this atomizer unit, the liquid nozzle is manufactured additively from polyamide powder using a Formiga P100 SLS printer (EOS GmbH). Its tip is designed as a cylinder characterized by the liquid nozzle tip diameter $d_\mathrm{l,tip}$, and the liquid nozzle tip protrusion length $l_\mathrm{l,tip}$, which determines how far the liquid nozzle protrudes into the gas flow field (see Fig. 3.1). The former is fixed at 14.5 mm, while, for the latter, three different liquid nozzles are available, featuring a liquid nozzle tip protrusion length $l_\mathrm{l,tip}$ of 2.5 mm, 3.5 mm and 4.5 mm, respectively. Here, the baseline case corresponding to the design of the atomizer unit of the powder production plant discussed in Section 3.1.1 is $l_\mathrm{l,tip} = 3.5\,\mathrm{mm}$. Finally, the liquid nozzle is characterized by the liquid nozzle diameter d_l (see Fig. 3.1), which, as the geometrically similar baseline case, is equal to 4 mm, but can be exchanged for 3 mm or 5 mm.

3.1.3 Fluid Supply

The two lines required for supplying gas and liquid to the atomizer unit are completely independent of each other, allowing for flexible and separate adjustments of the respective flow rates.

Gas Supply

The gas supply line provides compressed air for the gas nozzle in the atomizer unit. Here, not only a high pressure is important, but a large volume is also required in order to allow for a sufficiently long measurement time t_{meas}.

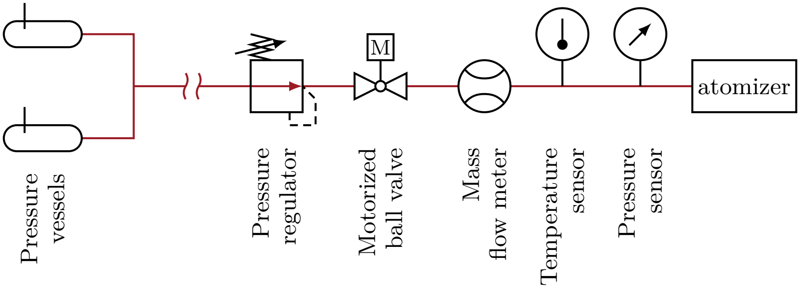

Figure 3.2: Schematic illustration of the gas supply line.

A schematic illustration of the entire gas supply line up to the atomizer unit is shown in Fig. 3.2. Two connected pressure vessels are available, providing up to 18 m^3 of air at a maximum pressure of about 3.5 MPa. As soon as the pressure falls below a critical level, the vessels are automatically refilled. The gas stagnation pressure $p_{\mathrm{t,g}}$ is set manually using a pressure regulator. For safety reasons, a motorized ball valve closes off the connection to the atomizer unit. A Proline Promass F300 Coriolis mass flow meter (Endress+Hauser AG) is used for monitoring the gas mass flow rate $\dot{m}_{\mathrm{g}}$. The gas stagnation pressure $p_{\mathrm{t,g}}$ as well as the gas stagnation temperature $T_{\mathrm{t,g}}$ are measured in a reservoir just upstream of the gas nozzle. Additionally, the ambient pressure p_{a} as well as the ambient temperature T_{a} are monitored, as these define the conditions downstream of the gas nozzle.

Liquid Supply

In the context of the close-coupled atomization of liquid metal, the liquid is fed to the atomizer unit by means of a tundish positioned on top of the atomizer unit (Henein et al., 2017). The liquid is either solely gravity-driven or additionally pressurized (see Section 2.1). In both cases, considering the high liquid density ρ_{l}, the liquid mass flow rate $\dot{m}_{\mathrm{l}}$ is a function of the liquid level inside of the tundish, that is, it decreases as the liquid level decreases. Additionally, it is coupled to the gas flow downstream of the atomizer, which determines the pressure at the liquid nozzle exit (Miller et al., 1996). Consequently, the design of the liquid supply line is crucial for enabling systematic experimental studies under constant and well-defined set points of operation.

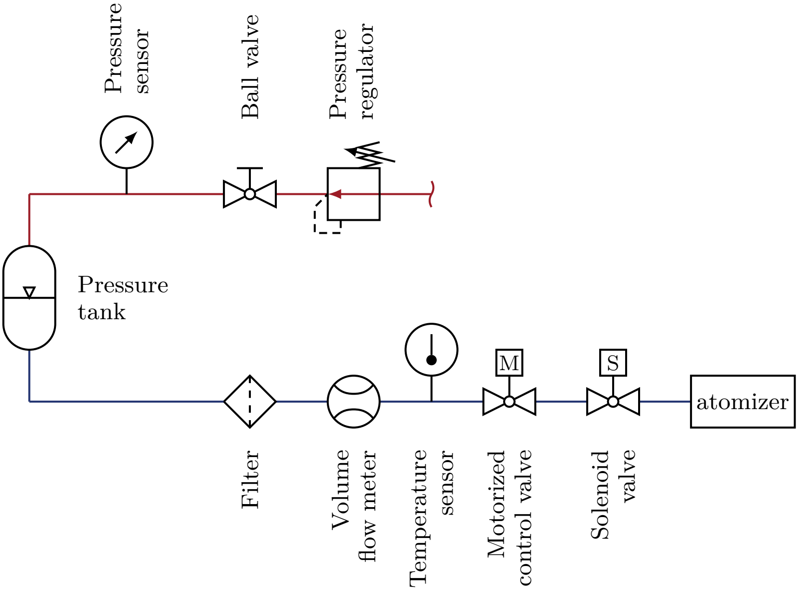

Figure 3.3: Schematic illustration of the liquid supply line.

In Fig. 3.3, a schematic illustration of the entire liquid supply line up to the atomizer unit is shown. Liquid is supplied by means of a custom pressure tank (Walther Spritz- und Lackiersysteme GmbH), which provides up to $42.8\,\mathrm{dm}^3$ of liquid at a constant liquid overpressure Δp_l of up to $1\,\mathrm{MPa}$ and, therefore, reduces fluctuations in the liquid mass flow rate $\dot{m}_\mathrm{l}$. Additionally, the tank features a controlled heating system, which allows for heating the liquid up to a temperature T_l of $85\,°\mathrm{C}$. Upon exiting the pressure tank, the liquid is filtered in order to remove particulate residue. The liquid volume flow rate $\dot{V}_\mathrm{l}$ is monitored using a Picomag DMA15 electromagnetic flowmeter

(Endress+Hauser AG). The subsequent measurement of the liquid temperature T_l allows for calculating physical liquid properties. An electromotive proportional valve (Bürkert GmbH & Co. KG) is used to actively control the liquid mass flow rate $\dot{m}_\mathrm{l}$. For this reason, it is coupled with a PID controller implemented in LabVIEW 2018 (National Instruments Corp.) This is an important feature of the liquid supply line as it allows for flexibly setting and maintaining liquid mass flow rates $\dot{m}_\mathrm{l}$ independently from the gas flow, effectively decoupling the liquid and the gas flow. Finally, a solenoid valve closes off the connection to the atomizer unit.

The pressure tank is connected to an outlet of the high pressure supply line and the pressure is reduced and set manually using a pressure regulator. For safety reasons, a manually operated ball valve closes off the connection. The liquid overpressure Δp_l is monitored upstream of the pressure tank. Consequently, the liquid supply line can be operated in two different modes. In the first mode, the liquid overpressure Δp_l is set constant to a value high enough to provide the maximum liquid mass flow rate $\dot{m}_\mathrm{l,max}$, while the control valve is used to set and maintain the target liquid mass flow rate $\dot{m}_\mathrm{l}$ by reducing the flow cross-section; hence, the gas and liquid flows are decoupled. In the second mode, the control valve is fully opened and the liquid overpressure Δp_l is set to a constant value, allowing for the gas flow to influence the liquid mass flow rate $\dot{m}_\mathrm{l}$.

3.1.4 Operational Parameter Range

For a given geometric atomizer design and a fixed combination of physical fluid properties, the set point of operation of the supersonic close-coupled atomizer research facility is well-defined by the gas stagnation pressure $p_\mathrm{t,g}$ and the liquid mass flow rate $\dot{m}_\mathrm{l}$: both can be varied independently from each other. In fact, the ranges that have been employed for the experimental investigations are $0.4\,\mathrm{MPa} \leq p_\mathrm{t,g} \leq 1.6\,\mathrm{MPa}$ for the gas stagnation pressure and $1\,\mathrm{kg\,min^{-1}} \leq \dot{m}_\mathrm{l} \leq 9\,\mathrm{kg\,min^{-1}}$ for the liquid mass flow rate. As a consequence of the range of the gas stagnation pressure $p_\mathrm{t,g}$, the convergent-divergent gas nozzle described in Section 3.1.2 has always been operated in an underexpanded condition (i.e., at $p_\mathrm{t,g} > 0.24\,\mathrm{MPa}$, see Section 3.1.2).

However, the geometric design of the atomizer unit is not completely fixed, as variations to the geometric design of the liquid nozzle are possible. In detail, this includes changes to the liquid nozzle diameter d_l (i.e., 3 mm, 4 mm and 5 mm) and the liquid nozzle tip protrusion length $l_\mathrm{l,tip}$ (i.e., 2.5 mm, 3.5 mm and 4.5 mm). Furthermore, the research facility allows for varying the working liquid, which has a direct influence on the physical liquid properties. In total, four different working liquids have been considered. Besides the baseline case of water, this includes two aqueous glycerol solutions of different mass fractions (i.e., 20 % and 40 %) and one 30 % aqueous acetic acid solution.

Table 3.1: Physical properties of the four working liquids at an exemplary temperature T_l of 20 °C.

Liquid	Density in $\mathrm{kg\,m^{-3}}$	Dynamic viscosity in mPa s	Surface tension in $\mathrm{mN\,m^{-1}}$
Water	998	1.00	72.7
Aqueous glycerol solution, 20 %	1051	1.74	71.0
Aqueous glycerol solution, 40 %	1103	3.68	69.3
Aqueous acetic acid solution, 30 %	1032	1.93	43.4

In Table 3.1, the physical properties of the four working liquids are summarized for an exemplary liquid temperature T_l of 20 °C. This includes the liquid density ρ_l, the liquid dynamic viscosity μ_l as well as the surface tension σ. The physical properties of water have been calculated following recommendations by the The International Association for the Properties of Water and Steam (2007, 2008, 2014). For the aqueous glycerol solutions, the physical properties have been computed using instructions from the VDI Society Chemical and Process Engineering (2010) and the method proposed by Cheng (2008). Similarly, the physical properties of the aqueous acetic acid solution have been calculated employing the methods proposed by Sun et al. (1995), Teja and Rice (1981) and Wang et al. (2011). Additionally, values for the surface tension σ have been validated using a DCAT 25 tensiometer (DataPhysics Instruments GmbH). As can be seen in Table 3.1, the two aqueous glycerol solutions are characterized by an increase in the liquid dynamic viscosity μ_l

when compared to water. Relative differences in the other two physical liquid properties are at least one order of magnitude smaller. In contrast, compared to water, the aqueous acetic acid solution is characterized by a lower surface tension σ and a higher liquid dynamic viscosity μ_l.

Table 3.2: Ranges of the dimensionless numbers covered in this study.

Dimensionless number	Minimum	Maximum
Liquid Reynolds number	3.7×10^3	40.9×10^3
Gas Weber number	1.3×10^4	12.1×10^4
Ohnesorge number	1.8×10^{-3}	8.3×10^{-3}
Exit Mach number	1.2	1.2
Pressure ratio	1.5	6.2
Gas-to-liquid ratio	0.9	11.0

The operational range of the research facility can be summarized in terms of the global dimensionless numbers employed in Section 3.1.1. Considering that the research facility allows for the variation of the two operational parameters, the geometric design of the atomizer unit and the physical liquid properties, it is possible to cover wide ranges of the dimensionless numbers. An overview of the ranges covered is given in Table 3.2.

3.2 Phase Doppler Measurement Technique

Characterization of the atomization result in terms of local particle size and velocity distributions is a crucial means for gaining insight into how operational parameters, physical liquid properties and geometric design parameters influence the atomization process. However, in the context of supersonic close-coupled atomization, this is a challenging task due to three main reasons. First, accelerated by the high absolute gas velocities u_g of up to several hundred meters per second, the droplets in the spray are particularly fast, resulting in the requirement to resolve short time scales (Kirmse & Chaves, 2016). Second, the particle size distributions span a range of up to two orders of magnitude, requiring a wide measurement range as well as the possibility to resolve small length scales (Urionabarrenetxea et al., 2021). Third, the spray is optically dense, leading to a low signal-to-noise ratio (SNR) (Domnick et al., 1998). As a result, existing experimental studies investigating supersonic close-coupled atomization have mostly been carried out by analyzing raw metal powders subsequent to the actual atomization process, for instance, using sieving, sedimentation or laser diffraction (Biancaniello et al., 1990). This approach has several shortcomings. Most importantly, it is neither time-resolved nor does it provide spatially resolved information. In fact, the powders produced are the integral result of the atomization process taking place over a finite time interval. However, for liquid supplies designed as a filled tundish, the liquid mass flow rate $\dot{m}_\mathrm{l}$ is dependent on the hydrostatic pressure, which is determined by the decreasing liquid level inside of the tundish (see Section 2.1). Consequently, under these conditions, the entire atomization process is inherently time-dependent, which, as has been shown by Allimant et al. (2009), has a strong influence on the particle size.

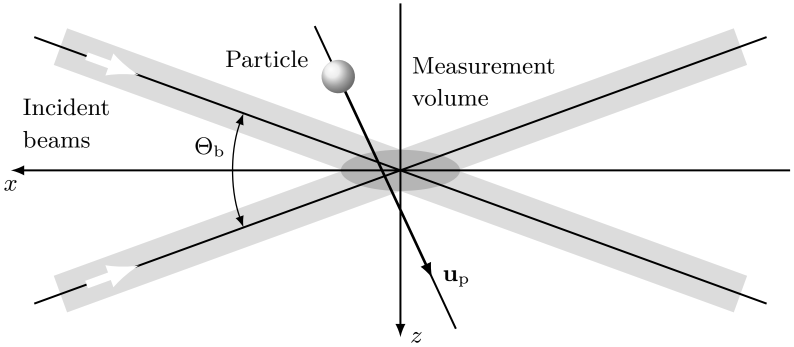

Figure 3.4: Schematic illustration of a spherical particle traversing the measurement volume formed by two intersecting laser beams. (Adapted from Albrecht et al., 2003, with permission from Springer Nature. © 2003 Springer Nature.)

The phase Doppler measurement technique, on the other hand, provides a non-invasive means of obtaining local particle size and velocity distributions in a time-resolved manner. It can be understood as an extension of the laser Doppler measurement technique. A comprehensive introduction to both of the measurement principles has been given by Albrecht et al. (2003). Both techniques are based on the scattering from a single spherical homogeneous particle traversing the finite measurement volume formed by two laser beams of wavelength λ_b intersecting at an angle Θ_b, resulting in a burst signal. This situation is illustrated schematically in Fig. 3.4.

The laser Doppler measurement technique exploits the fact that light scattered on a moving particle and detected by a stationary receiver experiences a frequency shift caused by the Doppler effect. However, this Doppler shift is too small relative to the frequency of the incident laser beam to be resolved experimentally. Instead, two laser beams are used, resulting in two scattered signals, each being characterized by a corresponding Doppler shift. The Doppler frequency f_D, which is the difference in the Doppler shift due to the superposition of the two signals on the stationary receiver, contains the velocity information of the particle (vom Stein & Pfeifer, 1969). In fact, the measured Doppler frequency f_D is linearly proportional to the absolute value of the component of the particle velocity vector $\mathbf{u}_\mathrm{p}$ denoted by $u_{\mathrm{p}\perp}$, which lies in the plane formed by the two laser beams and is perpendicular to their bisector:

$$f_\mathrm{D} = \frac{2\sin\left({}^{\Theta_\mathrm{b}}/_{2}\right)}{\lambda_\mathrm{b}} \left|u_{\mathrm{p}\perp}\right| . \tag{3.2}$$

For the configuration shown in Fig. 3.4, the velocity component perpendicular to the laser beam bisector $u_{\mathrm{p}\perp}$ is equal to the velocity component in the z-direction u_z. Directional sensitivity is achieved by introducing a frequency shift to one of the laser beams, for instance, by utilizing a Bragg cell (Lanz et al., 1971). Further velocity components can be obtained by introducing additional pairs of laser beams with the appropriate orientation in space, taking into account a bisector perpendicular to the velocity component to be measured. However, the burst signals corresponding to the individual velocity components have to be distinguished, for instance, by using different beam wavelengths λ_b (Albrecht et al., 2003).

While the Doppler frequency f_D is independent of the position of the receiver in space, the phase of the detected burst signal is not. By extending the optical configuration of the laser Doppler system with an additional receiver in a different spatial position, the difference in phase between the burst signals detected by the two receivers 1 and 2, denoted by $\Delta\Phi_{12}$, can be measured. The phase Doppler measurement technique exploits the fact that this phase difference $\Delta\Phi_{12}$ is a function of the particle size (Bachalo & Houser, 1984). Indeed, for a dominating scattering order N, there is a linear relationship between the measured phase difference $\Delta\Phi_{12}^{(N)}$ and the particle diameter d_p:

$$d_\mathrm{p} = \left|F_\Phi^{(N)}\right| \left|\Delta\Phi_{12}^{(N)}\right| . \tag{3.3}$$

Here, $F_\Phi^{(N)}$ is the phase conversion factor for the scattering order N, which is a function of the relative refractive index M, the laser beam wavelength λ_b, the laser beam intersection angle Θ_b and the position of the two receivers in space, usually defined in terms of the receiver elevation angle ψ_r and the receiver off-axis angle ϕ_r. The relationship between the particle diameter d_p and the measured phase difference $\Delta\Phi_{12}^{(N)}$ is only unambiguous for phase differences of up to 2π rad. This phase ambiguity can be resolved by introducing an additional receiver, which results in an extended measurement size range (Albrecht et al., 2003).

Being non-invasive and allowing for the local measurement of high absolute particle velocities u_p as well as small particle diameters d_p, the phase Doppler measurement technique is an appropriate choice for the investigation of complex sprays. In fact, its suitability for the application in supersonic close-coupled atomization has been shown successfully by, for instance, Wolf and Bergmann (2002), employing a system described by Domnick et al. (1997, 1998) for the on-line process monitoring during the atomization of a number of different alloys.

3.2.1 Optical Configuration

For the characterization of the spray produced by the supersonic close-coupled atomizer described in Section 3.1, a dual-mode phase Doppler measurement system has been employed. It combines a standard system and a planar system, which are positioned in perpendicular planes, thus, not only resolving the phase ambiguity but additionally allowing for the measurement of two components of the particle velocity vector $\mathbf{u}_\mathrm{p}$. A schematic illustration of an exemplary dual-mode phase Doppler configuration is shown in Fig. 3.5.

The system consists of commercial components from Dantec Dynamics A/S. In detail, it comprises a FlowExplorer DPSS laser transmitter and a 112 mm HiDense PDA probe receiver. The two wavelengths provided by the transmitter for the standard system and the planar system are $\lambda_\mathrm{b,st} = 561\,\mathrm{nm}$ and $\lambda_\mathrm{b,pl} = 532\,\mathrm{nm}$, respectively. The laser power per beam is 200 mW. For

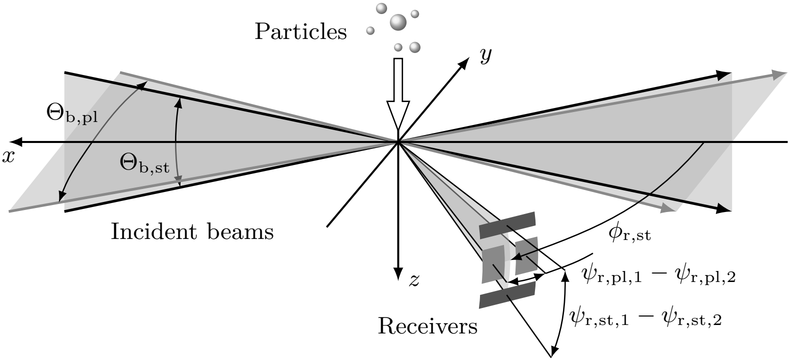

Figure 3.5: Schematic illustration of a dual-mode phase Doppler configuration combining a standard and a planar system. (Adapted from Albrecht et al., 2003, with permission from Springer Nature. © 2003 Springer Nature.)

the raw data acquisition, a Dual PDA detector unit as well as a BSA P60 flow and particle processor operated with BSA Flow software v6.50 have been used, while further data processing has been performed in MATLAB (The MathWorks, Inc.). However, it is important to note that the original hardware of the BSA P60 flow and particle processor had been upgraded, increasing the maximum frequency as well as the maximum frequency bandwidth. This is necessary for resolving the high absolute particle velocities u_p encountered in supersonic close-coupled atomization, resulting in short particle transit times and high Doppler frequencies f_D. In fact, the former are typically in the order of 10^{-7} s. After the upgrade, the system allows for measuring absolute particle velocities u_p as high as $468\,\mathrm{m\,s^{-1}}$. The frequency shift employed for directional sensitivity is 80 MHz.

In terms of the particle size measurement, the system has been set up for a scattering angle $\varphi = \phi_{\mathrm{r,st}}$ of 27°, operating in dominating first-order refraction (i.e., $N = 2$). An overview of specifications characterizing the optical configuration of the system is given in Table 3.3. The resulting phase conversion factors of the standard system and the planar system are $F^{(2)}_{\Phi,\mathrm{st}} = 9.089\,\mathrm{\mu m\,rad^{-1}}$ and $F^{(2)}_{\Phi,\mathrm{pl}} = 23.501\,\mathrm{\mu m\,rad^{-1}}$, respectively. However, the calculation of the particle diameter d_p using Eq. (3.3) is solely based on the phase difference measured by the standard system $\Delta\Phi_{12,\mathrm{st}}$, since it exhibits a higher sensitivity and is less prone to oscillations in the phase-diameter

Table 3.3: Specifications characterizing the optical configuration of the dual-mode phase Doppler measurement setup.

Specification	Value
Transmitter focal length	500 mm
Beam diameter	1.75 mm
Beam spacing	60 mm
Beam intersection angle	6.867°
Receiver focal length	500 mm
Scattering angle	27°
Spatial slit filter width	0.025 mm
Aperture mask	A

relation for small particles than the planar system (Albrecht et al., 2003). Additionally, a non-acceptance band has been defined for phase differences measured by the planar system $\Delta\Phi_{12,\mathrm{pl}}$ larger than $13/9\pi$ rad, since these can originate from particularly small particles resulting in negative phase differences. As a consequence, the maximum detectable particle diameter $d_{\mathrm{p,max}}$ for a perfectly spherical particle is about 107 µm.

While the dual-mode configuration increases the measurement size range of the standard system by resolving the phase ambiguity and allows for obtaining an additional velocity component, it also provides means for assessing the sphericity of the detected particles. This is possible, since the standard system and the planar system determine the particle diameter d_{p} in perpendicular planes, enabling a direct comparison. As a consequence, the dual-mode configuration is an effective means for reducing the Gaussian beam effect as well as the slit effect (Tropea et al., 1996). For an exemplary measurement, a phase plot is shown in Fig. 3.6. It compares the phase differences measured by the standard system and the planar system, which are $\Delta\Phi_{12,\mathrm{st}}$ and $\Delta\Phi_{12,\mathrm{pl}}$, respectively. Here, each data point corresponds to a single detected particle, the total number n_{p} being 40 917. However, for the sake of clarity, only every fifth data point is shown. Since noise and small deformations prohibit perfect agreement between the obtained phase differences, an acceptance band has been introduced to allow for a tolerable deviation. It is defined in such a way that, for a given phase difference measured by the planar system $\Delta\Phi_{12,\mathrm{pl}}$,

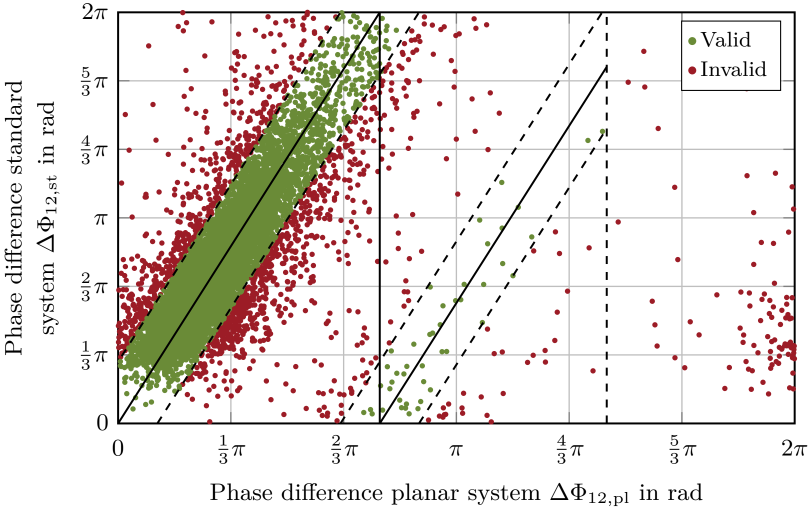

Figure 3.6: Exemplary phase plot comparing the phase differences measured by the standard system and the planar system, $\Delta\Phi_{12,\mathrm{st}}$ and $\Delta\Phi_{12,\mathrm{pl}}$, respectively. For the sake of clarity, out of a total of $n_\mathrm{p} = 40\,917$ data points, only every fifth one is shown. The sphericity validation $\vartheta_\mathrm{sphere}$ is 81.6 %.

the phase difference measured by the standard system $\Delta\Phi_{12,\mathrm{st}}$ is allowed to deviate from the ideal case by up to 15 % of the maximum value (i.e., by up to 15 % of $\Delta\Phi_{12,\mathrm{st,max}} = 2\pi\,\mathrm{rad}$). Only particles falling within this acceptance band are validated as spherical. This is expressed in terms of the sphericity validation $\vartheta_\mathrm{sphere}$, which is defined as the fraction of the total number of detected particles n_p corresponding to particles that are spherical within the defined tolerance. For the data shown in Fig. 3.6, the sphericity validation $\vartheta_\mathrm{sphere}$ is 81.6 %. Another consequence of the introduction of the tolerance band is that the maximum detectable particle diameter $d_\mathrm{p,max}$ is increased from about 107 µm to about 114 µm.

Both the transmitter and the probe receiver are mounted on the same three-axis traverse system, allowing for the measurement position to be varied accurately and flexibly within the spray. This is illustrated schematically in Fig. 3.7 as a side view and a top view of the spray downstream of the atomizer. Here, a Cartesian coordinate system $\{x, y, z\}$ has been introduced

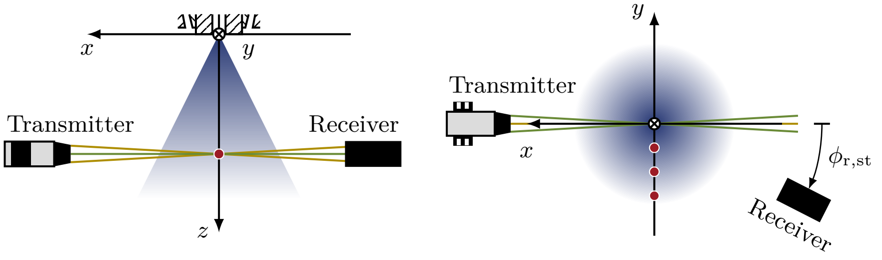

(a) Side view **(b)** Top view

Figure 3.7: Schematic illustration of the dual-mode phase Doppler measurement setup (● exemplary measurement position) and definition of the Cartesian coordinate system $\{x,\, y,\, z\}$. (Adapted from Apell et al., 2021.)

with the origin at the center of the liquid nozzle exit and the z-axis pointing downstream as the central axis of the radially symmetric spray cone. The x-axis is parallel to the bisector of the laser beams, pointing toward the transmitter. Consequently, the components of the particle velocity vector $\mathbf{u}_{\mathrm{p}}$ measured by the standard system and the planar system are $u_{\mathrm{p},z}$ and $u_{\mathrm{p},y}$, respectively. While the former is always equal to the axial particle velocity $u_{\mathrm{p,ax}}$, the latter depends on the position of the measurement volume within the spray. For instance, for positions in the xz-plane (i.e., for $y = 0\,\mathrm{mm}$) the planar system measures the tangential particle velocity $u_{\mathrm{p,tan}}$ and for positions in the yz-plane (i.e., for $x = 0\,\mathrm{mm}$) the measured velocity component $u_{\mathrm{p},y}$ is equal to the radial particle velocity $u_{\mathrm{p,rad}}$. Since the dual-mode phase Doppler system does not measure the third component of the particle velocity vector $\mathbf{u}_{\mathrm{p}}$, the absolute particle velocity u_{p} is approximated employing only the two measured components:

$$u_{\mathrm{p}} = \lVert \mathbf{u}_{\mathrm{p}} \rVert \approx \left(u_{\mathrm{p},y}^2 + u_{\mathrm{p},z}^2\right)^{\frac{1}{2}} . \tag{3.4}$$

Due to the radial symmetry of the spray cone, this approximation is expected to result in only a negligible error when restricting the measurement position to the yz-plane (i.e., to $x = 0\,\mathrm{mm}$), as is indicated in Fig. 3.7b.

3.2.2 Bias Correction

When calculating meaningful distributions from the raw data obtained using the phase Doppler measurement technique, additional care has to be taken to correct for potential bias, which is due to the measurement principle being based on individual realizations and the measurement time t_meas being finite. For instance, McLaughlin and Tiederman (1973) have identified bias in time-based velocity distributions obtained from laser Doppler data for the continuous phase. In this case, the bias is due to the data rate f_data, that is, the number of detected particles per unit time, depending on the absolute velocity of the tracer particles u_p, which is assumed to equal the absolute velocity of the continuous phase. An appropriate method for correction has been proposed by Hoesel and Rodi (1977) and further investigated by Buchhave et al. (1979). However, in the context of phase Doppler measurements in a spray, number-weighted distributions are derived for the particles themselves. In addition, the particles are generally not uniform in size. When correcting for bias, both of these aspects have to be taken into account.

In terms of the particle number concentration c, that is, the number of particles per unit volume, bias occurs when detected particles do not contribute equally to the particle number concentration c, but are weighted equally in the calculation of the distribution of interest. For a finite measurement time t_meas, the particle number concentration c is defined as

$$c = \frac{1}{t_\mathrm{meas}} \sum_{i=1}^{n_\mathrm{p}} \frac{1}{A_{\mathrm{det},i}\, u_{\mathrm{p},i}} \approx \frac{1}{t_\mathrm{meas}} \sum_{i=1}^{n_\mathrm{p}} \frac{t_{\mathrm{p,trans},i}}{V_{\mathrm{det},i}}, \tag{3.5}$$

where $u_{\mathrm{p},i}$ is the absolute velocity of the specific particle i and $A_{\mathrm{det},i}$ is the size of the corresponding detection area. As has been recommended by Edwards (1987), an approximation of the particle number concentration c based on the transit time $t_{\mathrm{p,trans},i}$ it takes the specific particle i to traverse the detection volume and on the size $V_{\mathrm{det},i}$ of the corresponding detection volume has been used in Eq. (3.5). This also resolves issues for particularly slow particles, which can arise due to the absolute particle velocity $u_{\mathrm{p},i}$ being in the denominator in Eq. (3.5) (Hoesel & Rodi, 1977). It is important to note that the size of the detection volume $V_{\mathrm{det},i}$, and therefore also the size of the detection area $A_{\mathrm{det},i}$, is dependent on the size of the specific particle i. This is due to the fact that the laser beams do not have a uniform intensity profile and the intensity of the scattered light depends on the particle diameter d_p (Albrecht et al., 2003). Consequently, from Eq. (3.5) it can be seen that the contribution of large particles to the number concentration c is overestimated compared to the contribution of small particles, leading to bias in the particle size distribution. Similarly, the contribution of fast particles to the number concentration c is overestimated when compared to the contribution of slow particles. This leads to bias in the particle velocity distribution.

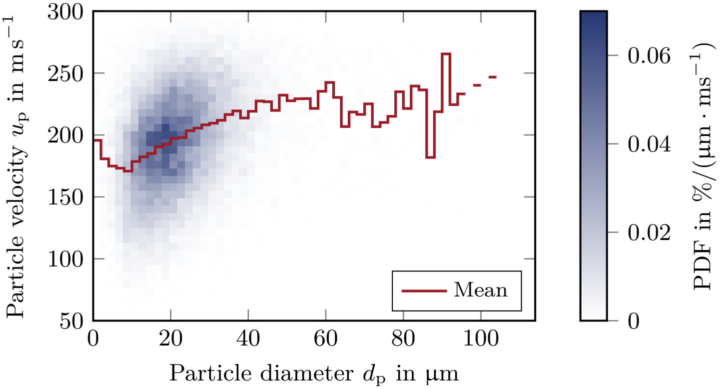

Figure 3.8: Correlation between the particle diameter d_p and the absolute particle velocity u_p for an exemplary measurement. Shown are the discrete probability density function and the corresponding mean value. (Adapted from Apell et al., 2023, with permission from Elsevier Ltd. © 2023 Elsevier Ltd.)

In cases where the particle diameter d_p and the absolute particle velocity u_p are correlated, bias in the particle size distribution can lead to bias in the particle velocity distribution, and vice versa. Such a case is depicted in Fig. 3.8 for an exemplary measurement. Here, the relationship between the particle diameter d_p and the absolute particle velocity u_p is shown as a discrete probability density function (PDF) along with the corresponding mean value. As is obvious, both quantities are positively correlated.

In order to correct for the bias, based on Eq. (3.5), a normalized weighting factor w_i has been introduced for every individual particle i that is detected:

$$w_i = \frac{1}{\sum\limits_{j=1}^{n_\mathrm{p}} \frac{t_{\mathrm{p,trans},j}}{V_{\mathrm{det},j}}} \frac{t_{\mathrm{p,trans},i}}{V_{\mathrm{det},i}}. \tag{3.6}$$

The transit time $t_{\mathrm{p,trans},i}$ of the specific particle i is recorded by the BSA flow and particle processor and, therefore, readily available. The size of the corresponding detection volume $V_{\mathrm{det},i}$, on the other hand, has to be estimated.

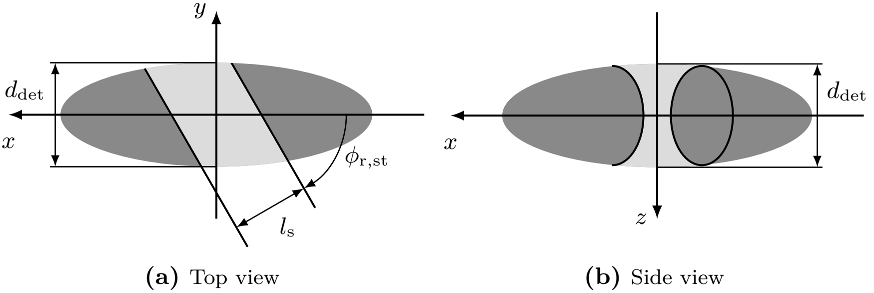

(a) Top view

(b) Side view

Figure 3.9: Schematic illustration of the detection volume approximated as an ellipsoid truncated by the spatial slit filter. (Adapted from Albrecht et al., 2003, with permission from Springer Nature. © 2003 Springer Nature.)

The detection volume has been assumed to have the shape of an ellipsoid truncated by the spatial slit filter in front of the receiving optics. This is illustrated schematically in Fig. 3.9. Using the approximation of a cylinder, the size of the detection volume is

$$V_{\mathrm{det},i} = \frac{\pi}{4} \frac{d_{\mathrm{det},i}^2 l_\mathrm{s}}{\sin\left(\phi_\mathrm{r,st}\right)}, \tag{3.7}$$

where $d_{\mathrm{det},i}$ is the effective detection volume diameter corresponding to the specific particle i and l_s is the spatial slit filter width (Albrecht et al., 2003). The former, however, can be estimated only for a specific class k of particle diameters d_p. This has been done by employing the definition of the particle burst length $L_{\mathrm{p},i} = u_{\mathrm{p},i}\, t_{\mathrm{p,trans},i}$ and assuming a two-dimensional particle trajectory in the yz-plane (i.e., assuming $u_{\mathrm{p},x,i} = 0\,\mathrm{m\,s^{-1}}$):

$$d_{\mathrm{det},k} = \frac{4}{\pi} \frac{l_\mathrm{s} \sum\limits_{i=1}^{n_{\mathrm{p},k}} L_{\mathrm{p},i}}{n_{\mathrm{p},k} l_\mathrm{s} - |\cos\phi_\mathrm{r}| \sum\limits_{i=1}^{n_{\mathrm{p},k}} L_{\mathrm{p},i} \left|\gamma_{\mathrm{p},y,i}\right|}. \tag{3.8}$$

Here, $\gamma_{\mathrm{p},y,i} = u_{\mathrm{p},y,i}/u_{\mathrm{p},i}$ is the directional cosine of the y-component of the particle velocity vector $\mathbf{u}_{\mathrm{p},i}$ corresponding to the specific particle i and $n_{\mathrm{p},k}$ is the number of particles in the specific particle diameter class k. Using classes is necessary, since the particle burst length $L_{\mathrm{p},i}$ obtained from a single particle i traversing the detection volume is not a reliable measure of the effective detection volume diameter $d_{\mathrm{det},i}$ due to its dependence on the specific particle trajectory. In other words, while a particle traversing the outer region of the detection volume may still be detected, its corresponding burst length $L_{\mathrm{p},i}$ is comparatively short (Albrecht et al., 2003). This also means that particle diameter classes k containing a number of particles $n_{\mathrm{p},k}$ not statistically sufficient for sampling the detection volume do not allow for a reliable estimate of the effective detection volume diameter $d_{\mathrm{det},k}$.

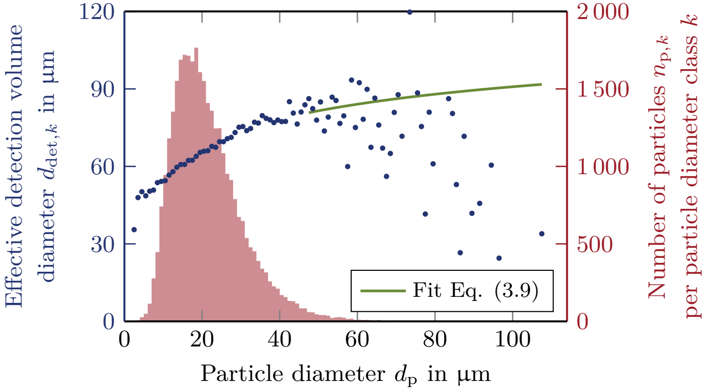

Figure 3.10: Effective detection volume diameter $d_{\mathrm{det},k}$ as a function of the particle diameter $d_{\mathrm{p},k}$ for an exemplary measurement. Additionally shown in red is the number of particles $n_{\mathrm{p},k}$ inside of the particle diameter classes k used for the evaluation of the effective detection volume diameter $d_{\mathrm{det},k}$ according to Eq. (3.8).

In Fig. 3.10, the relationship between the effective detection volume diameter d_det and the particle diameter d_p calculated according to Eq. (3.8) and using particle diameter classes of 1 µm width is shown for an exemplary measurement of a total of $n_\mathrm{p} = 33\,357$ particles. Additionally depicted is the number of particles $n_{\mathrm{p},k}$ within each particle diameter class k. As can be seen, while, for particle diameter classes containing a large number of particles $n_{\mathrm{p},k}$, the effective detection volume diameter d_det increases with increasing particle diameter d_p, small numbers of particles $n_{\mathrm{p},k}$ in a given class k result in scattering due to the dependence of the particle burst length L_p on the particle trajectory. For sufficiently large particles, this has been resolved by fitting a logarithmic function of the form

$$d^2_{\mathrm{det},k} = C_1 \ln\left(d_{\mathrm{p},k}\right) + C_2, \tag{3.9}$$

into the particle diameter classes containing a sufficient number of particles $n_{\mathrm{p},k}$, where C_1 and C_2 are fitting parameters. Here, the minimum number

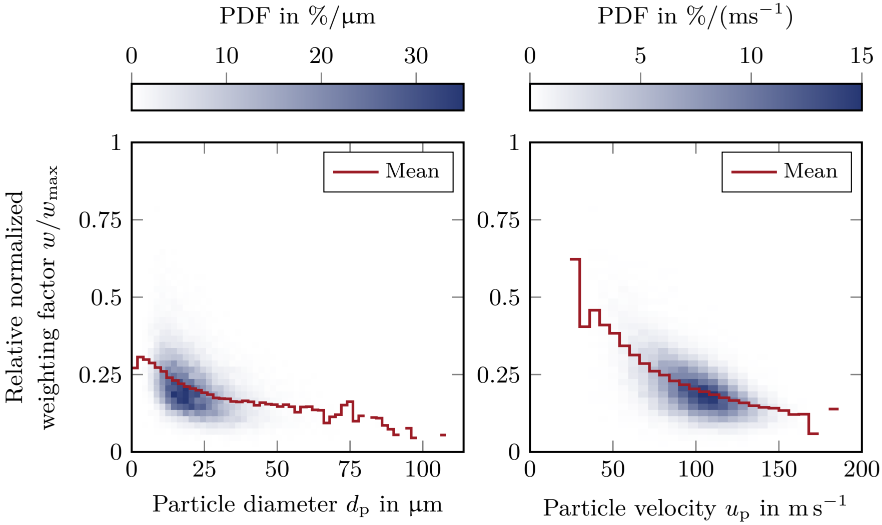

Figure 3.11: Relative normalized weighting factor w/w_max as a function of the particle diameter d_p and the absolute particle velocity u_p for an exemplary measurement. Shown are the discrete probability density function and the corresponding mean value.

of particles assumed to be necessary for obtaining a valid estimate of the effective detection volume diameter $d_{\mathrm{det},k}$ is $n_{\mathrm{p},k,\mathrm{min}} = 75$. In Fig. 3.10, the fit obtained for the exemplary measurement employing a non-linear least squares method is additionally shown. For small particles, however, this approach is unreliable and the effective detection volume diameter $d_{\mathrm{det},k}$ calculated using Eq. (3.8) has been used instead (Dantec Dynamics A/S, 2011).

For the same $n_{\mathrm{p}} = 33\,357$ particles included in Fig. 3.10, the calculated normalized weighting factors w are shown in Fig. 3.11 as a function of the particle diameter d_{p} as well as the absolute particle velocity u_{p}, relative to the maximum normalized weighting factor w_{max}. In detail, the data is presented as a discrete probability density function and the corresponding mean value. As can be seen, large particles as well as fast particles are weighted less strongly, contrary to the influence of the bias. In particular, the inversely proportional relationship between the normalized weighting factor w and the particle velocity u_{p} is obvious, which is also apparent from Eq. (3.5).

3.2.3 Calculation of Particle Size and Velocity Statistics

The dual-mode phase Doppler measurement setup described in Section 3.2.1 has been used to detect individual particles and characterize them in terms of size (i.e., diameter d_{p}) and the two velocity components $u_{\mathrm{p},y}$ and $u_{\mathrm{p},z}$. Due to the inherently heterogeneous nature of the atomization process, these quantities are expected to vary from particle to particle (Lefebvre & McDonell, 2017). Consequently, the spray is locally characterized in terms of particle size and velocity distributions of finite width. Taking into account the normalized weighting factor w introduced in Section 3.2.2 for bias correction, these distributions have been obtained from the raw data in terms of discrete probability density functions (PDF) and corresponding discrete cumulative distribution functions (CDF). The former illustrate what fraction of the total number of particles n_{p} is associated with a given particle diameter d_{p}, absolute particle velocity u_{p} or component of the particle velocity vector $\mathbf{u}_{\mathrm{p}}$. The latter, on the other hand, describe what fraction of the total number of particles n_{p} is smaller than or equal in size to a given particle diameter d_{p} or slower than or equal in velocity to a given absolute particle velocity u_{p} or component of the particle velocity vector $\mathbf{u}_{\mathrm{p}}$. The uniform widths of the diameter classes and the velocity classes used for the construction of these distributions have been calculated employing the method proposed by Freedman and Diaconis (1981) and found to be 1 µm and $3\,\mathrm{m\,s^{-1}}$, respectively.

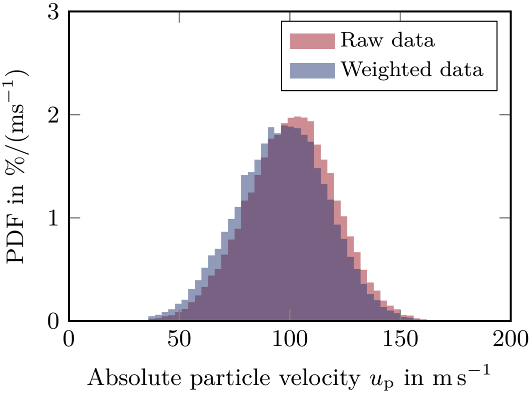

Figure 3.12: Comparison between raw and weighted discrete probability density functions of the absolute particle velocity u_p for an exemplary measurement.

In Fig. 3.12, the discrete probability function of the absolute particle velocity u_p is shown for an exemplary measurement. Here, the distribution of the raw data is compared to the distribution corrected for bias using the normalized weighting factor w introduced in Eq. (3.6). As can be seen, due to the faster particles being weighted less strongly, the discrete probability function is shifted more toward the slower particles, as has already been discussed in Section 3.2.2.

In terms of the particle size distribution, an additional volume-weighted distribution has been introduced, which is, in fact, equal to the mass-weighted distribution due to the constant liquid density ρ_l. This introduction is necessary, since, in the context of powder production, the total mass of product, which meets the requirements in terms of particle size and, therefore, can be sold without further treatment, is of economic importance. In Fig. 3.13, a particle size distribution for an exemplary measurement is shown as a discrete probability density function as well as the corresponding cumulative distribution function. The same data is presented in two different ways, as a number-weighted distribution in Fig. 3.13a and as a volume-weighted distribution in Fig. 3.13b. As can be seen, due to the cubic relationship

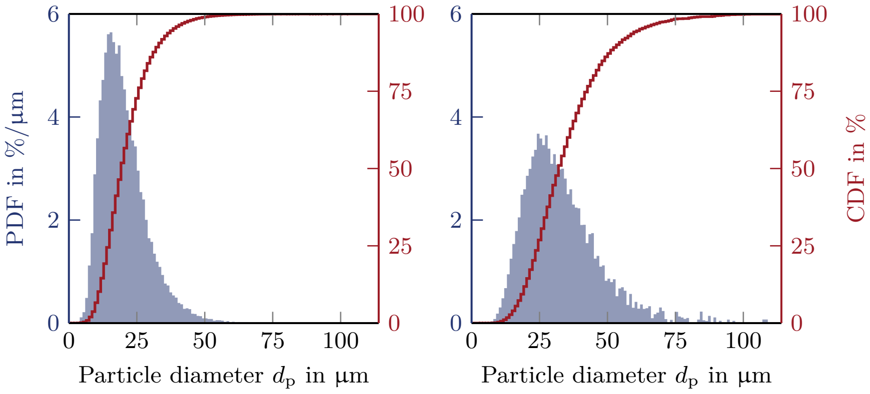

(a) Number-weighted **(b)** Volume-weighted

Figure 3.13: Particle size distribution, weighted in two different ways, for an exemplary measurement. In each case, the discrete probability density function as well as the corresponding discrete cumulative distribution function are shown.

between the particle diameter d_p and the particle volume V_p, few large particles contribute strongly to the total volume of the particles.

Particle Statistics

While discrete probability density functions and cumulative distribution functions provide a complete description of the atomization result, it is convenient to reduce these to a number of statistics, which allow for a quantitative comparison of atomization results while still being representative of the main features of the actual distributions. For this purpose, two statistics have been introduced for every particle size and velocity distribution, the first one being a measure of centrality and the second one being a measure of dispersion. Furthermore, owing to the necessity to consider number-weighting as well as volume-weighting, two additional statistics have been introduced only for the particle size distributions. All statistics have been derived taking into account the normalized weighting factor w introduced in Section 3.2.2.

A summary of the relevant statistics is given in Table 3.4. For the particle velocity distributions, this includes the arithmetic mean value, denoted by an overline, as a measure of centrality as well as the standard deviation s as

Table 3.4: Statistics derived from particle size and velocity distributions.

Measure	Weighting	Particle diameter (d_p)	Particle velocity (u_p, $u_{\mathrm{p},y}$, $u_{\mathrm{p},z}$)
Centrality	Number	$d_{0.5,n}$	$\bar{u}_\mathrm{p}$, $\bar{u}_{\mathrm{p},y}$, $\bar{u}_{\mathrm{p},z}$
	Volume	$d_{0.5,V}$	–
Dispersion	Number	IQR_n	s_{u_p}, $s_{u_{\mathrm{p},y}}$, $s_{u_{\mathrm{p},z}}$
	Volume	IQR_V	–

a measure of dispersion. The particle size distributions, one the other hand, have been characterized by the median diameter $d_{0.5}$ and the interquartile range IQR. The latter is defined as the difference between the upper quartile diameter $d_{0.75}$ and the lower quartile diameter $d_{0.25}$ (i.e., as $IQR = d_{0.75} - d_{0.25}$). Both quantities have been evaluated for the number-weighted as well as for the volume-weighted particle size distributions.

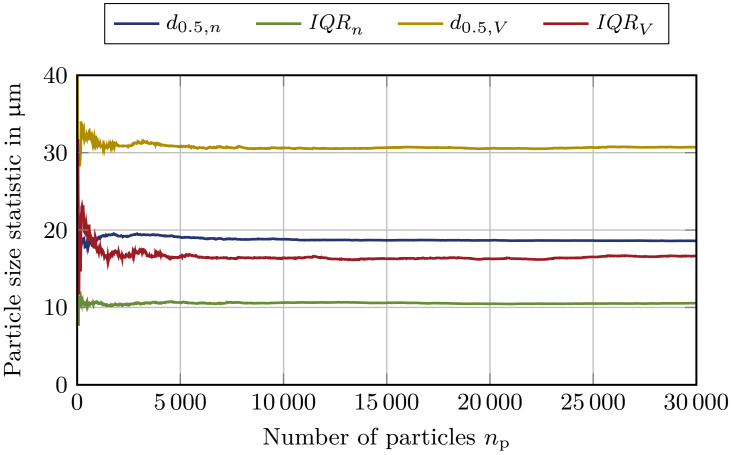

Figure 3.14: Variation of several particle size statistics with increasing number of particles n_p. The statistics are evaluated in steps of 10 particles.

It is important to note that it is necessary to detect and validate a statistically sufficient number of particles n_p in order to obtain meaningful and constant particle size and velocity distributions. This is illustrated in Fig. 3.14 for an exemplary measurement. Here, the variation of the four particle size statistics, that is, the number median diameter $d_{0.5,n}$, the number interquartile range IQR_n, the volume median diameter $d_{0.5,V}$ and the volume interquartile range IQR_V, with increasing number of particles n_p is shown. As can be seen, all four statistics fluctuate for small numbers of particles n_p. This is especially the case for the volume-weighted statistics, as a single large particle can affect the total particle volume strongly due to the cubic weighting. However, for large numbers of particles n_p, the four particle size statistics remain constant, indicating a sufficiently converged measurement.

Calculation of Global Particle Statistics

Finally, while the phase Doppler measurement technique has been used to obtain local particle size and velocity data, it is possible to combine data from several measurements taken for identical operational conditions but at different positions in the same xy-plane (see Fig. 3.7). This way, global particle size and velocity distributions can be constructed, which are representative of the entire spray cross-section. Furthermore, global particle and velocity statistics can be calculated from these global distributions, which, in the following, are denoted by a circumflex. This has been done by employing a normalized weighting factor w similar to the one based on the definition of the particle number concentration c and introduced in Section 3.2.2 for bias correction. However, there are two distinct differences.

First, it is necessary to spatially integrate the local data. This has been achieved by dividing the spray cross-section into several smaller segments, each of which corresponds to a single local measurement. Here, it has been assumed that the local data is representative of the entire segment it is associated with. Consequently, a fine grid of local measurements reduces the error due to spatial integration, especially in locations characterized by gradients in the particle properties. For local measurements restricted to the negative y-axis (see Fig. 3.7), this approach is depicted schematically in Fig. 3.15. Second, considering the definition of the local particle number concentration c given in Eq. (3.5), it has to be taken into account that the time t_meas necessary to detect and validate a constant number of particles n_p varies across the spray cross-section. In other words, there are local differences in the data rate

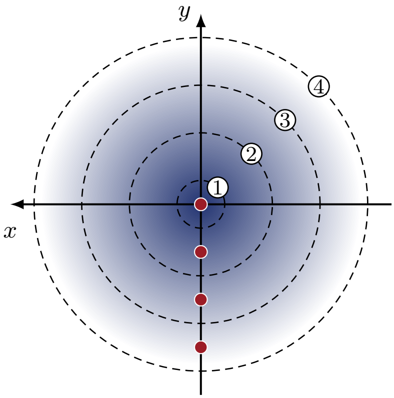

Figure 3.15: Exemplary division of the spray cross-section into smaller segments for a number of four corresponding measurement positions ●. The dashed lines indicate the four segments associated with the individual measurement positions.

f_{data}. Consequently, the following normalized weighting factor w_i has been introduced for every individual particle i:

$$w_i = \frac{1}{\sum\limits_{k=1}^{n_{\mathrm{seg}}} \sum\limits_{j=1}^{n_{\mathrm{p},k}} A_{\mathrm{seg},j} \frac{n_{\mathrm{p},j}}{t_{\mathrm{meas},j}} \frac{t_{\mathrm{p,trans},j}}{V_{\mathrm{det},j}}} A_{\mathrm{seg},i} \frac{n_{\mathrm{p},i}}{t_{\mathrm{meas},i}} \frac{t_{\mathrm{p,trans},i}}{V_{\mathrm{det},i}}. \tag{3.10}$$

Here, n_{seg} is the total number of segments forming the cross-section of the spray and $A_{\mathrm{seg},i}$ is the size of the particular segment which corresponds to the measurement position of the specific particle i. Similarly, $n_{\mathrm{p},i}$ and $t_{\mathrm{meas},i}$ are the number of particles and the measurement time associated with the measurement position of the specific particle i, respectively. Since the normalized weighting factor w is based on the particle number concentration c, it also includes a correction for the associated bias.

3.2.4 Estimation of Measurement Uncertainties

An important aspect of the characterization of the atomization result is the quantitative identification of sensitivities, that is, the influence of operational and geometric design parameters as well as physical liquid properties on the particle diameter d_{p} and the particle velocity vector $\mathbf{u}_{\mathrm{p}}$. These influences are expressed in terms of changes in the statistics described in Section 3.2.3. Consequently, it is crucial to quantify measurement uncertainties associated with the phase Doppler measurement technique in order to allow for a meaningful comparison of data and to identify statistically significant effects on the atomization result. Two components of the uncertainty have been considered, one being due to random effects and the other one being due to systematic effects (International Bureau of Weights and Measures, 2008). Both components have been quantified in terms of a standard uncertainty, assuming independence. Consequently, in the following chapters, statistics derived from data obtained by means of the phase Doppler measurement technique are reported together with an expanded combined standard uncertainty, employing a coverage factor K of 1.96, unless explicitly stated otherwise.

Random Effects

Treating the component of uncertainty due to random effects by means of a rigorous type A evaluation, as defined by the International Bureau of Weights and Measures (2008), requires a sufficiently large number of observations. In other words, it involves repeating experiments a certain number of times under identical conditions. However, since experiments in the context of supersonic close-coupled atomization are expensive, this is not feasible for an extensive measurement campaign. On the other hand, a type B evaluation of this component of uncertainty, that is, a comprehensive analytical treatment, is also not feasible. This is due to the fact that such an analysis of the phase Doppler measurement technique would have to include the optical configuration, the signal processing as well as the spray itself, as has been pointed out by Blagojević and Bajsić (1996), resulting in a high level of complexity. While there are analytical expressions for calculating estimates of the uncertainty component due to random effects, this is only the case for specific statistics and not the particular ones introduced in Table 3.4 for the particle size distributions (Benedict & Gould, 1996). Therefore, this component of uncertainty has been estimated numerically for all statistics employing the bootstrap method.

A comprehensive introduction to the bootstrap method has been given by Efron and Tibshirani (1994), however, the general procedure is summarized schematically in Fig. 3.4. Here, a sample distribution of size n_p is obtained

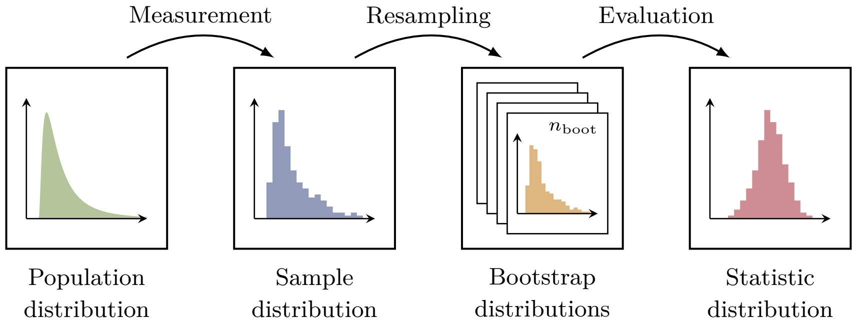

Figure 3.16: Schematic illustration of the bootstrap method.

from an unknown population distribution by means of a measurement. From this sample distribution, a bootstrap distribution is generated by drawing exactly n_{p} values with replacement. This step is repeated n_{boot} times, resulting in a total of n_{boot} bootstrap distributions. For each of these bootstrap distributions, the statistic of interest is evaluated. This, in turn, leads to a distribution of this particular statistic. Finally, the dispersion of the statistic, which is expressed in terms of the standard deviation s of the statistic distribution, is employed as an estimate of the uncertainty component due to random effects of the statistic evaluated from the sample distribution. In other words, the sample distribution is treated as the population distribution and the bootstrap distributions obtained from resampling act as a substitute for repeated measurements. This method is based on the idea that the bootstrap distributions are related to the sample distribution in the same way the sample distribution is related to the population distribution. Consequently, in order to obtain a useful estimate of the uncertainty component due to random effects, it is essential that the sample distribution is a good representation of the population distribution.

It is important to note that the bootstrap method requires a sufficiently large number of bootstrap distributions n_{boot} for the statistic distribution to converge, making the method computationally expensive. For an exemplary measurement, the variation of the standard deviation of the bootstrapped volume median diameter distribution $s_{d_{0.5,V},\mathrm{boot}}$ with increasing number of bootstrap distributions n_{boot} is shown in Fig. 3.17. As can be seen, for

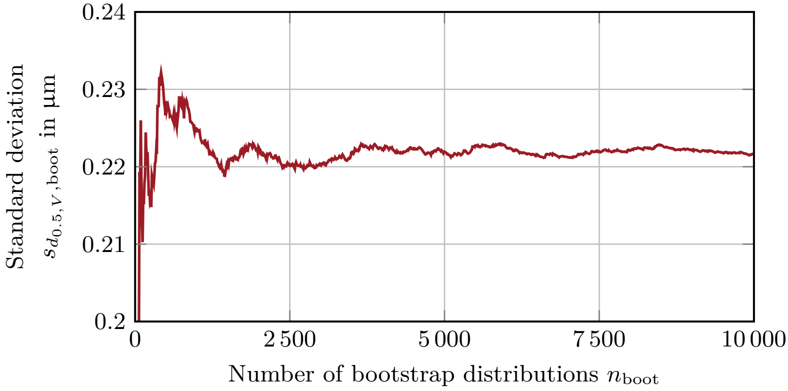

Figure 3.17: Variation of the standard deviation $s_{d_{0.5,V},\mathrm{boot}}$ of the bootstrapped volume median diameter distribution with increasing number of bootstrap distributions n_{boot}. The standard deviation $s_{d_{0.5,V},\mathrm{boot}}$ is evaluated in steps of 10 bootstrap distributions.

small numbers of bootstrap distributions n_{boot}, there are fluctuations in the standard deviation $s_{d_{0.5,V},\mathrm{boot}}$, which decrease with increasing number of bootstrap distributions n_{boot}, indicating a converged statistic distribution.

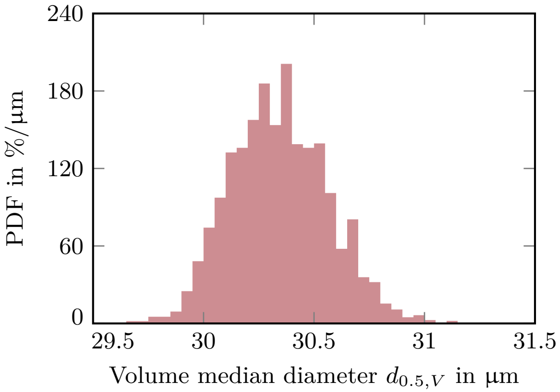

Figure 3.18: Bootstrapped distribution of the volume median diameter $d_{0.5,V}$ for an exemplary measurement. Shown is the discrete probability density function.

The final bootstrapped distribution of the volume median diameter $d_{0.5,V}$ using $n_{\mathrm{boot}} = 10\,000$ bootstrap distributions is shown in Fig. 3.18 as a discrete probability density function. Its standard deviation $s_{d_{0.5,V},\mathrm{boot}} \approx 0.22\,\mu\mathrm{m}$ is an estimate of the uncertainty component due to random effects of the volume median diameter $d_{0.5,V}$ for this particular measurement.

In order to validate the application of the bootstrap method for phase Doppler measurements in the spray produced by the supersonic close-coupled atomizer described in Section 3.1, a series of 15 measurements have been carried out in a short period of time for the same set point of operation, that is, both the gas stagnation pressure $p_{\mathrm{t,g}}$ and the liquid mass flow rate $\dot{m}_{\mathrm{l}}$ differ less than 0.5 % from the respective arithmetic mean value over all 15 measurements.

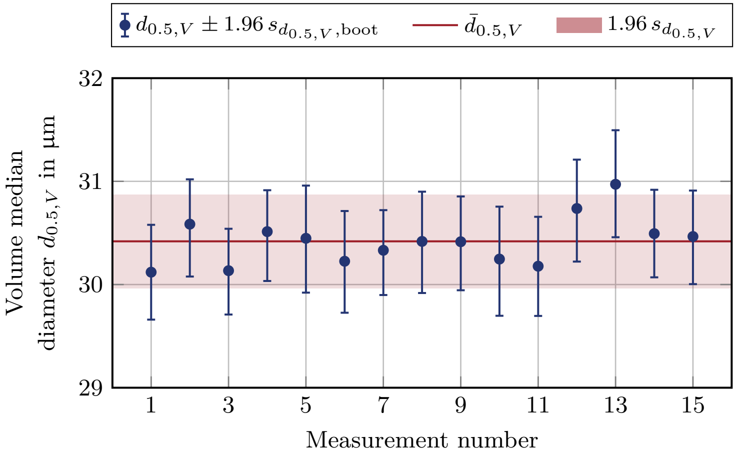

Figure 3.19: Comparison between measured random fluctuations of the volume median diameter $d_{0.5,V}$, expressed in terms of the sample standard deviation $s_{d_{0.5,V}}$, and bootstrapped estimates of the uncertainty component due to random effects $s_{d_{0.5,V},\mathrm{boot}}$. (Adapted from Apell et al., 2022b.)

In Fig. 3.19, the volume median diameter $d_{0.5,V}$ is presented for the 15 data sets obtained. Additionally shown are the arithmetic mean value over the entire sample $\bar{d}_{0.5,V}$ as well as the expanded sample standard deviation $s_{d_{0.5,V}}$, calculated from the 15 individual volume median diameters $d_{0.5,V}$ obtained and using a coverage factor K of 1.96. As expected, small random fluctuations of the volume median diameter $d_{0.5,V}$ are evident. For the sake of comparison, the bootstrapped estimate of the expanded standard deviation $s_{d_{0.5,V},\mathrm{boot}}$ for each measurement is indicated as error bars, also employing a coverage factor K of 1.96. As can be seen, the agreement is good. Consequently, the bootstrap method has been deemed to be a suitable means for estimating the uncertainty component due to random effects for statistics derived from the phase Doppler measurement data.

Systematic Effects

A second component of the uncertainty has been considered, which is due to systematic effects. These become apparent on a time scale much longer than the one characteristic of the random fluctuations, that is, when measurements are repeated over a sufficiently large period of time under identical set points of operation. Characteristic of these systematic effects is an offset in the evaluated statistics, which exceeds the uncertainty component due to random effects and does not fluctuate in the same manner. Importantly, however, they do not affect the qualitative trends in the measurement data.

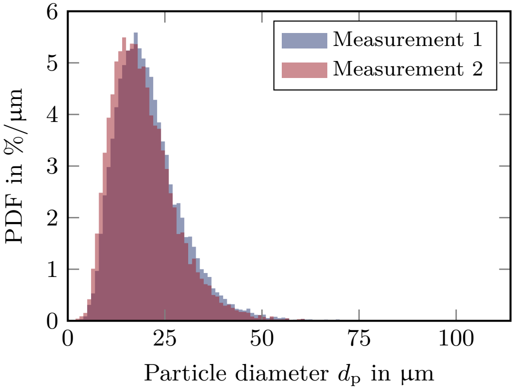

Figure 3.20: Comparison between two number-weighted discrete probability density functions of the particle diameter d_p obtained for the same set point of operation.

An example is given in Fig. 3.20, where two number-weighted particle size distributions are compared, which have been obtained from two different measurements. Here, as well as in the following, the set points of operation defined by the gas stagnation pressure $p_{\mathrm{t,g}}$ and the liquid mass flow rate $\dot{m}_{\mathrm{l}}$ (see Section 3.1.4) are reported in terms of an arithmetic mean value and 1.96 times the sample standard deviation s as a measure of dispersion. For the data shown in Fig. 3.20, the corresponding set points of operation are characterized by a gas stagnation pressure $p_{\mathrm{t,g}}$ of $(0.80 \pm 0.05)\,\mathrm{MPa}$ and $(0.80 \pm 0.05)\,\mathrm{MPa}$, respectively, and by a liquid mass flow rate $\dot{m}_{\mathrm{l}}$ of $(5.01 \pm 0.04)\,\mathrm{kg\,min^{-1}}$ and $(5.00 \pm 0.05)\,\mathrm{kg\,min^{-1}}$, respectively, exhibiting negligible differences. Still, the distributions are shifted with respect to each other. This is expressed in terms of differences in the particle size statistics defined in Table 3.4. For the number median diameter $d_{0.5,n}$ and the volume median diameter $d_{0.5,V}$, the differences are $(1.3 \pm 0.2)\,\mathrm{\mu m}$ and $(1.6 \pm 0.6)\,\mathrm{\mu m}$, respectively, where the bootstrapped estimate of the uncertainty due to random effects is also reported, using a coverage factor K of 1.96. Clearly, the shift is significant relative to the random fluctuations. On the other hand, for the number interquartile range IQR_n and the volume interquartile range IQR_V, the differences are $(0.1 \pm 0.3)\,\mathrm{\mu m}$ and $(1.0 \pm 1.0)\,\mathrm{\mu m}$, respectively, indicating that the distributions are indeed only shifted. It has to be noted, however, that this consideration also includes effects, which are due to the supersonic close-coupled atomization process itself and not covered by the definition of the set point of operation (see Section 3.1.4). As an example, Wolf and Bergmann (2002) have noticed that the gas jet profile is highly sensitive to the ambient conditions, influencing the atomization result. Since the atomizer described in Section 3.1 features a completely open design in order to improve the accessibility for various measurement techniques, such effects cannot be avoided.

Ideally, the uncertainty component due to systematic effects is treated by introducing an additive correction or a correction factor and, subsequently, quantifying the uncertainty associated with these quantities (International Bureau of Weights and Measures, 2008). However, this approach requires an estimate of the systematic error, which is not easily available without knowledge of a *true* value of the measured quantity[1] or a suitable calibration measurement. Therefore, following recommendations by the International Bureau of Weights and Measures (2008), this component of uncertainty has been evaluated by means of a Type A evaluation of uncertainty. In detail, 15 measurements have been carried out over the course of the entire measurement

---

[1] Which, by nature, is indeterminate.

campaign for the same representative set point of operation, that is, both the gas stagnation pressure $p_{\mathrm{t,g}}$ and the liquid mass flow rate $\dot{m}_{\mathrm{l}}$ differ less than 0.5 % from the respective arithmetic mean value over all 15 measurements. As a result, distributions have been obtained for all relevant particle statistics (see Section 3.2.3). The corresponding standard deviations s serve as an estimate of the uncertainty components due to systematic effects. Here, it has been assumed that the obtained standard deviations s are representative of all set points of operation considered.

3.3 Imaging Techniques

Visualization is an import tool for investigating sprays, as it provides insight into the mechanisms responsible for liquid breakup. Consequently, appropriate imaging techniques have to be chosen, which can be applied to supersonic close-coupled atomization. However, as has already been established in Section 3.2, the sprays produced by these atomizers are characterized by short time scales, small length scales and a high optical density, making this a challenging task.

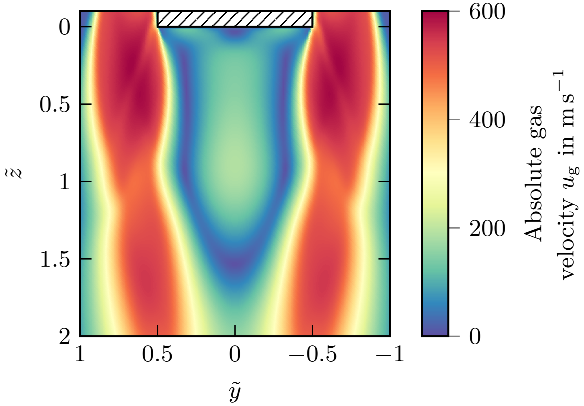

Figure 3.21: Axisymmetric steady-state simulation results for the local absolute gas velocity u_{g} in the gas-only flow field downstream of the liquid nozzle for an exemplary gas stagnation pressure $p_{\mathrm{t,g}}$ of 1 MPa. The numerical data has been provided by the research partner SMS as part of the IGSTC project PPAM.

In fact, the flow field immediately downstream of the liquid nozzle can be divided into two regions with distinctly different characteristics. Numerical simulation results for the absolute gas velocity u_g in the gas-only flow field are shown in Fig. 3.21. The data has been provided by the research partner SMS as part of the IGSTC project PPAM. Here, as well as in all of the following figures, the spatial Cartesian coordinates $\{x,\ y,\ z\}$ (see Fig. 3.7) are non-dimensionalized using the liquid nozzle tip diameter $d_\mathrm{l,tip}$ as a reference length scale (see Section 3.1.2):

$$\tilde{x} = \frac{x}{d_\mathrm{l,tip}}, \qquad \tilde{y} = \frac{y}{d_\mathrm{l,tip}}, \qquad \tilde{z} = \frac{z}{d_\mathrm{l,tip}}. \tag{3.11}$$

As can be seen, the absolute gas velocity u_g varies locally by up to two orders of magnitude. Indeed, while the wake downstream of the liquid nozzle tip is characterized by a comparatively low absolute gas velocity u_g, the gas in the surrounding jet exiting from the gas nozzle is particularly fast. Although the introduction of liquid certainly has a modifying effect on the flow field, leading to changes that are not captured by the gas-only simulation, this large difference in the local absolute gas velocity u_g indicates that there are two separate regions having different requirements for the visualization.

Immediately upon exiting the liquid nozzle, the liquid first interacts with the gas flow inside of the wake downstream of the liquid nozzle tip, leading to primary atomization. Here, the local absolute liquid velocity u_l is typically in the order of $10\,\mathrm{m\,s^{-1}}$ (Bigg & Mullis, 2020). Furthermore, the size of the resulting liquid ligaments is typically in the order of $10^{-4}\,\mathrm{m}$ (Amatriain et al., 2022). In contrast, the interaction of the liquid with the high-velocity gas jet as part of secondary atomization results in even smaller particles having a velocity typically in the order of $10^{2}\,\mathrm{m\,s^{-1}}$ (Kirmse & Chaves, 2016). Consequently, visualization of the interaction between the liquid and the high-velocity gas jet requires a higher spatial and temporal resolution than visualization of the primary atomization.

3.3.1 High-speed Imaging

For the visualization of the primary atomization in the wake downstream of the liquid nozzle, a high-speed imaging setup has been developed based on the diffuse backlight illumination technique. It provides sufficient spatial and temporal resolution to capture the motion and the breakup of the liquid exposed to the comparatively low-velocity gas flow in the wake.

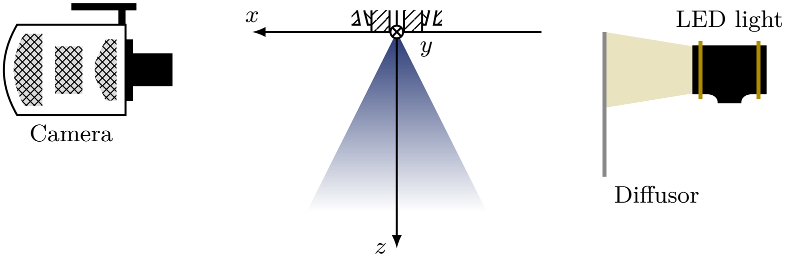

Figure 3.22: Schematic illustration of the side-view of the high-speed imaging setup.

In Fig. 3.22, a schematic illustration of the side-view of the high-speed imaging setup is shown, including a Cartesian coordinate system $\{x, y, z\}$, which is identical to the one introduced in Section 3.2.1. In detail, the setup comprises a monochrome Phantom v2012 high-speed camera (Vision Research Inc.) and a pulsed Constellation 120E LED light source (Veritas, Integrated Design Tools Inc.). The latter is positioned opposite the high-speed camera, on the other side of the spray cone. Additionally, the high-speed camera and the LED light source are synchronized, with the former providing the trigger signal. Diffuse backlight illumination has been achieved by placing a 30° Light Shaping Diffusor sheet (Luminit LLC) in front of the LED light source.

Table 3.5: Specifications of the Phantom v2012 high-speed camera.

Specification	Value
Frame rate	57 000 Hz
Sensor resolution	608 px × 512 px
Sensor size	35.84 mm × 22.4 mm
Exposure time	500 ns
Pixel size	28 µm
Pixel depth	12 bit

An overview of the specifications of the Phantom v2012 high-speed camera is given in Table 3.5. Here, it has to be noted that the sensor resolution, while allowing for a maximum of 1280 px × 800 px, has been reduced in order to increase the frame rate, which is only 22 600 Hz at full resolution. The high-speed camera has been equipped with a SP 180 mm f/3.5 Di Macro lens (Tamron Europe GmbH) and positioned at a working distance of $x = 450\,\mathrm{mm}$ from the center of the liquid nozzle. For this configuration, the spatial resolution achieved is 52.7 µm/px. Consequently, considering the exposure time given in Table 3.5, the maximum absolute liquid velocity $u_{\mathrm{l,max}}$ that can be resolved with minimal motion blur[2] is $105\,\mathrm{m\,s^{-1}}$.

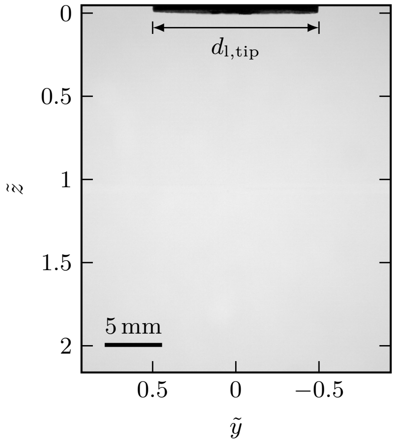

Figure 3.23: Field of view of the high-speed imaging setup. As a reference, the liquid nozzle tip diameter $d_{\mathrm{l,tip}}$ is indicated.

The resulting field of view (FoV) of the high-speed imaging setup is depicted in Fig. 3.23. The image shows the background with no gas flow and no liquid flow. As a reference, the tip of the liquid nozzle having a diameter $d_{\mathrm{l,tip}}$ of 14.5 mm (see Section 3.1.2) is indicated at the top of the image.

3.3.2 Double-frame Imaging

Visualization of the interaction between the liquid and the high-velocity gas jet requires particularly high temporal resolution as well as particularly short

---

[2] Defined as the relative motion between the liquid and the camera equal to a distance of more than 1 px within the exposure time.

exposure times in order to resolve the liquid breakup and the motion of the resulting small liquid particles while minimizing motion blur. These requirements are challenging to meet using a traditional high-speed imaging setup like the one described in Section 3.3.1. For instance, liquid having an absolute velocity u_l of $100\,\mathrm{m\,s^{-1}}$ travels a distance of 10 px during the exposure time given in Table 3.5 for an exemplary spatial resolution of 5 µm/px. The result is severe motion blur.

Since the demanding requirements in terms of spatial resolution, temporal resolution and motion blur cannot be fully met, a compromise has been reached by using a double-frame imaging setup with ultra-short diffuse backlight illumination. Even though this approach does not allow for resolving the gas-liquid interaction in time, it minimizes the motion blur while maintaining a high spatial resolution. In addition, the double-frame approach provides a means of obtaining components of the local velocity vector of the liquid $\mathbf{u}_\mathrm{l}$.

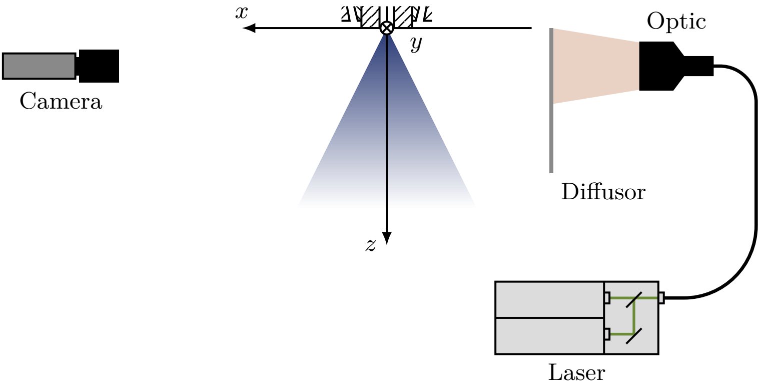

Figure 3.24: Schematic illustration of the side-view of the double-frame imaging setup.

A schematic illustration of the side-view of the double-frame imaging setup is presented in Fig. 3.24. The Cartesian coordinate system $\{x, y, z\}$ introduced in Section 3.2.1 is included as a reference. The setup consists of a FlowSense EO 2M double-frame camera, a DualPower 145-15 dual-cavity Nd:YAG laser and a ShadowStrobe illumination unit. All of the components are from Dantec Dynamics A/S. As can be seen, the spatial positioning of the double-frame camera and the illumination unit is similar to the high-speed imaging setup discussed in Section 3.3.1. The laser is connected to the illumination unit by means of a light guide and is synchronized with the double-frame camera via a timer box providing all of the necessary trigger signals. A diffuse background has been achieved by placing a Light Shaping Diffusor sheet (Luminit LLC) in front of the illumination unit.

Table 3.6: Specifications of the FlowSense EO 2M double-frame camera.

Specification	Value
Sensor resolution	2 Mpx: 1600 px × 1200 px
Sensor size	11.84 mm × 8.88 mm
Pixel size	7.4 µm
Pixel depth	10 bit

An overview of the specifications of the FlowSense EO 2M double-frame camera is given in Table 3.6. It has been operated at full sensor resolution and the aperture of its lens has been set so that no ambient light is detected. The laser emits two accurately timed pulses with a wavelength λ of 532 nm, which excite a fluorescent dye insert inside of the illumination unit. The light emitted this way is a broad orange spectral band. While the maximum pulse energy of the laser is 145 mJ, an attenuator has been employed in order to avoid pixel saturation and prevent damage to the light guide. The pulse length of 10 ns determines the illumination time of the setup and is two orders of magnitude shorter than the exposure time of the double-frame camera. As a result, the motion blur is minimized, effectively freezing the spray in time. The laser does, however, have a limited repetition rate, which has been set to 12 Hz and, therefore, is orders of magnitude too small for resolving the time-scales of the atomization process.

The double-frame camera has been equipped with one of three lenses, depending on the necessary field of view. As a consequence, the setup allows for flexibly capturing just the interaction between the liquid and the high-velocity gas jet as well as a large part of the entire spray cone. In detail, the far-field of the spray cone has been captured using a Makro-Planar T* 2/50 mm lens (Carl Zeiss AG). For the mid-field, the same SP 180 mm f/3.5 Di Macro lens (Tamron Europe GmbH) used for the high-speed imaging setup described in Section 3.3.1 has been employed. The highest spatial resolution has been achieved by capturing the near-field of the gas-liquid interaction using a QM 100 long distance microscope (Questar Corporation) in combination with a 1.5× barlow lens.

Table 3.7: Specifications of the three optical configurations used for the double-frame imaging setup.

Specification	Far-field	Mid-field	Near-field
Working distance in mm	350	450	335
Diffusor angle	60°	30°	5°
Interframe time in ns	650	1200	300
f-number	8.0	3.5	6.0
Spatial resolution in µm/px	49.8	18.7	1.2

The specifications of the three different optical configurations are summarized in Table 3.7, emphasizing important differences. As can be seen, not only are the spatial resolutions different, but all three configurations have also been operated at different interframe times. This is necessary in order to evaluate the velocity information included in the double-frame images. Additionally, it has to be noted that the configuration used for capturing the near-field is diffraction-limited. That is, taking into account the f-number of 6.0 of the QM 100 long distance microscope for the given working distance (see Table 3.7) and assuming a wavelength λ of 610 nm for the orange light, the physical resolution limit of the configuration is 4.5 µm, according to the Rayleigh criterion (Hecht, 2017).

The fields of view of the three different optical configurations used for the double-frame imaging setup are shown in Fig. 3.25. As a reference, the field of view of the mid-field is included in the field of view of the far-field. Similarly, the field of view of the near-field is depicted in the field of view of the mid-field, visualizing the large difference in spatial resolution.

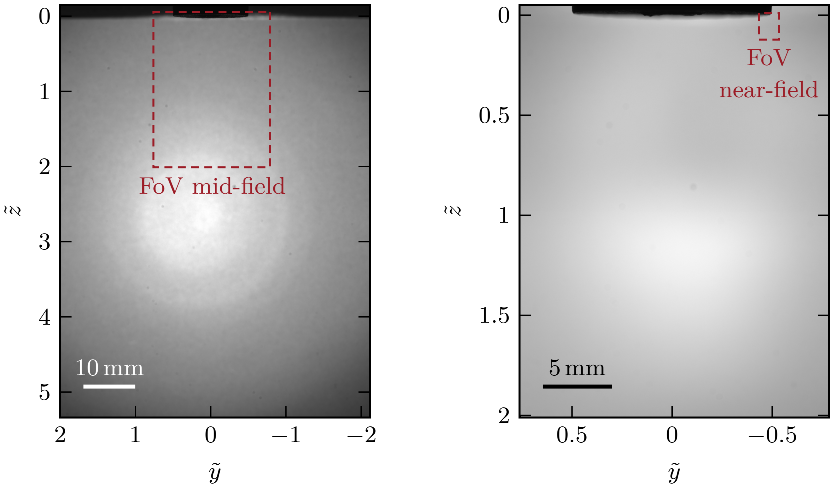

(a) Far-field **(b)** Mid-field

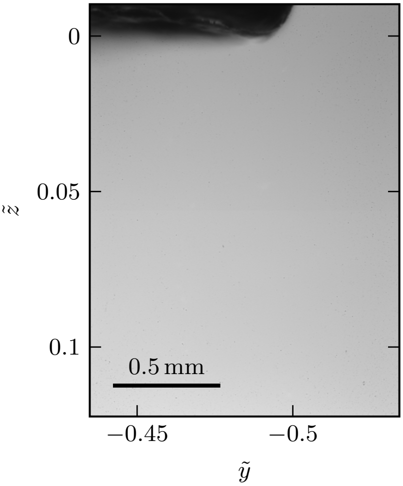

(c) Near-field

Figure 3.25: Fields of view of the three optical configurations of the double-frame imaging setup: far-field, mid-field and near-field. As a reference, the next smaller field of view is indicated for the first two configurations.

3.3.3 Evaluation of Velocity Information

The acquisition of double-frame images using the setup described in Section 3.3.2 allows for the evaluation of local velocity information for the liquid phase. This is possible by determining the two-dimensional displacement of the liquid between two frames acquired at a known interframe time. For this, the methods developed in the context of particle image velocimetry (PIV) have been used. These are based on dividing the frames into a number of interrogation areas (IA), for each of which a displacement vector is determined by means of the statistical method of cross-correlation combined with a peak detection scheme. A comprehensive introduction to particle image velocimetry has been given by Raffel et al. (2018). However, there are two distinct differences to the traditional approach of particle image velocimetry (Weber & Leick, 2014). First, backlight illumination has been used instead of a light sheet illumination (see Section 3.3.2). This is possible, since the velocity information relevant for evaluation is only contained in the liquid at the edge of the spray, which is in the focus of the double-frame imaging setup. Second, no additional tracer particles have been added to the flow field. Instead, the displacement of the liquid surface has been determined. This has two important implications. For instance, it is important to keep the interframe time short enough to reduce the error due to liquid breakup and deformation, while still allowing for a displacement large enough for the evaluation. In addition, local velocity information can only be obtained in parts of the field of view where liquid is present at the time of the image acquisition.

Image Pre-processing

Prior to the actual velocity evaluation, all of the double-frame images have been pre-processed in two steps. Since the entire research facility tends to vibrate slightly during the atomization process, it is necessary to first stabilize all of the images belonging to the same measurement. For this, the liquid nozzle has been tracked within the images and used as a reference for aligning the images and subsequently trimming them to the same size. As a result, pre-processed images from different measurements also differ in size depending on the extent of the vibrations. The stabilization is especially important for the near-field configuration due to the large magnification (see Table 3.7).

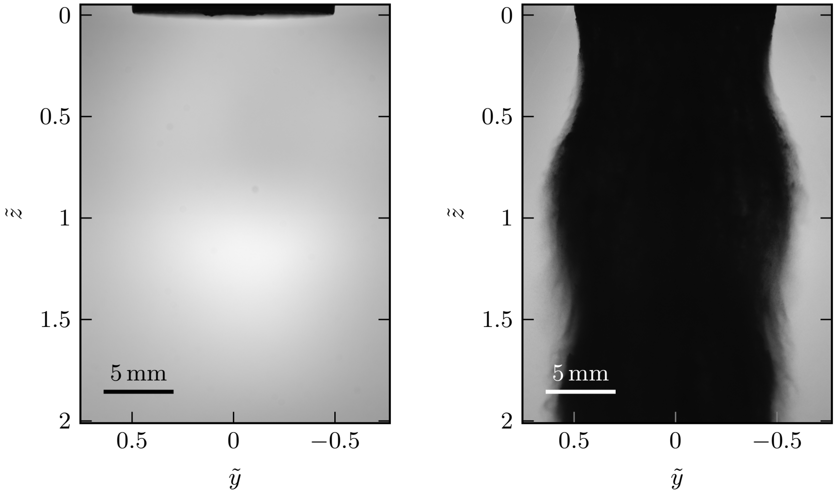

(a) Background image **(b)** Raw image

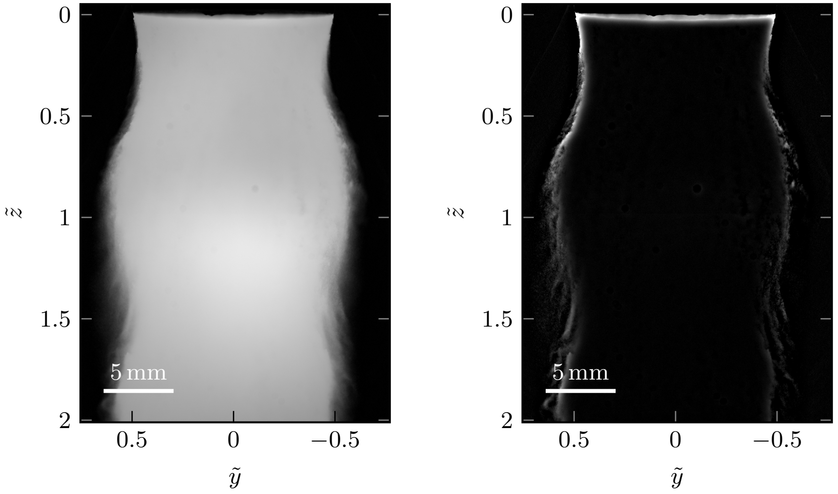

(c) Difference image **(d)** Filtered image

Figure 3.26: Second image pre-processing step prior to the evaluation of the velocity information. For the filtered image (d), the contrast has been artificially increased in order to show more detail.

However, stabilization is only possible in the horizontal or radial direction (i.e., in the y-direction), as there is no reference in the vertical or axial direction (i.e., in the z-direction). It is important to note that the vibration is evident only between double-frame images but not between the individual frames belonging to the same double-frame image. This is due to the fact that the double-frame images have been acquired at a rate of 12 Hz, while the interframe time is in the order of 10^{-7} s to 10^{-6} s (see Section 3.3.2).

In the second pre-processing step, the double-frame images have been prepared for the evaluation procedure. An overview of this step is given in Fig. 3.26 for an exemplary raw image, which is shown in Fig. 3.26b. First, the corresponding background image, which can be seen in Fig. 3.26a, is subtracted, thus, removing all of the information not affected by the atomization process. As part of the measurement procedure, background images have been captured immediately prior to each individual measurement. The result of the subtraction is depicted in Fig. 3.26c in terms of a difference image. As can be seen, the remaining intensity information corresponds to the liquid present in the field of view. Finally, the difference image is filtered using a sliding window subtract minimum filter. The window size is 9 px × 9 px for the far-field configuration, 11 px × 11 px for the mid-field configuration and 101 px × 101 px for the near-field configuration (see Section 3.3.2). The resulting filtered image is shown in Fig. 3.26d. Here, the contrast has been artificially increased in order to show more detail. It is evident that the filter successfully removes the opaque center of the spray while preserving the detail at the edge of the spray where the velocity information is contained.

Velocity Evaluation

The velocity information has been obtained from the double-frame images using the commercial software DaVis 10 (LaVision GmbH). Two different schemes have been employed. Standard cross-correlation has been used to evaluate velocity vector fields for individual double-frame images. That is, two frames belonging to the same double-frame image have been evaluated, resulting in an instantaneous velocity vector field. In order to obtain time-averaged velocity vector fields, the Sum-of-Correlation (SoC) scheme has been used for ensemble averaging. Here, the correlation maps obtained from individual double-frame images have been averaged before extracting a single average velocity vector field (Meinhart et al., 2000). This is necessary, since the local availability of velocity information depends on the distribution of liquid in the field of view. In other words, a local deficit of liquid results in a low signal-to-noise ratio. Consequently, the simple averaging of instantaneous velocity vector fields is not a valid means for obtaining time-averaged velocity vector fields.

Table 3.8: Specifications of the cross-correlation and the Sum-of-Correlation schemes employed for the evaluation of velocity information from double-frame images captured using the three optical configurations of the double-frame imaging setup.

Specification	Far-field	Mid-field	Near-field
Images	150	150	200
Initial IA size in px^2	64 × 64	128 × 128	256 × 256
Final passes	6	6	8
Final IA size in px^2	32 × 32	48 × 48	96 × 96
Spatial resolution in px (in mm)	32 (1.59)	48 (0.90)	96 (0.12)
Vector spacing in px (in mm)	8 (0.40)	12 (0.22)	24 (0.03)

For both schemes, a multi-grid, multi-pass approach with decreasing interrogation area size and adaptive interrogation area shape and orientation suitable for the application in velocity gradients has been used (Raffel et al., 2018). The final overlap is 75 %, but the specific settings are depended on the optical configuration of the double-frame imaging setup (see Section 3.3.2). An overview of the specifications is given in Table 3.8, highlighting the differences between the three optical configurations (see Section 3.3.2).

For a meaningful interpretation of the velocity vector fields, it is crucial to understand that the individual velocity vectors are representative of the average in-plane displacement within the respective interrogation area (Raffel et al., 2018). Thus, the introduction of interrogation areas results in a spatial averaging. The effect of out-of-plane motion has been assumed to be small, since velocity information has only been evaluated for the edge of the spray. Furthermore, it is important to note that only liquid resolved by the optical configuration of the double frame-imaging contributes to the velocity vector field. As can be seen in Table 3.7, the far-field configuration, for instance, does not resolve individual small particles.

Vector Post-processing

Subsequently to the velocity evaluation, the velocity vector fields obtained have been post-processed in the form of a validation procedure. In detail, only velocity vectors meeting all four of the following criteria have been considered to be valid. First, the corresponding normalized correlation value has been required to be at least 0.7. Second, the corresponding peak ratio, that is, the ratio of the correlation values of the two largest peaks in the respective correlation map, has been required to be at least 4. Third, the calculated displacement has been required to be at least 1 px. Fourth, only positive displacements in the axial direction (i.e., in the z-direction) have been allowed. Velocity vectors not meeting one or more of these criteria have been discarded as invalid.

Estimation of Measurement Uncertainties

Measurement uncertainties have been estimated using two different approaches, depending on the evaluation scheme employed. For the cross-correlation scheme, which provides instantaneous velocity vector fields for individual double-frame images, the DaVis 10 software allows an estimate of the uncertainty for individual velocity vectors to be calculated using a method based on the correlation statistics described by Wieneke, 2015. As a result, the two standard deviations $s_{u_{\mathrm{l},y}}$ and $s_{u_{\mathrm{l},z}}$ for the two components of the local liquid velocity vector $\mathbf{u}_\mathrm{l}$ have been obtained.

An estimate of the uncertainty for the averaged velocity vector fields calculated by means of the Sum-of-Correlation scheme has been obtained numerically using the bootstrap method, which has been introduced in Section 3.2.4 in the context of phase Doppler measurements. In detail, for individual measurements comprising a number of n_img double-frame images (see Table 3.8), a number of n_boot bootstrap distributions have been created by randomly drawing n_img double-frame images with replacement. Evaluation of these bootstrap distributions using the Sum-of-Correlation scheme has resulted in n_boot velocity vector fields and, consequently, in a distribution for each individual local velocity vector. As a result, the two standard deviations $s_{u_{\mathrm{l},y}}$ and $s_{u_{\mathrm{l},z}}$ have been obtained as estimates of the uncertainty of the two components of the local liquid velocity vector $\mathbf{u}_\mathrm{l}$. However, this approach is computationally expensive. Consequently, the number of bootstrap distributions n_boot has been limited to 200, which in turn limits the convergence of the uncertainty estimate. Furthermore, estimates of the uncertainty cannot be obtained for each individual measurement using this expensive approach, making it necessary to assume that individual estimates are representative of the entire measurements campaign.

In the following, expanded standard uncertainties are reported employing a coverage factor K of 1.96 for liquid velocity data obtained by means of image evaluation, unless explicitly stated otherwise.

Part IV

Results

4 Atomizer Operational Characteristics

The performance of a supersonic close-coupled atomizer is particularly sensitive to the specific geometric design of the atomizer unit, as it determines the gas flow field as well as the interaction between the gas phase and the liquid phase, leading to liquid breakup (see Section 2.1). Consequently, in order to establish comparability with geometric designs, it is necessary to characterize the operational characteristics of the specific atomizer unit described in Section 3.1.2. In addition, this provides a first understanding of the flow phenomena involved in supersonic close-coupled atomization, which is necessary for gaining insight into mechanisms responsible for liquid breakup.

In Section 4.1, the gas-only flow is discussed in terms of the flow field, emphasizing the importance of compressibility effects, as well as in terms of characteristic quantities highlighting the influence of the gas stagnation pressure $p_{\mathrm{t,g}}$ on the flow field. Similarly, in Section 4.2, the liquid-only flow is described with regard to the liquid mass flow rate $\dot{m}_{\mathrm{l}}$. This also includes a description of the liquid jet breakup. Finally, the multiphase flow is treated in Section 4.3, putting the focus on the two-way coupling of the gas and the liquid flow. For this purpose, the liquid mass flow rate $\dot{m}_{\mathrm{l}}$ as well as the process of the spray formation are studied. For all of these considerations, unless explicitly stated otherwise, the baseline case design of the atomizer unit is employed (i.e., $d_{\mathrm{l}} = 4\,\mathrm{mm}$ and $l_{\mathrm{l,tip}} = 3.5\,\mathrm{mm}$, see Section 3.1.2). Furthermore, water is the only working liquid considered in this chapter.

The numerical data discussed in this chapter has been provided by the research partner SMS as part of the IGSTC project PPAM.

Parts of this chapter have already been covered in the thesis of Apell, 2019 and presented in Odenthal et al. (2021).

4.1 Gas-only Flow

As a two-fluid atomization process, the high-velocity gas flow is an important aspect of the supersonic close-coupled atomization of liquids, since it provides the kinetic energy that is transferred during the gas-liquid interaction, leading to liquid breakup (Lasheras & Hopfinger, 2000). Thus, an understanding of the gas flow field is crucial for gaining insights into the mechanisms responsible for the atomization. This is especially important, since, for supersonic close-coupled atomization, the gas flow is characterized by compressibility effects, which are often neglected in traditional atomization processes.

4.1.1 Mass Flow Rate

While the gas supply line of the research facility described Section 3.1.3 allows for measuring the gas mass flow rate $\dot{m}_\mathrm{g}$ during the experimental investigations, it can also be determined analytically as an explicit function of the gas stagnation properties. This allows for predicting the gas mass flow rate $\dot{m}_\mathrm{g}$ for a given gas, geometric design of the gas nozzle and set point of operation. For this purpose, the gas mass flow rate $\dot{m}_\mathrm{g}$ has been expressed in terms of quantities evaluated at the throat of the convergent-divergent gas nozzle, denoted by the superscript $*$. Here, the local Mach number Ma^* is unity due to the gas nozzle being operated in choked condition for the entire range of gas stagnation pressures $p_\mathrm{t,g}$ considered as part of this experimental investigation (see Section 3.1.4). Assuming the flow to be steady, quasi-one-dimensional and isotropic and the gas to be calorically perfect, these quantities have been related to the gas stagnation properties (Anderson, 1990):

$$\dot{m}_\mathrm{g} = \rho_\mathrm{g}^* a_\mathrm{g}^* A_\mathrm{g}^* = \frac{p_\mathrm{t,g}}{RT_\mathrm{t,g}} \left(\frac{2}{\kappa+1}\right)^{\frac{1}{\kappa-1}} \left(\kappa R T_\mathrm{t,g}\right)^{\frac{1}{2}} \left(\frac{2}{\kappa+1}\right)^{\frac{1}{2}} A_\mathrm{g}^*. \tag{4.1}$$

Here, A_g^* is the cross-sectional area at the gas nozzle throat. From Eq. (4.1) it follows that, for a constant gas stagnation temperature $T_\mathrm{t,g}$, the gas mass flow rate $\dot{m}_\mathrm{g}$ is a linear function of the gas stagnation pressure $p_\mathrm{t,g}$. Furthermore, it is important to note that the gas mass flow rate $\dot{m}_\mathrm{g}$ is independent of the flow conditions downstream of the gas nozzle due to the supersonic nature of the flow. In other words, the analytical expression in Eq. (4.1) is not only valid during the gas-only flow but also during the multiphase flow.

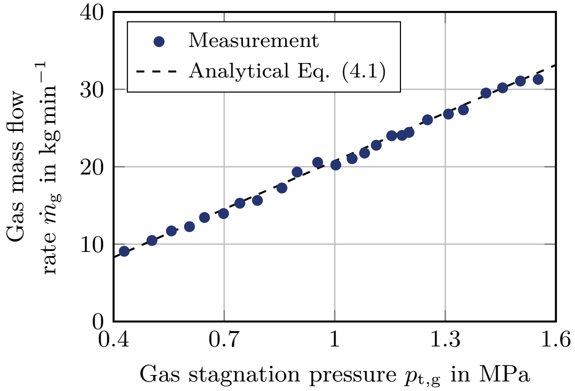

Figure 4.1: Comparison between the measured gas mass flow rate $\dot{m}_{\mathrm{g}}$ and the analytical solution in Eq. (4.1) as a function of the gas stagnation pressure $p_{\mathrm{t,g}}$. The corresponding expanded standard uncertainty, employing a coverage factor K of 1.96, is smaller than the size of the markers.

In Fig. 4.1, the measured gas mass flow rate $\dot{m}_{\mathrm{g}}$ is shown as a function of the gas stagnation pressure $p_{\mathrm{t,g}}$. Here, as well as in the following, the data obtained from the sensors integrated into the research facility (see Section 3.1) is reported in terms of an arithmetic mean value and the corresponding expanded combined standard uncertainty, employing a coverage factor K of 1.96 and taking into account the experimental standard deviation of the mean value[1] as well as the uncertainty associated with the respective sensor. Additionally depicted is Eq. (4.1) evaluated at the same set points of operation. As can be seen, the measured data shows a linear behavior, as predicted by Eq. (4.1). That is, the gas mass flow rate $\dot{m}_{\mathrm{g}}$ increases with increasing gas stagnation pressure $p_{\mathrm{t,g}}$. Furthermore, the analytical expression in Eq. (4.1) is in good agreement with the measurement data, confirming its predictive capabilities. In fact, the mean absolute relative error of the gas mass flow rate $\dot{m}_{\mathrm{g}}$ is 1.8 %. Consequently, since the gas stagnation temperature $T_{\mathrm{t,g}}$ varies only slightly between the individual measurements, the gas stagnation pressure $p_{\mathrm{t,g}}$ as well as the gas mass flow rate $\dot{m}_{\mathrm{g}}$ can be used interchangeably for characterizing the set point of operation of the atomizer. This fact has

---

[1] Defined according to the International Bureau of Weights and Measures (2008) as $s/\sqrt{n_{\mathrm{data}}}$, where n_{data} is the number of independent repeated observations.

motivated the introduction of the gas-to-liquid ratio GLR in Eq. (2.6) as a single quantity describing the set point of operation.

4.1.2 Flow Field

The actual gas flow field downstream of the liquid nozzle of a supersonic close-coupled atomizer has been extensively described in the literature, both experimentally and numerically. This is partly due to the fact that the geometric design of the atomizer unit is similar to the design of the truncated plug nozzles used in aerospace propulsion for altitude compensation, which have been studied in great detail. Here, notable examples include the work of Mueller et al. (1972), Sule and Mueller (1973), Hagemann et al. (1998), Nasuti and Onofri (2001) and Chutkey et al. (2014). In the context of supersonic close-coupled atomization, the gas flow field has been studied and discussed by, among others, Mi et al. (1997), Espina and Piomelli (1998), Ting and Anderson (2004), Mates and Settles (2005a), Motaman et al. (2015) and Urionabarrenetxea et al. (2022). The particular gas flow field of the atomizer unit described in Section 3.1.2 has been investigated experimentally by Luh et al. (2018) using focusing Schlieren imaging. Additionally, it has been studied numerically by Vogl et al. (2019), showing good agreement with the experimental results. Consequently, here, only the most important characteristic features of the gas flow field are briefly discussed, which are necessary for developing an understanding of the atomization process.

As has been established in Section 3.1.4, the convergent-divergent gas nozzle of the research facility has exclusively been operated in underexpanded condition (i.e., at $PR > 1$) as part of this experimental investigation. In this condition, the gas flow field downstream of the nozzle is characterized by an alternating pattern of expansion and compression waves. This can be seen, for instance, in Fig. 4.2, which shows focusing Schlieren images of the flow field. These images have been captured by Luh et al. (2018) using a horizontal grid, thus, visualizing vertical gradients in the local gas density $\partial\rho_\mathrm{g}/\partial z$ (Settles, 2001). In detail, images are shown for four different gas stagnation pressures $p_\mathrm{t,g}$ (i.e., for $0.3\,\mathrm{MPa}$, $0.7\,\mathrm{MPa}$, $1.1\,\mathrm{MPa}$ and $1.5\,\mathrm{MPa}$), which also correspond to four different pressure ratios PR (i.e., to 1.16, 2.71, 4.26 and 5.81, respectively), that is, different degrees of underexpansion of the gas flow. In general, the images are in good agreement with the experimental results

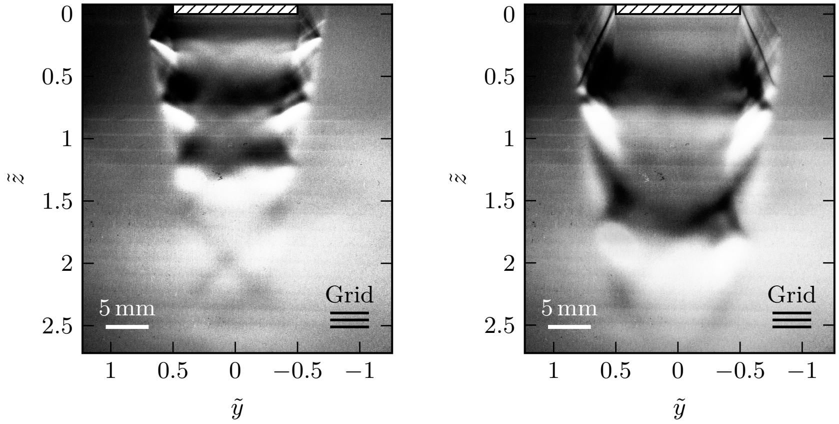

(a) $p_{\mathrm{t,g}} = 0.3\,\mathrm{MPa}$ ($PR = 1.16$)

(b) $p_{\mathrm{t,g}} = 0.7\,\mathrm{MPa}$ ($PR = 2.71$)

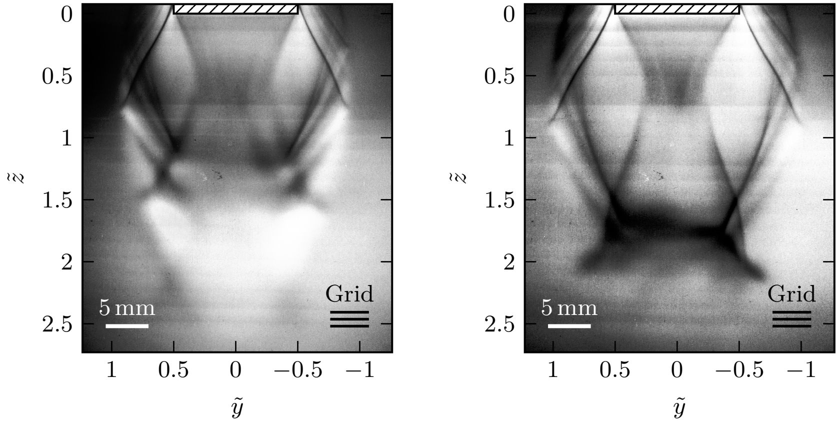

(c) $p_{\mathrm{t,g}} = 1.1\,\mathrm{MPa}$ ($PR = 4.26$)

(d) $p_{\mathrm{t,g}} = 1.5\,\mathrm{MPa}$ ($PR = 5.81$)

Figure 4.2: Focusing Schlieren images of the gas-only flow field downstream of the liquid nozzle for four different gas stagnation pressures $p_{\mathrm{t,g}}$ captured using a horizontal grid. (Focusing Schlieren images adapted from Luh et al., 2018.)

presented by Mates and Settles (2005a). As can be seen, with increasing gas stagnation pressure $p_{\mathrm{t,g}}$, the alternating pattern of expansion and compression waves is stretched in the axial direction (i.e., in the z-direction), extending further downstream. Simultaneously, the expansion of the gas flow leads to the characteristic necking of the wake downstream of the liquid nozzle, resulting in a three-dimensional hourglass-like shape (Ting & Anderson, 2004). Another important feature of the gas flow field is evident in Fig. 4.2d as a particularly dark area below the liquid nozzle at a non-dimensional axial distance $\tilde{z}$ of about 1.75, indicating a strong local change in gas density ρ_{g}. In fact, this is a Mach disk, that is, a strong normal shock, closing off the wake. Consequently, for this gas stagnation pressure $p_{\mathrm{t,g}} = 1.5\,\mathrm{MPa}$, the supersonic close-coupled atomizer is operated in *closed wake* condition, as opposed to the *open wake* condition at lower gas stagnation pressures $p_{\mathrm{t,g}}$ (Ting et al., 2002).

Results for the local Mach number Ma downstream of the liquid nozzle obtained by means of numerical simulation allow for gaining additional insights into the gas flow field. In Fig. 4.3, numerical data provided by the research partner SMS as part of the IGSTC project PPAM is shown. Analogous to Fig. 4.2, four different gas stagnation pressures $p_{\mathrm{t,g}}$ (i.e., $0.32\,\mathrm{MPa}$, $0.74\,\mathrm{MPa}$, $1.16\,\mathrm{MPa}$ and $1.58\,\mathrm{MPa}$) are considered. In fact, the set points of operation are reasonably close to those used for the focusing Schlieren images presented in Fig. 4.2. While the exit Mach number Ma_{e} of about 1.2 is constant and determined solely by the geometric design of the convergent-divergent gas nozzle described in Section 3.1.2, the expansion of the gas flow results in higher local Mach numbers Ma further downstream of the nozzle, reaching up to $Ma = 4$ for the highest gas stagnation pressure $p_{\mathrm{t,g}}$. In fact, the annular supersonic gas jet extends far downstream of the liquid nozzle, enclosing the wake and merging into a circular jet further downstream. For the highest gas stagnation pressure $p_{\mathrm{t,g}}$ considered here (i.e., for $p_{\mathrm{t,g}} = 1.58\,\mathrm{MPa}$), shown in Fig. 4.3d, the Mach disk already discussed in the context of the focusing Schlieren image in Fig. 4.2d is visible at a non-dimensional axial distance $\tilde{z}$ of about 1.75, suggesting closed wake condition. Additionally indicated in Fig. 4.3 are the local flow direction as well as the stagnation points in the flow field. Within the gas jet, the flow is mainly directed in the axial direction (i.e., the z-direction), but the expansion and compression waves can be clearly seen to also influence the flow direction. However, inside of the wake downstream of the liquid nozzle, the flow field is characterized by a three-dimensional

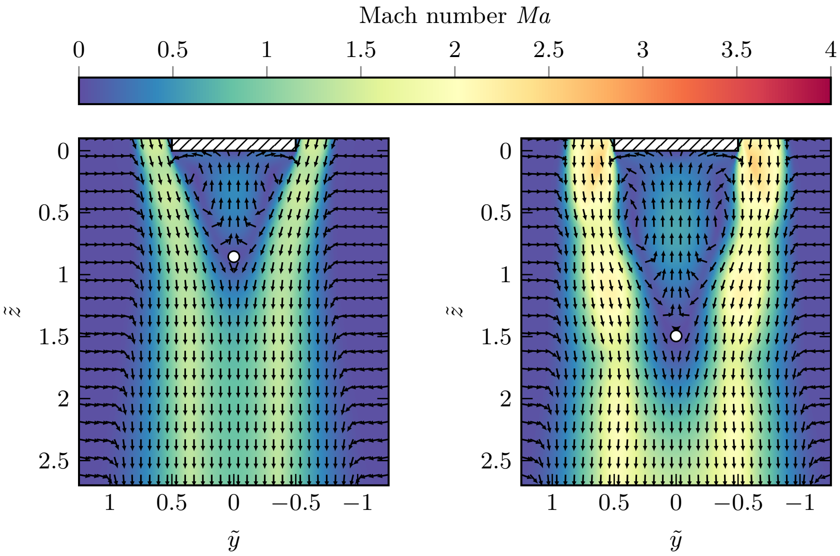

(a) $p_{\mathrm{t,g}} = 0.32\,\mathrm{MPa}$ ($PR = 1.24$)

(b) $p_{\mathrm{t,g}} = 0.74\,\mathrm{MPa}$ ($PR = 2.87$)

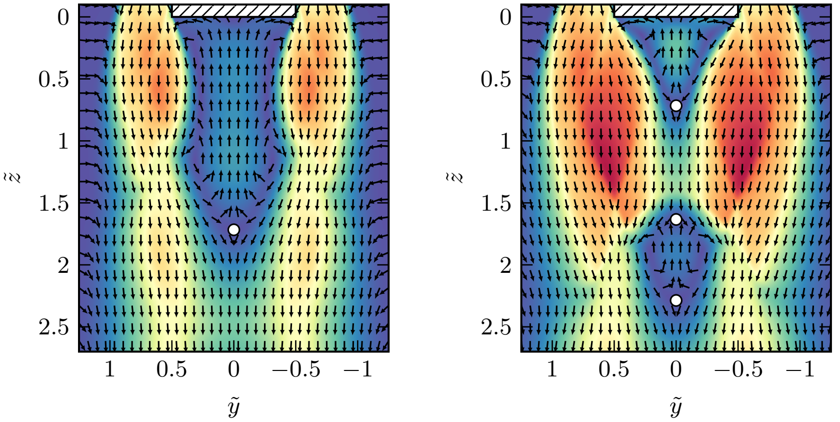

(c) $p_{\mathrm{t,g}} = 1.16\,\mathrm{MPa}$ ($PR = 4.50$)

(d) $p_{\mathrm{t,g}} = 1.58\,\mathrm{MPa}$ ($PR = 6.12$)

Figure 4.3: Axisymmetric steady-state simulation results for the local Mach number Ma in the gas-only flow field downstream of the liquid nozzle for four different gas stagnation pressures $p_{\mathrm{t,g}}$. Additionally indicated are the local flow direction and the stagnation points ○. The numerical data has been provided by the research partner SMS as part of the IGSTC project PPAM.

recirculation zone (Ünal, 1989a). Starting from a stagnation point at the lower end of the wake, the gas flows upstream toward the liquid nozzle. Below the tip of the liquid nozzle, the flow is directed radially outwards and the gas is entrained in the high-velocity gas jet. In the closed wake condition, shown in Fig. 4.3d, a second recirculation zone featuring two more stagnation points can be seen downstream of the Mach disk, as has also been noted by Ting et al. (2002) and Motaman et al. (2015). Considering the multiphase flow, the recirculation zone in the wake right downstream of the liquid nozzle is an important feature of the flow field of a supersonic close-coupled atomizer, since it determines the first interaction between the gas flow and the liquid flow and, therefore, directly affects the primary atomization (Miller et al., 1996). This is discussed in more detail in Section 6.1. Finally, from Fig. 4.3 it is also evident that ambient gas is entrained by the high-velocity gas jet, forming a mixing layer.

Another consequence of the expansion of the gas flow after exiting the gas nozzle is a rapid decrease in the local gas temperature T_g. In Fig. 4.4, simulation results for the local gas temperature T_g downstream of the liquid nozzle are shown for two of the stagnation pressures $p_\mathrm{t,g}$ already presented as part of Fig. 4.3 (i.e., for $p_\mathrm{t,g} = 0.32\,\mathrm{MPa}$ and $p_\mathrm{t,g} = 1.58\,\mathrm{MPa}$). It is evident that the gas in the jet exiting the gas nozzle and undergoing expansion is colder than the surrounding ambient gas and the gas in the wake downstream of the liquid nozzle. In fact, for high pressure ratios PR, this effect is even more pronounced due to the stronger expansion. Consequently, this is an indicator that, in the multiphase flow, both the liquid nozzle and the liquid itself are subject to a large drop in temperature. In the context of metal powder production, this is an important consideration, since the low gas temperature T_g can cause the molten metal to freeze, resulting in clogging of the liquid nozzle and, hence, in the termination of the atomization process. This can be avoided by, for instance, applying a sufficient superheat ΔT_l to the molten metal (Henein et al., 2017). However, a low liquid mass flow rate $\dot{m}_\mathrm{l}$ increases the risk of freezing. Consequently, it is necessary to select the liquid nozzle diameter d_l, the liquid overpressure Δp_l as well as the liquid superheat ΔT_l accordingly in order to ensure a stable atomization process (Ünal, 1987).

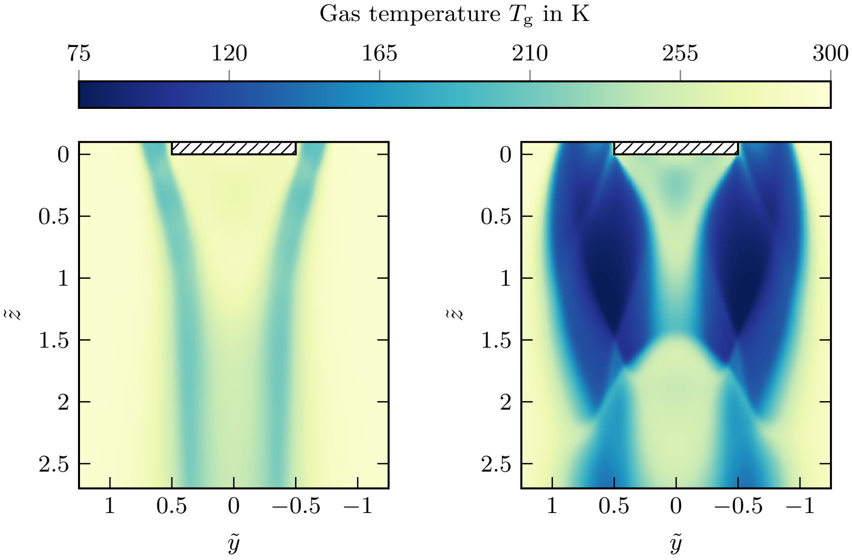

(a) $p_{t,g} = 0.32\,\mathrm{MPa}$ ($PR = 1.24$) **(b)** $p_{t,g} = 1.58\,\mathrm{MPa}$ ($PR = 6.12$)

Figure 4.4: Axisymmetric steady-state simulation results for the local gas temperature T_g in the gas-only flow field downstream of the liquid nozzle for two different gas stagnation pressures $p_{t,g}$. The numerical data has been provided by the research partner SMS as part of the IGSTC project PPAM.

4.1.3 Aspiration Pressure

An important quantity characteristic of the specific geometric design of an atomizer unit is the aspiration pressure p_{asp}, which is the pressure in the center of the base of the liquid nozzle tip during the gas-only flow. This is indicated in the schematic illustration in Fig. 4.5.

Depending on the gas stagnation pressure $p_{t,g}$, the aspiration pressure p_{asp} can vary over a wide range, resulting in an overpressure or an underpressure relative to the ambient pressure p_a. For a stable atomization process, an underpressure is favorable in order to promote the liquid flow. An overpressure, on the other hand, can lead to a *blow-back* condition, which is characterized by gas flowing upstream through the liquid supply (Wolf & Bergmann, 2002). This is a critical condition, especially for the case of the atomization of molten

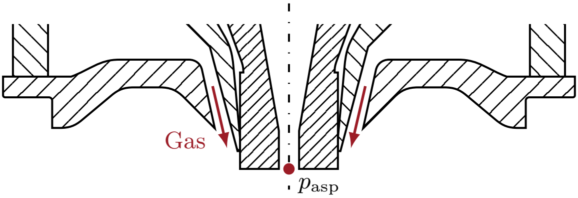

Figure 4.5: Schematic illustration indicating the measurement position (●) of the aspiration pressure p_asp in the center of the base of the liquid nozzle tip.

metal, since the gas-liquid interaction can lead to the molten metal freezing inside of the liquid nozzle, thus terminating the atomization process (Espina & Piomelli, 1998). Consequently, knowledge of the aspiration pressure p_asp in dependence of the set point of operation of the specific atomizer unit is crucial for the process stability. However, it is important to note that the aspiration pressure p_asp is a quantity characteristic of the gas-only flow, as it cannot be determined for the multiphase flow.

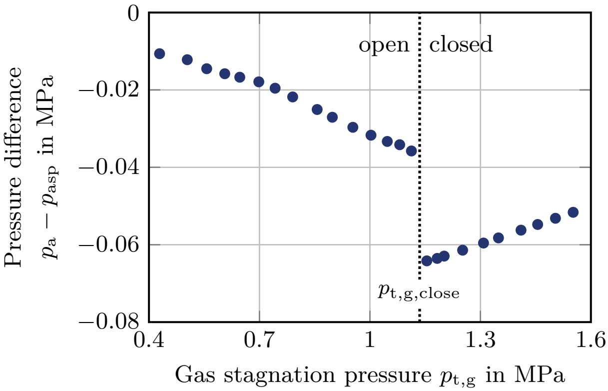

Figure 4.6: Difference between the ambient pressure p_a and the aspiration pressure p_asp as a function of the gas stagnation pressure $p_\mathrm{t,g}$. The corresponding expanded standard uncertainty, employing a coverage factor K of 1.96, is smaller than the size of the markers. Additionally indicated as a reference is the wake closure pressure $p_\mathrm{t,g,close}$, separating open and closed wake condition.

For the baseline case design of the atomizer unit described in Section 3.1.2, the difference between the ambient pressure p_a and the aspiration pressure p_asp is shown as a function of the gas stagnation pressure $p_\mathrm{t,g}$ in Fig. 4.6. Here, the aspiration pressure p_asp has been measured by inserting a tube connected to a pressure sensor from the top through the liquid nozzle. For this purpose, the tube has been positioned in the center of the liquid nozzle with a tight seal and aligned flush with the base of the liquid nozzle tip. As can be seen, the aspiration pressure p_asp results in an underpressure in the entire range of gas stagnation pressures $p_\mathrm{t,g}$ considered as part of this experimental investigation (see Section 3.1.4). The magnitude of the underpressure, however, is dependent on the specific gas stagnation pressure $p_\mathrm{t,g}$. In detail, the dependence is non-monotonic with a distinct minimum apparent at a gas stagnation pressure $p_\mathrm{t,g}$ of about 1.15 MPa (see Fig. 4.5). This is the maximum aspiration condition, which is characterized by the strongest underpressure in the parameter range (Espina & Piomelli, 1998). Furthermore, starting at a gas stagnation pressure $p_\mathrm{t,g}$ of about 1.13 MPa, there is a strong decrease in aspiration pressure p_asp (see Fig. 4.5). The particular gas stagnation pressure $p_\mathrm{t,g}$ associated with this decrease is the wake closure pressure $p_\mathrm{t,g,close}$, as it defines the minimum gas stagnation pressure $p_\mathrm{t,g}$ necessary for the formation of a Mach disk downstream of the liquid nozzle (Mates & Settles, 2005a). In other words, for gas stagnation pressures $p_\mathrm{t,g}$ higher than this value, the wake is closed. This is also evident from the focusing Schlieren images shown in Fig. 4.2 and discussed in Section 4.1.2. As an additional characteristic, in the closed wake condition, the ratio of the aspiration pressure p_asp and the gas stagnation pressure $p_\mathrm{t,g}$ is constant, as can be seen from the constant slope in Fig. 4.6.

In general, the aspiration curve shown in Fig. 4.6 is in good qualitative agreement with the experimental results presented by Ridder et al. (1992), Espina and Piomelli (1998) and Wolf and Bergmann (2002). The former have interpreted the aspiration pressure p_asp to be a result of the expansion of the annular gas jet surrounding the liquid nozzle, which leads to alternating patterns of expansion and compression waves downstream of the liquid nozzle (see Fig. 4.2). Depending on the position of the base of the liquid nozzle tip relative to these aerodynamic flow features, it is exposed to a different pressure inside of the gas jet.

The aspiration pressure p_asp is not only a function of the gas stagnation pressure $p_\mathrm{t,g}$, but it also depends on the specific geometric design of the liquid nozzle tip. For instance, in Fig. 4.7, additional measurement results are

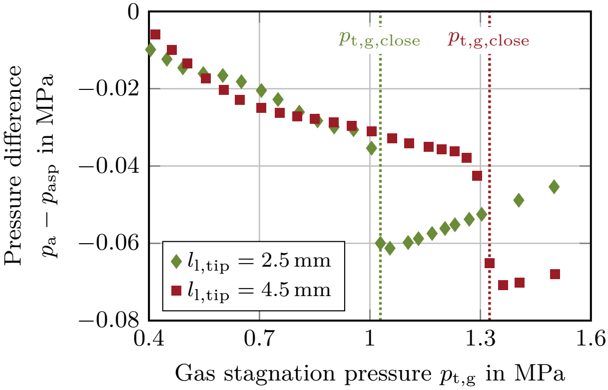

Figure 4.7: Difference between the ambient pressure p_a and the aspiration pressure p_asp as a function of the gas stagnation pressure $p_\mathrm{t,g}$ for two different liquid nozzle tip protrusion lengths $l_\mathrm{l,tip}$. The corresponding expanded standard uncertainty, employing a coverage factor K of 1.96, is smaller than the size of the markers. Additionally indicated as a reference are the respective wake closure pressures $p_\mathrm{t,g,close}$, separating open and closed wake condition.

shown for the difference between the ambient pressure p_a and the aspiration pressure p_asp. In contrast to Fig. 4.6, however, here, the liquid nozzle tip protrusion length $l_\mathrm{l,tip}$ has been varied compared to the baseline case design (i.e., compared to $l_\mathrm{l,tip} = 3.5\,\mathrm{mm}$). In detail, two different liquid nozzle tip protrusion lengths $l_\mathrm{l,tip}$ have been used, which are $l_\mathrm{l,tip} = 2.5\,\mathrm{mm}$ and $l_\mathrm{l,tip} = 4.5\,\mathrm{mm}$ (see Section 3.1.2). As can be seen, while the aspiration curves are qualitatively similar, there are distinct quantitative differences. For instance, increasing the liquid nozzle tip protrusion length $l_\mathrm{l,tip}$ results in a shift of the wake closure pressure $p_\mathrm{t,g,close}$ to a higher value (see Fig. 4.7). In fact, the wake closure pressures $p_\mathrm{t,g,close}$ corresponding to the shorter and the longer liquid nozzle tip are about 1.03 MPa and 1.32 MPa, respectively. Similarly, the maximum aspiration condition is also shifted and the corresponding underpressure appears to increase with increasing liquid nozzle tip protrusion length $l_\mathrm{l,tip}$. Consequently, small changes to the geometric design of the liquid nozzle provide means for systematically influencing the aspiration curve. While these findings are in good qualitative agreement with the results of Wolf and Bergmann (2002) and Ting et al. (2002), it is still important to note that they are not universal, but can only be applied to the specific geometric design of the atomizer unit under consideration. For instance, Baram et al. (1988) have conducted an extensive experimental study using two different gas nozzle designs and several different liquid nozzle tip shapes and protrusion lengths $l_{\mathrm{l,tip}}$, showing a wide variation in aspiration curves and in sensitivity to parameter changes. Similarly, Anderson and Figliola (1988) and Anderson et al. (1991) have shown that the aspiration pressure p_{asp} differs depending on the taper of the specific liquid nozzle tip as well as its protrusion length $l_{\mathrm{l,tip}}$.

Whether or not the aspiration pressure p_{asp} has any significance for the atomizer performance has been the subject of much discussion in the literature. Anderson and Figliola (1988) and Anderson et al. (1991) have provided experimental evidence that the maximum aspiration condition is correlated with an improved refinement of the resulting particle size. Similarly, Biancaniello et al. (1989) have observed the highest yield of fine particles at maximum aspiration condition. While Ridder and Biancaniello (1988) have reported a reduced dispersion of the particle size at maximum aspiration condition, they have also observed an increase in the particle size when increasing the liquid mass flow rate $\dot{m}_{\mathrm{l}}$ at an identical gas stagnation pressure $p_{\mathrm{t,g}}$. In contrast, Miller et al. (1996) have questioned the justification for deriving statements about the multiphase flow from the aspiration pressure p_{asp}, a quantity characteristic of the gas-only flow. Indeed, Ünal (2006) has not been able to experimentally confirm a correlation between maximum aspiration condition and particle size refinement. Consequently, in order to contribute to this discussion, the significance of the aspiration pressure p_{asp} for the atomizer performance is further investigated as part of Section 4.3 as well as Chapter 5, taking advantage of the accessibility for a variety of measurement techniques provided by the research facility described in Section 3.1.

4.2 Liquid-only Flow

While the supersonic gas flow certainly is responsible for many of the characteristic features of the close-coupled atomization process under investigation, it is still beneficial to briefly describe the liquid-only[2] flow. In fact, this allows

---

[2] Here, the term *liquid-only* refers to the flow of a liquid into quiescent ambient air.

to identify the influence of the gas flow when investigating the multiphase flow in Section 4.3.

4.2.1 Mass Flow Rate

Similarly to the gas mass flow rate $\dot{m}_\mathrm{g}$ discussed in Section 4.1.1, the liquid supply line of the research facility described in Section 3.1.3 allows for monitoring the liquid mass flow rate $\dot{m}_\mathrm{l}$. However, in order to identify the influence of the aspiration pressure p_asp introduced in Section 4.1.3 on the liquid mass flow rate $\dot{m}_\mathrm{l}$, it is necessary to derive an analytical description. For this purpose, the Bernoulli equation has been employed, initially assuming quasi-one-dimensional, steady, inviscid and incompressible flow as well as conservative body forces (Spurk & Aksel, 2020). In order to still take losses into account, an a priori unknown discharge coefficient C_d has been introduced, which combines the losses associated with the entire liquid supply line. The resulting expression is:

$$\dot{m}_\mathrm{l} = C_\mathrm{d} \frac{\pi d_\mathrm{l}^2}{4} \left[2\rho_\mathrm{l} \left(\Delta p_\mathrm{l} + \rho_\mathrm{l} g \Delta h_\mathrm{l} \right) \right]^{\frac{1}{2}} . \tag{4.2}$$

Here, g is the gravitational acceleration, which acts along the axial direction as defined in Fig. 3.7 (i.e., along the z-direction), and Δh_l is the difference in height between the liquid surface and the liquid nozzle exit. For the research facility described in Section 3.1.2, the latter is negative, since the pressure vessel is located below the atomizer unit. It is important to note that, in Eq. (4.2), the discharge coefficient C_d has been assumed to be constant. This is reasonable, since the range of liquid Reynolds numbers Re_l covered in this experimental investigation (see Table 3.2) indicates turbulent flow (Lefebvre & McDonell, 2017).

In order to validate the model proposed in Eq. (4.2), the liquid mass flow rate $\dot{m}_\mathrm{l}$ has been measured for a wide range of applied liquid overpressures Δp_l. The results are shown in Fig. 4.8. In addition, Eq. (4.2) has been fitted to the measurement data employing a non-linear least squares approach. As a result, the determined discharge coefficient C_d has been found to be 0.52. As can be seen, the expression in Eq. (4.2) works well for describing the dependence of the liquid mass flow rate $\dot{m}_\mathrm{l}$ on the liquid overpressure Δp_l. In fact, the mean absolute relative error of the liquid mass flow rate $\dot{m}_\mathrm{l}$ is 2.7 %.

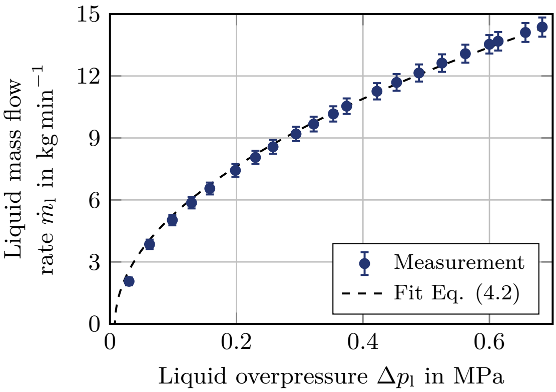

Figure 4.8: Comparison between the measured liquid mass flow rate $\dot{m}_g$ and the analytical solution in Eq. (4.2) as a function of the liquid overpressure Δp_l. The error bars correspond to the expanded standard uncertainty, employing a coverage factor K of 1.96. For some data points, the expanded standard uncertainty is smaller than the size of the corresponding marker.

Consequently, Eq. (4.2) provides adequate means for predicting the liquid mass flow rate $\dot{m}_l$.

4.2.2 Jet Breakup

In the absence of a gas flow, the liquid-only flow is characterized by the disintegration of a liquid jet emanating from a single nozzle into quiescent ambient air. Although seemingly simple, this topic has been treated in great detail in the literature (Birouk & Lekic, 2009). This is due to the fact that the properties of the resulting spray have been found to depend on a large number of interacting parameters (Lin & Reitz, 1998). Depending on the dominant forces acting on the liquid jet responsible for its disintegration, four different breakup regimes are commonly defined, taking into account different combinations of liquid inertia, surface tension σ and aerodynamic forces (Reitz, 1978). This classification is based on the gas Weber number We_g, as defined in Eq. (2.4), considering that the absolute gas velocity u_g is $0\,\mathrm{m\,s^{-1}}$, and the Ohnesorge number Oh, as defined in Eq. (2.5). Here, the dimensionless numbers are considered as global quantities based on the liquid nozzle diameter d_l as the characteristic length scale l (see Sections 2.2.1 and 3.1.1). In detail, the four regimes are as follows:

- Rayleigh breakup regime ($We_\mathrm{g} < 1.2 + 3.41\, Oh^{0.9}$)
- First wind-induced regime ($1.2 + 3.41\, Oh^{0.9} < We_\mathrm{g} < 13$)
- Second wind-induced regime ($13 < We_\mathrm{g} < 40.3$)
- Atomization regime ($40.3 < We_\mathrm{g}$)

It is important to note, however, that this classification does not take into account any flow effects (Lin & Reitz, 1998). Indeed, it is well documented in the literature that, for instance, turbulence, flow separation, cavitation and the velocity profile have a significant influence on the disintegration of the liquid jet (Birouk & Lekic, 2009; Lefebvre & McDonell, 2017).

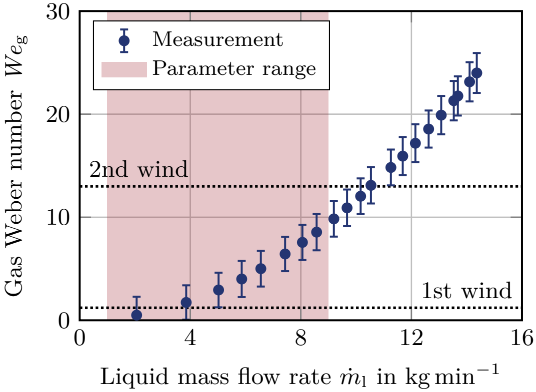

Figure 4.9: Gas Weber number We_g as a function of the liquid mass flow rate $\dot{m}_\mathrm{l}$. The error bars correspond to the expanded standard uncertainty, employing a coverage factor K of 1.96. Additionally indicated as a reference are the range of the liquid mass flow rate $\dot{m}_\mathrm{l}$ as defined in Section 3.1.4 for this experimental investigation as well as the boundaries of the two relevant breakup regimes.

For the same set points of operation already presented in Fig. 4.8, the gas Weber number We_g is shown as a function of the liquid mass flow rate $\dot{m}_\mathrm{l}$ in Fig. 4.9. Additionally indicated are the boundaries of the two relevant breakup regimes as well as the range of the liquid mass flow rate $\dot{m}_\mathrm{l}$ defined for this experimental investigation in Section 3.1.4. As can be seen, for liquid mass flow rates $\dot{m}_\mathrm{l}$ smaller than $3\,\mathrm{kg\,min^{-1}}$, the relevant breakup regime is the Rayleigh regime, whereas, for liquid mass flow rates $\dot{m}_\mathrm{l}$ higher than $3\,\mathrm{kg\,min^{-1}}$, the liquid-only flow is located in the first wind-induced regime. While the former is characterized by the growth of axisymmetric, long-wavelength, small-amplitude disturbances on the jet surface induced by surface tension effects, in the latter these disturbances are additionally amplified by aerodynamic forces (Reitz, 1978; Lin & Reitz, 1998). In both cases, however, the size of the resulting droplets is in the order of the liquid nozzle diameter d_l and breakup occurs far downstream of the liquid nozzle, that is, the jet breakup length is relatively long (Reitz & Bracco, 1986).

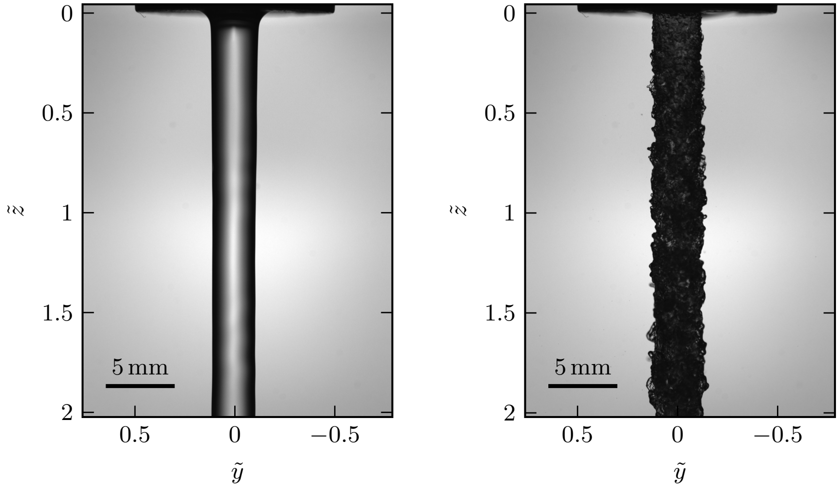

(a) $\dot{m}_\mathrm{l} = (0.99 \pm 0.01)\,\mathrm{kg\,min^{-1}}$ ($Re_\mathrm{l} \approx 0.6 \times 10^4$)

(b) $\dot{m}_\mathrm{l} = (8.01 \pm 0.02)\,\mathrm{kg\,min^{-1}}$ ($Re_\mathrm{l} \approx 4.7 \times 10^4$)

Figure 4.10: Ultra-short diffuse background illumination images of the liquid jet at two different liquid mass flow rates $\dot{m}_\mathrm{l}$ captured using the mid-field configuration described in Section 3.3.2.

In Fig. 4.10, images of the liquid jet are shown for two different liquid mass flow rates $\dot{m}_\mathrm{l}$ (i.e., for $(0.99 \pm 0.01)\,\mathrm{kg\,min^{-1}}$ and $(8.01 \pm 0.02)\,\mathrm{kg\,min^{-1}}$), corresponding to the Rayleigh regime and the first wind-induced regime, respectively. The images have been captured using the mid-field configuration of the ultra-short diffuse background illumination imaging setup described in Section 3.3.2 and are in good agreement with the results presented by Biancaniello et al. (1989). As can be seen, for both images, the field of view is not large enough to resolve the breakup length of the jet. The same is true for images captured using the far-field configuration, which are not shown here. This indicates that jet breakup occurs far downstream of the liquid nozzle. In fact, for the lower liquid mass flow rate $\dot{m}_\mathrm{l}$, the surface of the liquid jet remains essentially undisturbed within the available field of view (see Fig. 4.10a). Interestingly, for the higher liquid mass flow rate $\dot{m}_\mathrm{l}$, the initial disturbance of the liquid surface is neither axisymmetric nor characterized by a long wavelength λ, as would be characteristic of the first wind-induced regime (see Fig. 4.10b). Instead, irregular disturbances of smaller length scales are visible on the surface of the liquid jet. Although this does not allow for predictions about the spatial evolution of the liquid surface further downstream, it is a first indication that, in this case, the turbulence of the nozzle flow dominates the initial development of the disturbances. This is reasonable, since the liquid Reynolds number Re_l is in the order of 10^4.

In the context of the two-fluid supersonic close-coupled atomization process, these considerations are important, as they suggest that the liquid jet is unlikely to undergo significant breakup before first interacting with the gas flow. In other words, the gas-liquid interaction is dominating the primary atomization. This is further discussed in Section 6.1.

4.3 Multiphase Flow

Following the separate description of the gas-only flow and the liquid-only flow, it is instructive to additionally investigate the multiphase flow. This serves the purpose of identifying how the gas flow and the liquid flow affect each other and whether or not this coupling has to be taken into account when modeling the atomization process.

4.3.1 Liquid Mass Flow Rate

As has been successfully demonstrated in Section 4.2.1, for the liquid-only flow, the liquid mass flow rate $\dot{m}_\mathrm{l}$ can be predicted in dependence of the liquid overpressure Δp_l by employing the Bernoulli equation and introducing an additional discharge coefficient C_d (see Eq. (4.2)). Furthermore, in Section 4.1.3, the gas-only flow has been shown to result in a sub-ambient aspiration pressure p_asp at the exit of the liquid nozzle, which is a function of the gas stagnation pressure $p_\mathrm{t,g}$ (see Fig. 4.6). Consequently, if the liquid flow does not affect the gas flow, it should be possible to predict the liquid mass flow rate $\dot{m}_\mathrm{l}$ for a given gas stagnation pressure $p_\mathrm{t,g}$ by using Eq. (4.2) and taking into account the additional suction caused by the aspiration pressure p_asp.

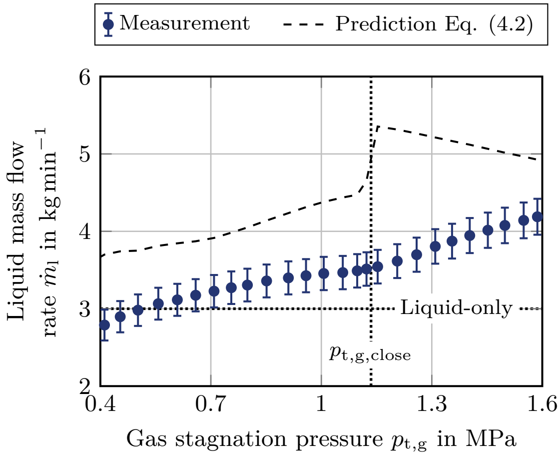

Figure 4.11: Comparison between the measured liquid mass flow rate $\dot{m}_\mathrm{l}$ as a function of the gas stagnation pressure $p_\mathrm{t,g}$ and the prediction made by employing Eq. (4.2) and taking into account the aspiration pressure p_asp presented in Fig. 4.6. The error bars correspond to the expanded standard uncertainty, employing a coverage factor K of 1.96. Additionally indicated as a reference are the liquid mass flow rate $\dot{m}_\mathrm{l}$ for the liquid-only flow corresponding to the same constant liquid overpressure Δp_l as well as the wake closure pressure $p_\mathrm{t,g,close}$ obtained for the gas-only flow.

In Fig. 4.13, the liquid mass flow rate $\dot{m}_\mathrm{l}$ measured as a function of the gas stagnation pressure $p_\mathrm{t,g}$ is compared to the prediction made by employing Eq. (4.2). Here, the liquid overpressure Δp_l has been set to result in a liquid mass flow rate $\dot{m}_\mathrm{l}$ of $3\,\mathrm{kg\,min^{-1}}$ for the liquid-only flow and has been kept constant for all set points of operation (i.e., at $\Delta p_\mathrm{l} = (0.042 \pm 0.003)\,\mathrm{MPa}$). However, the following observations have been found to be true for other liquid overpressures Δp_l as well. Furthermore, the liquid supply line has been operated with a completely opened control valve, allowing the gas flow to freely influence the liquid flow (see Section 3.1.3) and emulating the operational characteristic of an industrial supersonic close-coupled atomizer. As can be seen, the gas flow leads to an increased liquid mass flow rate $\dot{m}_\mathrm{l}$ compared to the case of the liquid-only flow (i.e., compared to $\dot{m}_\mathrm{l} = 3\,\mathrm{kg\,min^{-1}}$) for a wide range of gas stagnation pressures $p_\mathrm{t,g}$. However, contrary to the prediction based on the aspiration pressure p_asp, which results in an underpressure for all gas stagnation pressures $p_\mathrm{t,g}$ considered (see Fig. 4.6), there appears to be a range of low gas stagnation pressures $p_\mathrm{t,g}$ in which the liquid mass flow rate $\dot{m}_\mathrm{l}$ is reduced compared to the liquid-only flow. In general, the liquid mass flow rate $\dot{m}_\mathrm{l}$ is overestimated by the analytical prediction for the entire range of relevant gas stagnation pressures $p_\mathrm{t,g}$. In fact, the mean absolute relative error is 28 %. These results are in good agreement with the findings of Miller et al. (1996) and Le et al. (1999) as well as with the uncertainties in predicting the liquid mass flow rate $\dot{m}_\mathrm{l}$ reported by Wolf and Bergmann (2002), using molten metal as the working liquid. Furthermore, the measured liquid mass flow rate $\dot{m}_\mathrm{l}$ shows a qualitatively different dependence on the gas stagnation pressure $p_\mathrm{t,g}$ (see Fig. 4.11). That is, the liquid mass flow rate $\dot{m}_\mathrm{l}$ increases monotonically with increasing gas stagnation pressure $p_\mathrm{t,g}$. More specifically, it shows neither the strong increase at the wake closure pressure $p_\mathrm{t,g,close} \approx 1.13\,\mathrm{MPa}$ nor a gradual decrease in closed wake condition, both of which are predicted based on the aspiration curve in Fig. 4.6. There is, however, a distinct change in the slope noticeable at approximately the wake closure pressure $p_\mathrm{t,g,close}$. As a result, it is concluded that the liquid mass flow rate $\dot{m}_\mathrm{l}$ during the multiphase flow does not correlate well with the aspiration pressure p_asp, a characteristic of the gas-only flow. In other words, the aspiration pressure p_asp does not provide means to accurately predict the liquid mass flow rate $\dot{m}_\mathrm{l}$.

In addition, these results are a first indication that the introduction of liquid alters the flow field due to mass loading effects (see Section 2.2.4). For instance, the absence of a sudden increase in the liquid mass flow rate $\dot{m}_\mathrm{l}$ at the wake closure pressure $p_\mathrm{t,g,close}$ suggests that the liquid flow prevents the formation of a Mach disk and, consequently, forces the wake to stay open over the entire range of gas stagnation pressures $p_\mathrm{t,g}$ considered. Both experimental studies by Mates and Settles (2005b) and numerical studies by, among others, Zhang et al. (2021) and Amatriain et al. (2022) have reported similar mass loading effects for the atomization of liquid metal. Furthermore, based on an observed hysteresis in the aspiration curve, Ting et al. (2002) and Ting and Anderson (2004) have argued that the closed wake condition becomes unstable when either the Mach disk or the compression waves inside of the gas jet are displaced from their equilibrium positions or perturbed, for instance, by the introduction of liquid into the flow field.

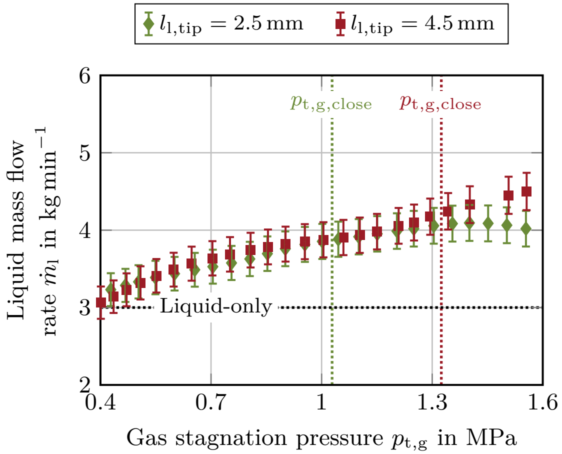

Figure 4.12: Liquid mass flow rate $\dot{m}_{\mathrm{l}}$ as a function of the gas stagnation pressure $p_{\mathrm{t,g}}$ for two different liquid nozzle tip protrusion lengths $l_{\mathrm{l,tip}}$. The error bars correspond to the expanded standard uncertainty, employing a coverage factor K of 1.96. Additionally indicated as a reference are the liquid mass flow rate $\dot{m}_{\mathrm{l}}$ for the liquid-only flow corresponding to the same constant liquid overpressure Δp_{l} as well as the respective wake closure pressures $p_{\mathrm{t,g,close}}$ obtained for the gas-only flow.

In Section 4.1.3, the aspiration pressure p_{asp} has been investigated for two additional liquid nozzle tip protrusion lengths $l_{\mathrm{l,tip}}$ different from the baseline case geometric design (i.e., different from $l_{\mathrm{l,tip}} = 3.5\,\mathrm{mm}$), one being shorter and one being longer in comparison (i.e., $l_{\mathrm{l,tip}} = 2.5\,\mathrm{mm}$ and $l_{\mathrm{l,tip}} = 4.5\,\mathrm{mm}$, respectively). These considerations have revealed a dependence of the wake closure pressure $p_{\mathrm{t,g,close}}$ as well as the maximum aspiration condition on the liquid nozzle tip protrusion length $l_{\mathrm{l,tip}}$. The corresponding liquid mass flow rates $\dot{m}_\mathrm{l}$ measured as a function of the gas stagnation pressure $p_\mathrm{t,g}$ are shown in Fig. 4.12. Here, the liquid nozzle diameter d_l has been 4 mm and the liquid overpressure Δp_l has been set to result in a liquid mass flow rate $\dot{m}_\mathrm{l}$ of $3\,\mathrm{kg\,min^{-1}}$ for the liquid-only flow. Thus, Fig. 4.12 also allows for a comparison with the data presented in Fig. 4.11. As can be seen, the measured liquid mass flow rates $\dot{m}_\mathrm{l}$ consistently do not correlate well with the respective aspiration curves shown in Fig. 4.7. In particular, no sudden increase at the respective wake closure pressures $p_\mathrm{t,g,close}$ can be observed, which are indicated in Fig. 4.12 as a reference. While not explicitly shown here, the predictions made by using Eq. (4.2) have consistently been found to overestimate the respective liquid mass flow rates $\dot{m}_\mathrm{l}$. In general, for both liquid nozzle tip protrusion lengths $l_\mathrm{l,tip}$ considered, the measured liquid mass flow rate $\dot{m}_\mathrm{l}$ qualitatively agrees well with the results for the baseline case design shown in Fig. 4.11. Notably, this is the case despite the significant differences between the respective aspiration curves (see Figs. 4.6 and 4.7). However, one specific qualitative difference can be seen for the shorter liquid nozzle tip protrusion length $l_\mathrm{l,tip}$ of 2.5 mm. That is, there appears to be a distinct maximum in the liquid mass flow rate $\dot{m}_\mathrm{l}$ at a gas stagnation pressure $p_\mathrm{t,g}$ of about 1.4 MPa, which is followed by a decrease in the liquid mass flow rate $\dot{m}_\mathrm{l}$ for even higher gas stagnation pressures $p_\mathrm{t,g}$. A decrease in the liquid mass flow rate $\dot{m}_\mathrm{l}$ for certain set points of operation has also been observed for the atomization of liquid metal by Jeyakumar et al. (2009) and Zhang et al. (2021). They have argued that the shear forces exerted on the liquid by the gas flow in the recirculation zone downstream of the liquid nozzle contribute to the increase in the liquid flow, but vary as a function of the gas stagnation pressure $p_\mathrm{t,g}$.

In conclusion, the dependence of the liquid mass flow rate $\dot{m}_\mathrm{l}$ on the gas stagnation pressure $p_\mathrm{t,g}$ as a function of the liquid nozzle tip protrusion length $l_\mathrm{l,tip}$ is more complex than suggested by the evaluation of the aspiration pressure p_asp, a quantity characteristic of the gas-only flow. In particular, there is no obvious qualitative trend that allows the change in the liquid mass flow rate $\dot{m}_\mathrm{l}$ due to a change in liquid nozzle tip protrusion length $l_\mathrm{l,tip}$ to be predicted.

Finally, as has been discussed in Section 4.1.1, due to the supersonic nature of the gas flow, the gas mass flow rate $\dot{m}_\mathrm{g}$ does not depend on the flow conditions downstream of the gas nozzle. Consequently, it is not affected by

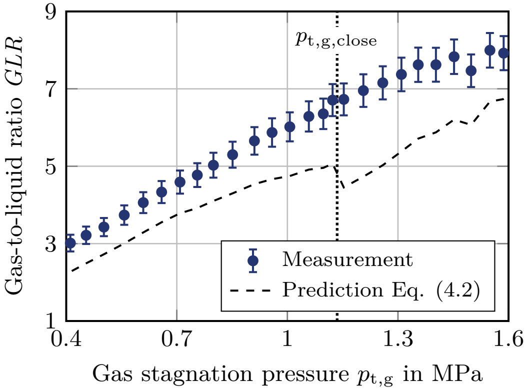

Figure 4.13: Comparison between the measured gas-to-liquid ratio GLR as a function of the gas stagnation pressure $p_{\mathrm{t,g}}$ and the prediction made by employing Eq. (4.2) and taking into account the aspiration pressure p_{asp} presented in Fig. 4.6. The error bars correspond to the expanded standard uncertainty, employing a coverage factor K of 1.96. Additionally indicated as a reference is the wake closure pressure $p_{\mathrm{t,g,close}}$ obtained for the gas-only flow.

the introduction of liquid into the flow field. The gas-to-liquid ratio GLR, on the other hand, directly depends on both fluid mass flow rates. Therefore, the above considerations regarding the liquid mass flow rate $\dot{m}_{\mathrm{l}}$ also apply to the gas-to-liquid ratio GLR. For the same measurements presented in Fig. 4.11, the gas-to-liquid ratio GLR measured as a function of the gas stagnation pressure $p_{\mathrm{t,g}}$ is compared to the prediction made by employing Eq. (4.2) in Fig. 4.13. Here, the measured gas mass flow rate $\dot{m}_{\mathrm{g}}$ has been used for the prediction instead of the analytical model proposed in Eq. (4.1). Even though the liquid mass flow rate increases monotonically with increasing gas stagnation pressure $p_{\mathrm{t,g}}$, the gas-to-liquid ratio GLR is also a monotonically increasing function of the gas stagnation pressure $p_{\mathrm{t,g}}$. This is due to the fact that the gas mass flow rate $\dot{m}_{\mathrm{g}}$ is more sensitive to changes in the gas stagnation pressure $p_{\mathrm{t,g}}$ than the liquid mass flow rate $\dot{m}_{\mathrm{l}}$, as can be seen by comparing Figs. 4.1 and 4.11. As a consequence, the atomizer efficiency gradually decreases with increasing gas stagnation pressure $p_{\mathrm{t,g}}$, as the gas consumption increases faster than the liquid throughput (see Section 3.1.1). As expected, the gas-to-liquid ratio GLR is underestimated by the prediction based on the aspiration pressure p_{asp}. In fact, the mean absolute relative error is 21.5 %. Most importantly, in contrast to the prediction based on the aspiration pressure p_{asp}, the measured data does not show a sudden increase in the efficiency at the wake closure pressure $p_{\mathrm{t,g,close}}$, which is indicated as a reference in Fig. 4.13.

Considering the question whether or not the aspiration pressure p_{asp} has any significance for the atomizer performance, which has been raised in Section 4.1.3, two conclusions can be drawn. First, the maximum aspiration condition neither correlates well with the liquid mass flow rate $\dot{m}_{\mathrm{l}}$ nor with the gas-to-liquid ratio *GLR*. In particular, for this specific operational condition, there is no extremum in the atomizer efficiency, which could result in an improvement in particle size. Second, the formation of a Mach disk during the multiphase flow is unlikely. Consequently, the interaction between liquid and the strong normal shock is unlikely to contribute to a particle size refinement as part of the atomization process. Further insights into this are discussed as part of Chapter 5.

4.3.2 Spray Formation

Although important for developing an understanding of the atomization process, in the context of supersonic close-coupled atomization, detailed insight into the interaction between the gas flow and the liquid flow is challenging to obtain experimentally with high spatial and temporal resolution (see Section 3.2). However, the imaging techniques described in Section 3.3 provide means for visualizing the resulting spray, which allows for gaining a first understanding of the spray formation.

In Fig. 4.14, exemplary images of the resulting spray are shown for four different gas stagnation pressures $p_{\mathrm{t,g}}$ (i.e., for (0.40 ± 0.02) MPa, (0.80 ± 0.05) MPa, (1.20 ± 0.07) MPa and (1.60 ± 0.10) MPa) and a constant liquid mass flow rate $\dot{m}_{\mathrm{l}}$ of $6\,\mathrm{kg\,min^{-1}}$. The images have been captured using the far-field configuration of the ultra-short diffuse background illumination imaging setup described in Section 3.3.2 and serve as a basis for describing the general characteristics of the spray. An important feature to note is that the spray is not in the form of a generic cone emanating from the exit of the central liquid nozzle. Instead, liquid is drawn into the high-velocity gas jet surrounding the base of the liquid nozzle tip, resulting in an optically dense curtain of liquid

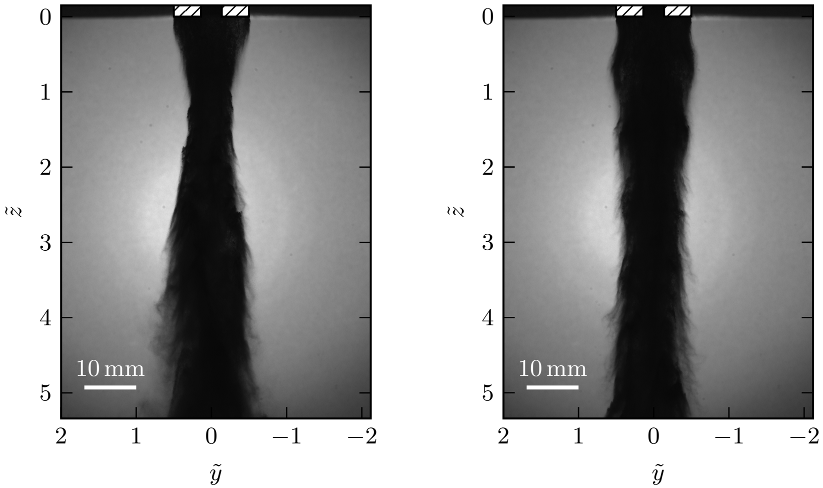

(a) $p_{\mathrm{t,g}} = (0.40 \pm 0.02)\,\mathrm{MPa}$,
$\dot{m}_{\mathrm{l}} = (6.02 \pm 0.02)\,\mathrm{kg\,min^{-1}}$

(b) $p_{\mathrm{t,g}} = (0.80 \pm 0.05)\,\mathrm{MPa}$,
$\dot{m}_{\mathrm{l}} = (6.02 \pm 0.02)\,\mathrm{kg\,min^{-1}}$

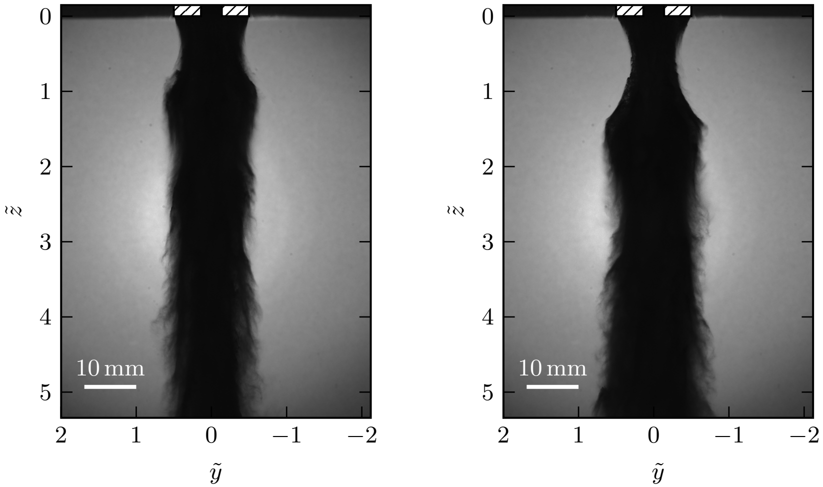

(c) $p_{\mathrm{t,g}} = (1.20 \pm 0.07)\,\mathrm{MPa}$,
$\dot{m}_{\mathrm{l}} = (6.02 \pm 0.03)\,\mathrm{kg\,min^{-1}}$

(d) $p_{\mathrm{t,g}} = (1.60 \pm 0.10)\,\mathrm{MPa}$,
$\dot{m}_{\mathrm{l}} = (6.01 \pm 0.04)\,\mathrm{kg\,min^{-1}}$

Figure 4.14: Ultra-short diffuse background illumination images of the spray for four different gas stagnation pressures $p_{\mathrm{t,g}}$ and a constant liquid mass flow rate $\dot{m}_{\mathrm{l}}$ of about $6\,\mathrm{kg\,min^{-1}}$ captured using the far-field configuration described in Section 3.3.2.

concealing the wake downstream of the liquid nozzle. This characteristic of the supersonic close-coupled atomization process, which has also been observed by Mates and Settles (1996), is a distinct difference from the atomization of a liquid jet by means of an annular coaxial gas flow (Lasheras & Hopfinger, 2000). Furthermore, this indicates that the liquid directly interacts with the high-velocity gas flow, a mechanism that is likely to contribute to the liquid breakup. The implications of this for the atomization process are further investigated as part of Section 6.2. Another important consequence of the high optical density is that the interaction between the gas flow and the liquid flow in the wake downstream of the liquid nozzle, that is, the primary atomization, is not accessible by means of diffuse background illumination imaging. This restriction as well as the underlying mechanism are further discussed in Section 6.1. While the core of the spray is not visible, it is clear that the outer part of the spray is influenced by the expanding high-velocity gas jet. In fact, the alternating pattern of expansion and compression waves, which has already been discussed in Section 4.1.2, directly affects the shape of the contour of the spray, as has also been observed by Mates and Settles (1996, 2005b) for the atomization of liquid tin. Furthermore, in Fig. 4.14 as the non-dimensional axial distance from the liquid nozzle $\tilde{z}$ increases, clusters of particles are seen to form in the outer part of the spray. For a generic subsonic two-fluid atomizer, the formation of particle clusters has been investigated experimentally by Heinlein and Fritsching (2006), linking it to the effect of intermittency as well as vortices in the shear layer. Interestingly, despite the dependence of the particle inertia on the particle size, they have found no correlation between the latter and the occurrence of particle clusters. Similarly, Lampa and Fritsching (2011, 2013) have studied particle clusters in the context of two-fluid atomization by means of imaging as well as numerical simulation, relating the formation of the clusters to gas entrainment and shear instabilities in the mixing layer. In the context of this experimental investigation, the particle clusters are an interesting feature, as the velocity information contained in them can be evaluated employing the method described in Section 3.3.3, which is made use of in Chapter 6.

The effect of the expanding high-velocity gas jet on the shape of the spray is visualized in more detail in Fig. 4.15. Here, focusing Schlieren images of the gas-only flow field captured by Luh et al. (2018) using a horizontal grid are compared to time-averaged diffuse background illumination images

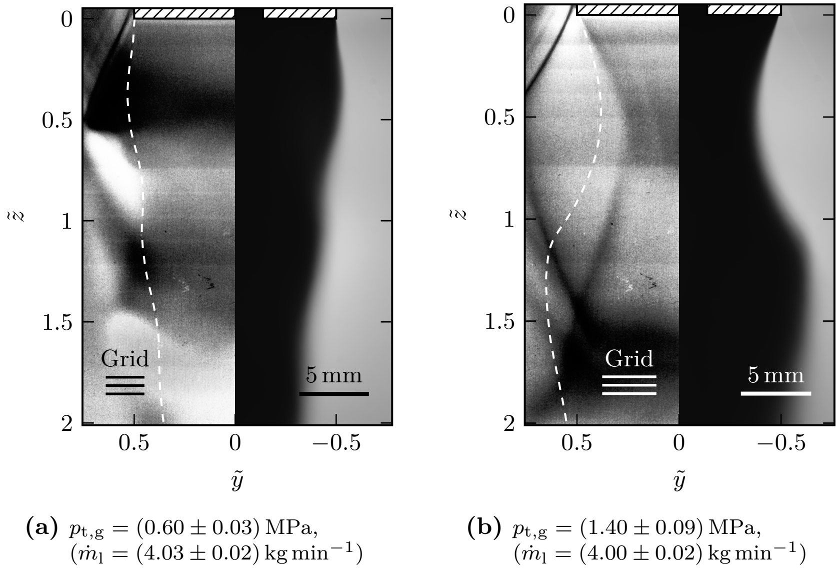

(a) $p_{\mathrm{t,g}} = (0.60 \pm 0.03)\,\mathrm{MPa}$, ($\dot{m}_{\mathrm{l}} = (4.03 \pm 0.02)\,\mathrm{kg\,min^{-1}}$)

(b) $p_{\mathrm{t,g}} = (1.40 \pm 0.09)\,\mathrm{MPa}$, ($\dot{m}_{\mathrm{l}} = (4.00 \pm 0.02)\,\mathrm{kg\,min^{-1}}$)

Figure 4.15: Comparison between focusing Schlieren images of the gas-only flow field (left half) captured using a horizontal grid and time-averaged ultra-short diffuse background illumination images (right half) captured using the mid-field configuration described in Section 3.3.2 for two different gas stagnation pressures $p_{\mathrm{t,g}}$ and a constant liquid mass flow rate $\dot{m}_{\mathrm{l}}$ of $4\,\mathrm{kg\,min^{-1}}$. Additionally indicated as a reference in the focusing Schlieren images (left half) are the contours of the respective time-averaged sprays. (Focusing Schlieren images adapted from Luh et al., 2018.)

of the spray present in the multiphase flow for two different gas stagnation pressures $p_{\mathrm{t,g}}$ (i.e., for $(0.60 \pm 0.03)\,\mathrm{MPa}$ and $(1.40 \pm 0.09)\,\mathrm{MPa}$), which have been captured using the mid-field configuration described in Section 3.3.2. For the multiphase flow, the liquid mass flow rate $\dot{m}_{\mathrm{l}}$ has been set to $4\,\mathrm{kg\,min^{-1}}$. Time-averaging has been done by first stabilizing and subsequently averaging all of the images captured as part of a single measurement at a constant set point of operation (see Section 3.3.3). For the mid-field configuration, this includes a total of 150 images (see Table 3.8). Additionally, the contours of the respective sprays are indicated in the focusing Schlieren images as a reference. These have been evaluated by time-averaging background-subtracted images of the spray and subsequently applying a global threshold for binarization, which has been obtained by means of the method proposed by Otsu (1979). The contours shown are the arithmetic mean of the left side and the right side of the spray. As can be seen, while the general shape of the spray contour does indeed correlate well with the expansion and the compression of the gas jet, there are distinct quantitative differences, especially in the case of the higher gas stagnation pressure $p_{\mathrm{t,g}}$ shown in Fig. 4.15b, which also corresponds to a higher pressure ratio PR. For instance, the liquid appears to restrict the expansion of the gas flow in the radial direction (i.e., in the y-direction). Similarly, the wave pattern can be seen to also be shortened in the axial direction (i.e., in the z-direction). This indicates that the liquid does influence the expansion waves and compression waves inside of the surrounding gas jet. In fact, as has been shown experimentally and numerically by Vogl et al. (2019) for the atomizer unit described in Section 3.1.2, the introduction of liquid into the flow field does not qualitatively alter the general wave structure inside of the gas jet. It does, however, affect the position of the waves. A similar conclusion has been reached by Mates and Settles (1996) for the atomization of liquid tin. As has been described in Section 4.3.1, according to Ting et al. (2002) and Ting and Anderson (2004), this is an indication that a Mach disk can no longer form in the flow field downstream of the liquid nozzle. Indeed, considering the core of the merged gas jet further downstream, Mates and Settles (2005b) have provided experimental evidence that compression waves are prevented from crossing the liquid and, instead, are reflected at the liquid surface. Furthermore, they have assumed that the liquid mass loading results in a reduced absolute gas velocity u_{g} in the center of the spray. Notably, this assumption is in good agreement with the numerical results presented by Zhang et al. (2021) and Amatriain et al. (2022).

While the expanding high-velocity gas jet clearly has an effect on the shape of the resulting spray, as has been shown in Figs. 4.14 and 4.15, at the same time, the liquid mass loading also alters the gas flow field. In order to further investigate the influence of the liquid mass loading, mean contours of the spray in close proximity to the liquid nozzle are shown in Fig. 4.16 as a function of the liquid mass flow rate $\dot{m}_{\mathrm{l}}$ for two different gas stagnation pressures $p_{\mathrm{t,g}}$ (i.e., for $0.6\,\mathrm{MPa}$ and $1.4\,\mathrm{MPa}$), that is, for two different degrees of underexpansion. In detail, for each gas stagnation pressure $p_{\mathrm{t,g}}$, three different liquid mass loadings are considered, which can also be expressed

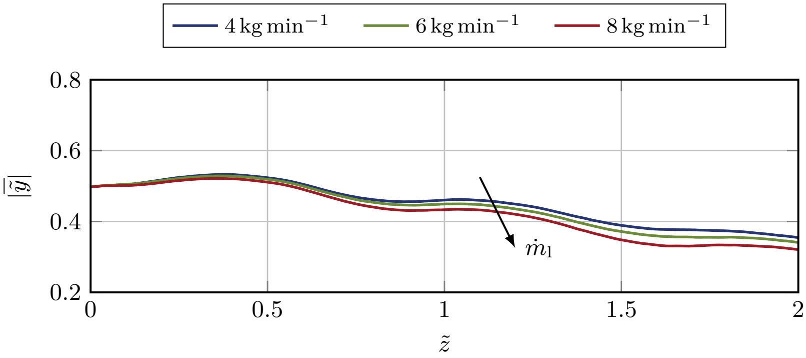

(a) $p_\mathrm{t,g} = 0.6\,\mathrm{MPa}$ ($\dot{m}_\mathrm{g} \approx 12\,\mathrm{kg\,min^{-1}}$)

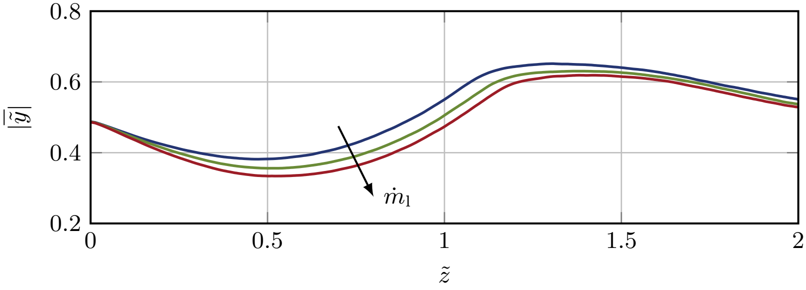

(b) $p_\mathrm{t,g} = 1.4\,\mathrm{MPa}$ ($\dot{m}_\mathrm{g} \approx 28\,\mathrm{kg\,min^{-1}}$)

Figure 4.16: Mean contours of the spray in close proximity to the liquid nozzle as a function of the liquid mass flow rate $\dot{m}_\mathrm{l}$ for two different gas stagnation pressures $p_\mathrm{t,g}$.

in terms of the gas-to-liquid ratio *GLR* as defined in Eq. (2.6), taking into account that a low liquid mass loading corresponds to a high gas-to-liquid ratio *GLR*, and vice versa. Specifically, the ranges covered in Figs. 4.16a and 4.16b are $1.5 \leq GLR \leq 3$ and $3.5 \leq GLR \leq 7$, respectively. As can be seen, while the shape of the spray is not qualitatively affected by a change in the liquid mass flow rate $\dot{m}_\mathrm{l}$, the resistance to the expansion of the gas jet differs as a function of the specific liquid mass loading. Indeed, this affects the radial expansion (i.e., in the y-direction) as well as the axial length of the flow patterns (i.e., in the z-direction) and is especially pronounced for the higher gas stagnation pressure $p_{\mathrm{t,g}}$ shown in Fig. 4.16b. Interestingly, an increase in the liquid mass flow rate $\dot{m}_{\mathrm{l}}$ does not result in a wider spray contour. In fact, the lowest liquid mass flow rate $\dot{m}_{\mathrm{l}}$ considered here (i.e., $\dot{m}_{\mathrm{l}} = 4\,\mathrm{kg\,min^{-1}}$, which has already been considered in Fig. 4.15) corresponds to the widest spray contour, with a further increase in the liquid mass flow rate $\dot{m}_{\mathrm{l}}$ resulting in a gradual narrowing of the spray. In order to understand this result, besides the gas stagnation pressure $p_{\mathrm{t,g}}$ and the liquid mass flow rate $\dot{m}_{\mathrm{l}}$, an additional parameter has to be taken into account.

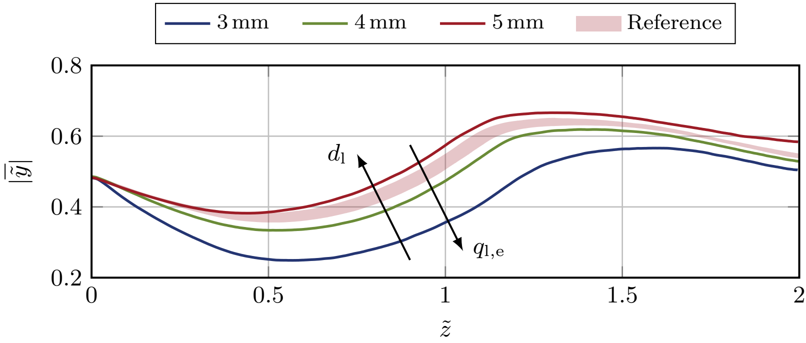

Figure 4.17: Mean contour of the spray in close proximity to the liquid nozzle as a function of the liquid nozzle diameter d_{l} for a constant gas stagnation pressure $p_{\mathrm{t,g}}$ of 1.4 MPa and a constant liquid mass flow rate $\dot{m}_{\mathrm{l}}$ of $8\,\mathrm{kg\,min^{-1}}$. The shaded area corresponds to the difference between the mean contours for a liquid mass flow rate $\dot{m}_{\mathrm{l}}$ of $4\,\mathrm{kg\,min^{-1}}$ and of $6\,\mathrm{kg\,min^{-1}}$ shown in Fig. 4.16b for a liquid nozzle diameter d_{l} of 4 mm and serves as a reference for the mean contour corresponding to a liquid nozzle diameter d_{l} of 5 mm depicted in this figure.

For a given geometric design of the liquid nozzle, the liquid supply line described in Section 3.1.3 allows for setting the liquid mass flow rate $\dot{m}_{\mathrm{l}}$ by adjusting the absolute velocity of the liquid at the nozzle exit $u_{\mathrm{l,e}}$. Consequently, a change in the liquid mass flow rate $\dot{m}_{\mathrm{l}}$ corresponds to a change in the liquid momentum flux at the liquid nozzle exit[3] $q_{\mathrm{l,e}} = \rho_{\mathrm{l,e}} u_{\mathrm{l,e}}^2$. However, the influence of these two parameters can be separated by additionally varying the liquid nozzle diameter d_{l} (see Section 3.1.2). In Fig. 4.17, the mean

---

[3] Due to the definition of the absolute liquid velocity at the liquid nozzle exit $u_{\mathrm{l,e}}$ in Eq. (3.1) as an area-averaged quantity, the liquid momentum flux at the liquid nozzle exit $q_{\mathrm{l,e}}$ is also an area-averaged quantity, assuming a constant liquid density ρ_{l}.

contour of the spray is shown as a function fo the liquid nozzle diameter d_l for a constant gas stagnation pressure $p_\mathrm{t,g}$ of 1.4 MPa and a constant liquid mass flow rate $\dot{m}_\mathrm{l}$ of $8\,\mathrm{kg\,min^{-1}}$. As can be seen, an increasing liquid nozzle diameter d_l, that is, a decreasing liquid momentum flux at the liquid nozzle exit $q_\mathrm{l,e}$, results in more resistance to the expansion of the gas jet. In other words, the spray contour becomes wider as the liquid momentum flux at the liquid nozzle exit $q_\mathrm{l,e}$ decreases.

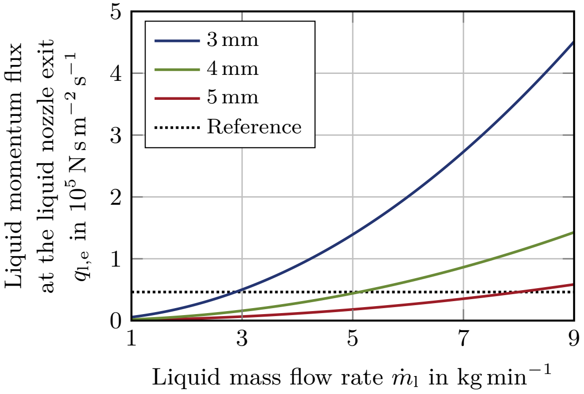

Figure 4.18: Liquid momentum flux at the liquid nozzle exit $q_\mathrm{l,e}$ as a function of the liquid mass flow rate $\dot{m}_\mathrm{l}$ for three different liquid nozzle diameters d_l and a constant liquid temperature T_l of 20 °C. As a reference, the liquid momentum flux at the liquid nozzle exit $q_\mathrm{l,e}$ for a liquid mass flow rate $\dot{m}_\mathrm{l}$ of $8\,\mathrm{kg\,min^{-1}}$ and a liquid nozzle diameter d_l of 5 mm is indicated.

In Fig. 4.18, the liquid momentum flux at the liquid nozzle exit $q_\mathrm{l,e}$ is shown as a function of the liquid mass flow rate $\dot{m}_\mathrm{l}$ for the three different liquid nozzle diameters d_l considered (i.e., for 3 mm, 4 mm and 5 mm). Here, the data covers the entire range of the liquid mass flow rate $\dot{m}_\mathrm{l}$ considered for this experimental investigation (see Section 3.1.4) and has been calculated for an exemplary liquid temperature T_l of 20 °C. As can be seen, for the liquid mass flow rate $\dot{m}_\mathrm{l}$ of $8\,\mathrm{kg\,min^{-1}}$ considered in Fig. 4.17, the liquid nozzle diameter d_l of 5 mm results in a liquid momentum flux at the liquid nozzle exit $q_\mathrm{l,e}$ which is 59 % lower than the one corresponding to the liquid nozzle diameter d_l of 4 mm. As a result, for the liquid nozzle diameter d_l of 4 mm, a comparable liquid momentum flux at the liquid nozzle exit $q_\mathrm{l,e}$ is achieved by decreasing the liquid mass flow rate $\dot{m}_\mathrm{l}$ to $5.12\,\mathrm{kg\,min^{-1}}$ (i.e., to 64 % of $8\,\mathrm{kg\,min^{-1}}$), as is additionally indicated in Fig. 4.18. In Fig. 4.16b, spray contours are shown for a liquid mass flow rate $\dot{m}_\mathrm{l}$ of $4\,\mathrm{kg\,min^{-1}}$ as well as of $6\,\mathrm{kg\,min^{-1}}$. The difference between these two contours is additionally depicted in Fig. 4.17 as a reference. As can be seen, the agreement with the result for the liquid nozzle diameter d_l of 5 mm is quite good. Consequently, these results suggest that the flow field in close proximity to the liquid nozzle is mainly determined by the gas stagnation pressure $p_\mathrm{t,g}$ and the liquid momentum flux at the liquid nozzle exit $q_\mathrm{l,e}$. This can be explained by considering the numerical results for the gas-only flow field presented in Fig. 4.3 and discussed as part of Section 4.1.2. While these results do not take into account the liquid mass loading, they still indicate that, immediately upon exiting the liquid nozzle, the liquid jet interacts with a counter-flowing gas jet in the center of the recirculation zone downstream of the liquid nozzle. In other words, for a given gas stagnation pressure $p_\mathrm{t,g}$, the liquid momentum flux at the liquid nozzle exit $q_\mathrm{l,e}$ determines how far the liquid jet travels in the axial direction (i.e., in the z-direction) before it is displaced in the radial direction (i.e., in the y-direction). The more liquid mass m_l remains close to the liquid nozzle, the stronger is the resistance to the initial expansion of the gas jet. This is further discussed and supported with experimental evidence in Section 6.1.

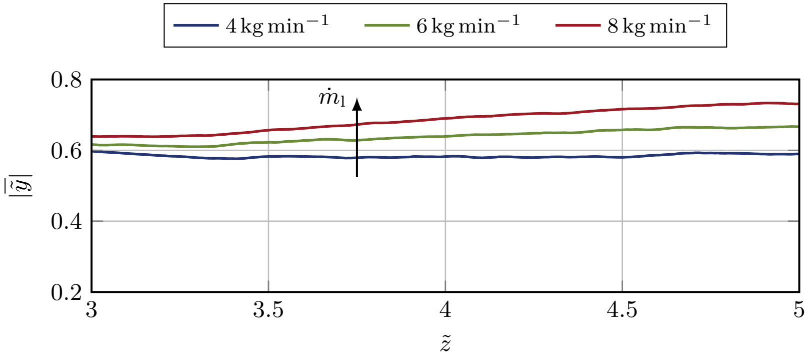

Figure 4.19: Mean contours of the spray further downstream of the liquid nozzle as a function of the liquid mass flow rate $\dot{m}_\mathrm{l}$ for a gas stagnation pressure $p_\mathrm{t,g}$ of 1.4 MPa.

The far-field configuration of the imaging setup described in Section 3.3.2

allows for evaluating the spray contour further downstream of the liquid nozzle. Indeed, in Fig. 4.19, the mean contours of the spray are shown for the same set points of operation already presented in Fig. 4.16b, but up to a non-dimensional axial distance $\tilde{z}$ of 5. As can be seen, here, the trend is opposite to what has been observed in close proximity to the liquid nozzle. That is, an increase in the liquid mass flow rate $\dot{m}_\mathrm{l}$ results in a widening of the spray.

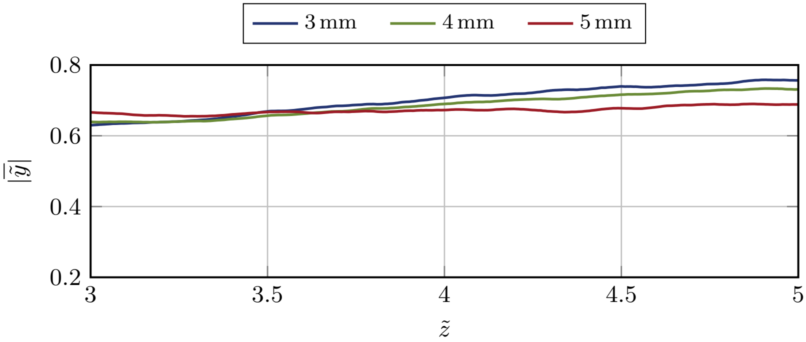

Figure 4.20: Mean contour of the spray further downstream of the liquid nozzle as a function of the liquid nozzle diameter d_l for a constant gas stagnation pressure $p_\mathrm{t,g}$ of 1.4 MPa and a constant liquid mass flow rate $\dot{m}_\mathrm{l}$ of 8 kg min^{-1}.

Considering that, for the liquid supply line described in Section 3.1.3, a change in the the liquid mass flow rate $\dot{m}_\mathrm{l}$ corresponds to a change in the liquid momentum flux at the liquid nozzle exit $q_\mathrm{l,e}$, varying the liquid nozzle diameter d_l provides means for investigating the significance of these two parameters. For this purpose, mean contours of the spray are shown in Fig. 4.20 for the same set points of operation already presented in Fig. 4.17. Notably, the effect of the liquid momentum flux at the liquid nozzle exit $q_\mathrm{l,e}$ is less pronounced than in close proximity to the liquid nozzle and, additionally, reverses with increasing non-dimensional axial distance $\tilde{z}$. In fact, the contour of the spray appears to be less sensitive to changes in the liquid momentum flux at the liquid nozzle exit $q_\mathrm{l,e}$ than to changes in the liquid mass flow rate $\dot{m}_\mathrm{l}$ (see Fig. 4.19). This indicates that, far downstream of the liquid nozzle, the liquid mass flow rate $\dot{m}_\mathrm{l}$ is more important for determining the formation of the spray.

In conclusion, these results indicate that the interaction between the gas flow and the liquid flow is governed not only by the gas stagnation pressure $p_{\mathrm{t,g}}$ and the liquid mass flow rate $\dot{m}_{\mathrm{l}}$, but also by the liquid momentum flux at the liquid nozzle exit $q_{\mathrm{l,e}}$. In particular, this appears to be true for the primary atomization, which is further studied in Section 6.1. However, the implications of these considerations for the atomization result, that is, the particle size, are investigated in Chapter 5.

4.4 Summary and Conclusions

In this chapter, the operational characteristics of the atomizer unit described in Section 3.1.2 have been studied for the range of operational parameters outlined in Section 3.1.4. For this purpose, the gas-only flow, the liquid-only flow as well as the multiphase flow have been considered separately.

The gas-only flow field has been shown to be characterized by an alternating pattern of expansion and compression waves inside of the high-velocity gas jet as well as a recirculation zone in the wake downstream of the liquid nozzle. For high gas stagnation pressures $p_{\mathrm{t,g}}$, the atomizer has been found to operate in closed wake condition, which is characterized by the formation of a Mach disk. An analysis of the aspiration pressure p_{asp} has revealed that the gas flow results in an underpressure at the exit of the liquid nozzle for the entire range of set points of operation considered, which is an indicator for a stable atomizer operation. Finally, by means of an analytical model, the gas stagnation pressure $p_{\mathrm{t,g}}$ and the gas mass flow rate $\dot{m}_{\mathrm{g}}$ have been shown to be interchangeable in describing the set point of operation of the atomizer.

In terms of the liquid-only flow, the liquid mass flow rate $\dot{m}_{\mathrm{l}}$ has been successfully modeled as a function of the liquid overpressure by employing the Bernoulli equation and introducing a discharge coefficient. In the absence of a gas flow, the liquid jet has been found not to break up significantly within a short axial distance from the liquid nozzle, indicating that primary atomization is dominated by the interaction between the gas flow and the liquid flow.

In regard to the multiphase flow, the gas flow has been found to affect the liquid mass flow rate $\dot{m}_{\mathrm{l}}$ and, therefore, the liquid mass loading present in the flow field. Importantly, the aspiration pressure p_{asp}, a quantity characteristic of the gas-only flow, has been discovered not to be a suitable means for predicting the liquid mass flow rate $\dot{m}_\mathrm{l}$ during the multiphase flow. Similarly, by comparing Schlieren images of the gas-only flow field and images of the spray, the introduction of liquid has been found to affect the position of the pattern of expansion waves and compression waves in the high-velocity gas jet. Indeed, the contour of the spray has been discovered to depend on the wave pattern of the gas jet as well as the liquid mass loading. In particular, the liquid momentum flux at the liquid nozzle exit $q_\mathrm{l,e}$ has been shown to affect the contour of the spray in close proximity to the liquid nozzle. Furthermore, no evidence for an operation of the atomizer in the closed wake condition, that is, the formation of a Mach disk, has been observed. While water has been used as the working liquid for all of the experimental investigations, good agreement has been found with reported results for liquid metal.

To conclude, the results of this chapter indicate that a model describing the supersonic close-coupled atomization process has to take into account effects of compressibility as well as the two-way coupling between the gas flow an the liquid flow, in order to accurately predict the liquid mass loading, the multiphase flow field and the interaction between the two fluids. The significance of these parameters for the atomization process is further discussed in Chapters 5 and 6.

5 Spray Characteristics

In order to develop an understanding of the physics involved in the supersonic close-coupled atomization process and, ultimately, to derive predictive modeling capabilities, it is necessary to investigate how operational parameters, physical fluid properties and the geometric design of the atomizer unit influence the atomization result, that is, the particle diameter d_p as well as the absolute particle velocity u_p. Some of these sensitivities have been studied as part of this experimental investigation by means of the phase Doppler measurement technique described in Section 3.2, placing the focus on the effect of the set point of operation as well as of the liquid dynamic viscosity μ_l on the atomization result.

An overview of the design of experiments is given in Section 5.1, where the relevant measurement positions are defined and the data quality achieved is briefly assessed. The structure of the resulting spray is investigated in Section 5.2. This involves radial distributions of the particle diameter d_p and the absolute particle velocity u_p as well as a study of the local sensitivity of these quantities to changes in the set point of operation. In Section 5.3, the influence of the set point of operation, defined by the gas stagnation pressure $p_\mathrm{t,g}$ and the liquid mass flow rate $\dot{m}_\mathrm{l}$ (see Section 3.1.4), is discussed in more detail. In addition, this includes a critical evaluation of the significance of the gas-to-liquid ratio GLR in the context of atomization models. In terms of the physical fluid properties, the effect of the liquid dynamic viscosity μ_l on the atomization result is studied in Section 5.4. This allows for evaluating the influence of the liquid Reynolds number Re_l, a quantity often considered to be important for the modeling of conventional atomization processes. Finally, in Section 5.5, the empirical atomization models introduced in Section 2.2 are briefly discussed in terms of how consistent they are with the results obtained in this experimental investigation. This provides insights into shortcomings of the existing models and results in recommendations for the future development of novel modeling approaches. For all of these considerations, unless explicitly stated otherwise, the baseline case design of the atomizer unit is employed (i.e., $d_\mathrm{l} = 4\,\mathrm{mm}$ and $l_\mathrm{l,tip} = 3.5\,\mathrm{mm}$, see Section 3.1.2).

Parts of this chapter have already been covered in the thesis of Schrimpl (2021), presented in Apell et al. (2021, 2022b, 2022a) and published in Apell et al. (2023).

5.1 Design of Experiments

As has been shown in Section 3.2.3, for a meaningful evaluation of the particle size and velocity statistics from the phase Doppler measurement raw data, a sufficient number of particles n_p has to be detected and validated. For the spray produced by the supersonic close-coupled atomizer described in Section 3.1.2, the minimum number of particles $n_\mathrm{p,min}$ has been found to be in the order of 10^4 (see Fig. 3.14). Consequently, for this experimental investigation, at least 20 000 particles have been validated for each individual measurement. However, besides the number of detected particles n_p, the specific individual measurement positions are important as well, as, for a meaningful comparison in the context of metal powder production, only results corresponding to the finished atomization process are of relevance. Furthermore, in an optically dense spray, the specific measurement position makes a difference in terms of the data quality. In the following, both of these aspects are studied in more detail, considering water as the working liquid.

5.1.1 Measurement Positions

For this experimental investigation, all of the phase Doppler measurement data has been obtained in a plane at an axial distance z of $500\,\mathrm{mm}$ downstream of the liquid nozzle (i.e., at $\tilde{z} \approx 34.5$), where the spray is fully developed. This has the additional benefit that, compared to measurement positions closer to the liquid nozzle, the reduced optical density results in an acceptable signal-to-noise ratio and the absolute particle velocity u_p is low enough to be resolved using the optical configuration described in Section 3.2.1.

Whether or not the spray is fully developed, that is, whether or not there is further secondary atomization, is usually expressed in terms of the gas Weber number We_g, as defined in Eq. (2.4) (Lefebvre & McDonell, 2017). Indeed, for the secondary breakup of a spherical particle to occur, the aerodynamic forces acting on the particle have to be sufficiently large relative to the surface tension force counteracting the disruptive forces (Hinze, 1955). In other words, the gas Weber number We_{g} has to exceed a critical value, which is the critical gas Weber number $We_{\mathrm{g,crit}}$ and usually differs depending on the specific gas flow field and the transient characteristics of the gas flow (Hinze, 1955). Furthermore, the critical gas Weber number $We_{\mathrm{g,crit}}$ has been found to depend on the liquid dynamic viscosity μ_{l}, which is expressed in terms of the Ohnesorge number Oh, as defined in Eq. (2.5), and generally results in an increase in the critical gas Weber number $We_{\mathrm{g,crit}}$ (Hinze, 1955). However, as has been shown by Hsiang and Faeth (1995), for Ohnesorge numbers Oh lower than 0.1, the effect of the liquid dynamic viscosity μ_{l} is negligible and a reasonable conservative estimate of the critical gas Weber number $We_{\mathrm{g,crit}}$ is 12 (Lefebvre & McDonell, 2017).

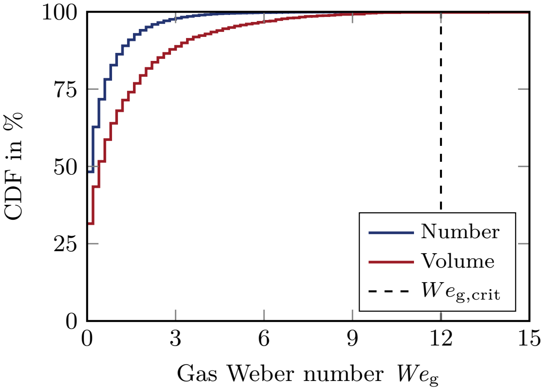

Figure 5.1: Estimated distribution of the gas Weber number We_{g} in the center of the spray (i.e., at $x = y = 0\,\mathrm{mm}$) for a gas stagnation pressure $p_{\mathrm{t,g}}$ of $(1.61 \pm 0.11)\,\mathrm{MPa}$ and a liquid mass flow rate $\dot{m}_{\mathrm{l}}$ of $(9.00 \pm 0.03)\,\mathrm{kg\,min^{-1}}$. Shown are the number-weighted as well as the volume-weighted cumulative distribution function. Additionally indicated is the critical gas Weber number $We_{\mathrm{g,crit}}$.

Using phase Doppler measurement data obtained in the center of the spray (i.e., at $x = y = 0\,\mathrm{mm}$) for a gas stagnation pressure $p_{\mathrm{t,g}}$ of $(1.61 \pm 0.11)\,\mathrm{MPa}$ and a liquid mass flow rate $\dot{m}_{\mathrm{l}}$ of $(9.00 \pm 0.03)\,\mathrm{kg\,min^{-1}}$, the local distribution of the gas Weber number We_{g} has been estimated. Here, it has to be noted that this set point of operation corresponds to the most extreme operational conditions considered in this experimental investigation (see Section 3.1.4). For the local absolute gas velocity u_g and the local gas density ρ_g, axisymmetric steady-state simulation results for the gas-only flow field provided by the research partner SMS as part of the IGSTC project PPAM have been employed. Therefore, this can be understood as a conservative estimate, since the weakening effect of the liquid mass loading on the gas flow has been neglected (see Section 4.3.2). In Fig. 5.1, results for the estimate of the local gas Weber number We_g are presented in the form of a number-weighted and a volume-weighted discrete cumulative distribution function. Additionally indicated is the critical gas Weber number $We_\mathrm{g,crit}$, which is assumed to be 12 due to the Ohnesorge number being in the order of 10^{-3} (see Table 3.2). As can be seen, most of the particles as well as most of the liquid volume correspond to gas Weber numbers We_g smaller than the critical gas Weber number $We_\mathrm{g,crit}$. In other words, the particles are subjected to aerodynamic forces that are too small to cause further breakup. The same has been found to be true for measurement positions not directly in the center of the spray. Consequently, these results indicate that significant secondary atomization is unlikely to occur at an axial distance z of 500 mm downstream of the liquid nozzle, that is, that the spray is fully developed.

Additionally, under the assumption of radial symmetry, all of the measurement positions considered as part of this experimental investigation have been restricted to the negative y-axis (see Fig. 3.7). This serves the purpose of reducing the adverse effect of obscuration on the data quality and allows for measuring the radial particle velocity $u_\mathrm{p,rad}$ using the planar system (see Section 3.2.1). Consequently, the more descriptive radial coordinate $r = -y$ is introduced and used in the following for convenience.

5.1.2 Data Quality

The optical configuration of the dual-mode phase Doppler measurement system discussed in Section 3.2.1 has been fine-tuned employing a monodisperse droplet chain produced by a generator (FMP Technology GmbH) based on the excited Rayleigh breakup of a laminar jet (see Section 4.2.2), showing good agreement with results for the droplet diameter d_p obtained by means of imaging. However, since the raw data additionally depends on the spray itself and the settings applied to the processor for signal evaluation, these considerations cannot simply be applied to the spray produced by the supersonic close-coupled atomizer described in Section 3.1.2 (Albrecht et al., 2003). Instead, three different numerical metrics have been employed for assessing the data quality and adjusting the settings of the processor for the actual spray. In detail, these metrics include the burst validation ϑ_{burst}, the sphericity validation $\vartheta_{\text{sphere}}$ and the data rate f_{data}. The former is defined as the fraction of the total number of detected burst signals that passes the internal validation criteria of the processor and is, therefore, assumed to originate from real particles. The subsequent sphericity validation $\vartheta_{\text{sphere}}$, on the other hand, is defined as the fraction of these validated burst signals corresponding to particles passing the sphericity criterion introduced in Section 3.2.1. Only burst signals passing both validation criteria contribute to the data rate f_{data}, which is defined as the number of validated signals per unit time (see Section 3.2.2).

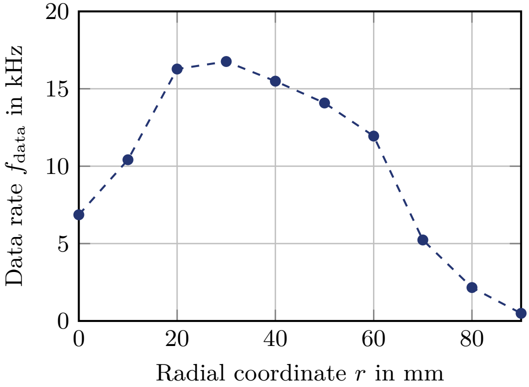

Figure 5.2: Radial distribution of the data rate f_{data} for a gas stagnation pressure $p_{\text{t,g}}$ of 0.8 MPa and a liquid mass flow rate $\dot{m}_{\text{l}}$ of 5 kg min^{-1}. (Adapted from Apell et al., 2023, with permission from Elsevier Ltd. © 2023 Elsevier Ltd.)

For an exemplary set point of operation, which is characterized by a gas stagnation pressure $p_{\text{t,g}}$ of (0.80 ± 0.05) MPa and a liquid mass flow rate $\dot{m}_{\text{l}}$ of (5.01 ± 0.05) kg min^{-1} and is, therefore, considered to be moderate, a distribution of the data rate f_{data} obtained in increments of 10 mm in radial direction r is shown in Fig. 5.3. Here, the edge of the spray has been defined as the radial coordinate r corresponding to a data rate f_{data} lower than 500 Hz and found to be at a radial coordinate r of about 90 mm. As can be seen, there is a distinct local minimum in the data rate f_{data} in the center of the spray (i.e., at a radial coordinate r of 0 mm), indicating either a reduction in the signal quality due to obscuration and the high optical density of the spray or a reduced local particle flux[1]. Furthermore, there is a maximum in the data rate f_{data} at a radial position r of about 30 mm, reaching values as high as 16.8 kHz. As a consequence, the measurement time t_{meas} necessary to validate a sufficient number of particles n_{p} is particularly short. Qualitatively, these results have been found to be representative of all set points of operation considered.

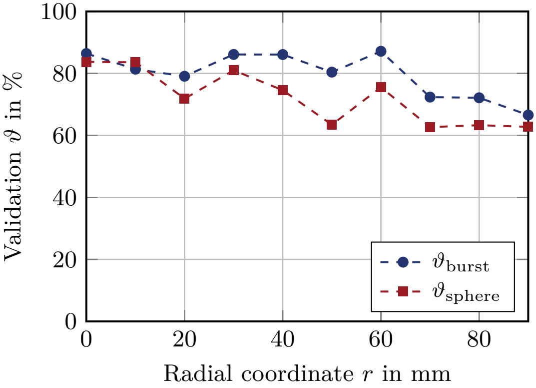

Figure 5.3: Radial distributions of the two validation criteria for a gas stagnation pressure $p_{\mathrm{t,g}}$ of (0.80 ± 0.05) MPa and a liquid mass flow rate $\dot{m}_{\mathrm{l}}$ of $(5.01 \pm 0.05)\,\mathrm{kg\,min^{-1}}$. (Adapted from Apell et al., 2023, with permission from Elsevier Ltd. © 2023 Elsevier Ltd.)

For the same data sets presented in Fig. 5.2, radial distributions of both of the introduced validation criteria are shown in Fig. 5.3. As can be seen, a large fraction of the detected signals is validated, with a gradual decrease with increasing radial coordinate r. Notably, neither the burst validation $\vartheta_{\mathrm{burst}}$ nor the sphericity validation $\vartheta_{\mathrm{sphere}}$ shows a local minimum in the center of the spray. While this does not provide information about signals not being able to trigger the processor, it does indicate that the probability for detected signals

---

[1] Defined according to Albrecht et al. (2003) as the number of particles per unit time.

to be validated and to contribute to the data rate f_{data} is not lower in the center of the spray. Consequently, in the absence of other metrics quantifying the signal quality, this suggests that the local particle flux is indeed reduced in the center of the spray. In a qualitative manner, these results have been found to be representative of all set points of operation considered.

To conclude, the dual-mode phase Doppler measurement system outlined in Section 3.2.1 has been found to achieve high values of the burst validation $\vartheta_{\mathrm{burst}}$, the sphericity validation $\vartheta_{\mathrm{sphere}}$ as well as the data rate f_{data} in a spray produced by the supersonic close-coupled atomizer described in Section 3.1.2, allowing a high confidence in the validity of the obtained measurement data. Notably, this is despite the challenging spray and particle characteristics, which are discussed in more detail in the following.

5.2 Spray Structure

In Section 4.3.2, it has been established that, in supersonic close-coupled atomization, the spray is not formed as a generic cone emanating from the central liquid nozzle, but instead is formed by the interaction between the liquid flow and the surrounding high-velocity gas jet undergoing expansion and compression in an alternating manner. Consequently, it is interesting to investigate how the spray formation affects the structure of the resulting spray, that is, the local variation in the particle size and velocity statistics (see Section 3.2.3). For this purpose, the spray cross-section has been traversed in radial direction r in increments of 10 mm, considering water as the working liquid.

5.2.1 Radial Distributions

In the following, findings are discussed for a set point of operation characterized by a gas stagnation pressure $p_{\mathrm{t,g}}$ of $(0.80 \pm 0.05)\,\mathrm{MPa}$ and a liquid mass flow rate $\dot{m}_{\mathrm{l}}$ of $(5.01 \pm 0.05)\,\mathrm{kg\,min^{-1}}$, which is identical to the one presented in Section 5.1. For this particular set point of operation, the edge of the spray has been determined to be at a radial coordinate r of about 90 mm, as has been described in Section 5.1.2. Importantly, in a qualitative manner, the following results have been found to be representative of all set points of operation considered.

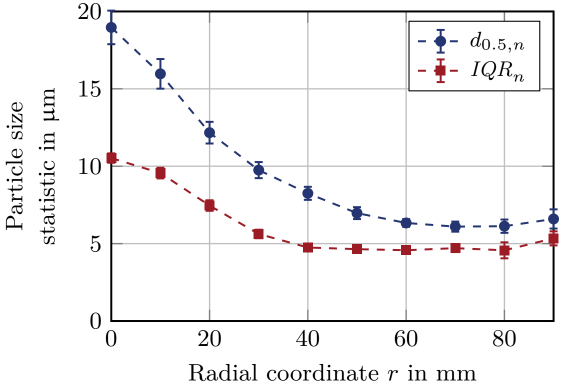

Figure 5.4: Radial distributions of the number median diameter $d_{0.5,n}$ and the number interquartile range IQR_n for a gas stagnation pressure $p_{\mathrm{t,g}}$ of $(0.80 \pm 0.05)\,\mathrm{MPa}$ and a liquid mass flow rate $\dot{m}_{\mathrm{l}}$ of $(5.01 \pm 0.05)\,\mathrm{kg\,min^{-1}}$. The error bars correspond to the expanded standard uncertainty, employing a coverage factor K of 1.96. For some data points, the expanded standard uncertainty is smaller than the marker size. (Adapted from Apell et al., 2023, with permission from Elsevier Ltd. © 2023 Elsevier Ltd.)

In terms of the particle size, radial distributions of the relevant number-weighted statistics are shown in Fig. 5.4, including the number median diameter $d_{0.5,n}$ as well as the number interquartile range IQR_n. As can be seen, the former indicates that the particle size tends to be largest in the center of the spray and decreases with increasing radial coordinate r. Similarly, the dispersion of the particle size is highest in the center of the spray and decreases with increasing radial coordinate r, as is indicated by the number interquartile range IQR_n. Interestingly, in the outer part of the spray, that is, at a radial coordinate r larger than about 60 mm, the particle size remains virtually constant. While not explicitly shown here, these results have been found to also be true for the volume-weighted particle size statistics, that is, for the volume median diameter $d_{0.5,V}$ and the volume interquartile range IQR_V. Furthermore, they agree well with the data obtained by Allimant et al. (2009) using a patternator-like sampling system during the atomization of an aluminum alloy. Additionally, similar trends have been reported by Domnick et al. (1997, 1998) and Wolf and Bergmann (2002) for the atomization of pure copper.

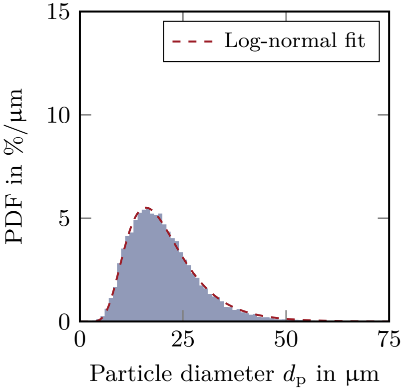

(a) $r = 0\,\mathrm{mm}$ **(b)** $r = 40\,\mathrm{mm}$

Figure 5.5: Particle size distributions for a gas stagnation pressure $p_{\mathrm{t,g}}$ of $(0.80 \pm 0.05)\,\mathrm{MPa}$ and a liquid mass flow rate $\dot{m}_\mathrm{l}$ of $(5.01 \pm 0.05)\,\mathrm{kg\,min^{-1}}$ at two different radial positions r. Shown are the discrete probability density functions. Additionally indicated are fits of log-normal distributions. (Adapted from Apell et al., 2023, with permission from Elsevier Ltd. © 2023 Elsevier Ltd.)

A more detailed insight into the local variation of the particle size is gained by studying the actual local number-weighted particle size distributions, which are shown in Fig. 5.5 as discrete probability density functions for two radial coordinates r (i.e., for $r = 0\,\mathrm{mm}$ and for $r = 40\,\mathrm{mm}$). Consistent with the results presented in Fig. 5.4, the overall particle size decreases and the particle size distribution becomes narrower with increasing radial coordinate r. Furthermore, the particle size distributions are not symmetric, but are characterized by a positive skewness. In fact, they can be described well using log-normal distributions, as can be seen from the fits obtained by means of a non-linear least squares method, which are additionally indicated in Fig. 5.5. Notably, this is in good agreement with the findings of Ünal (1987), Srivastava and Ojha (2006) and Urionabarrenetxea et al. (2021), who have analyzed the global particle size distributions of metal powders produced from aluminum alloys and a number of different pure metals. According to Panão (2023), this is an indication of an exponential increase in the particle size dispersion due to the atomization process.

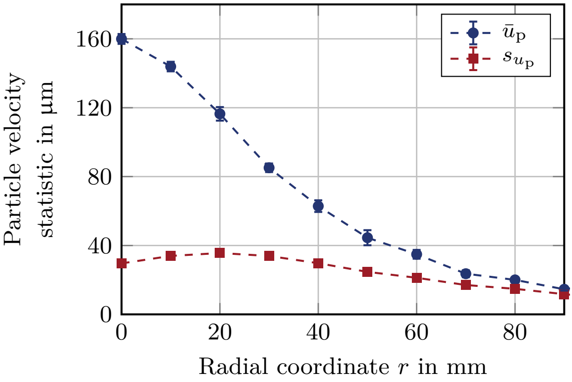

Figure 5.6: Radial distributions of the mean absolute particle velocity $\bar{u}_\mathrm{p}$ and the standard deviation of the absolute particle velocity s_{u_p} for a gas stagnation pressure $p_\mathrm{t,g}$ of $(0.80 \pm 0.05)\,\mathrm{MPa}$ and a liquid mass flow rate $\dot{m}_\mathrm{l}$ of $(5.01 \pm 0.05)\,\mathrm{kg\,min^{-1}}$. The error bars correspond to the expanded standard uncertainty, employing a coverage factor K of 1.96. For some data points, the expanded standard uncertainty is smaller than the marker size. (Adapted from Apell et al., 2023, with permission from Elsevier Ltd. © 2023 Elsevier Ltd.)

In Fig. 5.6, radial distributions of the mean absolute particle velocity $\bar{u}_\mathrm{p}$ and the standard deviation of the absolute particle velocity distribution s_{u_p} are shown. As can be seen, similar to the number median diameter $d_{0.5,n}$ presented in Fig. 5.4, the mean absolute particle velocity $\bar{u}_\mathrm{p}$ is highest in the center of the spray, but decreases with increasing radial coordinate r. In fact, on average, particles in the center of the spray are one order of magnitude faster than particles close to the edge of the spray. Furthermore, while not explicitly shown here, it has to be noted that the mean axial particle velocity $\bar{u}_\mathrm{p,ax}$ (i.e., in the z-direction) is up to two order of magnitude higher than the mean radial particle velocity $\bar{u}_\mathrm{p,rad}$ (i.e., in the r-direction). Indeed, the latter is negligibly small in the center of the spray and increases only slightly with increasing radial coordinate r, as would be expected for a radially symmetric spray with a small opening angle[2]. Interestingly, while the standard deviation of the absolute particle velocity distribution s_{u_p} also decreases in the outer

---

[2] Considering that the respective particle data has been obtained at an axial distance from the liquid nozzle z of 500 mm and that, in this plane, the spray cross-section has a diameter of about 180 mm, the spray opening angle can be estimated to be about 20°.

part of the spray, in contrast to the dispersion of the particle size, there is a local minimum in the center of the spray and a maximum at a radial coordinate r of about 20 mm. In contrast, Domnick et al. (1997, 1998) and Wolf and Bergmann (2002) have reported a reduced mean absolute particle velocity $\bar{u}_\mathrm{p}$ in the center of the spray for the atomization of pure copper, possibly due to a loss of gas momentum caused by the atomization process. Here, however, it has to be noted that these authors have employed a purely convergent gas nozzle design (see Section 2.1), which has been found by Anderson and Terpstra (2002) and Schwenck et al. (2017) to be less efficient than convergent-divergent designs such as the one described in Section 3.1.2.

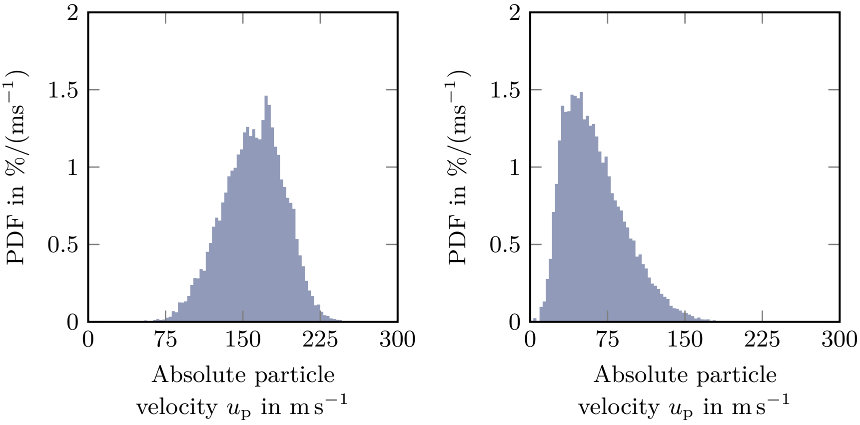

(a) $r = 0\,\mathrm{mm}$ **(b)** $r = 40\,\mathrm{mm}$

Figure 5.7: Absolute particle velocity distributions for a gas stagnation pressure $p_\mathrm{t,g}$ of (0.80 ± 0.05) MPa and a liquid mass flow rate $\dot{m}_\mathrm{l}$ of $(5.01 \pm 0.05)\,\mathrm{kg\,min^{-1}}$ at two different radial positions r. Shown are the discrete probability density functions.

Finally, for the same two radial coordinates r considered in Fig. 5.5, actual distributions of the absolute particle velocity u_p are shown in Fig. 5.7 as discrete probability density functions. As can be seen, while the distribution is almost symmetric in the center of the spray, it is characterized by a positive skewness in the outer part of the spray. This indicates that, even though the mean absolute particle velocity $\bar{u}_\mathrm{p}$ decreases with increasing radial coordinate

r, there is a small fraction of comparatively fast particles in the outer part of the spray. The fastest particles, however, are in the center of the spray, reaching up to $250\,\mathrm{m\,s^{-1}}$ for the set point of operation under consideration. In fact, for a gas stagnation pressure $p_{\mathrm{t,g}}$ of $1.6\,\mathrm{MPa}$, which corresponds to the highest gas stagnation pressure $p_{\mathrm{t,g}}$ considered in this experimental investigation (see Section 3.1.4), absolute particle velocities u_{p} as high as $380\,\mathrm{m\,s^{-1}}$ have been measured.

In conclusion, the spray produced by the supersonic close-coupled atomizer described in Section 3.1.2 has been found to feature a core region, which is characterized by the accumulation of comparatively large and fast particles. This is an important result, since, in the context of metal powder production, these large particles usually cannot be sold for the application in additive manufacturing. As a result, they determine the amount of post-treatment, such as sieving or winnowing, required to achieve the desired product quality. This, however, raises the production costs. Consequently, one of the aims of improving the supersonic close-coupled atomization process has to be to specifically influence the particle size in the center of the spray. This is further discussed in Section 5.3. Here, it is important to note that the obtained particle size and velocity data does not provide information about the history of the specific particles, which includes, for instance, the particle trajectory and the locations of breakup. In other words, a particle detected in the center of the spray may not necessarily have originated from the center downstream of the liquid nozzle.

5.2.2 Local Sensitivity

Having established in Section 5.2.1 that both the particle size and the particle velocity vary across the spray cross-section, it is instructive to investigate how the sensitivity of the particle statistics to changes in the set point of operation varies locally. This serves the purpose of identifying how the particle statistics can be influenced during the atomization process and is particularly important for the particle size, which, in the context of metal powder production, is a major determinant of the product quality.

As an example, in Fig. 5.8, the radial distribution of the change in the number median diameter $d_{0.5,n}$ for an increase in the liquid mass flow rate $\dot{m}_{\mathrm{l}}$ from $(4.07 \pm 0.05)\,\mathrm{kg\,min^{-1}}$ to $(6.01 \pm 0.04)\,\mathrm{kg\,min^{-1}}$ is shown. Here, the

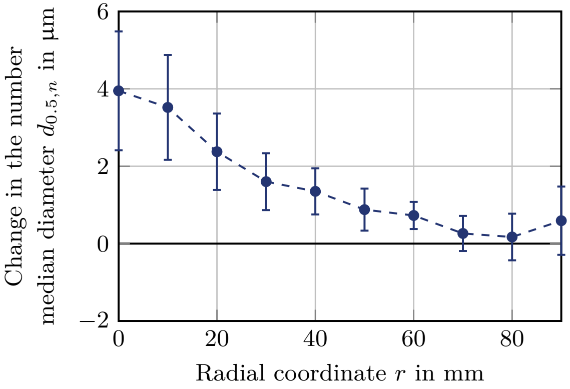

Figure 5.8: Radial distribution of the change in the number median diameter $d_{0.5,n}$ for an increase in the liquid mass flow rate $\dot{m}_\mathrm{l}$ from $(4.07 \pm 0.05)\,\mathrm{kg\,min^{-1}}$ to $(6.01 \pm 0.04)\,\mathrm{kg\,min^{-1}}$ and a constant gas stagnation pressure of $(0.80 \pm 0.05)\,\mathrm{MPa}$. The error bars correspond to the expanded standard uncertainty, employing a coverage factor K of 1.96. (Adapted from Apell et al., 2023, with permission from Elsevier Ltd. © 2023 Elsevier Ltd.)

gas stagnation pressure $p_{\mathrm{t,g}}$ has been kept constant at $(0.80 \pm 0.05)\,\mathrm{MPa}$ for both set points of operation. Additionally indicated are error bars, which correspond to the expanded standard uncertainty, employing a coverage factor K of 1.96 (see Section 3.2.4). As can be seen, the increase in the liquid mass flow rate $\dot{m}_\mathrm{l}$ results in an increase in the number median diameter $d_{0.5,n}$ over the entire spray cross-section. However, the absolute change is larger in the center of the spray than in the outer region, that is, it decreases gradually with increasing radial coordinate r. In fact, for radial coordinates r larger than 60 mm, the change is not significant relative to the measurement uncertainty. This correlates well with the fact that, in Fig. 5.4, the particle size has been found to be independent of the radial coordinate r in the outer region of the spray (i.e., for $r > 60\,\mathrm{mm}$). Qualitatively, these results have been found to be true for all set points of operation considered and, importantly, also for changes in the gas stagnation pressure $p_{\mathrm{t,g}}$. In other words, adjustments to the set point of operation provide means for affecting the size of the comparatively large particles, which accumulate in the center of the spray, and, therefore, for improving the product quality.

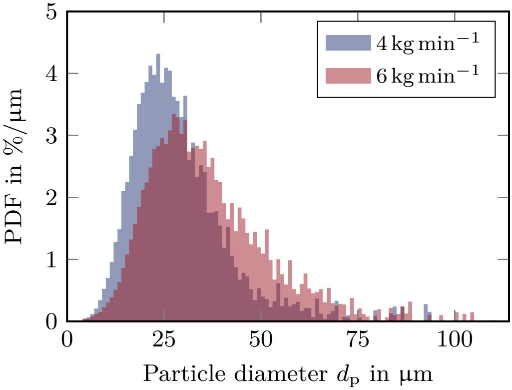

Figure 5.9: Comparison between two volume-weighted global particle size distributions obtained for a liquid mass flow rate $\dot{m}_\mathrm{l}$ of $(4.07 \pm 0.05)\,\mathrm{kg\,min^{-1}}$ and $(6.01 \pm 0.04)\,\mathrm{kg\,min^{-1}}$, respectively, and a constant gas stagnation pressure $p_\mathrm{t,g}$ of $(0.80 \pm 0.05)\,\mathrm{MPa}$. Shown are the discrete probability density functions.

However, it has to be noted that, so far, only local particle size distributions have been considered, which, when compared with each other, do not provide any information about the absolute number of particles n_p corresponding to a certain particle diameter d_p. As has been discussed in Section 3.2.3, this absolute number of particles n_p depends on many parameters, including the local particle flux, which, when approximated as the local data rate f_data, has been found to vary across the spray cross-section (see Fig. 5.2). Consequently, it is necessary to consider global particle size distributions, in order to make meaningful comparisons. For this reason, the global volume-weighted particle size distributions corresponding to the two set points of operation considered in Fig. 5.8 are compared in Fig. 5.9 as discrete probability density functions. These are of particular interest in the context of metal powder production, since they provide information about the mass m corresponding to a certain particle diameter d_p. As can be seen, the increase in the liquid mass flow rate $\dot{m}_\mathrm{l}$ from $(4.07 \pm 0.05)\,\mathrm{kg\,min^{-1}}$ to $(6.01 \pm 0.04)\,\mathrm{kg\,min^{-1}}$ results in significantly more mass m corresponding to comparatively larger particle diameters d_p. In fact, it corresponds to an increase in the global volume median diameter $\hat{d}_{0.5,V}$ from $(26.6 \pm 1.0)\,\mathrm{µm}$ to $(33.3 \pm 1.0)\,\mathrm{µm}$. In comparison, for the global number median diameter $\hat{d}_{0.5,n}$, the change in the set point of operation corresponds to an increases from $(14.7 \pm 0.4)\,\mu\mathrm{m}$ to $(16.2 \pm 0.4)\,\mu\mathrm{m}$.

To summarize, not only has the particle size in the center of the spray been found to be comparatively large relative to the particle size in other parts of the spray cross-section, but, in terms of absolute differences, it has also been shown to be most sensitive to changes in the set point of operation. Furthermore, these local sensitivities of the particle size to changes in the set point of operation have been found to directly translate into the global particle size distribution also being sensitive to changes in the set point of operation in a qualitatively similar manner. This suggests that local measurements, especially in the center of the spray, allow for estimating trends in the global particle size, that is, how it is affected by changes in the set point of operation. As a result, these effects on the particle size and velocity distributions are studied in more detail in Section 5.3.

5.3 Influence of the Operational Parameters

As has been established in Section 5.2, the atomization result is sensitive to changes in the set point of operation, which is defined by the gas stagnation pressure $p_{\mathrm{t,g}}$ and the liquid mass flow rate $\dot{m}_{\mathrm{l}}$ (see Section 3.1.4). Indeed, knowledge of the specific dependencies is not only important for achieving a desired powder quality when operating a powder production plant, but it is also necessary for validating suitable models predicting the atomization process. Due to its decoupled fluid supply lines, the research facility described in Section 3.1 allows for a systematic study of the influence of the set point of operation on the atomization result. For this purpose, phase Doppler measurements have been performed in the center of the spray (i.e., at $r = 0\,\mathrm{mm}$) for systematically varying set points of operation, using water as the working liquid.

5.3.1 Gas Stagnation Pressure

The effect of the gas stagnation pressure $p_{\mathrm{t,g}}$ on the particle size has been extensively studied in the existing literature. This is due to the fact that the gas stagnation pressure $p_{\mathrm{t,g}}$ is the operational parameter that is easiest to measure and adjust during the operation of a powder production plant. Among others, Mates and Settles (2005b) and Urionabarrenetxea et al. (2021)

have analyzed powders produced by the atomization of liquid tin and liquid copper, respectively. They have consistently reported that an increase in the gas stagnation pressure $p_{\mathrm{t,g}}$ results in a decrease in the particle size as well as in its dispersion. However, they have also found that, as the gas stagnation pressure $p_{\mathrm{t,g}}$ increases, the effectiveness of influencing the particle size decreases. In other words, further increases in the gas stagnation pressure $p_{\mathrm{t,g}}$ result in only comparatively small changes in the particle size.

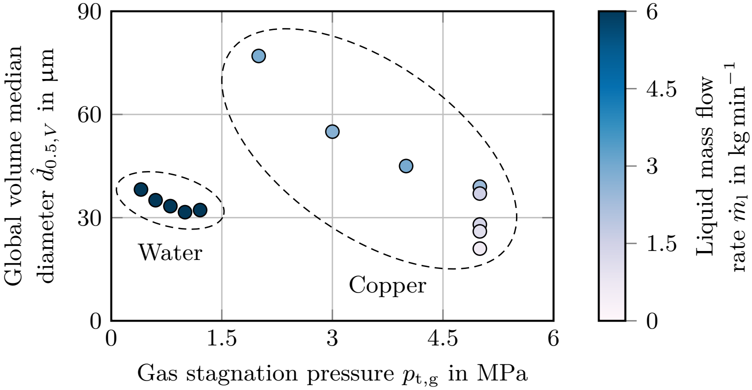

Figure 5.10: Global volume median diameter $\hat{d}_{0.5,V}$ as a function of the gas stagnation pressure $p_{\mathrm{t,g}}$. Shown are results obtained by Urionabarrenetxea et al. (2021) for powders produced by means of the atomization of pure copper using nitrogen as well as results obtained as part of this experimental investigation for the atomization of water using air. For the latter, the expanded standard uncertainty is smaller than the marker size.

Since the influence of the gas stagnation pressure $p_{\mathrm{t,g}}$ on the particle size has been extensively studied in the literature, it serves as a suitable means for validating whether the use of water as a substitute liquid allows the same trends observed for the atomization of liquid metals to be replicated (see Section 3.1.1). For this purpose, the global volume median diameter $\hat{d}_{0.5,V}$ obtained by Urionabarrenetxea et al. (2021) for powders produced by means of the atomization of liquid copper using nitrogen is shown as a function of the stagnation pressure $p_{\mathrm{t,g}}$ in Fig. 5.10. As can be seen, the global volume median diameter $\hat{d}_{0.5,V}$ decreases with increasing gas stagnation pressure $p_{\mathrm{t,g}}$. However, for a constant liquid mass flow rate $\dot{m}_{\mathrm{l}}$, it also appears to approach a lower limit. Additionally shown are exemplary results obtained as part of this experimental investigation for the atomization of water using air. Here, it is important to note that a direct quantitative comparison between the two data sets is not possible due to differences in the geometric design of the respective atomizer units. Still, qualitatively, both results show similar trends. Consequently, this supports the assumption made in Section 3.1.1 that water is a suitable substitute liquid for studying the resulting particle size.

The results reported by Urionabarrenetxea et al. (2021) show another important characteristic common for studies investigating the supersonic close-coupled atomization process. As can be seen in Fig. 5.10, the liquid mass flow rate $\dot{m}_\mathrm{l}$, which has not been measured, but, instead, has been estimated as a time average based on the total mass of atomized liquid copper m_l and the duration of the atomization process, varies strongly. Indeed, even for a seemingly constant gas stagnation pressure $p_\mathrm{t,g}$ of 5 MPa, the liquid mass flow rate $\dot{m}_\mathrm{l}$ differs by up to 1.9 kg min^{-1}. This is due to the fact that the liquid mass flow rate $\dot{m}_\mathrm{l}$ is sensitive to changes in the gas stagnation pressure $p_\mathrm{t,g}$, as has been discussed in Section 4.3.1. In contrast, the experimental

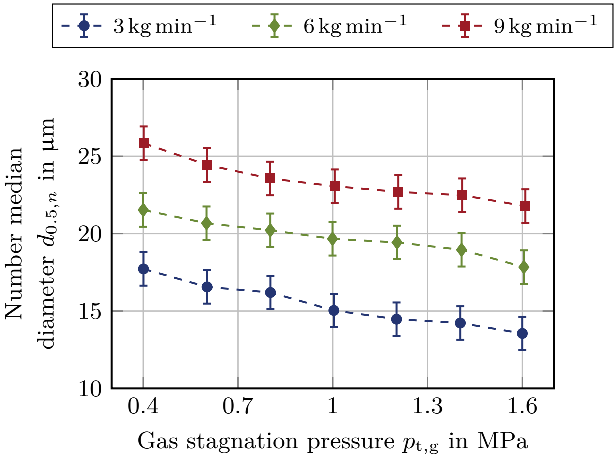

Figure 5.11: Number median diameter $d_{0.5,n}$ as a function of the gas stagnation pressure $p_\mathrm{t,g}$ for three different liquid mass flow rates $\dot{m}_\mathrm{l}$ in the center of the spray. The error bars correspond to the expanded standard uncertainty, employing a coverage factor K of 1.96.

data obtained for water is characterized by a constant liquid mass flow rate $\dot{m}_\mathrm{l}$. This emphasizes the importance of a suitable control system in the liquid supply line (see Section 3.1.3) when systematically investigating the atomization process.

In Fig. 5.11, the number median diameter $d_{0.5,n}$ in the center of the spray (i.e., at $r = 0\,\mathrm{mm}$) is shown as a function of the gas stagnation pressure $p_\mathrm{t,g}$ for three different liquid mass flow rates $\dot{m}_\mathrm{l}$ (i.e., for $3\,\mathrm{kg\,min^{-1}}$, $6\,\mathrm{kg\,min^{-1}}$ and $9\,\mathrm{kg\,min^{-1}}$), which cover the entire range considered as part of this experimental investigation (see Section 3.1.4). Consistent with the considerations discussed so far, the number median diameter $d_{0.5,n}$ decreases with increasing gas stagnation pressure $p_\mathrm{t,g}$, independent of the respective liquid mass flow rate $\dot{m}_\mathrm{l}$. However, compared to the volume-weighted statistics, which are particularly sensitive to the proportion of the larger particles due to the cubic relationship between the particle diameter d_p and the particle volume V_p, the absolute change is rather small. This is in good agreement with the results presented by Thompson et al. (2016) for metal powders.

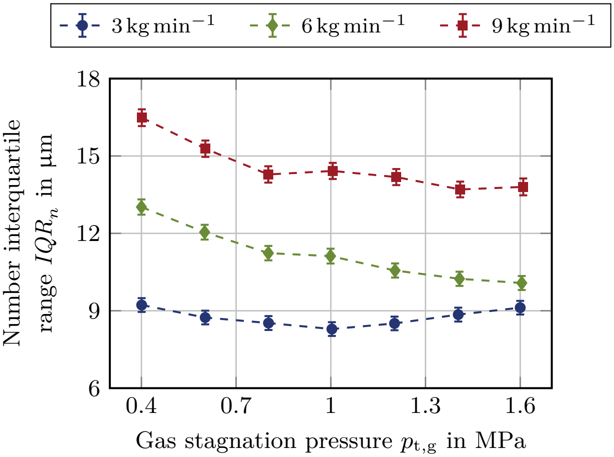

Figure 5.12: Number interquartile range IQR_n as a function of the gas stagnation pressure $p_\mathrm{t,g}$ for three different liquid mass flow rates $\dot{m}_\mathrm{l}$ in the center of the spray. The error bars correspond to the expanded standard uncertainty, employing a coverage factor K of 1.96.

Similarly, the number interquartile ranges IQR_n corresponding to the set points of operation considered in Fig. 5.11 are shown in Fig. 5.12. For the two highest liquid mass flow rates $\dot{m}_\mathrm{l}$ considered (i.e., for $6\,\mathrm{kg\,min^{-1}}$ and $9\,\mathrm{kg\,min^{-1}}$), the results are consistent with the findings in the literature. That is, the dispersion of the particle size initially decreases with increasing gas stagnation pressure $p_\mathrm{t,g}$, but is barely affected for higher gas stagnation pressures $p_\mathrm{t,g}$. Notably, for the lowest liquid mass flow rate $\dot{m}_\mathrm{l}$ of $3\,\mathrm{kg\,min^{-1}}$, the effect of the gas stagnation pressure $p_\mathrm{t,g}$ on the number interquartile range IQR_n is rather small and, for high gas stagnation pressures $p_\mathrm{t,g}$, even opposite to the other results. That is, the dispersion of the particle size increases slightly. The former is likely due to the fact that the overall particle size is already particularly small, leaving little potential for further reduction in its dispersion. Similarly, the increase in the number interquartile range IQR_n can also be attributed to the comparatively large number of the particularly small particles, which have been found to be difficult to detect and validate using the phase Doppler measurement setup described in Section 3.2.1, leading to an underestimation. In fact, for the set point of operation characterized by a gas stagnation pressure $p_\mathrm{t,g}$ of $(1.60 \pm 0.10)\,\mathrm{MPa}$ and a liquid mass flow

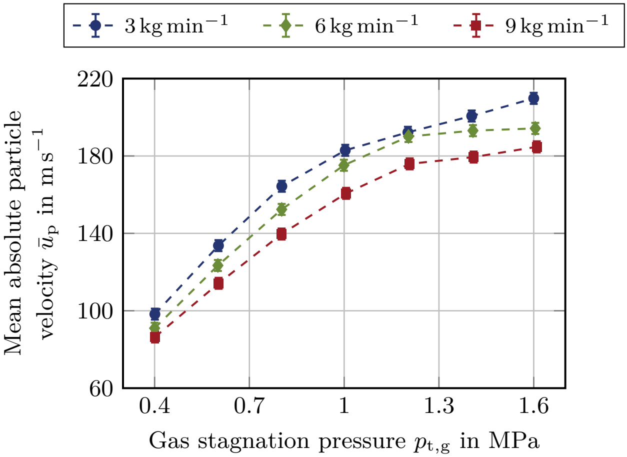

Figure 5.13: Mean absolute particle velocity $\bar{u}_\mathrm{p}$ as a function of the gas stagnation pressure $p_\mathrm{t,g}$ for three different liquid mass flow rates $\dot{m}_\mathrm{l}$ in the center of the spray. The error bars correspond to the expanded standard uncertainty, employing a coverage factor K of 1.96.

rate $\dot{m}_\mathrm{l}$ of $(2.99 \pm 0.12)\,\mathrm{kg\,min^{-1}}$, which corresponds to the smallest number median diameter $d_{0.5,n}$ in Fig. 5.11, the sphericity validation $\vartheta_\mathrm{sphere}$ has been found to be reduced to 54 % (see Fig. 5.3), possibly due to the planar system erroneously detecting negative phase differences $\Delta\Phi_{12,\mathrm{pl}}$, as has been described in Section 3.2.1.

Finally, in Fig. 5.13, the mean absolute particle velocity $\bar{u}_\mathrm{p}$ is shown for the same set points of operation. As can be seen, an increase in the gas stagnation pressure $p_\mathrm{t,g}$ results in an increase in the mean absolute particle velocity $\bar{u}_\mathrm{p}$. However, for gas stagnation pressures $p_\mathrm{t,g}$ higher than about 1.2 MPa, the increase becomes less pronounced. Furthermore, with increasing liquid mass flow rate $\dot{m}_\mathrm{l}$, which corresponds to an increasing particle size (see Figs. 5.11 and 5.12), the mean absolute particle velocity $\bar{u}_\mathrm{p}$ decreases. This is reasonable, considering that an increased liquid mass loading weakens the gas jet and that small particles are accelerated faster due to lower inertia (Amatriain et al., 2022; Ünal, 1989b).

In conclusion, the gas stagnation pressure $p_\mathrm{t,g}$ has been shown to provide means to influence the particle size in the center of the spray, which, in the context of metal powder production, is crucial for the product quality (see Sections 5.2.1 and 5.2.2).

5.3.2 Liquid Mass Flow Rate

As has already been established (see Section 4.3.1), for the atomization of liquid metal, the liquid mass flow rate $\dot{m}_\mathrm{l}$ is difficult to accurately set, maintain and measure, making systematic studies challenging to conduct in the context of metal powder production. On the other hand, it is an important parameter, as it directly determines the powder production rate. As a result, it is of economic interest to increase the liquid mass flow rate $\dot{m}_\mathrm{l}$ as much as possible, provided that neither the powder quality nor the process stability is adversely affected. However, Biancaniello et al. (1990) and Allimant et al. (2009) have suggested that increasing the liquid mass loading of the flow field results in a lower yield of fine powder. Consequently, the effect on the particle size is studied in detail in the following.

For three different gas stagnation pressures $p_\mathrm{t,g}$ (i.e., for 0.4 MPa, 1.0 MPa and 1.6 MPa), which cover the entire range considered as part of this experimental investigation (see Section 3.1.4), the number median diameter $d_{0.5,n}$ is

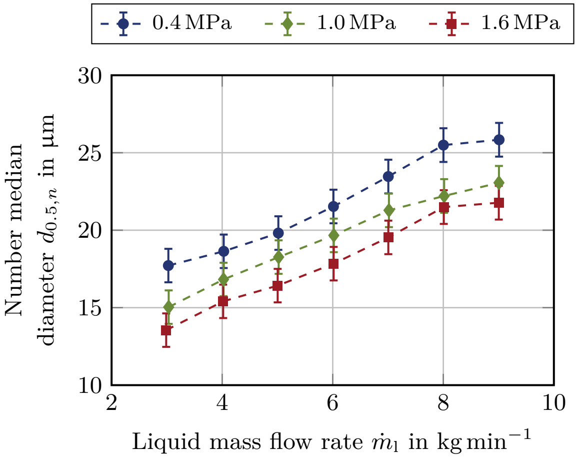

Figure 5.14: Number median diameter $d_{0.5,n}$ as a function of the liquid mass flow rate $\dot{m}_\mathrm{l}$ for three different gas stagnation pressures $p_\mathrm{t,g}$ in the center of the spray. The error bars correspond to the expanded standard uncertainty, employing a coverage factor K of 1.96.

shown as a function of the liquid mass flow rate $\dot{m}_\mathrm{l}$ in Fig. 5.14. The data has been obtained in the center of the spray (i.e., at $r = 0\,\mathrm{mm}$). As can be seen, independent of the respective gas stagnation pressure $p_\mathrm{t,g}$, the number median diameter $d_{0.5,n}$ increases with increasing liquid mass flow rate $\dot{m}_\mathrm{l}$. Notably, the relationship appears to be almost linear, which is in good agreement with the results published by Ünal (1987), Urionabarrenetxea et al. (2013, 2014, 2021) and Thompson et al. (2016) for different metal powders. Furthermore, for the set points of operation considered, the number median diameter $d_{0.5,n}$ is more sensitive to changes in the liquid mass flow rate $\dot{m}_\mathrm{l}$ than to changes in the gas stagnation pressure $p_\mathrm{t,g}$. This is even more emphasized for the volume median diameter $d_{0.5,V}$, which is not explicitly shown here, but can be seen from Fig. 5.9.

In Fig. 5.15, the number interquartile range IQR_n is presented for the same set points of operation considered in Fig. 5.14, showing a dependence on the liquid mass flow rate $\dot{m}_\mathrm{l}$ similar to the number median diameter $d_{0.5,n}$. That is, an increase in the liquid mass flow rate $\dot{m}_\mathrm{l}$ results in an increase in the dispersion of the particle size, which appears to follow a linear relationship.

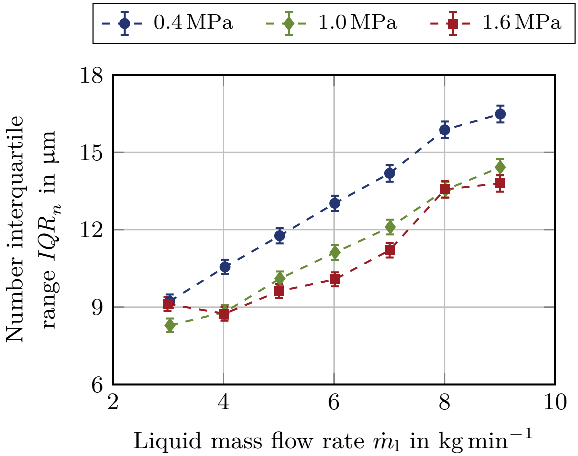

Figure 5.15: Number interquartile range IQR_n as a function of the liquid mass flow rate $\dot{m}_\mathrm{l}$ for three different gas stagnation pressures $p_\mathrm{t,g}$ in the center of the spray. The error bars correspond to the expanded standard uncertainty, employing a coverage factor K of 1.96.

Possibly an outlier can be seen for a set point of operation characterized by a gas stagnation pressure $p_\mathrm{t,g}$ of (1.60 ± 0.10) MPa and a liquid mass flow rate $\dot{m}_\mathrm{l}$ of $(2.99 \pm 0.12)\,\mathrm{kg\,min^{-1}}$. This has already been discussed in Section 5.3.1 and is likely due to difficulties in resolving particularly small particles using the phase Doppler measurement system described in Section 3.2.1. In general, qualitatively similar results for the relationship between the dispersion of the particle size and the liquid mass flow rate $\dot{m}_\mathrm{l}$ have been observed by Ünal (1987) for the atomization of an aluminum alloy using different inert gases.

As has been described in Section 4.3.2, for a constant liquid nozzle diameter d_l, a change in the liquid mass flow rate $\dot{m}_\mathrm{l}$ corresponds to a change in the liquid momentum flux at the liquid nozzle exit $q_\mathrm{l,e}$. Interestingly, the latter has been found to affect the spray formation in close proximity to the liquid nozzle (see Figs. 4.16 and 4.17). Consequently, it is instructive to investigate whether the changes in the particle size observed in Figs. 5.14 and 5.15 are due to changes in the liquid mass flow rate $\dot{m}_\mathrm{l}$ or due to changes in the liquid momentum flux at the liquid nozzle exit $q_\mathrm{l,e}$. For this purpose, experimental data has been obtained for identical set points of operation, but using liquid nozzles featuring different liquid nozzle diameters d_l (see Section 3.1.2).

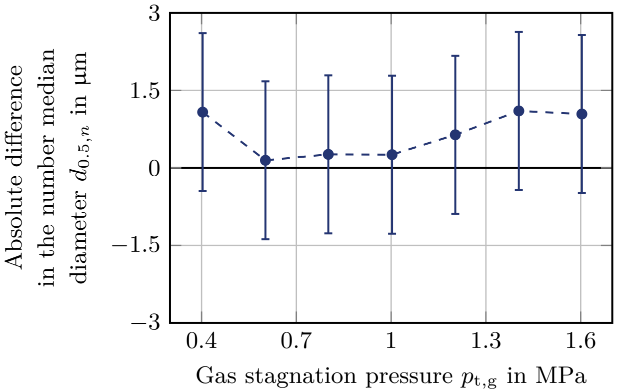

Figure 5.16: Absolute difference in the number median diameter $d_{0.5,n}$ as a function of the gas stagnation pressure $p_\mathrm{t,g}$ for a constant liquid mass flow rate $\dot{m}_\mathrm{l}$ of 5 kg min^{-1} in the center of the spray. The liquid nozzle diameters d_l considered are 3 mm and 5 mm. The error bars correspond to the expanded standard uncertainty, employing a coverage factor K of 1.96. (Adapted from Apell et al., 2023, with permission from Elsevier Ltd. © 2023 Elsevier Ltd.)

As an example, considering liquid nozzle diameters d_l of 3 mm and 5 mm, the absolute difference in the number median diameter $d_{0.5,n}$ is shown as a function of the gas stagnation pressure for a constant liquid mass flow rate $\dot{m}_\mathrm{l}$ of 5 kg min^{-1} in Fig. 5.16. As a reference, changing the liquid nozzle diameter d_l from 3 mm to 5 mm corresponds to a decrease in the liquid momentum flux at the liquid nozzle exit $q_\mathrm{l,e}$ of 87 % (see Fig. 4.18). However, as can be seen, the absolute difference in the number median diameter $d_{0.5,n}$ is not significant relative to the measurement uncertainty. Similar results have been obtained for the dispersion of the particle size and for other set points of operation considered. Furthermore, it is consistent with the findings by Li et al. (2019) and Costa da Silva et al. (2022) for the atomization of aluminum alloys and stainless steel, respectively. Consequently, this is an indication that the influence of the liquid momentum flux at the liquid nozzle exit $q_\mathrm{l,e}$ on the spray formation in close proximity to the liquid nozzle, which has been discussed in Section 4.3.2, does not affect the particle size. Instead, along with the gas stagnation pressure $p_\mathrm{t,g}$, the actual liquid mass flow rate $\dot{m}_\mathrm{l}$ appears to be the main determinant.

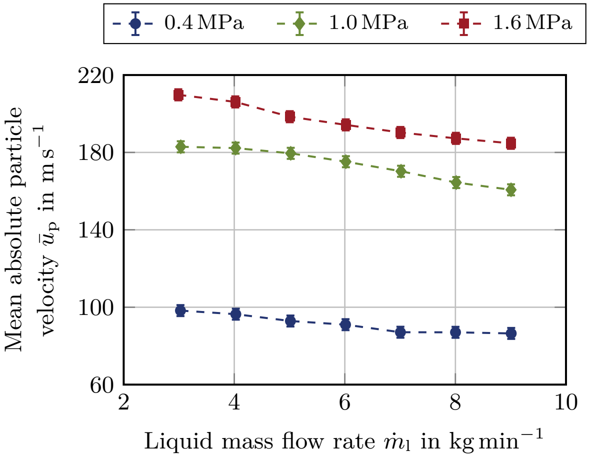

Figure 5.17: Mean absolute particle velocity $\bar{u}_\mathrm{p}$ as a function of the liquid mass flow rate $\dot{m}_\mathrm{l}$ for three different gas stagnation pressures $p_\mathrm{t,g}$ in the center of the spray. The error bars correspond to the expanded standard uncertainty, employing a coverage factor K of 1.96.

Finally, the mean absolute particle velocity $\bar{u}_\mathrm{p}$ is shown in Fig. 5.17 for the same set points of operation considered in Figs. 5.14 and 5.15. As has already been observed in Fig. 5.13, an increase in the liquid mass flow rate $\dot{m}_\mathrm{l}$ results in a decrease in the absolute mean particle velocity $\bar{u}_\mathrm{p}$. However, the absolute mean particle velocity $\bar{u}_\mathrm{p}$ is more sensitive to changes in the gas stagnation pressure $p_\mathrm{t,g}$.

To conclude, the liquid mass flow rate $\dot{m}_\mathrm{l}$ has been found to be an important parameter in determining the particle size. In fact, reducing the liquid mass flow rate $\dot{m}_\mathrm{l}$ has been shown to be an effective means for achieving a smaller and less dispersed particle size. However, in the context of metal powder production, this improvement comes at the cost of a reduced production rate. Furthermore, it increases the risk of the liquid nozzle freezing, as has been explained in Section 4.1.2, potentially reducing the process stability.

5.3.3 Gas-to-liquid Ratio

Finally, using the definition of the gas-to-liquid ratio GLR given in Eq. (2.6), the gas stagnation pressure $p_{\mathrm{t,g}}$ and the liquid mass flow rate $\dot{m}_{\mathrm{l}}$ can be combined into a single parameter describing the set point of operation. This is possible, since the gas mass flow rate $\dot{m}_{\mathrm{g}}$ is directly proportional to the gas stagnation pressure $p_{\mathrm{t,g}}$, as has been shown in Section 4.1.1. Not only is the gas-to-liquid ratio GLR used as a measure of the efficiency of the atomization process, but it is also often employed for modeling the atomization result. An example for this is the empirical model proposed by Lubanska (1970) (see Section 2.2.2). Consequently, it is interesting to investigate how the gas-to-liquid ratio GLR affects the particle size.

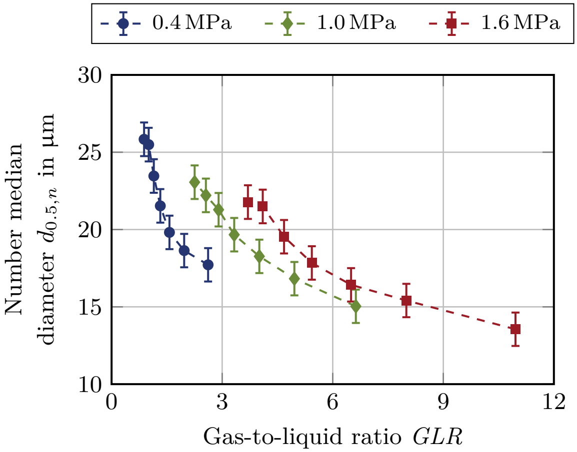

Figure 5.18: Number median diameter $d_{0.5,n}$ as a function of the gas-to-liquid ratio GLR for three different gas stagnation pressures $p_{\mathrm{t,g}}$ in the center of the spray. The error bars correspond to the expanded standard uncertainty, employing a coverage factor K of 1.96.

In Fig. 5.18, the number median diameter $d_{0.5,n}$ is shown as a function of the gas-to-liquid GLR for three different gas stagnation pressures $p_{\mathrm{t,g}}$ (i.e., for 0.4 MPa, 1.0 MPa and 1.6 MPa). This corresponds to the same data already presented in Fig. 5.11. A can be seen, an increase in the gas-to-liquid ratio GLR, that is, an operation of the atomizer in less efficient condition, results in a decrease in the number median diameter $d_{0.5,n}$. However, for particularly high gas-to-liquid ratios *GLR*, the number median diameter $d_{0.5,n}$ appears to approach a lower limit. In other words, it becomes less and less efficient to reduce the particle size further (Ünal, 2007a, 2007b). Notably, the number median diameter $d_{0.5,n}$ is not an unambiguous function of the gas-to-liquid ratio *GLR*, which is in good agreement with the results published by Park et al. (1996). In fact, it is possible to achieve the same number median diameter $d_{0.5,n}$ for different gas-to-liquid ratios *GLR*, depending on the specific gas stagnation pressure $p_{\mathrm{t,g}}$ and liquid mass flow rate $\dot{m}_{\mathrm{l}}$.

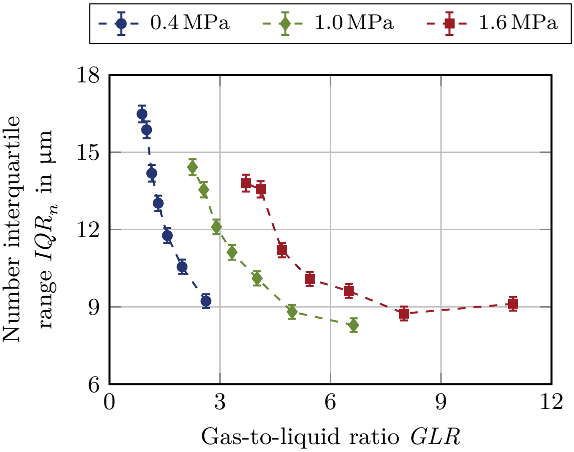

Figure 5.19: Number interquartile range IQR_n as a function of the gas-to-liquid ratio *GLR* for three different gas stagnation pressures $p_{\mathrm{t,g}}$ in the center of the spray. The error bars correspond to the expanded standard uncertainty, employing a coverage factor K of 1.96.

In regard to the dispersion of the particle size, the number interquartile range IQR_n is shown in Fig. 5.19 for the same set points of operation. The results are similar to the findings discussed for the number median diameter $d_{0.5,n}$. That is, an increasing gas-to-liquid ratio *GLR* results in a decreasing dispersion of the particle size, approaching a lower limit. Furthermore, the number interquartile range IQR_n is not an unambiguous function of the gas-to-liquid ratio *GLR*.

In conclusion, the gas-to-liquid ratio *GLR* has been found not to be suited for describing the set point of operation as a single operational parameter, which confirms the assumption made by Urionabarrenetxea et al. (2021). This is an important result, because it shows that the gas-to-liquid ratio GLR alone does not encompass any physical understanding of the atomization process. This is reasonable, since it does not contain any information about the local flow field and the interaction between the gas flow and the liquid flow. As a consequence, it is necessary to include both the gas stagnation pressure $p_{\mathrm{t,g}}$ and the liquid mass flow rate $\dot{m}_{\mathrm{l}}$ separately in models describing the atomization process. Furthermore, in Section 4.1.3, the question has been raised whether the aspiration pressure p_{asp} has any significance for the atomizer performance. However, as has been shown in Figs. 5.18 and 5.19, there is not one specific set point of operation that corresponds to the greatest refinement of the particle size. Instead, different combinations of the gas stagnation pressure $p_{\mathrm{t,g}}$ and the liquid mass flow rate $\dot{m}_{\mathrm{l}}$ can lead to the same atomization result. This indicates that the aspiration pressure p_{asp} does not determine the particle size.

5.4 Influence of the Liquid Dynamic Viscosity

The atomization of liquids is commonly described in terms of the dominant forces acting on the liquid (see Section 4.2.2). In the context of two-fluid gas atomization processes, which also include the supersonic close-coupled atomization under investigation, these forces are the aerodynamic force due to the additional gas flow, surface tension forces and viscous forces (Lefebvre & McDonell, 2017). Consequently, physics-based models describing the atomization process have to take into account these forces. However, the significance of the individual forces on the atomization result is not known a priori. The surface tension forces and the viscous forces, in particular, depend on the physical properties of the working liquid, that is, on the surface tension σ and the liquid dynamic viscosity μ_{l}, respectively. For the atomization of liquid metals, these properties can be influenced by varying the liquid superheat ΔT_{l} (Urionabarrenetxea et al., 2021). However, this has the disadvantage that both the surface tension σ and the liquid dynamic viscosity μ_{l} are affected at the same time, making it difficult to study the separate influence of each liquid property. For this experimental investigation, this difficulty has been resolved by considering a number of different working liquids (see Section 3.1.4). In particular, the influence of the liquid dynamic viscosity μ_l on the resulting particle size is studied in the following.

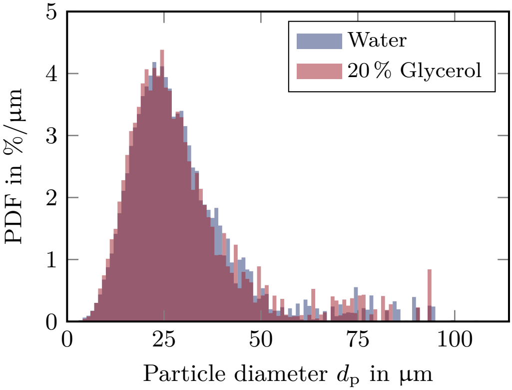

Figure 5.20: Comparison between two volume-weighted global particle size distributions obtained using two different working liquids for a constant gas stagnation pressure $p_\mathrm{t,g}$ of 1.0 MPa and a constant liquid mass flow rate $\dot{m}_\mathrm{l}$ of 4 kg min^{-1}. Considered as the working liquids are water and an aqueous glycerol solution with a glycerol mass fraction of 20 %. Shown are the discrete probability density functions.

In Fig. 5.20, two volume-weighted global particle size distributions are compared, which have been obtained using water and an aqueous glycerol solution with a glycerol mass fraction of 20 %. Compared to water, the latter is characterized by an increase in the liquid dynamic viscosity μ_l of 74 % (see Table 3.1). The relative differences in the liquid density ρ_l and in the surface tension σ compared to water, on the other hand, are less than 6 % and, therefore, assumed to be negligible (see Table 3.1). Furthermore, the two corresponding set points of operation are characterized by a gas stagnation pressure $p_\mathrm{t,g}$ of (1.00 ± 0.06) MPa and (1.00 ± 0.06) MPa, respectively, and by a liquid mass flow rate $\dot{m}_\mathrm{l}$ of (4.01 ± 0.06) kg min^{-1} and (4.00 ± 0.01) kg min^{-1}, respectively, exhibiting negligible differences. As can be seen, the two particle size distributions are virtually identical. In fact, the absolute differences in the global volume median diameter $\hat{d}_{0.5,V}$ and the global volume interquartile range $I\hat{Q}R_V$ are (0.4 ± 1.4) µm and (0.1 ± 2.0) µm, respectively. In terms of the number-weighted global particle size statistics, the differences in the global number median diameter $\hat{d}_{0.5,n}$ and the global number interquartile range $I\hat{Q}R_n$ are (0.1 ± 0.6) µm and (0.8 ± 1.4) µm, respectively. This suggests that the particle size is not sensitive to changes in the liquid dynamic viscosity μ_l, at least in the parameter range considered. That is, for the two particle size distributions shown in Fig. 5.20, the corresponding liquid Reynolds numbers Re_l, as defined in Eq. (2.3), are $19\,800 \pm 300$ for water and $10\,110 \pm 90$ for the 20 % aqueous glycerol solution. However, similar results have also been obtained for the other set points of operation considered.

In order to confirm these findings, a second aqueous glycerol solution has been considered, which is characterized by a glycerol mass fraction of 40 %. This corresponds to an increase in the liquid dynamic viscosity μ_l of 268 % compared to water (see Table 3.1). In comparison, the relative differences in the liquid density ρ_l and the surface tension σ are at least one order of magnitude smaller and, therefore, assumed to be negligible.

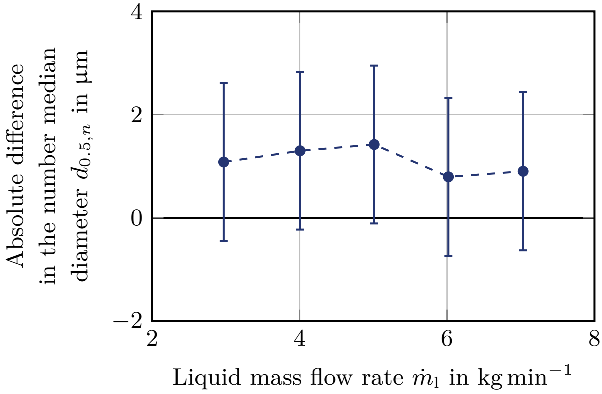

Figure 5.21: Absolute difference in the number median diameter $d_{0.5,n}$ between two different working liquids as a function of the liquid mass flow rate $\dot{m}_\mathrm{l}$ for a constant gas stagnation pressure $p_\mathrm{t,g}$ of 1.2 MPa in the center of the spray. The working liquids considered are water and an aqueous glycerol solution with a glycerol mass fraction of 40 %. The error bars correspond to the expanded standard uncertainty, employing a coverage factor K of 1.96. (Adapted from Apell et al., 2023, with permission from Elsevier Ltd. © 2023 Elsevier Ltd.)

As an example, for a constant gas stagnation pressure $p_\mathrm{t,g}$ of 1.2 MPa, the absolute difference in the number media diameter $d_{0.5,n}$ is shown as a function of the liquid mass flow rate $\dot{m}_\mathrm{l}$ in Fig. 5.21. The data has been obtained in the center of the spray (i.e., at $r = 0\,\mathrm{mm}$). As can be seen, the results are similar to those presented in Fig. 5.20 for the lower glycerol mass fraction of 20 %. That is, the measured absolute difference in the number median diameter is not significant relative to the measurement uncertainty. Similar results have also been obtained for the volume median diameter $d_{0.5,V}$. Notably, the lowest liquid Reynolds number Re_l considered here, which corresponds to a liquid mass flow rate $\dot{m}_\mathrm{l}$ of $(3.00 \pm 0.03)\,\mathrm{kg\,min^{-1}}$, is 3940 ± 40.

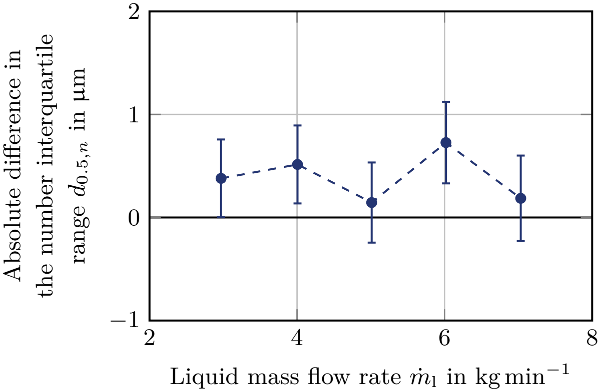

Figure 5.22: Absolute difference in the number interquartile range IQR_n between two different working liquids as a function of the liquid mass flow rate $\dot{m}_\mathrm{l}$ for a constant gas stagnation pressure $p_\mathrm{t,g}$ of 1.2 MPa in the center of the spray. The working liquids considered are water and an aqueous glycerol solution with a glycerol mass fraction of 40 %. The error bars correspond to the expanded standard uncertainty, employing a coverage factor K of 1.96. (Adapted from Apell et al., 2023, with permission from Elsevier Ltd. © 2023 Elsevier Ltd.)

Finally, in Fig. 5.22, the absolute difference in the number interquartile range IQR_n is shown obtained for the same set points of operation and working liquids. As can be seen, while the absolute difference is indeed significant relative to the measurement uncertainty for some of the set points of operation considered, it is in general small (i.e., below 1 µm). Consistent with the results shown in Fig. 5.20, this indicates that the liquid dynamic viscosity μ_l is not a major determinant of the dispersion of the particle size.

To conclude, the experimental results obtained indicate that, for the parameter range considered, the effect of the liquid dynamics viscosity μ_l on the particle size is negligibly small. In terms of the dimensionless liquid Reynolds number Re_l, as defined in Eq. (2.3), this appears to be true for values larger than at least 3900, which are indeed typical for the supersonic close-coupled atomization process (see Section 3.1.1). This is an important result, since it suggests that models describing the atomization process have to take into account neither the liquid dynamic viscosity μ_l nor the liquid Reynolds number Re_l. Considering that, for Ohnesorge numbers Oh lower than 0.1, the effects of liquid dynamic viscosity μ_l on droplet breakup have been found to be small, this is reasonable (Hsiang & Faeth, 1992). In fact, the Ohnesorge number Oh during the supersonic close-coupled atomization process is typically orders of magnitude lower than 0.1 (see Section 3.1.1) (Markus & Fritsching, 2006). Finally, these results may be an indication that, in comparison to the liquid dynamic viscosity μ_l, the surface tension σ or, more precisely, the gas Weber number We_g, as defined in Eq. (2.4), is a more important parameter influencing the atomization process. A similar conclusion has been reached by Bradley (1973a, 1973b) by means of a stability analysis and by Park et al. (1996) following an energy balance model. Indeed, Thompson et al. (2016) and Zhang et al. (2021) have observed a dependence of the particle size on the surface tension σ for the numerical simulation of the atomization of liquid metal.

5.5 Discussion of Empirical Atomization Models

Based on the experimental results presented in Sections 5.3 and 5.4, the particle size resulting form the supersonic close-coupled atomization process can be seen to be influenced by the set point of operation, defined by the gas stagnation pressure $p_\mathrm{t,g}$ and the liquid mass flow rate $\dot{m}_\mathrm{l}$, but not by the liquid dynamic viscosity μ_l. Furthermore, the particle size appears not to be an unambiguous function of the gas-to-liquid ratio GLR and, for a constant liquid mass flow rate $\dot{m}_\mathrm{l}$, it seems to not depend on the liquid nozzle diameter d_l. In fact, the latter questions the use of this geometric dimension as the characteristic length scale l for describing the supersonic close-coupled atomization process.

Having established which parameters affect the resulting particle size, this allows for a brief discussion of how well suited the empirical models introduced in Section 2.2.2 are for predicting the atomization result. For this purpose only qualitative trends are employed in the following.

To begin with, the model proposed by Lubanska (1970) relates the particle size to the liquid nozzle diameter d_l and explicitly depends on the liquid dynamic viscosity μ_l and the gas-to-liquid ratio GLR. Given that the fit of the correlation is based only on a single proportionality constant, it is unlikely to accurately predict the resulting particle size. In fact, Urionabarrenetxea et al. (2021) have found poor agreement with experimental data obtained for the atomization of molten metal. Similarly, Costa da Silva et al. (2022) have reported a need for improvements to be made to the correlation. Indeed, the extension of the model by Rao and Mehrotra (1981) has been found to result in a better fit by Urionabarrenetxea et al. (2021). This is due to the additional fitting parameter.

Furthermore, the empirical model proposed by Kishidaka (1972) and adapted by Urionabarrenetxea et al. (2021) depends on parameters similar to those used by Lubanska (1970). As a result, it also does not fully capture the trends in the particle size described above. However, Urionabarrenetxea et al. (2021) have found an improved agreement with their experimental data for the atomization of molten metal. This is reasonable considering that the correlation is based on a total of four fitting parameters, allowing for an improved weighting of the input parameters.

In contrast, the model adapted by Anderson and Achelis (2017), which is based on the work of Adelberg (1968) and Ingebo (1981), does not explicitly depend on the gas-to-liquid ratio GLR. However, it still depends on the liquid nozzle diameter d_l and the liquid dynamic viscosity μ_l, suggesting that it does not fully capture the trends in the particle size described above. In fact, Anderson and Achelis (2017) have reported poor agreement with data obtained for the atomization of molten metal.

Finally, modeling approaches solely based on the gas-to-liquid ratio GLR, such as the one proposed by Kamenov et al. (2021), present an inaccurate description of the atomization process. This is reasonable considering that the gas-to-liquid ratio GLR alone does not encompass any physical understanding of the atomization process, as it does not contain information about the local fluid flow fields and their interaction, which are crucial for the atomization.

In conclusion, the above considerations suggest that none of the empirical models introduced in Section 2.2.2 fully capture the qualitative trends observed in the experimentally obtained particle size. However, the model proposed by Kishidaka (1972) and adapted by Urionabarrenetxea et al. (2021) is likely to result in the most accurate prediction of the particle size, which is due to the increased number of fitting parameters. Consequently, there is a need for an improved empirical correlation between the resulting particle size and the operational parameters, the physical fluid properties and the geometric dimensions characteristic of the supersonic close-coupled atomization process. This is especially true considering that empirical models generally are a useful tool for obtaining a first estimate of the resulting particle size.

5.6 Summary and Conclusions

In this chapter, the spray produced by the supersonic close-coupled atomizer described in Section 3.1.2 has been investigated in terms of the resulting particle size and velocity distributions by means of the phase Doppler measurement technique discussed in Section 3.2.

Concerning the spray structure, the particle size has been found to be largest and most dispersed in the center of the fully developed spray and to gradually decrease with increasing radial distance. Consequently, influencing the center of the spray has been determined to be most critical for improving the quality of the powders produced by means of the supersonic close-coupled atomization process. However, the core region of the spray has also been shown to be most sensitive to changes in the set point of operation. In general, the particle size has been observed to follow a log-normal distribution. Regarding the particle velocity, the particles have been found to be one order of magnitude faster in the center of the spray than in the outer parts.

In terms of the influence of the operational parameters on the atomization result, consistent with the available data from the existing literature, the gas stagnation pressure $p_{\mathrm{t,g}}$ has been found to provide means for reducing the particle size as well as its dispersion. However, the particle size has also been shown to be more sensitive to changes in the liquid mass flow rate $\dot{m}_{\mathrm{l}}$. That is, an increase in the liquid mass flow rate $\dot{m}_{\mathrm{l}}$, which corresponds to an increase in the production rate, has been observed to result in an increase in the particle size as well as in its dispersion. Therefore, this is in conflict with economic interests. Notably, the liquid momentum flux at the liquid nozzle exit $q_{\mathrm{l,e}}$, which has been seen to affect the spray formation in close proximity to the liquid nozzle in Section 4.3.2, has been found to have negligible influence on the particle size. Finally, the particle size has been determined not to be an unambiguous function of the gas-to-liquid ratio GLR, which calls its use for modeling the atomization process into question.

In regard to the physical liquid properties, for liquid Reynolds numbers Re_{l} typical for the supersonic close-coupled atomization process, the effect of the liquid dynamic viscosity μ_{l} on the particle size has been shown to be negligibly small, suggesting that it does not have to be taken into account for modeling the atomization process.

Finally, the dependencies of the particle size on the operational parameters and the physical properties of the liquid obtained from these results have been found not to agree well with the predictions made employing the existing empirical models introduced in Section 2.2.

In conclusion, it has been found that the set point of operation defined by the gas stagnation pressure $p_{\mathrm{t,g}}$ and the liquid mass flow rate $\dot{m}_{\mathrm{l}}$ provides means for influencing the resulting particle size. This means that the particle size distribution is determined by the specific combination of these two parameters. Indeed, this is an important finding, especially since existing powder production plants often do not allow for actively influencing the liquid mass flow rate $\dot{m}_{\mathrm{l}}$. In addition, good qualitative agreement has been found between the data obtained from this experimental investigation employing substitute liquids and existing data from studies of metal powders in the literature. This is a good indication that the trends observed also apply to the atomization of liquid metals.

6 Atomization Process

One key element in the development of models describing an atomization process is the identification and subsequent mathematical description of the relevant breakup mechanisms. A priori, these mechanisms and their individual significance for the atomization result are unknown. Consequently, the description of an atomization process can be arbitrarily complex. This is particularly relevant for two-fluid atomization processes such as the supersonic close-coupled atomization under investigation, where the specific flow field and the interaction between the gas flow and the liquid flow are expected to have a strong influence on the atomization process. Therefore, in this chapter, the atomization process is analyzed in more detail with the aim of identifying the main mechanisms contributing to the liquid breakup. For this purpose, the process is divided into two separate steps, which are the primary atomization and the secondary atomization, as is common for the analysis of complex atomization processes (Lefebvre & McDonell, 2017). The former describes the disintegration of the liquid jet into droplets and ligaments due to the initial interaction with the gas flow in the wake downstream of the liquid nozzle. The latter includes all of the further breakup events that these droplets and ligaments undergo as they travel through the flow field until the atomization is finally completed.

The primary atomization is studied experimentally in Section 6.1. This includes a qualitative description of the process as well as a comparison with existing models for the atomization of liquid metal in the literature. Furthermore, the influence of the set point of operation defined by the gas stagnation pressure $p_{\mathrm{t,g}}$ and the liquid mass flow rate $\dot{m}_{\mathrm{l}}$ (see Section 3.1.4) on the primary atomization is investigated and the affect of the physical liquid properties is briefly discussed. In Section 6.2, the focus is put on the secondary atomization. That is, the mechanisms responsible for the secondary atomization are identified and described. In addition, the absolute velocity u_{l} of liquid interacting with the high-velocity gas flow is discussed. For all of these considerations, unless explicitly stated otherwise, the baseline case design of the atomizer unit is employed (i.e., $d_\mathrm{l} = 4\,\mathrm{mm}$ and $l_{\mathrm{l,tip}} = 3.5\,\mathrm{mm}$, see Section 3.1.2).

The numerical data discussed in this chapter has been provided by the research partner SMS as part of the IGSTC project PPAM.

Parts of this chapter have already been covered in the thesis of Mirschinka (2022).

6.1 Primary Atomization

As has been shown in Section 4.2.2, in the absence of a gas flow, the liquid jet emanating from the liquid nozzle does not disintegrate significantly in close proximity to the liquid nozzle for operating conditions typical for the supersonic close-coupled atomization process. However, during the multiphase flow of the actual atomization process, the liquid jet interacts with the recirculating gas flow in the wake downstream of the liquid nozzle (see Section 4.1.2), resulting in its disintegration. It is important to note that, while the gas flow in the recirculation zone is slower than the gas flow in the surrounding gas jet, it still reaches absolute velocities u_g in the order of $10^2\,\mathrm{m\,s^{-1}}$, resulting in a high gas momentum flux q_g. An indication for this can be seen, for instance, in the simulation results for the gas-only flow field presented in Figs. 3.21 and 4.3. Being gas-only, however, these neglect liquid mass loading effects weakening the gas flow (see Section 4.3.2).

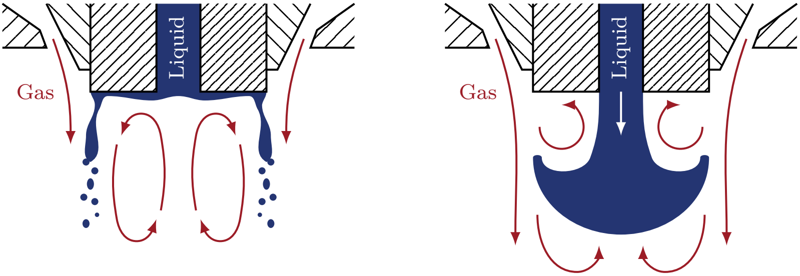

(a) Sheet formation model **(b)** Fountain formation model

Figure 6.1: Schematic illustration of the two models for the primary atomization according to Mates and Settles (2005a, 2005b).

Based on a literature study and experimental evidence obtained for the atomization of liquid tin, Mates and Settles (2005a, 2005b) have identified two different models describing the primary atomization in the supersonic close-coupled atomization process, which are the *sheet formation* model and the *fountain formation* model. Both are schematically illustrated in Fig. 6.1. In the sheet formation model, the liquid wets the base of the liquid nozzle tip immediately upon exiting the liquid nozzle due to the counter-flowing gas jet. This results in the formation of a thin liquid sheet, which is driven radially outwards by the recirculating gas flow. At the edge of the liquid nozzle tip, the liquid sheet interacts with the surrounding high-velocity gas jet and, as a result, is first stretched and then disintegrated into fine droplets. In contrast, in the fountain formation model, the liquid jet remains intact for a short distance downstream of the liquid nozzle before being displaced in radial direction by the recirculating gas flow, forming a fountain-like or mushroom-like shape and disintegrating into rather large droplets and ligaments.

The sheet formation model has been found to be mainly associated with comparatively low liquid mass flow rates $\dot{m}_\mathrm{l}$ (Mates & Settles, 2005a, 2005b). It has been observed experimentally for the atomization of liquid aluminum by Ünal (1989b), who has suggested that reducing the film thickness results in a particularly small particle size. This observation has motivated the formulation of the acceleration wave model for the resulting particle size by Anderson et al. (2005), which has been discussed in Section 2.2.2. On the other hand, for industrial-scale powder production plants, which are characterized by a comparatively high liquid mass flow rate $\dot{m}_\mathrm{l}$, the fountain formation model has been found to be predominantly applicable (Mates & Settles, 2005a, 2005b). Indeed, the formation of a liquid fountain during the atomization of liquid metal has been reported in experimental studies by Wang and Chen (2012), Schwenck et al. (2017) and Hernandez et al. (2019) and in numerical studies by Zeoli et al. (2011, 2012) and Hernandez et al. (2018), among others. An important difference between the two models for the primary atomization is that, for atomizers operating according to the fountain formation model, the production of particularly small particles is believed to be largely due to the subsequent secondary atomization (Mates & Settles, 2005a, 2005b). Notably, Mates and Settles (1996) have found that employing water as the working liquid results in a mixture of the sheet formation model and the fountain formation model.

6.1.1 Design of Experiments

In the context of supersonic close-coupled atomization, experimental investigations of the primary atomization are challenging. This is due to the fact that the spray formation results in an optically dense curtain of liquid concealing the wake downstream of the liquid nozzle, as has been shown in Section 4.3.2. As a result, the primary atomization is not directly accessible by means of conventional imaging techniques based on the diffuse backlight illumination. However, for this experimental investigation, this difficulty has been overcome by limiting the visualization to the very beginning of the atomization process. Specifically, the liquid has been introduced into the fully developed steady-state gas flow field at a constant liquid mass flow rate $\dot{m}_\mathrm{l}$ by abruptly opening the solenoid valve in the pressurized liquid supply line (see Section 3.1.3). For this purpose, the liquid supply line has been operated with a fully opened control valve. Therefore, as has been discussed in Section 4.3.1, the liquid mass flow rate $\dot{m}_\mathrm{l}$ has been determined by the combination of the applied liquid overpressure Δp_l and the effect of the gas flow, which is a function of the gas stagnation pressure $p_\mathrm{t,g}$.

It is important to note that the described procedure represents a simplification of the actual atomization process. That is, the introduction of liquid into the fully developed gas flow field neglects the effects of the liquid mass loading on the gas flow, which are evident in the fully developed multiphase flow (see Section 4.3.2). Furthermore, this procedure is contrary to the industrial process, where the gas flow is typically initiated subsequent to the liquid flow in order to avoid freezing of the liquid due to the low local gas temperatures T_g (see Section 4.1.2). However, as has been shown by Tong and Browne (2007, 2008) by means of numerical simulations, after a short start-up phase characterized by the displacement and the disturbance of the initially intact liquid jet, the same mechanisms described by the sheet formation model and the fountain formation model can be observed in the industrial process. Consequently, this difference between the experimental approach and the industrial process is assumed to be negligible.

For the actual visualization, the high-speed imaging setup described in Section 3.3.1 has been employed, which allows for resolving the inherently time-dependent process with a sufficiently high temporal resolution. In order to compare the data obtained, the time t has been non-dimensionalized using the absolute liquid velocity at the liquid nozzle exit $u_{\mathrm{l,e}}$ and the diameter of the liquid nozzle tip $d_{\mathrm{l,tip}}$ (see Section 3.1.2):

$$\tilde{t} = t\frac{u_{\mathrm{l,e}}}{d_{\mathrm{l,tip}}}. \tag{6.1}$$

The start time $t_0 = 0\,\mathrm{s}$ is defined as the instant of time when the liquid jet starts to emanate from the liquid nozzle exit. Consequently, the non-dimensional instant of time $\tilde{t}$ of unity corresponds to the intact liquid jet traveling an axial distance equal to the diameter of the liquid nozzle tip $d_{\mathrm{l,tip}}$ (i.e., $z = 14.5\,\mathrm{mm}$ or $\tilde{z} = 1$, see Section 3.1.2).

Besides the described simplification of the atomization process neglecting the liquid mass loading effects, the outlined approach for the experimental investigation of the primary atomization in the supersonic close-coupled atomization process results in two more limitations. First, the primary atomization is inherently random and three-dimensional, resulting in equally three-dimensional trajectories of the liquid inside of the wake downstream of the liquid nozzle. Since the visualization is based on a two-dimensional approach, this does not allow for an extensive quantitative evaluation of the data obtained. Second, for certain set points of operation characterized by a high gas stagnation pressure $p_{\mathrm{t,g}}$, the gas in the recirculation zone flowing upstream toward the liquid nozzle exit is particularly fast (see Fig. 4.3), that is, it is characterized by a particularly high gas momentum flux q_{g}. At low liquid momentum fluxes at the liquid nozzle exit $q_{\mathrm{l,e}}$, which require a low liquid overpressure Δp_{l} and, therefore, are comparatively sensitive to the gas flow (see Fig. 4.11), this can result in the liquid jet not being intact when emanating from the liquid nozzle exit.

As a consequence, the objective of this investigation is to qualitatively describe the mechanisms responsible for the primary atomization in the supersonic close-coupled atomization process and to identify how it can be influenced. Furthermore, since there are two existing models describing the primary atomization of liquid metal (see Section 6.1), this serves as a means for studying whether using a substitute for liquid metal as the working liquid leads to comparable results.

6.1.2 Qualitative Description

In order to develop a general understanding of the primary atomization in the supersonic close-coupled atomization process, it is instructive to study the temporal evolution of the liquid jet emanating from the liquid nozzle exit and its interaction with the recirculating gas flow in the wake downstream of the liquid nozzle. For this purpose, water has been considered as the working liquid.

In Fig. 6.2, images of the temporal evolution of the liquid jet are shown. In total, four different non-dimensional instants of time $\tilde{t}$ after the introduction of liquid into the wake downstream of the liquid nozzle are considered (i.e. $\tilde{t} = 0.25$, $\tilde{t} = 0.75$, $\tilde{t} = 1.25$ and $\tilde{t} = 1.75$). The corresponding set point of operation is characterized by a gas stagnation pressure $p_{\mathrm{t,g}}$ of $(1.00 \pm 0.06)\,\mathrm{MPa}$ and a liquid mass flow rate $\dot{m}_{\mathrm{l}}$ of $(6.16 \pm 0.05)\,\mathrm{kg\,min^{-1}}$. As can be seen, immediately upon exiting the liquid nozzle, the liquid jet interacts with the counter-flowing gas in the recirculation zone (see Fig. 6.2a). Indeed, the result is the formation of a fountain-like shape, similar to the fountain formation model described by Mates and Settles (2005a, 2005b). Small droplets are detached from the fountain and accelerated upstream. Additionally, the surface of the liquid jet is disturbed due to the relative motion of the gas flow and the liquid flow. Liquid drawn into the surrounding gas jet is atomized into a fine mist, starting to form the liquid curtain concealing the wake (see Section 4.3.2). However, the liquid jet still has approximately its initial absolute velocity $u_{\mathrm{l,e}}$, as can be seen from the non-dimensional axial distance $\tilde{z}$ covered, which is equal to the non-dimensional instant of time $\tilde{t}$ of 0.25. Consequently, the liquid jet travels further downstream, while its tip is further disintegrated (see Fig. 6.2b). At the same time, droplets and ligaments of different size are detached from the surface of the liquid jet and drawn into the surrounding gas jet. As a result, the liquid curtain becomes more optically dense. At a non-dimensional instant in time $\tilde{t}$ of 1.25, the liquid jet is noticeably displaced in the radial direction (i.e., in the y-direction, see Fig. 6.2c). The optical density of the liquid curtain has increased to the point where it conceals part of the wake, as more liquid mass m_{l} is drawn into the surrounding gas jet. Finally, the tip of the liquid jet no longer advances in the axial direction (i.e., in the z-direction, see Fig. 6.2d). Here, the maximum non-dimensional axial distance $\tilde{z}_{\max}$ covered is about 1.2, which is similar to the axial extent of the

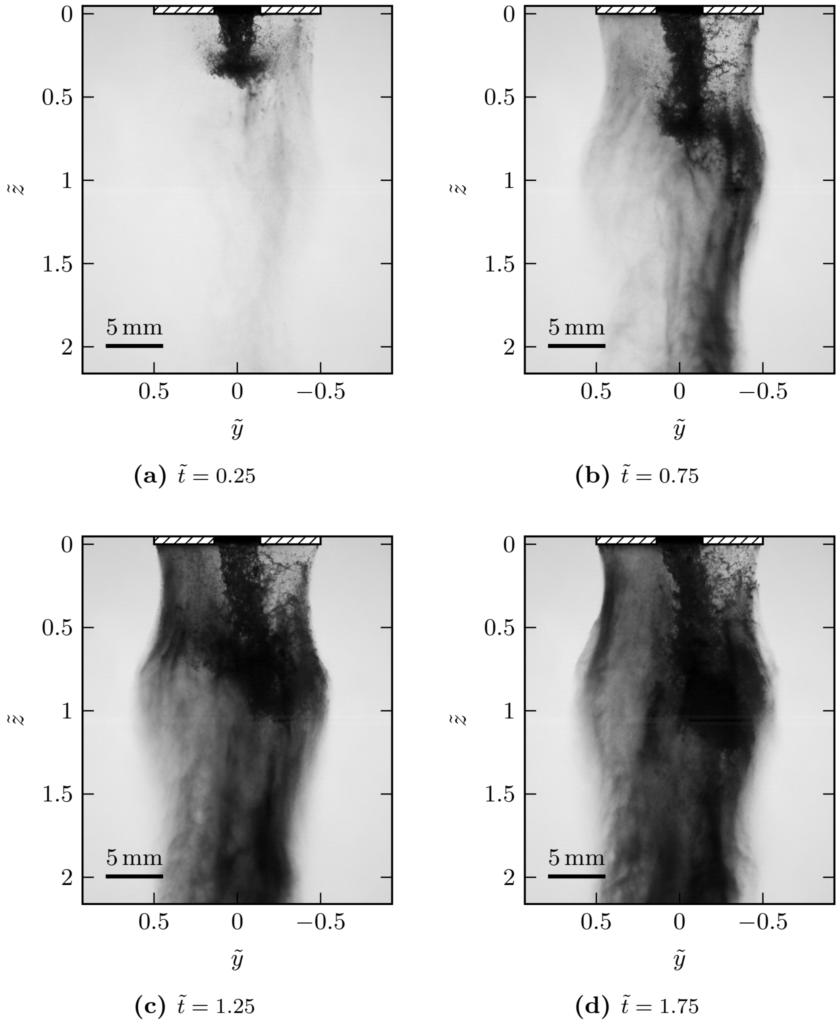

(a) $\tilde{t} = 0.25$ **(b)** $\tilde{t} = 0.75$

(c) $\tilde{t} = 1.25$ **(d)** $\tilde{t} = 1.75$

Figure 6.2: Temporal evolution of the liquid jet for a gas stagnation pressure $p_{\mathrm{t,g}}$ of $(1.00 \pm 0.06)\,\mathrm{MPa}$ and a liquid mass flow rate $\dot{m}_\mathrm{l}$ of $(6.16 \pm 0.05)\,\mathrm{kg\,min^{-1}}$.

recirculation zone (see Fig. 4.3). Instead, the liquid jet feeds liquid into the surrounding gas jet, while its surface is further disturbed and more droplets and ligaments are detached. Interestingly, while the high optical density does not allow for a definite statement, the tip of the liquid jet appears to be in direct contact with the surrounding gas jet. A similar asymmetry has been observed experimentally by Mullis et al. (2011) and Zerwas et al. (2021).

In summary, three main conclusions can be drawn from this qualitative description of the primary atomization. First, liquid is detached from the liquid jet along its entire length and drawn into the surrounding gas jet. Since the local absolute gas velocity u_g inside of the surrounding high-velocity gas jet varies in the axial direction (i.e., in the z-direction, see Figs. 3.21 and 4.3) due to the alternating pattern of expansion and compression waves, this may have an influence on the subsequent secondary atomization.

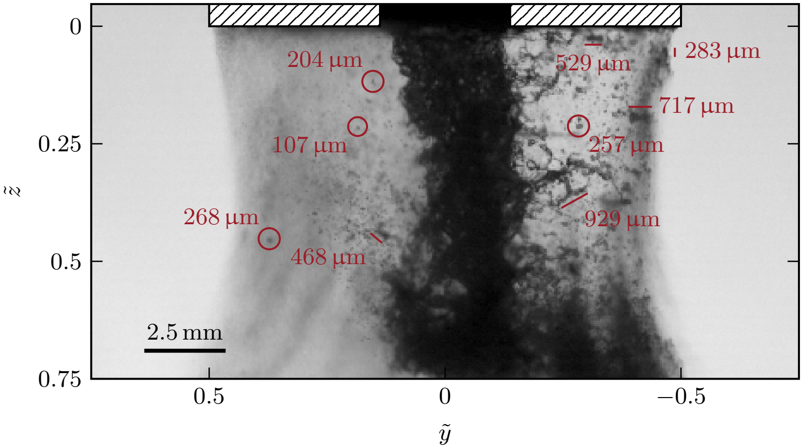

Figure 6.3: Magnified view of the liquid jet at a non-dimensional instant in time $\tilde{t}$ of 0.75 for a gas stagnation pressure $p_{\mathrm{t,g}}$ of (1.00 ± 0.06) MPa and a liquid mass flow rate $\dot{m}_\mathrm{l}$ of $(6.16 \pm 0.05)\,\mathrm{kg\,min^{-1}}$. As a reference, the approximate length scales of several exemplary droplets (diameter d) and ligaments (length l) are indicated.

Second, the droplets and ligaments resulting from the primary atomization vary in size by at least one order of magnitude. This can be seen, for instance, in Fig. 6.3, where a magnified view of the liquid jet at a non-dimensional instant in time $\tilde{t}$ of 0.75 is shown for a gas stagnation pressure $p_{\mathrm{t,g}}$ of (1.00 ± 0.06) MPa and a liquid mass flow rate $\dot{m}_{\mathrm{l}}$ of $(6.16 \pm 0.05)\,\mathrm{kg\,min^{-1}}$. This corresponds to the same image already shown in Fig. 6.2b. Here, approximate length scales of exemplary droplets and ligaments are indicated. The former are characterized by their diameter d and the latter by their length l. These length scales have to be understood as rough estimates, since they are based on a two-dimensional projection into the yz-plane and the high-speed imaging setup described in Section 3.3.1 is limited in its Depth of Field (DoF) and resolution. Still, these results suggest that, in addition to the varying local absolute gas velocity u_{g} inside of the surrounding high-velocity gas jet, the size of the droplets and ligaments resulting from the primary atomization may also have an influence on the subsequent secondary atomzation.

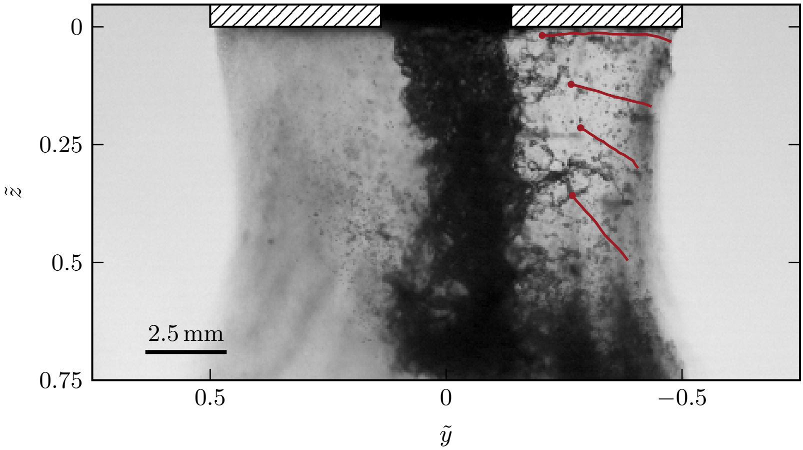

Figure 6.4: Magnified view of the liquid jet at a non-dimensional instant in time $\tilde{t}$ of 0.75 for a gas stagnation pressure $p_{\mathrm{t,g}}$ of (1.00 ± 0.06) MPa and a liquid mass flow rate $\dot{m}_{\mathrm{l}}$ of $(6.16 \pm 0.05)\,\mathrm{kg\,min^{-1}}$. Additionally indicated are the trajectories of exemplary droplets and ligaments projected into the yz-plane.

Third, the liquid jet does not remain intact for an extended non-dimensional axial distance $\tilde{z}$. Instead, it is disintegrated, feeding liquid into the recirculation zone, where it is transported further by the gas flow. Employing the same magnified view of the liquid jet shown in Fig. 6.3, the trajectories of exemplary droplets and ligaments projected into the yz-plane are shown in

Fig. 6.4. As can be seen, the liquid is primarily drawn radially outwards into the surrounding high-velocity gas jet. This suggests that most of the liquid mass m_l eventually interacts directly with the surrounding gas jet, which is an indication of the significance of the subsequent secondary atomization.

In general, the results presented in Fig. 6.2 have been found to be consistent with the fountain formation model for the primary atomization described by Mates and Settles (2005a, 2005b), indicating that the atomization of liquid metal and the atomization water as a substitute liquid are governed by similar mechanisms. In particular, the results are consistent with the images published by Anderson et al. (2011) for the atomization of a liquid stainless steel alloy.

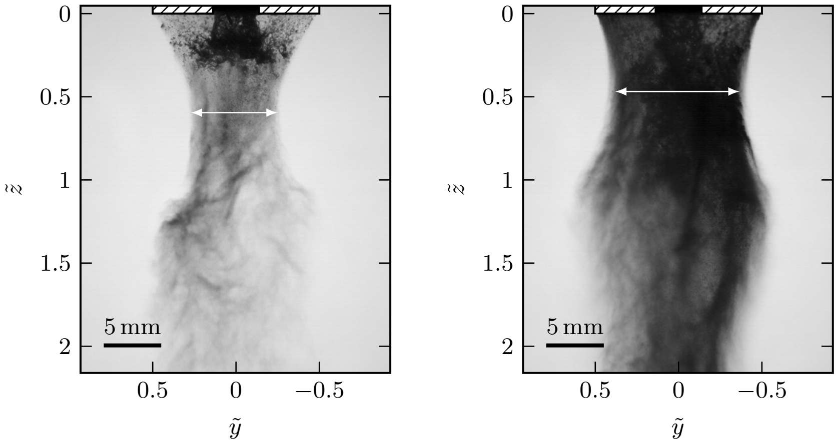

(a) $\tilde{t} = 0.50$ **(b)** $\tilde{t} = 2.00$

Figure 6.5: Comparison between two different non-dimensional instants of time $\tilde{t}$ after the introduction of liquid into the wake downstream of the liquid nozzle for a gas stagnation pressure $p_\mathrm{t,g}$ of $(1.21 \pm 0.08)\,\mathrm{MPa}$ and a liquid mass flow rate $\dot{m}_\mathrm{l}$ of $(7.55 \pm 0.05)\,\mathrm{kg\,min^{-1}}$. As a reference, for both non-dimensional instants of time $\tilde{t}$, the width of the neck of the spray contour is indicated.

In Section 4.3.2, it has been shown that the liquid mass loading has an influence on the flow field in close proximity to the liquid nozzle. In particular, it has been observed that the introduction of liquid results in a restriction of the expansion of the surrounding gas jet in the radial direction (i.e., in the y-direction). Since, for the investigation of the primary atomization, liquid is introduced into the fully developed steady-state gas flow field, the time-resolved visualization allows for providing further evidence supporting this finding. For this purpose, in Fig. 6.5, the temporal evolution of the flow field downstream of the liquid nozzle after the introduction of liquid is compared for two non-dimensional instants of time $\tilde{t}$ (i.e., for $\tilde{t} = 0.5$ and $\tilde{t} = 2.0$). The corresponding set point of operation is characterized by a gas stagnation pressure $p_{\mathrm{t,g}}$ of $(1.21 \pm 0.08)\,\mathrm{MPa}$ and a liquid mass flow rate $\dot{m}_{\mathrm{l}}$ of $(7.55 \pm 0.05)\,\mathrm{kg\,min^{-1}}$. As can be seen in Fig. 6.5a, shortly after the liquid jet starts to emanate from the liquid nozzle exit, which corresponds to the non-dimensional instant of time $\tilde{t}$ of 0.5, the surrounding gas jet still extends far in the radial direction (i.e., in the y-direction), resulting in the typical hourglass-like shape of the wake downstream of the liquid nozzle (see Section 4.1.2). This is indicated by the fine mist of droplets following the shape of the expanding and compressing gas jet. However, for the fully developed multiphase flow at a later non-dimensional instant of time $\tilde{t}$ of 2.0, the expansion of the gas flow in the radial direction (i.e., in the y-direction) can be seen to be restricted by the liquid (see Fig. 6.5b). That is, the resulting spray contour is wider, showing a less pronounced necking, as is also evident from the widths indicated in Fig. 6.5. Furthermore, consistent with the observations made in Section 4.3.2, the shortening of the wave pattern inside of the surrounding gas jet in the axial direction (i.e., in the z-direction) due to the liquid mass loading can also be seen in Fig. 6.5 as the displacement of the neck of the spray contour. As a result, this is another indication of the two-way coupling between the gas flow and the liquid flow evident in supersonic close-coupled atomization.

6.1.3 Influence of the Operational Parameters

While the description of the primary atomization in the supersonic close-coupled atomization process given in Section 6.1.2 has been found to be representative in a qualitative manner of all set points of operation considered, there are distinct differences depending on the specific set point of operation employed.

In Fig. 6.6, the state of the liquid jet after the introduction of liquid into the wake downstream of the liquid nozzle is compared for four different set

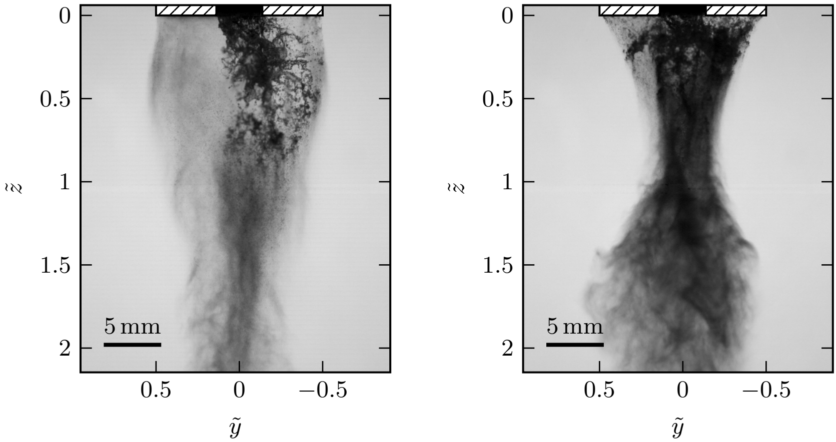

(a) $p_{\mathrm{t,g}} = (0.60 \pm 0.03)\,\mathrm{MPa}$,
$\dot{m}_{\mathrm{l}} = (3.98 \pm 0.03)\,\mathrm{kg\,min^{-1}}$

(b) $p_{\mathrm{t,g}} = (1.41 \pm 0.10)\,\mathrm{MPa}$,
$\dot{m}_{\mathrm{l}} = (3.96 \pm 0.02)\,\mathrm{kg\,min^{-1}}$

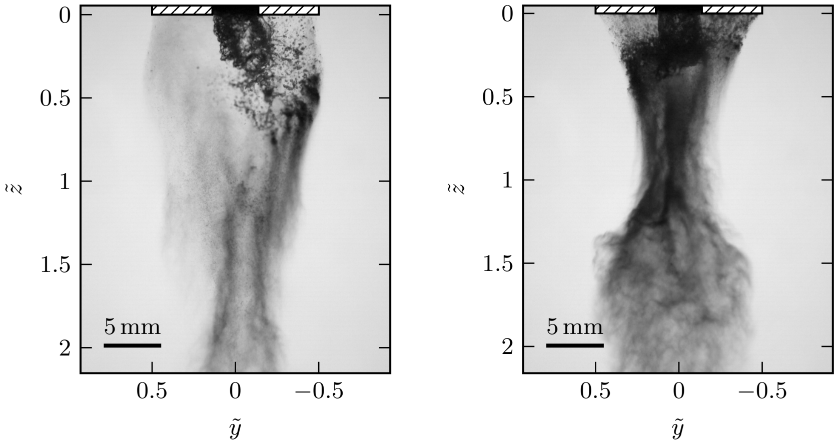

(c) $p_{\mathrm{t,g}} = (0.60 \pm 0.04)\,\mathrm{MPa}$,
$\dot{m}_{\mathrm{l}} = (7.95 \pm 0.08)\,\mathrm{kg\,min^{-1}}$

(d) $p_{\mathrm{t,g}} = (1.40 \pm 0.10)\,\mathrm{MPa}$,
$\dot{m}_{\mathrm{l}} = (7.84 \pm 0.04)\,\mathrm{kg\,min^{-1}}$

Figure 6.6: State of the liquid jet at a non-dimensional instant of time $\tilde{t}$ of 0.5 after the introduction of liquid into the wake downstream of the liquid nozzle for four different set points of operation.

points of operation. These differ in the combination of the gas stagnation pressure $p_{\mathrm{t,g}}$ (i.e., 0.6 MPa and 1.4 MPa) and the liquid mass flow rate $\dot{m}_{\mathrm{l}}$ (i.e., $4\,\mathrm{kg\,min^{-1}}$ and $8\,\mathrm{kg\,min^{-1}}$). The non-dimensional instant of time $\tilde{t}$ considered is 0.5 and water has been employed as the working liquid. As can be seen by comparing Figs. 6.6a and 6.6b or Figs. 6.6c and 6.6d, increasing the gas stagnation pressure $p_{\mathrm{t,g}}$ results in a faster disintegration of the liquid jet closer to the liquid nozzle exit. More liquid mass m_{l} is drawn into the surrounding gas jet, increasing the optical density of the spray. This is due to the increasing strength of the recirculating gas flow (see Fig. 4.3). However, with increasing liquid mass flow rate $\dot{m}_{\mathrm{l}}$, the length of the intact liquid jet also increases, as is evident from a comparison between Figs. 6.6b and 6.6d. In fact, for a liquid mass flow rate $\dot{m}_{\mathrm{l}}$ of $(3.96 \pm 0.02)\,\mathrm{kg\,min^{-1}}$, the liquid jet disintegrates almost immediately upon exiting the liquid nozzle (see Fig. 6.6b). While not explicitly shown here, a further decrease in the liquid mass flow rate $\dot{m}_{\mathrm{l}}$ results in the formation of a liquid sheet at the base of the liquid nozzle tip. This is in good agreement with the sheet formation model for the primary atomization of liquid metal described by Mates and Settles (2005a, 2005b) and, importantly, demonstrates that water can be employed as a working liquid in order to replicate this mechanism. Considering the lower gas stagnation pressure $p_{\mathrm{t,g}}$ of 0.6 MPa, the differences between the liquid jets for the two different liquid mass flow rates $\dot{m}_{\mathrm{l}}$ shown in Figs. 6.6a and 6.6c are minimal due to the weaker recirculating gas flow (see Fig. 4.3). However, at later non-dimensional instants of time $\tilde{t}$, which are not explicitly shown here, the higher liquid mass flow rate $\dot{m}_{\mathrm{l}}$ of $(7.95 \pm 0.08)\,\mathrm{kg\,min^{-1}}$ results in a longer length of the intact liquid jet, similar to the results for the higher gas stagnation pressure $p_{\mathrm{t,g}}$ of 1.4 MPa shown in Figs. 6.6b and 6.6d.

As has been described in Section 4.3.2, for a constant liquid nozzle diameter d_{l}, a change in the liquid mass flow rate $\dot{m}_{\mathrm{l}}$ corresponds to a change in the liquid momentum flux at the liquid nozzle exit $q_{\mathrm{l,e}}$. Interestingly, while the latter has been found in Section 4.3.2 to affect the spray formation in close proximity to the liquid nozzle, its influence on the resulting particle size has been shown to be negligible in Section 5.3.2. Consequently, it is instructive to investigate how the liquid momentum flux at the liquid nozzle exit $q_{\mathrm{l,e}}$ influences the primary atomization. For this purpose, three different liquid nozzle diameters d_{l} (i.e., 3 mm, 4 mm and 5 mm) have been considered (see Section 3.1.2). Furthermore, water has been employed as the working liquid.

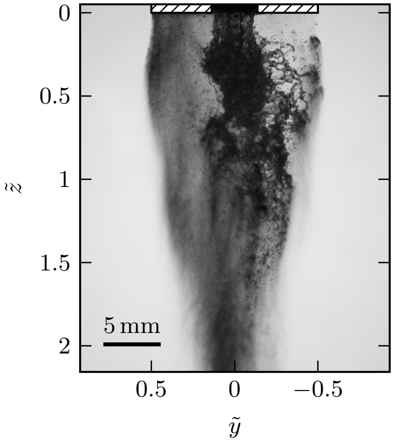

(a) $d_\mathrm{l} = 4\,\mathrm{mm}$

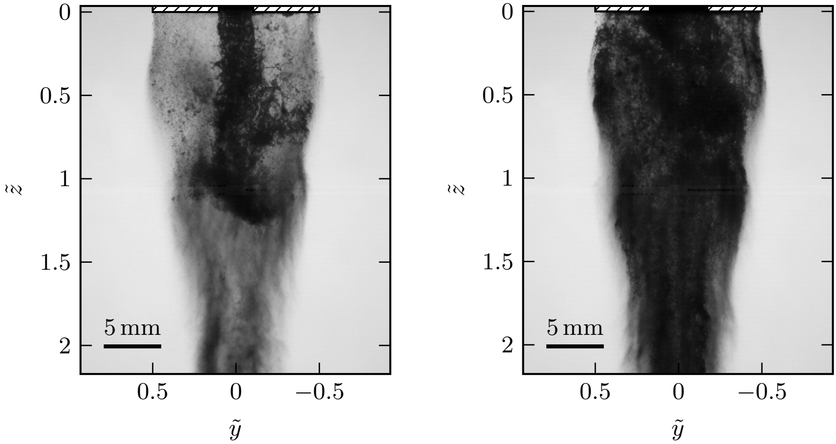

(b) $d_\mathrm{l} = 3\,\mathrm{mm}$ **(c)** $d_\mathrm{l} = 5\,\mathrm{mm}$

Figure 6.7: State of the liquid jet at a non-dimensional instant of time $\tilde{t}$ of 2.0 after the introduction of liquid into the wake downstream of the liquid nozzle for three different liquid nozzle diameters d_l and a set point of operation characterized by a gas stagnation pressure $p_{\mathrm{t,g}}$ of 0.6 MPa and a liquid mass flow rate $\dot{m}_\mathrm{l}$ of $8\,\mathrm{kg\,min^{-1}}$.

In Fig. 6.7, the state of the liquid jet after the introduction of liquid into the wake downstream of the liquid nozzle is compared for the three different liquid nozzle diameters d_l. Here, the baseline case geometric design (i.e., $d_\mathrm{l} = 4\,\mathrm{mm}$) presented in Fig. 6.7a serves as a reference. The non-dimensional instant of time $\tilde{t}$ considered is 2.0 and the corresponding set point of operation is characterized by a gas stagnation pressure $p_\mathrm{t,g}$ of $0.6\,\mathrm{MPa}$ and a liquid mass flow rate $\dot{m}_\mathrm{l}$ of $8\,\mathrm{kg\,min^{-1}}$. As can be seen, there are distinct differences between the liquid jets for the three liquid nozzle diameters d_l considered. Compared to the liquid nozzle diameter d_l of $4\,\mathrm{mm}$, the liquid momentum flux at the liquid nozzle exit $q_\mathrm{l,e}$ is increased by $216\,\%$ for the liquid nozzle diameter d_l of $3\,\mathrm{mm}$ (see Fig. 4.18), which leads to a longer length of the intact liquid jet. That is, the liquid jet covers a larger non-dimensional axial distance $\tilde{z}$. In contrast, for the liquid nozzle diameter d_l of $5\,\mathrm{mm}$, the liquid momentum flux at the liquid nozzle exit $q_\mathrm{l,e}$ is decreased by $59\,\%$ (see Fig. 4.18). As a result, the liquid jet is disintegrated faster and closer to the liquid nozzle exit. However, it is important to emphasize that, despite this influence of the liquid momentum flux at the liquid nozzle exit $q_\mathrm{l,e}$, the resulting particle size is the same for all three cases considered. As has been shown in Section 5.3.2, this is due to the liquid mass flow rate $\dot{m}_\mathrm{l}$ being the main determinant along with the gas stagnation pressure $p_\mathrm{t,g}$. This is a possible indication of the significance of the secondary atomization.

In conclusion, these considerations show that the primary atomization is mainly determined by the liquid momentum flux at the liquid nozzle exit $q_\mathrm{l,e}$ and the interaction between the liquid jet and the counter-flowing gas in the recirculation zone downstream of the liquid nozzle. Notably, this is in good agreement with the numerical results presented by Hernandez et al. (2018) for the atomization of liquid metal.

6.1.4 Influence of the Physical Liquid Properties

So far, water has been employed as the working liquid for investigating the primary atomization. However, in Section 5.4 the resulting particle size has been shown to be independent of the liquid dynamic viscosity μ_l for liquid Reynolds numbers Re_l typical for the supersonic close-coupled atomization process. Consequently, it is interesting to study whether there are differences in the primary atomization between different working liquids. For this purpose,

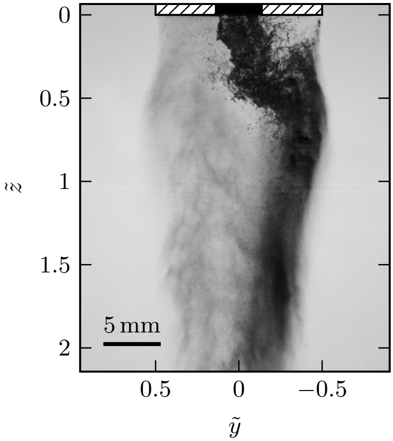

(a) Water

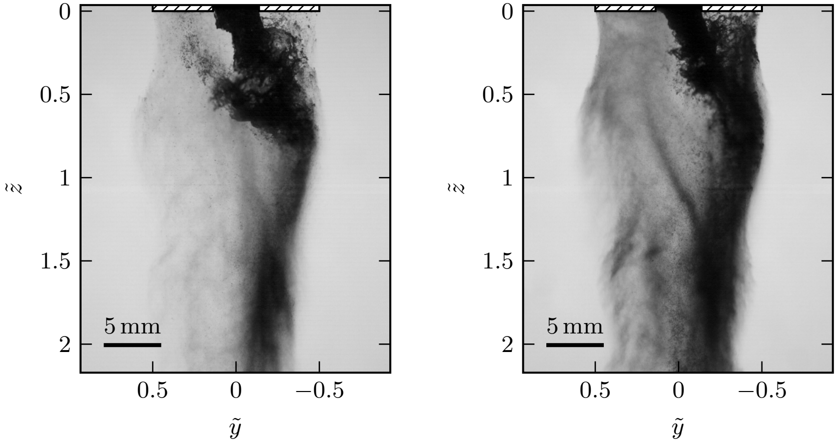

(b) 40 % aqueous glycerol solution

(c) 30 % aqueous acetic acid solution

Figure 6.8: State of the liquid jet at a non-dimensional instant of time $\tilde{t}$ of 0.5 after the introduction of liquid into the wake downstream of the liquid nozzle for three different working liquids and a set point of operation characterized by a gas stagnation pressure $p_{\mathrm{t,g}}$ of 0.8 MPa and a liquid mass flow rate $\dot{m}_{\mathrm{l}}$ of 4 kg min^{-1}.

three working liquids have been considered. Besides water as a reference, this includes an aqueous glycerol solution having a glycerol mass fraction of 40 % and an aqueous acetic acid solution having an acetic acid mass fraction of 30 %. Compared to water, the former is characterized by an increase in the liquid dynamic viscosity μ_l, while the latter additionally shows a decrease in the surface tension σ (see Table 3.1).

For a set point of operation characterized by a gas stagnation pressure $p_\mathrm{t,g}$ of 0.8 MPa and a liquid mass flow rate $\dot{m}_\mathrm{l}$ of $4\,\mathrm{kg\,min^{-1}}$, the state of the liquid jet after the introduction of liquid into the wake downstream of the liquid nozzle is compared in Fig. 6.8 for the three liquids. As a reference, the corresponding gas Weber numbers We_g, as defined in Eq. (2.4), are $37\,000 \pm 2000$, $38\,000 \pm 2000$ and $59\,000 \pm 4000$, respectively, and the corresponding liquid Reynolds numbers Re_l, as defined in Eq. (2.3), are $21\,500 \pm 100$, 5220 ± 50 and 9910 ± 40, respectively. Furthermore, the non-dimensional instant of time $\tilde{t}$ considered is 0.5. As can be seen, qualitatively, there are no obvious differences due to the different physical liquid properties. While this does not allow for quantitative statements, for instance, regarding the size of the resulting droplets and ligaments, this is an indication that the mechanisms governing the primary atomization of the liquid jets are the same. That is, the primary atomization is caused by the interaction between the liquid jet and the gas flow in the recirculation zone in the wake downstream of the liquid nozzle. This is reasonable, since not only is the gas stagnation pressure $p_\mathrm{t,g}$ constant for the set points of operation considered in Fig. 6.8, but the liquid momentum flux at the liquid nozzle exit $q_\mathrm{l,e}$ differs by less than 10 % due to the differences in the liquid density ρ_l (see Table 3.1).

6.2 Secondary Atomization

The secondary atomization in the supersonic close-coupled atomization process comprises all breakup events a droplet or ligament undergoes along its trajectory subsequent to its detachment from the initial liquid jet emanating from the liquid nozzle exit. This includes breakup in the recirculation zone in the wake downstream of the liquid nozzle as well as breakup due to the interaction with the surrounding high-velocity gas jet. Consequently, secondary atomization is a complex problem, which depends on the local flow conditions and, therefore, is governed by a variety of mechanisms. In fact, Mates and Settles (2005a, 2005b) have presented experimental evidence for the atomization of liquid tin, suggesting that the secondary atomization extends up to a non-dimensional axial distance $\tilde{z}$ of 10 downstream of the liquid nozzle. Furthermore, Ünal (1987) has estimated that about three quarters of all particles contributing to the final particle size distribution undergo secondary atomization. However, experimental data for the secondary atomization in the supersonic close-coupled atomization process is scarce. This is due to the fact that observing the breakup of small droplets and ligaments in a high-velocity gas flow requires a high spatial and temporal resolution, as Ridder et al. (1992) have noted.

6.2.1 Design of Experiments

As has been observed in Section 6.1, a significant proportion of the droplets and ligaments resulting from the primary atomization of the liquid jet are drawn into the surrounding gas jet and, consequently, interact with the high-velocity gas flow. Due to the large difference in the absolute velocity Δu between the gas jet and the liquid, this interaction is likely to be an important mechanism governing the secondary atomization. As a result, it is instructive to study this mechanism by means of visualization, which primarily allows for a qualitative description of the interaction, similar to Section 6.1.1. However, as an important difference to the approach for the investigation of the primary atomization discussed in Section 6.1.1, for the investigation of the secondary atomization the fully developed multiphase flow is considered.

For the purpose of visualizing the interaction between the liquid and the high-velocity gas jet, the near-field configuration of the double-frame imaging setup described in Section 3.3.2 has been employed, which is based on the diffuse background illumination technique and provides a high spatial resolution (see Table 3.7). Furthermore, despite the high absolute gas velocities u_g (see Fig. 3.21), the ultra-short illumination time provided by the pulsed laser light source allows for effectively freezing the interaction in time. Additionally, while this approach is not time-resolved, the method described in Section 3.3.2 provides means for evaluating two components of the local velocity vector of the liquid $\mathbf{u}_\mathrm{l}$ from the double-frame images (i.e., in the y-direction and in the z-direction, see Fig. 3.24).

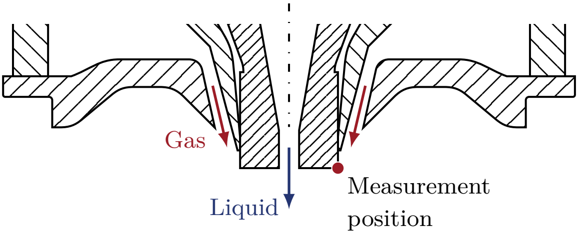

Figure 6.9: Schematic illustration indicating the measurement position (●) for the investigation of the secondary atomization at the edge of the base of the liquid nozzle tip.

It has to be noted that the contour of the resulting spray depends on the gas stagnation pressure $p_{\mathrm{t,g}}$ and the liquid mass flow rate $\dot{m}_{\mathrm{l}}$, as has been shown in Section 4.3.2. Consequently, the location of the interaction between the liquid and the high-velocity gas jet also varies with the set point of operation. This makes it challenging to define a specific measurement position which allows for comparability and repeatability of the measurement results. Furthermore, considering the slight vibrations of the research facility during the atomization process, which have been described in Section 3.3.2 and are significant relative to the high spatial resolution of the near-field configuration (see Table 3.7), this is even more important. In order to overcome this difficulty, the visualization has been limited to the edge of the base of the liquid nozzle tip (i.e., to $\tilde{y} = -0.5$ and $\tilde{z} = 0$). This is schematically illustrated in Fig. 6.9 and is additionally indicated in the field of view of the mid-field configuration shown in Fig. 3.25b. Consequently, the tip of the liquid nozzle serves as a visual reference, which not only defines the measurement position, but additionally allows for stabilizing the captured images (see Section 3.3.2). Considering that the local Mach number Ma inside of the surrounding gas jet is consistently high over the entire axial extent of the recirculation zone in the wake downstream of the liquid nozzle (see Fig. 4.3), the measurement position shown in Fig. 6.9 is assumed to be representative of the interaction between the liquid and the high-velocity gas jet.

Finally, the mid-field configuration of the double-frame imaging setup described in Section 3.3.2 has been employed for studying the interaction between the liquid and the high-velocity gas jet further downstream of the liquid nozzle. While this does not allow for spatially resolving individual droplets resulting form the secondary atomization (see Table 3.7), it provides insights into how clusters of droplets resulting from the secondary atomization are accelerated by the gas flow.

6.2.2 Identification of Breakup Mechanisms

Since information on the mechanisms responsible for the liquid breakup during secondary atomization generally is scarce in the context of supersonic close-coupled atomization, it is instructive to first identify the mechansims which are observed by means of visualization. For this purpose, water has been considered as the working liquid.

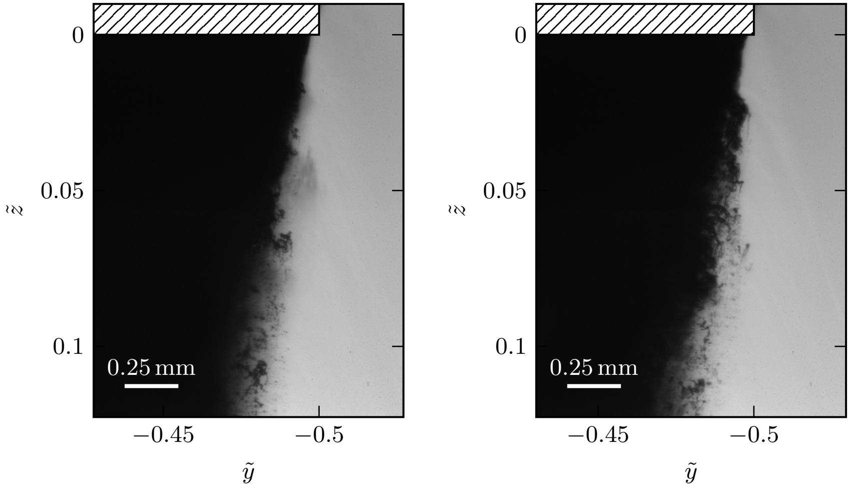

(a) Still image 1 **(b)** Still image 2

Figure 6.10: Exemplary still images of the secondary atomization due to the interaction between the liquid and the surrounding high-velocity gas jet for a gas stagnation pressure $p_{\mathrm{t,g}}$ of $(1.00 \pm 0.06)\,\mathrm{MPa}$ and a liquid mass flow rate $\dot{m}_{\mathrm{l}}$ of $(4.00 \pm 0.02)\,\mathrm{kg\,min^{-1}}$.

In Fig. 6.10, two exemplary still images of the secondary atomization due to the interaction between the liquid and the surrounding high-velocity gas jet are shown. The corresponding set point of operation is characterized by a gas stagnation pressure $p_{\mathrm{t,g}}$ of $(1.00 \pm 0.06)\,\mathrm{MPa}$ and a liquid mass flow rate $\dot{m}_{\mathrm{l}}$ of $(4.00 \pm 0.02)\,\mathrm{kg\,min^{-1}}$. Two conclusions can already be drawn from this. First, due to the high optical density of the spray, the inside of the wake downstream of the liquid nozzle is not accessible. This means that, for most set points of operation, the useful visualization is limited to the outer edge of the spray. Second, the interaction between the liquid and the surrounding high-velocity gas jet can be seen to be restricted to an area of small radial extent. In other words, the liquid does not penetrate far into the gas jet in the radial direction (i.e., in the y-direction) and, therefore, is not exposed to the highest absolute gas velocity u_{g}, which are present in the center of the gas jet (see Fig. 3.21). This is a first indication that, for the secondary atomization, the initial interaction between the liquid and the surrounding high-velocity gas jet is important, which is characterized by the strong radial velocity gradient $\partial u_{\mathrm{g}}/\partial y$ in the shear layer of the gas jet and the large absolute velocity difference Δu between the liquid and the gas.

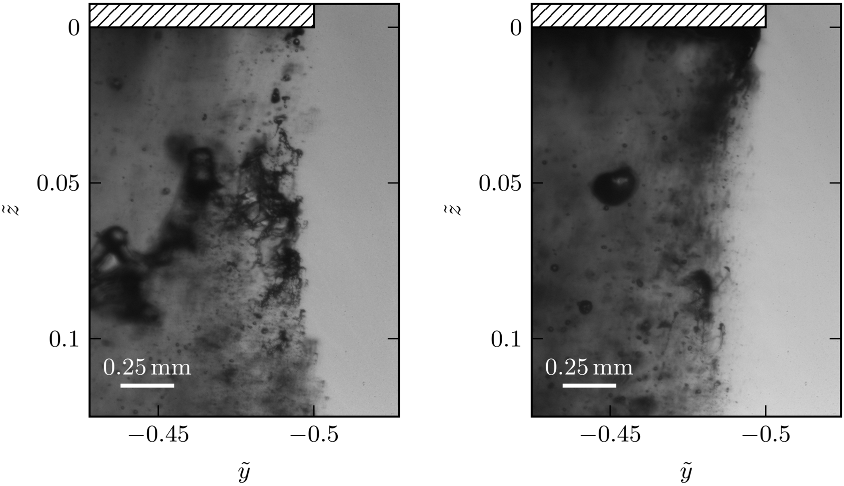

(a) Still image 1

(b) Still image 2

Figure 6.11: Exemplary still images of the secondary atomization due to the interaction between the liquid and the surrounding high-velocity gas jet for a gas stagnation pressure $p_{\mathrm{t,g}}$ of $(0.80 \pm 0.05)\,\mathrm{MPa}$ and a liquid mass flow rate $\dot{m}_{\mathrm{l}}$ of $(1.01 \pm 0.06)\,\mathrm{kg\,min^{-1}}$.

In order to confirm the second conclusion, two additional exemplary still images are shown in Fig. 6.11 for a gas stagnation pressure $p_{\mathrm{t,g}}$ of $(0.80 \pm 0.05)\,\mathrm{MPa}$ and a liquid mass flow rate $\dot{m}_{\mathrm{l}}$ of $(1.01 \pm 0.06)\,\mathrm{kg\,min^{-1}}$, which results in a lower liquid mass loading compared to Fig. 6.10. Consequently, this decreases the optical density of the spray and, therefore, allows for visualizing the wake downstream of the liquid nozzle. As can be seen, the liquid does indeed reach the surrounding high-velocity gas jet, is deformed and breaks up during this initial interaction. Furthermore, instead of traveling further radially outwards (i.e., in the y-direction), the liquid is accelerated downstream (i.e., in the z-direction), following the contour of the gas jet.

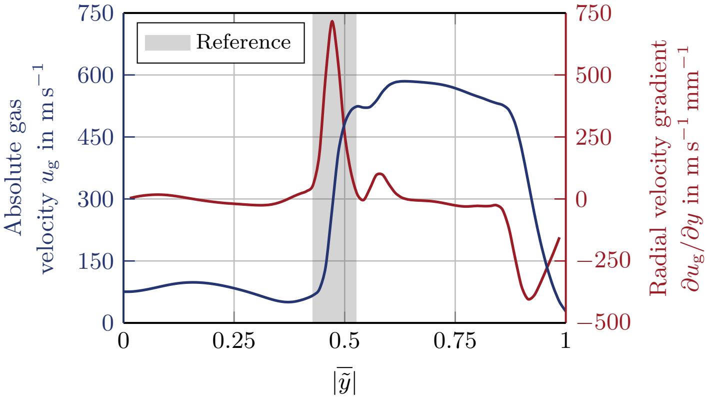

Figure 6.12: Axisymmetric steady-state simulation results for the radial profile of the absolute gas velocity u_{g} in the gas-only flow field at a non-dimensional axial distance $\tilde{z}$ of 0.1 downstream of the liquid nozzle. As a reference, the shaded area corresponds to the width of the field of view of the still images shown in Fig. 6.10. Considered is a gas stagnation pressure $p_{\mathrm{t,g}}$ of $1\,\mathrm{MPa}$. The numerical data has been provided by the research partner SMS as part of the IGSTC project PPAM.

This can be understood by considering the local absolute gas velocity u_{g}. For this purpose, numerical simulation results for the gas only flow-field at a gas stagnation pressure $p_{\mathrm{t,g}}$ of $1\,\mathrm{MPa}$, which corresponds to the same set point of operation used for capturing the two still images shown in Fig. 6.10, are evaluated. While this neglects the liquid mass loading effects discussed in Sections 4.3.2 and 6.1 and, therefore, represents a simplification, it still provides valuable qualitative information. In detail, the radial profile of the absolute gas velocity u_g as well as the radial profile of the radial gradient of the absolute gas velocity $\partial u_\mathrm{g}/\partial y$ at a non-dimensional axial distance $\tilde{z}$ of 0.1 downstream of the liquid nozzle are shown in Fig. 6.12. The data has been provided by the research partner SMS as part of the IGSTC project PPAM. Furthermore, as a reference, the width of the field of view of the still images shown in Fig. 6.10 is indicated. As can be seen, the liquid, which clearly stays inside of the field of view (see Fig. 6.10), does not penetrate far enough into the surrounding high-velocity gas jet to reach the highest absolute gas velocities u_g. However, it is exposed to a particularly strong radial velocity gradient $\partial u_\mathrm{g}/\partial y$ in the shear layer of the surrounding high-velocity gas jet. This is especially important considering that the characteristic length scale of some of the droplets and ligaments interacting with the gas jet is comparable in size to the radial extent of the shear layer (see Fig. 6.11). In other words, the aerodynamic force is not evenly distributed on the surface of the liquid, which causes an asymmetric deformation of the droplets and ligaments. This is a distinct difference to the models describing the breakup of a droplet in a homogeneous gas flow discussed in Section 2.2 and likely an important aspect of the secondary atomization in the supersonic close-coupled atomization process. In fact, Xu et al. (2020, 2022) have studied the breakup of individual droplets in the shear flow produced by a gas jet experimentally. They have observed an asymmetric deformation of the droplet leading to a breakup mechanism different from the classical bag breakup (Hsiang & Faeth, 1992). Furthermore, they have found that the deformation leads to a force lifting the droplet away from the gas jet. That is, it is counteracting the initial movement of the droplet, which is consistent with the observation made in Figs. 6.10 and 6.11 that the liquid does not penetrate far into the gas jet. In conclusion, this is an indication that the initial interaction between the liquid and the shear layer of the surrounding high-velocity gas jet is an important mechanism for the secondary atomization in the supersonic close-coupled atomization process. This is particularly relevant given that the absolute gas velocities u_g considered by Xu et al. (2020, 2022) are one order of magnitude lower than those characteristic of supersonic close-coupled atomization.

As an additional consideration, the high local absolute gas velocity u_g shown in Fig. 6.12 results in a rapid acceleration of the liquid. This can be seen, for instance, in Fig. 6.13, where the time-averaged field of the absolute liquid velocity u_l is shown for the near-field configuration and for

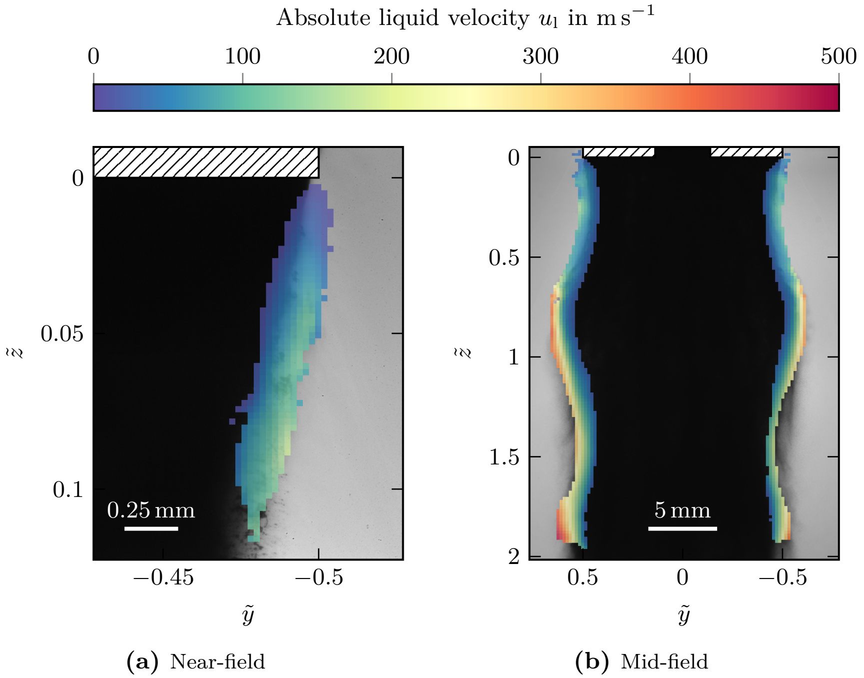

(a) Near-field **(b)** Mid-field

Figure 6.13: Time-averaged field of the absolute liquid velocity u_l for a gas stagnation pressure $p_{t,g}$ of 1.0 MPa and a liquid mass flow rate $\dot{m}_l$ of 4 kg min^{-1} obtained using two different optical configurations.

the mid-field configuration described in Section 3.3.2. Here, the set point of operation considered is the same as the one used in Fig. 6.10. The data has been obtained employing the Sum-of-Correlation scheme described in Section 3.3.3. In the near-field (see Fig. 6.13a), the liquid can be seen to reach absolute velocities u_l in the order of 10^2 m s^{-1} in close proximity to the liquid nozzle. This emphasizes the rapid acceleration due to the high-velocity gas jet. Furthermore, the absolute liquid velocity u_l clearly increases in the radial direction (i.e., in the y-direction). This is consistent with the radial gradient of the absolute gas velocity $\partial u_g/\partial y$ presented in Fig. 6.12. In terms of the mid-field (see Fig. 6.13b), a further increase in the absolute liquid velocity u_l can be seen further downstream of the liquid nozzle. In fact, in the outer region of the spray, the absolute liquid velocity u_l is comparable in magnitude to the local absolute gas velocity u_g presented in Fig. 3.21 for the gas-only flow. While this neglects the liquid mass loading effects discussed in Sections 4.3.2 and 6.1, it still indicates that the absolute velocity difference Δu between the liquid and the gas quickly decreases. This is important, since it suggests that the local gas Weber number We_g also decreases, which makes further secondary atomization less likely (see Section 5.1.1). However, it is important to note that the spatial resolution of the optical configuration employed for the mid-field is one order of magnitude smaller than of that employed for the near-field (see Section 3.3.2). As a result, the absolute liquid velocity u_l is more representative of clusters than of individual droplets and ligaments.

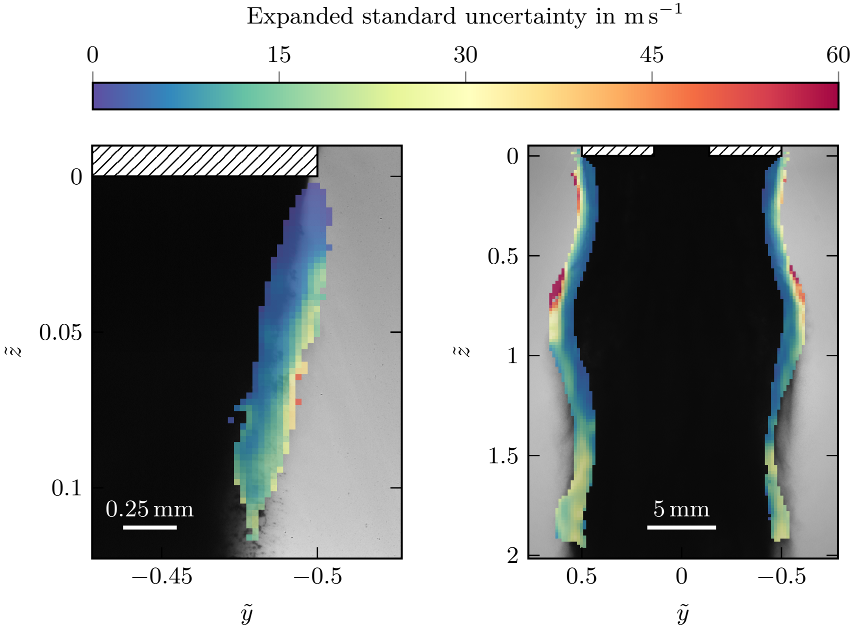

(a) Near-field

(b) Mid-field

Figure 6.14: Expanded standard uncertainty of the time-averaged field of the absolute liquid velocity u_l for a gas stagnation pressure $p_\mathrm{t,g}$ of 1.0 MPa and a liquid mass flow rate $\dot{m}_\mathrm{l}$ of 4 kg min^{-1} obtained using two different optical configurations, employing a coverage factor K of 1.96.

For a better assessment of the absolute liquid velocity u_l presented in Fig. 6.13, the field of the corresponding expanded standard uncertainty is shown in Fig. 6.14, employing a coverage factor K of 1.96. As can be seen, on average the expanded standard uncertainty is in the order of 10 % of the local absolute liquid velocity u_l.

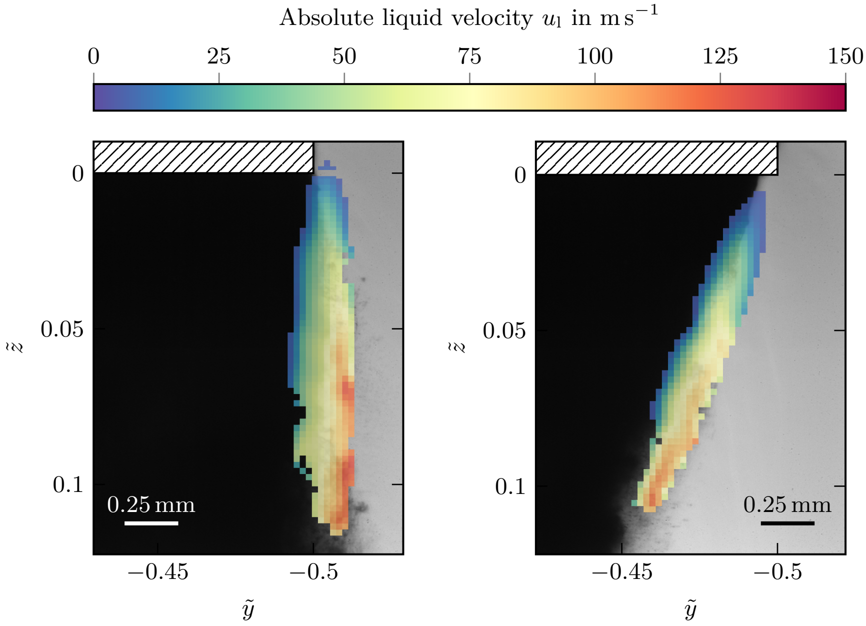

(a) $p_\mathrm{t,g} = (0.60 \pm 0.03)\,\mathrm{MPa}$ **(b)** $p_\mathrm{t,g} = (1.40 \pm 0.09)\,\mathrm{MPa}$

Figure 6.15: Time-averaged field of the absolute liquid velocity u_l for a constant liquid mass flow rate $\dot{m}_\mathrm{l}$ of $4\,\mathrm{kg\,min^{-1}}$ and two different gas stagnation pressures $p_\mathrm{t,g}$ obtained for the near-field.

Interestingly, neither the liquid mass flow rate $\dot{m}_\mathrm{l}$ nor the liquid momentum flux at the liquid nozzle exit $q_\mathrm{l,e}$ have been found to significantly affect the time-averaged field of the absolute liquid velocity u_l. The same is true for the liquid dynamic viscosity μ_l and the surface tension σ, which has been confirmed by additionally employing a 40 % aqueous glycerol solution and a 30 % aqueous acetic acid solution (see Table 3.1) for the atomization. Instead, the time-averaged local absolute liquid velocity u_l is mainly determined by the gas stagnation pressure p_{g}. This can be seen in Figs. 6.15 and 6.16 for the near-field and the mid-field, respectively. Here, the time-averaged field of the absolute liquid velocity u_{l} is shown for a constant liquid mass flow rate $\dot{m}_{\mathrm{l}}$ of $4\,\mathrm{kg\,min^{-1}}$ and two different gas stagnation pressures $p_{\mathrm{t,g}}$ (i.e., for $(0.60 \pm 0.03)\,\mathrm{MPa}$ and $(1.40 \pm 0.09)\,\mathrm{MPa}$). As can be seen, while, for the near-field, an increase in the gas stagnation pressures $p_{\mathrm{t,g}}$ does not significantly affect the magnitude of the time-averaged absolute liquid velocity u_{l} (see Fig. 6.15), there are distinct differences in the mid-field (see Fig. 6.16). That is, for the higher gas stagnation pressure considered (i.e., for $p_{\mathrm{t,g}} = (1.40 \pm 0.09)\,\mathrm{MPa}$), the liquid reaches higher absolute velocities u_{l}, but further downstream.

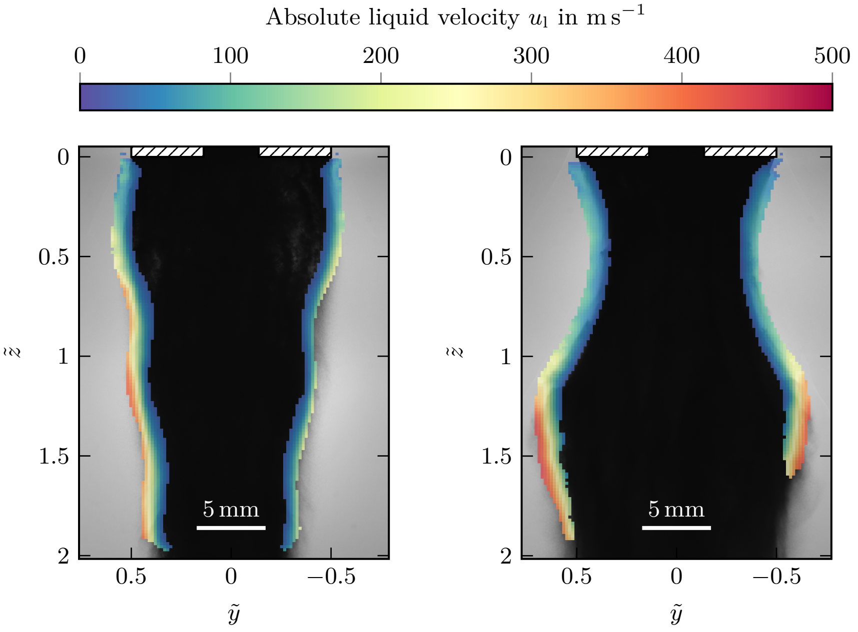

(a) $p_{\mathrm{t,g}} = (0.60 \pm 0.03)\,\mathrm{MPa}$ **(b)** $p_{\mathrm{t,g}} = (1.40 \pm 0.09)\,\mathrm{MPa}$

Figure 6.16: Time-averaged field of the absolute liquid velocity u_{l} for a constant liquid mass flow rate $\dot{m}_{\mathrm{l}}$ of $4\,\mathrm{kg\,min^{-1}}$ and two different gas stagnation pressures $p_{\mathrm{t,g}}$ obtained for the mid-field.

Finally, during the interaction between the liquid and the surrounding

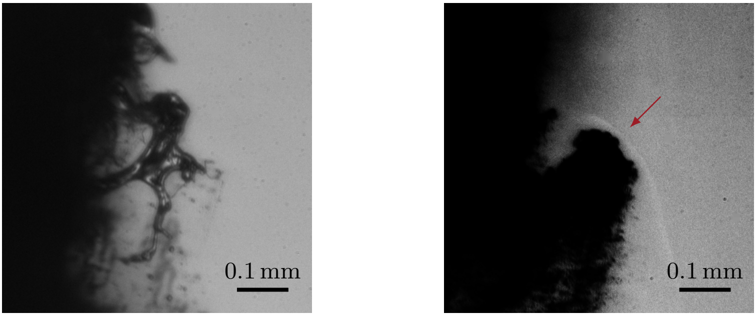

(a) Large ligaments **(b)** Shock formation

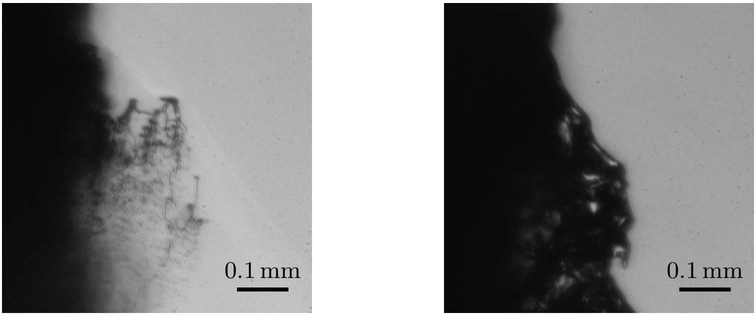

(c) Streamwise elongation **(d)** Surface instability

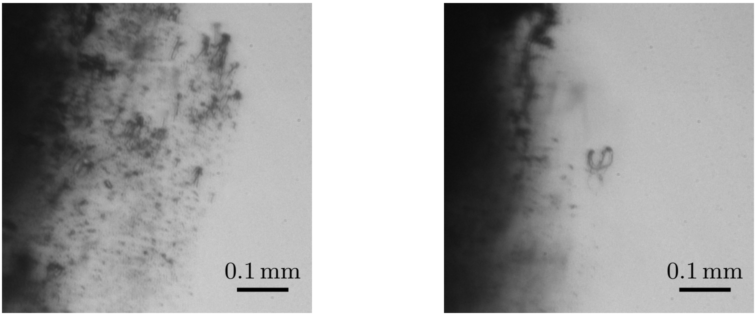

(e) Small droplets **(f)** Bag breakup

Figure 6.17: Overview of exemplary phenomena occurring during the interaction between the liquid and the surrounding high-velocity gas flow. For the shock formation (b), the contrast of the image has been artificially increased in order to show more detail. The shock is indicated by an additional arrow.

high-velocity gas jet a number of different phenomena can be observed. These are independent of the set point of operation and, therefore, characteristic of the secondary atomization under investigation. An overview consisting of six individual still images is given in Fig. 6.17. Here, the images have been cropped to allow for a magnified view of the phenomena of interest. Furthermore, the phenomena are listed in no particular order and the corresponding set points of operation are neither consistent not explicitly reported here. First, as has already been discussed in Section 6.1.2, the primary atomization results in droplets and ligaments spanning a wide range in size. Consequently, there are also particularly large ligaments undergoing secondary atomization, as can be seen in Fig. 6.17a. Second, the penetration of liquid into the supersonic gas flow leads to the formation of three-dimensional bow shocks, which additionally cause secondary atomzation. This is evident in Fig. 6.17b. Third, as a result of the high-velocity gas flow, droplets and ligaments are deformed and elongated in streamwise direction, which can be seen in Fig. 6.17c. Fourth, when large droplets and ligaments interact with the surrounding high-velocity gas jet, this leads to the development of instabilities on the liquid surface. An example is shown in Fig. 6.17d. Fifth, the secondary atomization results in a large number of particularly small droplets, as is evident in Fig. 6.17e. This is another indication of the importance of the secondary atomization for the final particle size distribution. Sixth, individual droplets undergo bag breakup in the high-velocity gas flow. This can be seen in Fig. 6.17f.

In summary, three main conclusions can be drawn from the considerations so far. First, the secondary atomization due to the interaction between the liquid and the surrounding high-velocity gas jet takes place in the shear layer of the gas jet. As a result, the liquid is exposed to a strong radial gradient of the absolute gas velocity $\partial u_{\mathrm{g}}/\partial y$ leading to asymmetric deformation and breakup. Second, the liquid is rapidly accelerated downstream by the high absolute gas velocities u_{g}, which results in a decrease in the absolute velocity difference Δu between the liquid and the gas. Third, depending on the liquid droplets and ligaments resulting from the primary atomization and the local gas flow field, a wide variety of phenomena occur during the secondary atomization. This complicates the development of suitable modeling approaches.

6.2.3 Shock Formation

As has been shown in Section 6.2.2, the interaction between the liquid and the surrounding supersonic gas jet results in the formation of three-dimensional bow shocks. This is an important finding, as the shock formation represents a novel breakup mechanism in the context of the supersonic close-coupled atomization process, which, to the authors' knowledge, has not been considered in existing approaches to modeling the atomization process. Consequently, the shock formation is studied in more detail in the following.

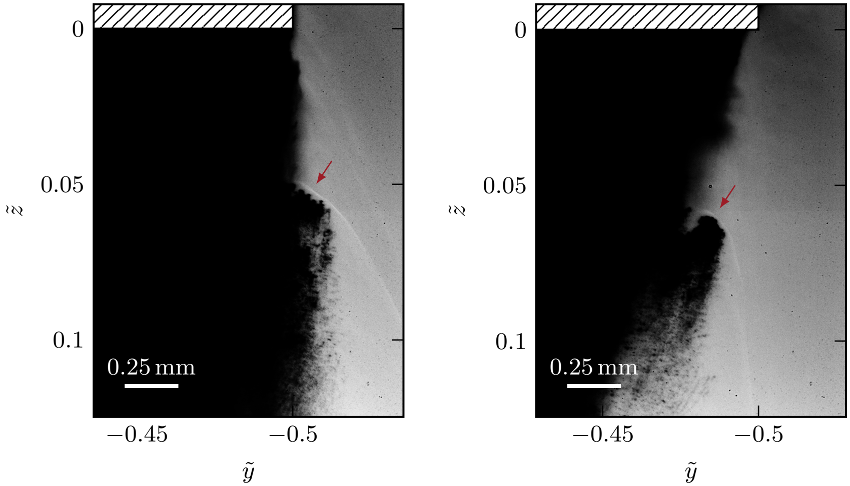

(a) $p_{\mathrm{t,g}} = (0.80 \pm 0.05)\,\mathrm{MPa}$, $\dot{m}_{\mathrm{l}} = (6.02 \pm 0.04)\,\mathrm{kg\,min^{-1}}$

(b) $p_{\mathrm{t,g}} = (1.40 \pm 0.10)\,\mathrm{MPa}$, $\dot{m}_{\mathrm{l}} = (6.02 \pm 0.05)\,\mathrm{kg\,min^{-1}}$

Figure 6.18: Exemplary still images of the liquid breakup due to the formation of a bow shock for two different set points of operation. The contrast of the images has been artificially increased in order to show more detail. The shocks are indicated by additional arrows.

As an example of the shock formation, two still images clearly showing the three-dimensional bow shock are presented in Fig. 6.18. The corresponding set points of operation are characterized by a gas stagnation pressure $p_{\mathrm{t,g}}$ of $(0.80 \pm 0.05)\,\mathrm{MPa}$ and $(1.40 \pm 0.10)\,\mathrm{MPa}$, respectively, and by a liquid mass flow rate $\dot{m}_{\mathrm{l}}$ of $(6.02 \pm 0.04)\,\mathrm{kg\,min^{-1}}$ and $(6.02 \pm 0.05)\,\mathrm{kg\,min^{-1}}$, respectively. In fact, the formation of shocks has been observed for all gas stagnation pressures $p_{\mathrm{t,g}}$ considered as part of this experimental investigation (see Section 3.1.4). This is reasonable given that the convergent-divergent gas nozzle described in Section 3.1.2 is operated in underexpanded condition and, therefore, produces jets which are supersonic in close proximity to the wake of the liquid nozzle (see Section 2.1).

As can be seen, the shocks form upstream of liquid which has penetrated further into the surrounding high-velocity gas jet, where it is exposed to supersonic flow conditions. Indeed, considering the gas stagnation pressure $p_{\mathrm{t,g}}$ of $1.4\,\mathrm{MPa}$ employed for capturing the still image shown in Fig. 6.18b, the local absolute gas velocity u_{g} in the location of the shock formation can be estimated to be about $490\,\mathrm{m\,s^{-1}}$. This estimate is based on numerical simulation results for the gas-only flow field provided by the research partner SMS as part of the IGSTC project PPAM and, therefore, neglects liquid mass loading effects on the flow field (see Sections 4.3.2 and 6.1). However, due to the short distance to the gas nozzle and the locally supersonic flow conditions, which prevent information transfer upstream, these effects are not expected to be significant. Furthermore, the liquid bulk velocity projected into the direction of the gas flow can be estimated to be about $54\,\mathrm{m\,s^{-1}}$, resulting in a relative velocity Δu of $436\,\mathrm{m\,s^{-1}}$. This estimate is based on the instantaneous field of the liquid velocity vector $\mathbf{u}_{\mathrm{l}}$ obtained for the double-frame image shown in Fig. 6.18b by means of the standard cross-correlation scheme described in Section 3.3.3. Finally, taking into account the local speed of sound a, also obtained from the numerical simulation results, this leads to a local Mach number Ma of about 1.8, which clearly confirms the supersonic conditions required for the formation of a shock.

In order to understand how the formation of a shock contributes to the secondary atomization, the mechanism is treated analytically. For this purpose the two-dimensional flow setup shown in Fig. 6.19 is considered, which is a simplification of the complex three-dimensional shock formation observed in Fig. 6.18. Here, a resting liquid volume of the initial characteristic length d_0 is suddenly exposed to a uniform supersonic gas flow characterized by the absolute gas velocity u_{g}, the gas pressure p_{g} and the gas density ρ_{g}. The gas is assumed to be calorically perfect with the heat capacity ratio κ and its flow to be inviscid. Furthermore, the liquid is assumed to be incompressible and characterized by the liquid density ρ_{l}, the liquid dynamic viscosity μ_{l} and the surface tension σ. As a result of the compressible nature of the

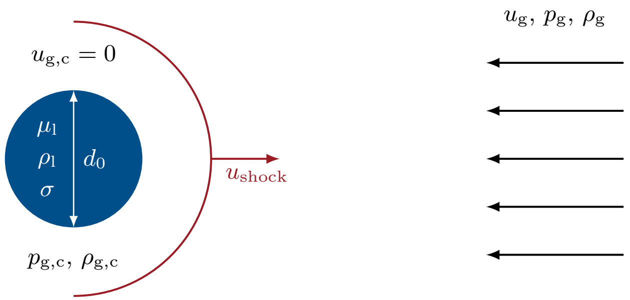

Figure 6.19: Schematic illustration of the shock formation due to the interaction between a liquid volume and a supersonic gas flow. (Adapted from Apell et al., 2022a.)

supersonic gas flow, a shock wave forms at the surface of the liquid volume during the initial interaction and travels upstream with the absolute shock velocity u_{shock}. As a simplification, the flow across the shock wave is assumed to be one-dimensional. Consequently, a normal shock wave is considered. This allows for formulating the conservation equations for mass, momentum and energy across the shock wave (Anderson et al., 1991):

$$\text{Mass:} \qquad \rho_{\text{g,c}} u_{\text{shock}} = \rho_{\text{g}} (u_{\text{g}} + u_{\text{shock}}) \tag{6.2}$$

$$\text{Momentum:} \qquad p_{\text{g,c}} + \rho_{\text{g,c}} u_{\text{shock}}^2 = p_{\text{g}} + \rho_{\text{g}} (u_{\text{g}} + u_{\text{shock}})^2 \tag{6.3}$$

$$\text{Energy:} \qquad \frac{\kappa}{\kappa - 1} \frac{p_{\text{g,c}}}{\rho_{\text{g,c}}} + \frac{u_{\text{shock}}^2}{2} = \frac{\kappa}{\kappa - 1} \frac{p_{\text{g}}}{\rho_{\text{g}}} + \frac{(u_{\text{g}} + u_{\text{shock}})^2}{2} \tag{6.4}$$

Here, $p_{\text{g,c}}$ and $\rho_{\text{g,c}}$ are the pressure and the density of the compressed gas downstream of the shock wave, respectively. Furthermore, the velocity of the compressed gas $u_{\text{g,c}}$ has been assumed to be zero, a condition that has to be met at the surface of the liquid volume during the initial formation of the shock wave considered here. Interestingly, the set of Eqs. (6.2) to (6.4) can be solved algebraically for the pressure difference across the shock wave $\Delta p_{\mathrm{shock}}$:

$$\begin{aligned}\Delta p_{\mathrm{shock}} &= p_{\mathrm{g,c}} - p_{\mathrm{g}} \qquad (6.5)\\ &= \frac{1}{4}\left\{\rho_{\mathrm{g}}\left(\kappa+1\right)u_{\mathrm{g}}^{2} + \rho_{\mathrm{g}}^{\frac{1}{2}}u_{\mathrm{g}}\left[16\kappa p_{\mathrm{g}} + \left(1+\kappa\right)^{2}\rho_{\mathrm{g}}u_{\mathrm{g}}^{2}\right]^{\frac{1}{2}}\right\}.\end{aligned}$$

Indeed, Eq. (6.5) is a remarkable result, since it allows for estimating the pressure difference across the shock wave $\Delta p_{\mathrm{shock}}$ solely from quantities characteristic of the supersonic gas flow without requiring knowledge of the absolute velocity of the shock wave u_{shock} and the state of the compressed gas. At this point, it is important to note that there is a distinct difference between the flow setup shown in Fig. 6.19 and a liquid volume exposed to a subsonic flow. That is, while for the subsonic flow the dynamic pressure $\frac{1}{2}\rho_{\mathrm{g}}u_{\mathrm{g}}^{2}$ of the gas flow determines the deformation of the liquid volume, for the supersonic flow the pressure difference across the forming shock wave $\Delta p_{\mathrm{shock}}$ is important.

In fact, employing the Bernoulli equation and neglecting the Laplace pressure due to the curvature of the surface of the liquid volume, an estimate of the characteristic velocity of the deformation of the liquid volume u_{def} can be obtained:

$$u_{\mathrm{def}} \approx \left(\frac{2\Delta p_{\mathrm{shock}}}{\rho_{\mathrm{l}}}\right)^{\frac{1}{2}}. \qquad (6.6)$$

Furthermore, the definition of the deformation velocity u_{def} allows for defining the appropriate local dimensionless numbers governing the deformation and the breakup of the liquid volume due to the interaction with a supersonic gas flow, which, besides the Mach number Ma and the Ohnesorge number Oh (as defined in Eqs. (2.1) and (2.5), respectively), are the deformation Weber number

$$We_{\mathrm{def}} = \frac{\rho_{\mathrm{l}}u_{\mathrm{def}}^{2}d_{0}}{\sigma} = \frac{2\Delta p_{\mathrm{shock}}d_{0}}{\sigma} \qquad (6.7)$$

and the deformation Reynolds number

$$Re_{\mathrm{def}} = \frac{\rho_{\mathrm{l}}u_{\mathrm{def}}d_{0}}{\mu_{\mathrm{l}}} = \frac{\left(2\Delta p_{\mathrm{shock}}\rho_{\mathrm{l}}\right)^{\frac{1}{2}}d_{0}}{\mu_{\mathrm{l}}}. \qquad (6.8)$$

In conclusion, the above considerations are a simplified description of how the formation of a shock during the interaction between a liquid volume and a supersonic gas flow leads to the deformation and breakup of the former. While this description is based on a number of assumptions and simplifications, it provides suitable means for formulating first models for this breakup mechanism.

6.3 Summary and Conclusions

In this chapter, the atomization process has been investigated. For this purpose, a distinction has been made between the primary atomization and the secondary atomization.

Concerning the primary atomization, it has been shown to be governed by the interaction between the liquid jet emanating form the liquid nozzle exit and the counter-flowing gas in the recirculation zone in the wake downstream of the liquid nozzle. The results have been found to be consistent with the sheet formation and fountain formation models existing in the literature. This indicates that substitute liquids allow the same mechanisms found for the atomization of liquid metal to be replicated. Notably, even though the liquid momentum flux at the liquid nozzle exit $q_{\mathrm{l,e}}$ has been revealed to affect the primary atomization, its effect on the resulting particle size has been found to be negligible in Section 5.3.2. This is a possible indication of the significance of the secondary atomization. In fact, it has been observed that the droplets and ligaments resulting from the primary atomization are subsequently drawn into the high-velocity gas jet.

In terms of the secondary atomization, the interaction between the liquid and the surrounding high-velocity gas flow has been found to be restricted to the shear layer of the gas jet, which indicates that the liquid being exposed to a strong radial gradient of the absolute gas velocity $\partial u_{\mathrm{g}}/\partial r$ is an important mechanism in the context of the supersonic close-coupled atomization. This is especially true considering that the characteristic length scale of some of the droplets and ligaments resulting from the primary atomization is comparable in size to the radial extent of the shear layer, leading to an asymmetric deformation and, ultimately, breakup. Furthermore, a variety of phenomena have been observed to occur during the secondary atomization, including the formation of surface instabilities and bag breakup. Notably, a new breakup mechanism due to the formation of a three-dimensional bow shock in the supersonic gas flow has been identified and described.

Part V

Closing

7 Closing Remarks

7.1 Summary and Conclusions

The application of the supersonic close-coupled atomization of molten metal for the production of high-quality metal powders is a complex process, which is becoming increasingly important economically. This has led to a strong demand for improved process control and efficiency and, consequently, has motivated efforts to develop reliable predictive modeling capabilities.

In this thesis, the supersonic close-coupled atomization has been investigated experimentally in a laboratory environment. For this purpose, a research facility has been set up as a one-to-one replica of an existing powder production plan. However, based on a dimensional analysis, the research facility employs air and various substitute liquids instead of inert gas and molten metal. This not only allows for extensive and systematic experimental investigations but it also improves the accessibility for a number of measurement techniques. In detail, the phase Doppler measurement technique has been employed for obtaining local particle size and velocity distributions, which are characteristic of the atomization result. Furthermore, high-speed imaging has been used to gain insight into the primary atomization. In addition, ultra-short illumination double-frame imaging has allowed for freezing the spray in time and investigating the mechanisms responsible for the secondary atomization, including the acceleration of the liquid. For these experimental investigations, the set point of operation defined by the gas stagnation pressure $p_{\mathrm{t,g}}$ and the liquid mass flow rate $\dot{m}_{\mathrm{l}}$ has been varied systematically in a wide range. Considering the physical properties of the liquid, the liquid dynamic viscosity μ_{l} has been varied by employing water and two aqueous glycerol solutions of different glycerol mass fractions.

The objectives of this thesis have been defined in Section 2.3 and serve as a guideline for the following discussion of the main conclusions drawn from the experimental investigation. Here, the focus is placed on conclusions relevant for the development of physics-based predictive modeling capabilities.

Justification for Employing Substitute Liquids

One of the major drivers of this thesis has been the idea to use substitute liquids instead of molten metal for investigating the supersonic close-coupled atomization. This has allowed for performing extensive and systematic experimental investigations. However, it is important to ensure that the results obtained from these investigations can be applied to the atomization of molten metal.

For this purpose, the research facility described in Section 3.1 has been based on the dimensional analysis presented in Section 3.1.1, which suggests that using certain substitute liquids allows for governing the same mechanisms present in the atomization of molten metal. In fact, many of the obtained results suggest that trends qualitatively similar to those for molten metal can be observed using substitute liquids. For instance, despite the large difference in the liquid density ρ_l between water and molten metal, the former has been shown in Section 4.3 to result in a two-way coupling between the liquid flow and the gas flow due to liquid mass loading effects, which is also characteristic of the atomization of molten metal. Furthermore, the radial distribution of the local particle size as well as the resulting log-normal particle size distributions have been found in Section 5.2 to be consistent with results for metal sprays in the literature. The same is true for the influence of the gas stagnation pressure on the particle size, which has been discussed in Section 5.3.1. Finally, the primary atomization of water has been observed in Section 6.1.2 to follow the sheet formation model and the fountain formation model, which are typically applied to the atomization of molten metal.

In conclusion, these similarities between the atomization of molten metal and the substitute liquids suggest that the latter can indeed be employed for investigating the supersonic close-coupled atomization of molten metal and allows for observing the same qualitative trends. This is an important result, since it suggests that atomization models developed and validated employing substitute liquids can serve as a useful starting point for modeling the atomization of molten metal.

Quantities Affecting the Atomization Result

Another advantage of employing substitute liquids for the atomization is that it allows for systematic investigations of the influence of the set point of operation on the atomization result. The set point of operation is well-defined by the gas stagnation pressure $p_{\mathrm{t,g}}$ and the liquid mass flow rate $\dot{m}_{\mathrm{l}}$. As an important feature of the research facility described in Section 3.1, it allows for decoupling the liquid flow and the gas flow and, therefore, for independently adjusting the two parameters characterizing the set point of operation. Notably, this is despite the fact that there exists a two-way coupling between the liquid flow and the gas flow, as has been confirmed in Section 4.3.

Consistent with the existing literature, the particle size has been shown in Section 5.3.1 to depend on the gas stagnation pressure $p_{\mathrm{t,g}}$. That is, increasing the gas stagnation pressure $p_{\mathrm{t,g}}$ provides means for reducing the overall particle size as well as its dispersion. However, in the parameter range considered, the particle size has been found in Section 5.3.2 to be more sensitive to changes in the liquid mass flow rate $\dot{m}_{\mathrm{l}}$. In fact, decreasing the liquid mass flow rate $\dot{m}_{\mathrm{l}}$ effectively decreases the overall particle size as well as its dispersion. Importantly, for a constant liquid mass flow rate $\dot{m}_{\mathrm{l}}$, the influence of the diameter of the liquid nozzle d_{l} on the particle size has been observed to be negligible. Furthermore, the dependence of the particle size on the gas-to-liquid ratio GLR has been investigated in Section 5.3.3. Notably, the particle size has been found not to be an unambiguous function of the gas-to-liquid ratio GLR, but, instead, to explicitly depend on both the gas stagnation pressure $p_{\mathrm{t,g}}$ and the liquid mass flow rate $\dot{m}_{\mathrm{l}}$.

In terms of the physical properties of the liquid, the effect of the liquid dynamic viscosity μ_{l} on the particle size has been investigated in Section 5.4 employing water and two aqueous glycerol solutions of different glycerol mass fractions. For liquid Reynolds numbers Re_{l} typical for the supersonic close-coupled atomization process, the differences between the particle size distributions obtained have been found to be negligible.

In conclusion, these results suggest that both the gas stagnation pressure $p_{\mathrm{t,g}}$ and the liquid mass flow rate $\dot{m}_{\mathrm{l}}$ are individually important parameters in determining the resulting particle size and, therefore, need to be included in models describing the atomization process. This is especially important considering that the gas-to-liquid ratio GLR, which has often been employed for modeling the atomization process (see Section 2.2.2), is not suitable as a single parameter for describing the set point of operation. Similarly, the results obtained question the use of the liquid nozzle diameter d_l as the length scale characteristic of the supersonic close-coupled atomization process. Furthermore, these results suggest that the liquid dynamic viscosity μ_l or, in terms of dimensionless numbers, the liquid Reynolds number Re_l can be neglected when modeling the atomization process. This leads to the assumption that the surface tension σ or, in terms of dimensionless numbers, the gas Weber number We_g is a more important parameter in determining the particle size. Finally, considering the industrial application of the supersonic close-coupled atomization of molten metal for the production of metal powders, these results indicate that a production plant design allowing for actively adjusting the liquid mass flow rate $\dot{m}_\mathrm{l}$ provides means for improving the process control.

Insights into the Primary Atomization

In supersonic close-coupled atomization, the primary atomization is characterized by the interaction between the liquid jet emanating from the liquid nozzle and the recirculating gas flow in the wake downstream of the liquid nozzle.

Consistent with the existing literature, the primary atomization has been observed in Section 6.1.2 to follow the sheet formation model and the fountain formation model. Which model is more appropriate has been found in Section 6.1.3 to depend on the strength of the recirculating gas flow and the liquid momentum flux at the liquid nozzle exit $q_\mathrm{l,e}$. That is, an increase in the latter promotes the formation of a fountain, while an increase in the former has the opposite effect. Indeed, the liquid momentum flux at the liquid nozzle exit $q_\mathrm{l,e}$ has an influence on the spray formation in close proximity to the liquid nozzle, as has been shown in Section 4.3.2. This is due to the fact that it influences the local amount of liquid mass m_l acting as a resistance to the expansion of the surrounding high-velocity gas jet. Notably, the visualization of the primary atomization presented in Section 6.1.2 indicates that most of the liquid mass m_l, which is characterized by a wide range of length scales, eventually interacts with the gas jet.

In conclusion, these results suggest that even though the primary atomization can be actively influenced by adjusting the set point of operation, the subsequent interaction between the resulting droplets and ligaments and the surrounding high-velocity gas jet still takes place. This is especially important considering that while the liquid momentum flux at the liquid nozzle exit $q_{\mathrm{l,e}}$ affects the mechanism responsible for the primary atomization, it has been found in Section 5.3.2 not to have an influence on the resulting particle size. This is a possible indication of the significance of the secondary atomization for the atomization result and, consequently, also for the development of predictive modeling capabilities.

Insights into the Secondary Atomization

Considering the secondary atomization, the interaction between the droplets and the ligaments resulting from the primary atomization and the surrounding high-velocity gas jet has been investigated in close proximity to the liquid nozzle.

By means of visualization, the interaction of the liquid and the surrounding high-velocity gas jet has been observed in Section 6.2.2 to be restricted to the shear layer formed by the gas jet. That is, the liquid is exposed to a strong gradient radial of the absolute gas velocity $\partial u_{\mathrm{g}}/\partial r$, the radial extent of which is comparable in size to the characteristic length scale of larger droplets and ligaments resulting from the primary atomization. This results in an asymmetric deformation and, ultimately, breakup of the liquid. Furthermore, the high absolute gas velocities u_{g} have been found to rapidly accelerate the droplets resulting from the secondary atomization in downstream direction. In addition, a number of different phenomena occurring during the secondary atomization have been identified in Section 6.2.2, including the formation of surface instabilities and bag breakup. Notably, a new breakup mechanism has been observed and described in Section 6.2.3, which is due to the formation of a three-dimensional bow shock in the supersonic gas flow.

In conclusion, these results suggest that one of the major mechanisms responsible for the secondary atomization is the asymmetric interaction between the liquid and the shear layer of the surrounding high-velocity gas jet. This mechanism has not been studied in detail in the existing literature, especially considering the particularly high absolute gas velocities u_{g} found in supersonic close-coupled atomization. Consequently, fundamental investigations of this mechanism are necessary for the development of atomization models. The same appears to be true for the liquid breakup due to the formation of a bow shock, which is a characteristic of the supersonic close-coupled atomization process.

7.2 Recommendations for Future Research

The insights into the supersonic close-coupled atomization process gained in this thesis serve the purpose of providing a foundation for the future development of novel physics-based modeling capabilities. Nevertheless, the results and conclusions summarized in Section 7.1 have also raised further questions, which are worth investigating in future work. A brief list of recommendations for suitable research questions and their motivation is given in the following.

While the liquid momentum flux at the liquid nozzle exit $q_{\mathrm{l,e}}$ has been found in Section 4.3.2 to affect the spray formation in close proximity to the liquid nozzle due to mass loading effects and in Section 6.1 to determine the primary atomization in the wake downstream of the liquid nozzle, its significance for the atomization result, that is, the resulting particle size, has been found in Section 5.3.2 to be negligible. Ultimately, this raises the question how significant the primary atomization is in determining the resulting particle size distribution. This is crucial for the development of atomization models suitable for industrial applications, since resolving the primary atomization affects the computational cost.

Furthermore, besides the gas stagnation pressure $p_{\mathrm{t,g}}$, the liquid mass flow rate $\dot{m}_{\mathrm{l}}$ has been found in Section 5.3.2 to be an important parameter in determining the particle size distribution resulting from the atomization process. However, since the imaging techniques employed for the visualization of the atomization process do not allow for determining how the liquid mass flow rate $\dot{m}_{\mathrm{l}}$ affects the atomization process and, in particular, the resulting local particle size, the physical mechanism responsible for the importance of the liquid mass flow rate $\dot{m}_{\mathrm{l}}$ is not full understood. Consequently, additional experimental investigations employing suitable quantitative measurement techniques with sufficient spatial and temporal resolution are required.

Considering the physical properties of the liquid, the results for the particle size distribution presented in Section 5.4 suggest that, for liquid Reynolds numbers Re_l typical for the supersonic close-coupled atomization, the liquid dynamic viscosity μ_l has negligible influence on the atomization result. While this suggests that the surface tension σ and, in terms of dimensionless numbers, the gas Weber number We_g, is a more important quantity affecting the particle size, this remains to be confirmed experimentally. In fact, this requires additional experimental investigations employing different substitute liquids. Since achieving a surface tension σ significantly higher than that of water is challenging without resorting to liquid metal, it may be necessary to employ liquids characterized by a lower surface tension σ. However, whether this maintains the comparability with liquid metal has to be verified.

The investigation of the secondary atomization due to the interaction between the liquid and the surrounding high-velocity gas jet in Section 6.2 has revealed that the liquid breaks up in the shear layer of the gas jet, that is, it is exposed to a strong radial gradient of the absolute gas velocity $\partial u_\mathrm{g}/\partial r$. Assuming that this mechanism is important for the secondary atomization in the supersonic close-coupled atomization process, additional fundamental experiments are required in order to understand and model the basic physics involved in the breakup of a liquid volume in a strong shear flow. In addition, the formation of a three-dimensional bow shock has been found in Section 6.2 to contribute to the secondary atomization. While a first analytical description of this mechanism has been proposed in Section 6.2.3, additional fundamental experiments are required for an extensive validation. Both of these experiments are likely to improve the understanding of the supersonic close-coupled atomization and, therefore, are crucial for the development of predictive modeling capabilities.

Bibliography

Adelberg, M. (1968). Mean drop size resulting from the injection of a liquid jet into a high-speed gas stream. *AIAA Journal*, *6*(6), 1143–1147. https://doi.org/10.2514/3.4686

Aksoy, A., & Ünal, R. (2006). Effects of gas pressure and protrusion length of melt delivery tube on powder size and powder morphology of nitrogen gas atomised tin powders. *Powder Metallurgy*, *49*(4), 349–354. https://doi.org/10.1179/174329006X89425

Albrecht, H.-E., Borys, M., Tropea, C., & Damaschke, N. (2003). *Laser Doppler and phase Doppler measurement techniques*. Springer. https://doi.org/10.1007/978-3-662-05165-8

Allimant, A., Planche, M. P., Bailly, Y., Dembinski, L., & Coddet, C. (2009). Progress in gas atomization of liquid metals by means of a de Laval nozzle. *Powder Technology*, *190*(1-2), 79–83. https://doi.org/10.1016/j.powtec.2008.04.071

Amatriain, A., Urionabarrenetxea, E., Avello, A., & Martín, J. M. (2022). Multiphase model to predict particle size distributions in close-coupled gas atomization. *International Journal of Multiphase Flow*, *154*, 104138. https://doi.org/10.1016/j.ijmultiphaseflow.2022.104138

Anderson, I. E., & Achelis, L. (2017). Two fluid atomization fundamentals. In H. Henein, V. Uhlenwinkel, & U. Fritsching (Eds.), *Metal sprays and spray deposition* (pp. 49–88). Springer International Publishing. https://doi.org/10.1007/978-3-319-52689-8_3

Anderson, I. E., & Figliola, R. S. (1988). Observations of gas atomization process dynamics. In P. U. Gummeson (Ed.), *Proceedings of the 1988 international powder metallurgy conference* (pp. 205–223). Metal Powder Industries Federation.

Anderson, I. E., Figliola, R. S., & Morton, H. (1991). Flow mechanisms in high pressure gas atomization. *Materials Science & Engineering A*, *148*(1), 101–114. https://doi.org/10.1016/0921-5093(91)90870-S

Anderson, I. E., Rieken, J., Meyer, J., Byrd, D., & Heidloff, A. (2011). *Visualization of atomization gas flow and melt break-up effects in response to nozzle design* (tech. rep.). Ames National Laboratory. Ames (IA, USA).

Anderson, I. E., & Terpstra, R. L. (2002). Progress toward gas atomization processing with increased uniformity and control. *Materials Science & Engineering A*, *326*(1), 101–109. https://doi.org/10.1016/S0921-5093(01)01427-7

Anderson, I. E., Terpstra, R. L., & Figliola, R. S. (2005). Visualization of enhanced primary atomization for powder size control. In Metal Powder Industries Federation (Ed.), *Proceedings of the 2005 international conference on powder metallurgy & particulate materials* (pp. 1–17, Vol. 1). Metal Powder Industries Federation.

Anderson, J. D. (1990). *Modern compressible flow: With historical perspective* (2nd ed.). McGraw-Hill.

Antipas, G. S. E. (2006). Modelling of the break up mechanism in gas atomization of liquid metals. Part I: The surface wave formation model. *Computational Materials Science*, *35*(4), 416–422. https://doi.org/10.1016/j.commatsci.2005.03.009

Antipas, G. S. E. (2009). Modelling of the break up mechanism in gas atomization of liquid metals. Part II: The gas flow model. *Computational Materials Science*, *46*(4), 955–959. https://doi.org/10.1016/j.commatsci.2009.04.046

Apell, N. (2019). *Experimental investigation of the influence of mass flow ratio in close-coupled atomization on droplet size distribution* [Master thesis]. Technical University of Darmstadt. Institute for Fluid Mechanics and Aerodynamics.

Apell, N., Roisman, I. V., Tropea, C., & Hussong, J. (2022a). Modeling of the characteristic size of drops in a spray produced by the supersonic gas atomization process. In Institute for Liquid Atomization and Spray Systems (Ed.), *Proceedings of the 31st European conference on liquid atomization & spray systems* (p. XII).

Apell, N., Tropea, C., Roisman, I. V., & Hussong, J. (2021). Experimental investigation of a close-coupled atomizer using the phase Doppler measurement technique. In Institute for Liquid Atomization and Spray Systems (Ed.), *Proceedings of the 15th international conference on liquid atomization & spray systems* (p. 96, Vol. 1). https://doi.org/10.2218/iclass.2021.5856

Apell, N., Tropea, C., Roisman, I. V., & Hussong, J. (2022b). Application of the phase Doppler measurement technique for the characterization of supersonic gas atomization. In Center for Innovation, Technology and Policy Research, IN+ (Ed.), *Proceedings of the 20th international symposium on applications of laser and imaging techniques to fluid mechanics* (pp. 1302–1321). https://doi.org/10.55037/lxlaser.20th.233

Apell, N., Tropea, C., Roisman, I. V., & Hussong, J. (2023). Experimental investigation of a supersonic close-coupled atomizer employing the phase doppler measurement technique. *International Journal of Multiphase Flow*, *167*, 104544. https://doi.org/10.1016/j.ijmultiphaseflow.2023.104544

Arachchilage, K. H., Haghshenas, M., Park, S., Le Zhou, Sohn, Y., McWilliams, B., Cho, K., & Kumar, R. (2019). Numerical simulation of high-pressure gas atomization of two-phase flow: Effect of gas pressure on droplet size distribution. *Advanced Powder Technology*, *30*(11), 2726–2732. https://doi.org/10.1016/j.apt.2019.08.019

Ashgriz, N. (Ed.). (2011). *Handbook of atomization and sprays: Theory and applications*. Springer. https://doi.org/10.1007/978-1-4419-7264-4

Bachalo, W. D., & Houser, M. (1984). Phase/Doppler spray analyzer for simultaneous measurements of drop size and velocity distributions. *Optical Engineering*, *23*. https://doi.org/10.1117/12.7973341

Baram, J. C., Veistinen, M. K., Lavernia, E. J., Abinante, M., & Grant, N. J. (1988). Pressure build-up at the metal delivery tube orifice in ultrasonic gas atomization. *Journal of Materials Science*, *23*(7), 2457–2463. https://doi.org/10.1007/BF01111903

Bauckhage, K. (1992). Atomization of metallic melts. *Chemie Ingenieur Technik*, *64*(4), 322–332. https://doi.org/10.1002/cite.330640404

Benedict, L. H., & Gould, R. D. (1996). Towards better uncertainty estimates for turbulence statistics. *Experiments in Fluids*, *22*(2), 129–136. https://doi.org/10.1007/s003480050030

Bergmann, D., Fritsching, U., & Bauckhage, K. (2000). A mathematical model for cooling and rapid solidification of molten metal droplets. *International Journal of Thermal Sciences*, *39*(1), 53–62. https://doi.org/10.1016/S1290-0729(00)00195-1

Biancaniello, F. S., Conway, J. J., Espina, P. I., Mattingly, G. E., & Ridder, S. D. (1990). Particle size measurement of inert-gas-atomized powder. *Materials Science & Engineering A*, *124*(1), 9–14. https://doi.org/10.1016/0921-5093(90)90329-2

Biancaniello, F. S., Espina, P. I., Mattingly, G. E., & Ridder, S. D. (1989). A flow visualization study of supersonic inert gas-metal atomization. *Materials Science & Engineering A*, *119*, 161–168. https://doi.org/10.1016/0921-5093(89)90535-2

Bigg, T. D., & Mullis, A. M. (2020). Spatially resolved velocity mapping of the melt plume during high-pressure gas atomization of liquid metals. *Metallurgical and Materials Transactions B*. https://doi.org/10.1007/s11663-020-01899-5

Birouk, M., & Lekic, N. (2009). Liquid jet breakup in quiescent atmosphere: A review. *Atomization and Sprays*, *19*(6), 501–528. https://doi.org/10.1615/AtomizSpr.v19.i6.20

Blagojević, B., & Bajsić, I. (1996). A symplified analysis of measurement uncertainty of spherical particle diameters using a standard phase-Doppler anemometer. *Strojniški vestnik - Journal of Mechanical Engineering*, *42*(5-6), 173–186.

Bradley, D. (1973a). On the atomization of a liquid by high-velocity gases: II. *Journal of Physics D: Applied Physics*, *6*(18), 2267–2272. https://doi.org/10.1088/0022-3727/6/18/312

Bradley, D. (1973b). On the atomization of liquids by high-velocity gases. *Journal of Physics D: Applied Physics*, *6*(14), 1724–1736. https://doi.org/10.1088/0022-3727/6/14/309

Brennen, R. (2022). *State of the PM industry in North America - 2022* (Metal Powder Industries Federation, Ed.; tech. rep.). Metal Powder Industries Federation. Princeton (NJ, USA).

Buchhave, P., George, W. K., & Lumley, J. L. (1979). The measurement of turbulence with the laser-Doppler anemometer. *Annual Review of Fluid Mechanics*, *11*(1), 443–503. https://doi.org/10.1146/annurev.fl.11.010179.002303

Bürger, M., Berg, E., Cho, S. H., & Schatz, A. (1989). Fragmentation processes in gas and water atomization plants for process optimization purposes: Part I: Discussion of the main fragmentation processes. *Powder Metallurgy International*, *21*(6), 10–15.

Bürger, M., Berg, E., Cho, S. H., & Schatz, A. (1992). Analysis of fragmentation processes in gas and water atomization plants for process optimization purposes: Part II: Modeling of growth and stripping of capillary waves in parallel shear flows - the basic fragmentation mechanism. *Powder Metallurgy International*, *24*(1), 32–38.

Carter Jr., W. T., & Jones, M. G. (1993). *Direct laser sintering of metals* (General Electric, Ed.; tech. rep.). General Electric - Corporate Research and Development Center.

Cheng, N.-S. (2008). Formula for the viscosity of a glycerol-water mixture. *Industrial & Engineering Chemistry Research*, *47*, 3285–3288. https://doi.org/10.1021/ie071349z

Chutkey, K., Vasudevan, B., & Balakrishnan, N. (2014). Analysis of annular plug nozzle flowfield. *Journal of Spacecraft and Rockets*, *51*, 478–490. https://doi.org/10.2514/1.A32617

Costa da Silva, F., Leite de Lima, M., & Fiocco Colombo, G. (2022). Evaluation of a mathematical model based on Lubanska equation to predict particle size for close-coupled gas atomization of 316L stainless steel. *Materials Research*, *25*. https://doi.org/10.1590/1980-5373-mr-2021-0364

Crist, S., Glass, D. R., & Sherman, P. M. (1966). Study of the highly underexpanded sonic jet. *AIAA Journal*, *4*(1), 68–71. https://doi.org/10.2514/3.3386

Dantec Dynamics A/S. (2011). *LDA and PDA reference manual* (Dantec Dynamics A/S, Ed.; tech. rep. No. 9040U1312). Dantec Dynamics A/S. Skovlunde (Denmark).

Dawes, J., Bowerman, R., & Trepleton, R. (2015). Introduction to the additive manufacturing powder metallurgy supply chain. *Johnson Matthey Technology Review*, *59*(3), 243–256. https://doi.org/10.1595/205651315X688686

Domnick, J., Raimann, J., Schutte, K., & Wolf, G. (1998). Phase Doppler anemometry in inert and liquid gas atomization. *Atomization and Sprays*, *8*(5), 521–546. https://doi.org/10.1615/AtomizSpr.v8.i5.30

Domnick, J., Raimann, J., Wolf, G., Berlemont, A., & Cabot, M.-S. (1997). On-line process control in melt spraying using phase-Doppler anemometry. *International Journal of Fluid Mechanics Research*, *24*(4-6), 694–706. https://doi.org/10.1615/InterJFluidMechRes.v24.i4-6.250

Edwards, R. V. (1987). Report of the special panel on statistical particle bias problems in laser anemometry. *Journal of Fluids Engineering*, *109*(2), 89–93. https://doi.org/10.1115/1.3242646

Efron, B., & Tibshirani, R. (1994). *An introduction to the bootstrap* (Vol. 57). Chapman & Hall. https://doi.org/10.1201/9780429246593

Espina, P., & Piomelli, U. (1998). Study of the gas jet in a close-coupled gas-metal atomizer. In American Institute of Aeronautics and Astronautics (Ed.), *Proceedings of the 36th AIAA aerospace sciences meeting and exhibit.* American Institute of Aeronautics and Astronautics. https://doi.org/10.2514/6.1998-959

Firmansyah, D. A., Kaiser, R., Zahaf, R., Coker, Z., Choi, T.-Y., & Lee, D. (2014). Numerical simulations of supersonic gas atomization of liquid metal droplets. *Japanese Journal of Applied Physics*, *53*(5S3), 05HA09. https://doi.org/10.7567/JJAP.53.05HA09

Franquet, E., Perrier, V., Gibout, S., & Bruel, P. (2015). Free underexpanded jets in a quiescent medium: A review. *Progress in Aerospace Sciences*, *77*, 25–53. https://doi.org/10.1016/j.paerosci.2015.06.006

Freedman, D., & Diaconis, P. (1981). On the histogram as a density estimator: L2 theory. *Zeitschrift für Wahrscheinlichkeitstheorie und Verwandte Gebiete*, *57*(4), 453–476. https://doi.org/10.1007/BF01025868

German Institute for Standardization. (2022). *Additive manufacturing - general principles - fundamentals and vocabulary.* (DIN EN ISO/ASTM 52900).

Gibson, I., Rosen, D., Stucker, B., & Khorasani, M. (2021). *Additive manufacturing technologies* (3rd ed.). Springer International Publishing. https://doi.org/10.1007/978-3-030-56127-7

Hagemann, G., Immich, H., & Terhardt, M. (1998). Flow phenomena in advanced rocket nozzles - the plug nozzle. In American Institute of Aeronautics and Astronautics (Ed.), *Proceedings of the 34th AIAA/ASME/SAE/ASEE joint propulsion conference and exhibit*. American Institute of Aeronautics and Astronautics. https://doi.org/10.2514/6.1998-3522

Hecht, E. (2017). *Optics* (5th ed.). Pearson Education Inc.

Heck, U., Fritsching, U., & Bauckhage, K. (2000). Gas flow effects on twin-fluid atomization of liquid metals. *Atomization and Sprays*, *10*(1), 25–46. https://doi.org/10.1615/AtomizSpr.v10.i1.20

Heinlein, J., & Fritsching, U. (2006). Droplet clustering in sprays. *Experiments in Fluids*, *40*(3), 464–472. https://doi.org/10.1007/s00348-005-0087-4

Henein, H., Uhlenwinkel, V., & Fritsching, U. (Eds.). (2017). *Metal sprays and spray deposition*. Springer International Publishing. https://doi.org/10.1007/978-3-319-52689-8

Hernandez, F., Riedemann, T., Tiarks, J., Kong, B., Anderson, I. E., Ward, T., & Regele, J. D. (2018). Simulation of primary breakup in planar close-coupled gas atomization. In Institute for Liquid Atomization and Spray Systems (Ed.), *Proceedings of the 14th international conference on liquid atomization & spray systems*.

Hernandez, F., Riedemann, T., Tiarks, J., Kong, B., Regele, J. D., Ward, T., & Anderson, I. E. (2019). Numerical simulation and validation of gas and molten metal flows in close-coupled gas atomization. In The Minerals, Metals & Materials Society (Ed.), *Supplemental proceedings of the TMS 2019 annual meeting & exhibition* (pp. 1507–1519). Springer International Publishing. https://doi.org/10.1007/978-3-030-05861-6_143

Hinze, J. O. (1955). Fundamentals of the hydrodynamic mechanism of splitting in dispersion processes. *AIChE Journal*, *1*(3), 289–295. https://doi.org/10.1002/aic.690010303

Hoesel, W., & Rodi, W. (1977). New biasing elimination method for laser-Doppler velocimeter counter processing. *Review of Scientific Instruments*, *48*(7), 910–919. https://doi.org/10.1063/1.1135131

Hoyas, S., Gil, A., Margot, X., Khuong-Anh, D., & Ravet, F. (2013). Evaluation of the Eulerian-Lagrangian spray atomization (ELSA) model in spray simulations: 2D cases. *Mathematical and Computer Modelling*, *57*(7-8), 1686–1693. https://doi.org/10.1016/j.mcm.2011.11.006

Hsiang, L.-P., & Faeth, G. M. (1992). Near-limit drop deformation and secondary breakup. *International Journal of Multiphase Flow*, *18*(5), 635–652. https://doi.org/10.1016/0301-9322(92)90036-G

Hsiang, L.-P., & Faeth, G. M. (1995). Drop deforamtion and breakup due to shock wave and steady disturbances. *International Journal of Multiphase Flow*, *21*(4), 545–560. https://doi.org/10.1016/0301-9322(94)00095-2

Ingebo, R. D. (1981). *Capillary and acceleration wave breakup of liquid jets in axial-flow airstreams* (National Aeronautics and Space Administration, Ed.; tech. rep. No. 1791). NASA Lewis Research Center. Cleveland (OH, USA).

International Bureau of Weights and Measures. (2008). Evaluation of measurement data: Guide to the expression of uncertainty in measurement.

Jeyakumar, M., Kumar, S., & Gupta, G. S. (2009). The influence of processing parameters on characteristics of an aluminum alloy spray deposition. *Materials and Manufacturing Processes*, *24*(6), 693–699. https://doi.org/10.1080/10426910902769384

Kaiser, R., Li, C., Yang, S., & Lee, D. (2018). A numerical simulation study of the path-resolved breakup behaviors of molten metal in high-pressure gas atomization: With emphasis on the role of shock waves in the gas/molten metal interaction. *Advanced Powder Technology*, *29*(3), 623–630. https://doi.org/10.1016/j.apt.2017.12.003

Kamenov, D., Achelis, L., Uhlenwinkel, V., & Fritsching, U. (2021). Investigating the performance of an airblast pressure swirl atomizer. In Institute for Liquid Atomization and Spray Systems (Ed.), *Proceedings of the 15th international conference on liquid atomization & spray systems* (p. 219, Vol. 1). https://doi.org/10.2218/iclass.2021.5963

Kirmse, C., & Chaves, H. (2016). Measurements of the velocity of drops in a melt atomization process using particle image velocimetry. *Steel Research International*, *87*(10), 1295–1301. https://doi.org/10.1002/srin.201500360

Kishidaka, H. (1972). Theory and production of atomized iron powder. In Japan Society for Powder and Powder Metallurgy (Ed.), *Proceedings of the multidisciplinary meeting on sintered metals and magnetic materials* (pp. 19–24, Vol. 2).

Lampa, A., & Fritsching, U. (2011). Spray structure analysis in atomization processes in enclosures for powder production. *Atomization and Sprays*, *21*(9), 737–752. https://doi.org/10.1615/AtomizSpr.2012003760

Lampa, A., & Fritsching, U. (2013). Large eddy simulation of the spray formation in confinements. *International Journal of Heat and Fluid Flow*, *43*, 26–34. https://doi.org/10.1016/j.ijheatfluidflow.2013.04.014

Lanz, O., Johnson, C. C., & Morikawa, S. (1971). Directional laser Doppler velocimeter. *Applied optics*, *10*(4), 884–888. https://doi.org/10.1364/AO.10.000884

Lasheras, J. C., & Hopfinger, E. J. (2000). Liquid jet instability and atomization in a coaxial gas stream. *Annual Review of Fluid Mechanics*, *32*(1), 275–308. https://doi.org/10.1146/annurev.fluid.32.1.275

Lasheras, J. C., Villermaux, E., & Hopfinger, E. J. (1998). Break-up and atomization of a round water jet by a high-speed annular air jet. *Journal of Fluid Mechanics*, *357*, 351–379. https://doi.org/10.1017/S0022112097008070

Le, T., Stefaniuk, R., Henein, H., & Huot, J. Y. (1999). Measurement and analysis of melt flowrate in gas atomization. *International Journal of Powder Metallurgy*, *35*(1), 51–59.

Lefebvre, A. H., & McDonell, V. G. (2017). *Atomization and sprays* (2nd ed.). CRC Press. https://doi.org/10.1201/9781315120911

Li, X.-G., Zhu, Q., Shu, S., Fan, J.-Z., & Zhang, S.-M. (2019). Fine spherical powder production during gas atomization of pressurized melts through melt nozzles with a small inner diameter. *Powder Technology*, *356*, 759–768. https://doi.org/10.1016/j.powtec.2019.09.023

Lin, S. P., & Reitz, R. D. (1998). Drop and spray formation from a liquid jet. *Annual Review of Fluid Mechanics*, *30*(1), 85–105. https://doi.org/10.1146/annurev.fluid.30.1.85

Longo, S. G. (2021). *Principles and applications of dimensional analysis and similarity*. Springer International Publishing. https://doi.org/10.1007/978-3-030-79217-6

Lubanska, H. (1970). Correlation of spray ring data for gas atomization of liquid metals. *JOM*, *22*(2), 45–49. https://doi.org/10.1007/BF03355938

Luh, M. F., Vogl, N., Odenthal, H.-J., Roisman, I. V., & Tropea, C. (2018). Focusing Schlieren imaging in close-coupled atomization: Comparison of experimental results with numerical simulations. In Institute for Liquid Atomization and Spray Systems (Ed.), *Proceedings of the 14th international conference on liquid atomization & spray systems* (p. 390).

Luo, S., Wang, H., Gao, Z., Wu, Y., & Wang, H. (2021). Interaction between high-velocity gas and liquid in gas atomization revealed by a new coupled simulation model. *Materials & Design*, *212*, 110264. https://doi.org/10.1016/j.matdes.2021.110264

Mandal, S., Sadeghianjahromi, A., & Wang, C.-C. (2022). Experimental and numerical investigations on molten metal atomization techniques – a critical review. *Advanced Powder Technology*, *33*(11), 103809. https://doi.org/10.1016/j.apt.2022.103809

Markus, S., & Fritsching, U. (2006). Discrete break-up modeling of melt sprays. *International Journal of Powder Metallurgy*, *42*, 23–32.

Markus, S., Fritsching, U., & Bauckhage, K. (2002). Jet break up of liquid metal in twin fluid atomisation. *Materials Science & Engineering A*, *326*(1), 122–133. https://doi.org/10.1016/S0921-5093(01)01422-8

Mates, S. P., & Settles, G. S. (1996). High-speed imaging of liquid metal atomization by two different close-coupled nozzles. *Advances in Powder Metallurgy and Particulate Materials*, *1*, 67–80.

Mates, S. P., & Settles, G. S. (2005a). A study of liquid metal atomization using close-coupled nozzles, part 1: Gas dynamic behavior. *Atomization and Sprays*, *15*(1), 19–40. https://doi.org/10.1615/AtomizSpr.v15.i1.20

Mates, S. P., & Settles, G. S. (2005b). A study of liquid metal atomization using close-coupled nozzles, part 2: Atomization behavior. *Atomization and Sprays*, *15*(1), 41–59. https://doi.org/10.1615/AtomizSpr.v15.i1.30

McLaughlin, D. K., & Tiederman, W. G. (1973). Biasing correction for individual realization of laser anemometer measurements in turbulent flows. *Physics of Fluids*, *16*(12), 2082–2088. https://doi.org/10.1063/1.1694269

Mehrotra, S. P. (1981a). Mathematical modelling of gas atomization process for metal powder production: Part 1. *Powder Metallurgy International*, *13*(2), 80–84.

Mehrotra, S. P. (1981b). Mathematical modelling of gas atomization process for metal powder production: Part 2. *Powder Metallurgy International*, *13*(3), 132–135.

Meinhart, C. D., Wereley, S. T., & Santiago, J. G. (2000). A PIV algorithm for estimating time-averaged velocity fields. *Journal of Fluids Engineering*, *122*(2), 285–289. https://doi.org/10.1115/1.483256

Mi, J., Figliola, R. S., & Anderson, I. E. (1996). A numerical simulation of gas flow field effects on high pressure gas atomization due to operating pressure variation. *Materials Science & Engineering A*, *208*(1), 20–29. https://doi.org/10.1016/0921-5093(95)10046-6

Mi, J., Figliola, R. S., & Anderson, I. E. (1997). A numerical investigation of gas flow effects on high-pressure gas atomization due to melt tip geometry variation. *Metallurgical and Materials Transactions B*, *28*(5), 935–941. https://doi.org/10.1007/s11663-997-0021-7

Milewski, J. O. (2017). *Additive manufacturing of metals: From fundamental technology to rocket nozzles, medical implants, and custom jewelry* (Vol. 258). Springer International Publishing. https://doi.org/10.1007/978-3-319-58205-4

Miller, R. S., Miller, S. A., Savkar, S. D., & Mourer, D. P. (1996). Two phase flow model for the close-coupled atomization of metals. *International Journal of Powder Metallurgy*, *32*(4), 341–352.

Mirschinka, D. (2022). *Experimental investigation of primary mechanisms in supersonic gas atomization employing optical measurement techniques* [Master thesis]. Technical University of Darmstadt. Institute for Fluid Mechanics and Aerodynamics.

Moreau, C. (2018). *The state of 3D printing: The data you need to understand the 3D printing world and build your 3D printing strategy: Edition 2018* (Sculpteo, Ed.; tech. rep.). Sculpteo. Villejuif (France).

Motaman, S., Mullis, A. M., Cochrane, R. F., & Borman, D. J. (2015). Numerical and experimental investigations of the effect of melt delivery nozzle design on the open- to closed-wake transition in closed-coupled gas atomization. *Metallurgical and Materials Transactions B*, *46*(4), 1990–2004. https://doi.org/10.1007/s11663-015-0346-6

Motaman, S., Mullis, A. M., Cochrane, R. F., McCarthy, I. N., & Borman, D. J. (2013). Numerical and experimental modelling of back stream flow during close-coupled gas atomization. *Computers & Fluids*, *88*, 1–10. https://doi.org/10.1016/j.compfluid.2013.08.006

Mueller, T. J., Sule, W. P., Fanning, A. E., Giel, T. V., & Galanga, F. L. (1972). *Analytical and experimental study of axisymmetric truncated plug nozzle flow fields* (National Aeronautics and Space Administration, Ed.; tech. rep. No. UNDAS-TN-601-FR-10). University of Notre Dame. Notre Dame (IN, USA).

Mullis, A. M., McCarthy, I. N., & Cochrane, R. F. (2011). High speed imaging of the flow during close-coupled gas atomisation: Effect of melt delivery nozzle geometry. *Journal of Materials Processing Technology*, *211*, 1471–1477. https://doi.org/10.1016/j.jmatprotec.2011.03.020

Mullis, A. M., McCarthy, I. N., Cochrane, R. F., & Adkins, N. (2012). Investigation of pulsation phenomenon in close-coupled gas atomization. In Metal Powder Industries Federation (Ed.), *Proceedings of the 2012 international conference on powder metallurgy & particulate materials.*

Nasuti, F., & Onofri, M. (2001). Prediction of open and closed wake in plug nozzles. In European Space Agency (Ed.), *Proceedings of the 4th European symposium on aerothermodynamics for space vehicles* (pp. 585–592, Vol. SP-487).

Neikov, O. D., Naboychenko, S. S., & Yefimov, N. A. (2019). *Handbook of non-ferrous metal powders: Technologies and applications* (2nd ed.). Elsevier. https://doi.org/10.1016/C2014-0-03938-X

Odenthal, H.-J., Vogl, N., Brune, T., Apell, N., Roisman, I. V., & Tropea, C. (2021). Recent modeling approaches to close-coupled atomization for powder production. In The Austrian Society for Metallurgy and Materials (Ed.), *Proceedings of the 9th international conference on modeling and simulation of metallurgical processes in steelmaking* (pp. 654–665).

Otsu, N. (1979). A threshold selection method from gray-level histograms. *IEEE Transactions on Systems, Man, and Cybernetics*, *9*(1), 62–66. https://doi.org/10.1109/TSMC.1979.4310076

Panão, M. R. O. (2023). Why drop size distributions in sprays fit the lognormal. *Physics of Fluids*, *35*(1), 011701. https://doi.org/10.1063/5.0135510

Park, B. K., Lee, J. S., & Kihm, K. D. (1996). Comparative study of twin-fluid atomization using sonic or supersonic gas jets. *Atomization and Sprays*, *6*(3), 285–304. https://doi.org/10.1615/AtomizSpr.v6.i3.30

Pérez-de León, G., Lamberti, V., Seals, R. D., Abu-Lebdeh, T., & Hamoush, S. (2016). Gas atomization of molten metal: Part I. Numerical modeling conception. *9*, 303–322. https://doi.org/10.3844/ajeassp.2016.303.322

Raffel, M., Willert, C. E., Scarano, F., Kähler, C. J., Wereley, S. T., & Kompenhans, J. (2018). *Particle image velocimetry* (3rd ed.). Springer International Publishing. https://doi.org/10.1007/978-3-319-68852-7

Rao, K. P., & Mehrotra, S. P. (1981). Effect of process variables on atomization of metals and alloys. *Modern Developments in Powder Metallurgy*, *12*, 113–130.

Reitz, R. D. (1978). *Atomization and other breakup regimes of a liquid jet* [Dissertation]. Princeton University. Department of Mechanical and Aerospace Engineering.

Reitz, R. D., & Bracco, F. V. (1986). Mechanisms of breakup of round liquid jets. In N. P. Cheremisinoff (Ed.), *Encyclopedia of fluid mechanics* (pp. 233–249, Vol. 3). Gulf Publishing Company.

Ridder, S. D., & Biancaniello, F. S. (1988). Process control during high pressure atomization. *Materials Science and Engineering*, *98*, 47–51. https://doi.org/10.1016/0025-5416(88)90124-3

Ridder, S. D., Osella, S., Espina, P., & Biancaniello, F. S. (1992). Intelligent control of particle size distribution during gas atomization. *International Journal of Powder Metallurgy*, *28*(2), 133–147.

Sarkar, S., Pimpalnerkar, S., Rogberg, B., Sivapresad, S., & Bakshi, S. (2011). Numerical modelling of gas and liquid metal flow in atomization chamber during powder production. In Institute for Liquid Atomization and Spray Systems (Ed.), *Proceedings of the 24th European conference on liquid atomization & spray systems*.

Sarkar, S., Sivaprasad, P. V., & Bakshi, S. (2016). Numerical modeling and prediction of particle size distribution during gas atomization of molten tin. *Atomization and Sprays*, *26*(1), 23–51. https://doi.org/10.1615/AtomizSpr.2015011680

Schrimpl, T. (2021). *Experimental investigation of the close-coupled atomization using the phase Doppler measurement technique* [Bachelor thesis]. Technical University of Darmstadt. Institute for Fluid Mechanics and Aerodynamics.

Schwenck, D., Ellendt, N., Fischer-Bühner, J., Hofmann, P., & Uhlenwinkel, V. (2017). A novel convergent–divergent annular nozzle design for close-coupled atomisation. *Powder Metallurgy*, *60*(3), 198–207. https://doi.org/10.1080/00325899.2017.1291098

Settles, G. S. (2001). *Schlieren and shadowgraph techniques: Visualizing phenomena in transparent media*. Springer. https://doi.org/10.1007/978-3-642-56640-0

Shi, Y., Lu, W., Sun, W., Zhang, S., Yang, B., & Wang, J. (2022). Impact of gas pressure on particle feature in Fe-based amorphous alloy powders via gas atomization: Simulation and experiment. *Journal of Materials Science & Technology*, *105*, 203–213. https://doi.org/10.1016/j.jmst.2021.06.075

Si, C., Tang, X., Zhang, X., Wang, J., & Wu, W. (2017). Characteristics of 7055Al alloy powders manufactured by gas-solid two-phase atomization: A comparison with gas atomization process. *Materials & Design*, *118*, 66–74. https://doi.org/10.1016/j.matdes.2017.01.028

Simon, I., & Gurley, M. (2022). *3D printing trend report 2022* (Hubs, Ed.; tech. rep.). Hubs. Amsterdam (Netherlands).

Slotwinski, J. A., & Garboczi, E. J. (2015). Metrology needs for metal additive manufacturing powders. *JOM*, *67*(3), 538–543. https://doi.org/10.1007/s11837-014-1290-7

Spurk, J. H., & Aksel, N. (2020). *Fluid mechanics* (3rd ed.). Springer International Publishing. https://doi.org/10.1007/978-3-030-30259-7

Srivastava, V. C., & Ojha, S. (2006). Effect of aspiration and gas-melt configuration in close coupled nozzle on powder productivity. *Powder Metallurgy*, *49*, 213–218. https://doi.org/10.1179/174329006X128304

Sule, W. P., & Mueller, T. J. (1973). Annular truncated plug nozzle flowfield and base pressure characteristics. *Journal of Spacecraft and Rockets*, *10*(11), 689–695. https://doi.org/10.2514/3.61949

Sun, T., Ly, D., & Teja, A. S. (1995). Densities of acetic acid + water mixtures at high temperatures and concentrations. *Industrial & Engineering Chemistry Research*, *34*(4), 1327–1331. https://doi.org/10.1021/ie00043a038

Teja, A. S., & Rice, P. (1981). Generalized corresponding states method for the viscosities of liquid mixtures. *Industrial & Engineering Chemistry Fundamentals*, *20*(1), 77–81. https://doi.org/10.1021/i100001a015

The International Association for the Properties of Water and Steam. (2007). *Revised release on the IAPWS industrial formulation 1997 for the thermodynamic properties of water and steam* (The International Association for the Properties of Water and Steam, Ed.; tech. rep. No. IAPWS R7-97(2012)). The International Association for the Properties of Water and Steam. Lucerne (Switzerland).

The International Association for the Properties of Water and Steam. (2008). *Release on the IAPWS formulation 2008 for the viscosity of ordinary water substance* (The International Association for the Properties of Water and Steam, Ed.; tech. rep. No. IAPWS R12-08). The International Association for the Properties of Water and Steam. Berlin (Germany).

The International Association for the Properties of Water and Steam. (2014). *Revised release on surface tension of ordinary water substance* (The International Association for the Properties of Water and Steam, Ed.; tech. rep. No. IAPWS R1-76(2014)). The International Association for the Properties of Water and Steam. Moscow (Russia).

Thompson, J. S., Hassan, O., Rolland, S. A., & Sienz, J. (2016). The identification of an accurate simulation approach to predict the effect of operational parameters on the particle size distribution (PSD) of powders produced by an industrial close-coupled gas atomiser. *Powder Technology*, *291*, 75–85. https://doi.org/10.1016/j.powtec.2015.12.001

Ting, J., & Anderson, I. E. (2004). A computational fluid dynamics (CFD) investigation of the wake closure phenomenon. *Materials Science & Engineering A*, *379*(1), 264–276. https://doi.org/10.1016/j.msea.2004.02.065

Ting, J., Peretti, M. W., & Eisen, W. B. (2002). The effect of wake-closure phenomenon on gas atomization performance. *Materials Science & Engineering A*, *326*(1), 110–121. https://doi.org/10.1016/S0921-5093(01)01437-X

Tong, M., & Browne, D. J. (2007). Modelling melt-gas dynamic interaction during initial stage gas atomisation of liquid intermetallic using a front tracking formulation. In The Minerals, Metals & Materials Society (Ed.), *Proceedings of the 2007 international symposium on liquid metal processing and casting.*

Tong, M., & Browne, D. J. (2008). Direct numerical simulation of melt–gas hydrodynamic interactions during the early stage of atomisation of liquid intermetallic. *Journal of Materials Processing Technology*, *202*(1), 419–427. https://doi.org/10.1016/j.jmatprotec.2007.10.012

Tropea, C., Xu, T.-H., Onofri, F., Géhan, G., Haugen, P., & Stieglmeier, M. (1996). Dual-mode phase-Doppler anemometer. *Particle & Particle Systems Characterization*, *13*(2), 165–170. https://doi.org/10.1002/ppsc.19960130216

Ünal, A. (1987). Effect of processing variables on particle size in gas atomization of rapidly solidified aluminium powders. *Materials Science and Technology*, *3*, 1029–1039. https://doi.org/10.1179/mst.1987.3.12.1029

Ünal, A. (1989a). Flow separation and liquid rundown in a gas-atomization process. *Metallurgical and Materials Transactions B*, *20*(5), 613–622. https://doi.org/10.1007/BF02655918

Ünal, A. (1989b). Liquid break-up in gas atomization of fine aluminum powders. *Metallurgical and Materials Transactions B*, *20*(1), 61–69. https://doi.org/10.1007/BF02670350

Ünal, R. (2006). The influence of the pressure formation at the tip of the melt delivery tube on tin powder size and gas/melt ratio in gas atomization method. *Journal of Materials Processing Technology*, *180*(1-3), 291–295. https://doi.org/10.1016/j.jmatprotec.2006.06.018

Ünal, R. (2007a). Improvements to close coupled gas atomisation nozzle for fine powder production. *Powder Metallurgy*, *50*(1), 66–71. https://doi.org/10.1179/174329007X164899

Ünal, R. (2007b). Investigation on metal powder production efficiency of new convergent divergent nozzle in close coupled gas atomisation. *Powder Metallurgy*, *50*(4), 302–306. https://doi.org/10.1179/174329007X189595

Upadhyaya, G. S. (2002). *Powder metallurgy technology*. Cambridge International Science Publishing.

Urionabarrenetxea, E., Avello, A., Rivas, A., & Martín, J. M. (2021). Experimental study of the influence of operational and geometric variables on the powders produced by close-coupled gas atomisation. *Materials & Design*, *199*, 109441. https://doi.org/10.1016/j.matdes.2020.109441

Urionabarrenetxea, E., Martín, J. M., Avello, A., & Rivas, A. (2022). Simulation and validation of the gas flow in close-coupled gas atomisation process: Influence of the inlet gas pressure and the throat width of the supersonic gas nozzle. *Powder Technology*, *407*, 117688. https://doi.org/10.1016/j.powtec.2022.117688

Urionabarrenetxea, E., Martín, J. M., Rivas, A., Iturriza, I., & Castro, F. (2013). Experiamental study and simulation of the gas flow in the atomisation chamber during close-coupled gas atomisation. In European Powder Metallurgy Association (Ed.), *Proceedings of the 2013 European powder metallurgy congress and exhibition* (pp. 257–262, Vol. 2).

Urionabarrenetxea, E., Martín, J. M., Rivas, A., Iturriza, I., & Castro, F. (2014). Influence of key operational and geometrical variables on the particle size during close-coupled gas atomisation. In European Powder Metallurgy Association (Ed.), *Proceedings of the 2014 European powder metallurgy congress and exhibition.*

VDI Society Chemical and Process Engineering (Ed.). (2010). *VDI heat atlas* (2nd ed.). Springer. https://doi.org/10.1007/978-3-540-77877-6

Vogl, N., Odenthal, H.-J., Hüllen, M., Luh, M., Roisman, I. V., & Tropea, C. (2019). Physical and numerical modeling of close-coupled atomization processes for metal powder production. In Steel Institute VDEh (Ed.), *Proceedings of the 4th European steel technology and application days.*

vom Stein, H. D., & Pfeifer, H. J. (1969). A Doppler difference method for velocity measurements. *Metrologia*, *5*(2), 59–61. https://doi.org/10.1088/0026-1394/5/2/006

Wang, M.-R., & Chen, P.-J. (2012). Mechanism and performance of a novel supersonic atomizer for metal powder production. In University of Auckland (Ed.), *Proceedings of the 23rd international symposium on transport phenomena* (pp. 435–440).

Wang, P., Anderko, A., & Young, R. D. (2011). Modeling surface tension of concentrated and mixed-solvent electrolyte systems. *Industrial & Engineering Chemistry Research*, *50*(7), 4086–4098. https://doi.org/10.1021/ie101915n

Wang, P., Li, J., Liu, H.-S., Wang, X., Du, B.-R., Gan, P., Shen, S.-Y., Fan, B., Ge, X.-Y., & Wang, M.-H. (2021). Process modeling gas atomization of close-coupled ring-hole nozzle for 316L stainless steel powder production. *Chinese Physics B*, *30*(5), 057502. https://doi.org/10.1088/1674-1056/abd771

Weber, D., & Leick, P. (2014). Structure and velocity field of individual plumes of flashing gasoline direct injection sprays. In Institute for Liquid Atomization and Spray Systems (Ed.), *Proceedings of the 26th European conference on liquid atomization & spray systems* (p. 176).

Wei, M., Chen, S., Sun, M., Liang, J., Liu, C., & Wang, M. (2020). Atomization simulation and preparation of 24CrNiMoY alloy steel powder using VIGA technology at high gas pressure. *Powder Technology*, *367*, 724–739. https://doi.org/10.1016/j.powtec.2020.04.030

Wieneke, B. (2015). PIV uncertainty quantification from correlation statistics. *Measurement Science and Technology*, *26*(7), 074002. https://doi.org/10.1088/0957-0233/26/7/074002

Wohlers, T., Campbell, R. I., Diegel, O., Kowen, J., Mostow, N., & Fidan, I. (2022). *Wohlers report 2022: 3D printing and additive manufacturing: Global state of the industry*. Wohlers Associates; ASTM International.

Wolf, G., & Bergmann, H. W. (2002). Investigations on melt atomization with gas and liquefied cryogenic gas. *Materials Science & Engineering A*, *326*(1), 134–143. https://doi.org/10.1016/S0921-5093(01)01433-2

Xu, Z., Wang, T., & Che, Z. (2020). Droplet deformation and breakup in shear flow of air. *Physics of Fluids*, *32*(5), 052109. https://doi.org/10.1063/5.0006236

Xu, Z., Wang, T., & Che, Z. (2022). Droplet breakup in airflow with strong shear effect. *Journal of Fluid Mechanics*, *941*, A54. https://doi.org/10.1017/jfm.2022.326

Yang, L., Hsu, K., Baughman, B., Godfrey, D., Medina, F., Menon, M., & Wiener, S. (2017). *Additive manufacturing of metals: The technology, materials, design and production*. Springer International Publishing. https://doi.org/10.1007/978-3-319-55128-9

Zeoli, N., & Gu, S. (2006). Numerical modelling of droplet break-up for gas atomisation. *Computational Materials Science*, *38*(2), 282–292. https://doi.org/10.1016/j.commatsci.2006.02.012

Zeoli, N., & Gu, S. (2008a). Computational simulation of metal droplet break-up, cooling and solidification during gas atomisation. *Computational Materials Science*, *43*(2), 268–278. https://doi.org/10.1016/j.commatsci.2007.10.005

Zeoli, N., & Gu, S. (2008b). Computational validation of an isentropic plug nozzle design for gas atomisation. *Computational Materials Science*, *42*(2), 245–258. https://doi.org/10.1016/j.commatsci.2007.07.013

Zeoli, N., Tabbara, H., & Gu, S. (2011). CFD modeling of primary breakup during metal powder atomization. *Chemical Engineering Science*, *66*(24), 6498–6504. https://doi.org/10.1016/j.ces.2011.09.014

Zeoli, N., Tabbara, H., & Gu, S. (2012). Three-dimensional simulation of primary break-up in a close-coupled atomizer. *Applied Physics A*, *108*(4), 783–792. https://doi.org/10.1007/s00339-012-6966-7

Zerwas, A. A., Avila, K., de Paiva, J. L., Guardani, R., Achelis, L., & Fritsching, U. (2021). Image analysis of the atomization process in a molten metal close-coupled atomizer for different gas pressures and temperature. In Institute for Liquid Atomization and Spray Systems (Ed.), *Proceedings of the 15th international conference on liquid atomization & spray systems* (p. 38, Vol. 1). https://doi.org/10.2218/iclass.2021.5813

Zhang, S., Alavi, S., Kashani, A., Ma, Y., Zhan, Y., Dai, W., Li, W., & Mostaghimi, J. (2021). Simulation of supersonic high-pressure gas atomizer for metal powder production. *Journal of Thermal Spray Technology*, *30*(7), 1968–1994. https://doi.org/10.1007/s11666-021-01256-1

Zhao, W., Cao, F., Ning, Z., Zhang, G., Li, Z., & Sun, J. (2012). A computational fluid dynamics (CFD) investigation of the flow field and the primary atomization of the close coupled atomizer. *Computers & Chemical Engineering*, *40*, 58–66. https://doi.org/10.1016/j.compchemeng.2012.02.014

Nomenclature

Lowercase Greek Letters

γ	$-$	Directional cosine
κ	$-$	Heat capacity ratio
λ	m	Wavelength
μ	Pa s	Dynamic viscosity
ϕ	°	Off-axis angle
φ	°	Scattering angle
ψ	°	Elevation angle
ρ	$\mathrm{kg\,m^{-3}}$	Density
σ	$\mathrm{N\,m^{-1}}$	Surface tension
ϑ	%	Validation

Uppercase Greek Letters

$\Delta\Phi$	rad	Phase difference
Δh	m	Height difference
Δp	Pa	Relative pressure
Δu	$\mathrm{m\,s^{-1}}$	Velocity difference
ΔT	K	Temperature difference

Θ	°	Intersection angle

Lowercase Roman Letters

a	$\mathrm{m\,s^{-1}}$	Speed of sound
c	$\mathrm{m^{-3}}$	Particle number concentration
d	m	Diameter
f	Hz	Frequency
g	$\mathrm{m\,s^{-2}}$	Gravitational acceleration
l	m	Length
m	kg	Mass
n	–	Number
p	Pa	Pressure
q	$\mathrm{N\,s\,m^{-2}\,s^{-1}}$	Momentum flux
r	m	Radial coordinate
s	Variable	Standard deviation
t	s	Time
u	$\mathrm{m\,s^{-1}}$	Velocity
w	–	Normalized weighting factor
$\{x, y, z\}$	m	Cartesian coordinates

Uppercase Roman Letters

C	Variable	Fitting parameter
C_d	–	Discharge coefficient

F_{Φ}	$\mathrm{m\,rad^{-1}}$	Phase conversion factor
K	–	Coverage factor
L	m	Burst length
M	–	Relative refractive index
N	–	Scattering order
T	K	Temperature
V	$\mathrm{m^3}$	Volume

Dimensionless Numbers

GLR	Gas-to-liquid ratio
Ma	Mach number
Oh	Ohnesorge number
PR	Pressure ratio
Re	Reynolds number
We	Weber number

Subscripts

$\perp$	Perpendicular
0	Initial
0.25	Lower quartile
0.5	Median
0.75	Upper quartile
32	Sauter mean

a	Ambient
asp	Aspiration
ax	Axial
back	Back
b	Beam
boot	Bootstrap
burst	Burst
c	Compressed
close	Wake closure
crit	Critical
data	Data
def	Deformation
det	Detection
dist	Disturbance
D	Doppler
e	Exit
g	Gas
img	Image
l	Liquid
max	Maximum
meas	Measurement
min	Minimum
p	Particle

pl	Planar
r	Receiver
rad	Radial
seg	Segment
shock	Shock
s	Spatial slit filter
st	Standard
t	Stagnation
tan	Tangential
tip	Tip
trans	Transit

Superscripts

$*$	Nozzle throat

Diacritical Marks

$\bar{\square}$	Arithmetic mean
$\dot{\square}$	Flow rate
$\hat{\square}$	Global statistic
$\tilde{\square}$	Non-dimensional

Abbreviations

AM	Additive manufacturing
CCA	Close-coupled atomization

CDF	Cumulative distribution function
DNS	Direct Numerical Simulation
DoF	Depth of Field
ELSA	Eulerian-Lagrangian Spray Atomization
FoV	Field of view
IA	Interrogation area
IGSTC	Indo German Science & Technology Centre
IISc	Indian Institute of Science Bengaluru
IIT	Indian Institute of Technology Kharagpur
LES	Large Eddy Simulation
PBF-L	Laser-based powder bed fusion
PDF	Probability density function
PIV	Particle image velocimetry
PPAM	Metal Powder Production for Additive Manufacturing
SEM	Scanning electron microscopy
SLA	Institute for Fluid Mechanics and Aerodynamics
SMS	SMS group GmbH
SNR	Signal-to-noise ratio
SoC	Sum-of-Correlation
TAB	Taylor Analogy Breakup
TUDa	Technical University of Darmstadt
VoF	Volume-of-Fluid

List of Figures

List of Tables